The Effect of Material Properties and Hemodynamics on Healing of Vascular Grafts in Baboons

A Thesis
Presented to
The Academic Faculty

by

James Robert Costello

In Partial Fulfillment
of the Requirements for the Degree
Doctor of Philosophy
from the
Wallace H. Coulter School of Biomedical Engineering

Georgia Institute of Technology
January 2004

The Effect of Material Properties and Hemodynamics on Healing of Vascular Grafts in Baboons

DATE APPROVED: 02/09/04

Don P. Giddens, Co-Chairman

Stephen R. Hanson, Co-Chairman

Robert M. Nerem

Hanjoong Jo

Changyi Chen

Dedication

This work is dedicated to my grandmother, Helen Brust.

Acknowledgements

In the completion of this work, I received invaluable help from many gracious people. Without this assistance, I would still be toiling away at this project. First and foremost, I would like to thank Dr. Giddens and Dr. Hanson for their guidance and tutelage during these years. Their insightful advice helped clarify otherwise very confusing issues. More importantly, their model for success will leave a lasting impression and will help mold many decisions and choices offset in the near future. On a career pathway, we seek examples of how others conduct themselves both professionally and personally. Both Dr. Giddens and Dr. Hanson accomplish this feat with grace and unspoken eloquence.

My thesis committee furnished many vital resources needed to complete this work. I would like to thank Dr. Chen for performing the surgical procedures. This work involved much effort on his behalf and for that I am very appreciative. Through the help of Dr. Nerem and the Georgia Tech Emory Center for Living Tissue, I acquired several important resources towards the completion of this study. Dr. Jo always offered a receptive ear in regards to rising concerns and challenges.

I am very thankful for the assistance of the Hanson lab family. I would like to particularly thank Steven Marzec for his computer assistance and friendship over the past four years. Through his help, I always had access to every available computer resource. Most importantly, his companionship will be missed. I am very grateful for the friendship and assistance from the Hanson lab family. Min Hui Ma, Ulla Marzec, Harry Kotze, and Tammy Hails always provided a forthgiving hand and encouraging support.

Likewise, I am very grateful for the friendships that were fostered in Dr. Gidden's lab. I would like to particularly thank Amanda Wake, Annica Wayman, Cecilia Curry, Dan Karolyi, Suo Jin, Narcisse N'Dri, and Joanne Wheately.

I would like to thank Dr. Oshinski for his very gracious assistance with the MRI scanning and to acknowledge Dr. Apkarian and Jeannette for their help with the Scanning Electron Microscopy.

In addition, I would like to thank the Emory University and Georgia Institute of Technology M.D./Ph.D. program for the opportunity to pursue this graduate work. In addition, I am very appreciative for the financial assistance offered by the Gellerstedt family endowment.

Lastly, I would like to thank my family for their encouraging words and loving care during this long journey. Without their help, many of the disappointments would have seemed far more daunting. Thank you, always.

Table of Contents

List of Tables

List of Figures

Nomenclature

α	Womersley number
b-FGF	Basic fibroblast growth factor
CFD	Computational fluid dynamics
ePTFE	Expanded polytetrafluoroethylene
ID	Inner diameter
μ	Dynamic viscosity
OSI	Oscillatory shear index
PDGF	Platlet derived growth factor
ρ	Density
Q	Volumetric flow rate
RBC	Red blood cell
Re	Reynold's number
Sc	Schmidt number
$\tau avg(z)$	Spatially averaged temporal mean WSS
$\tau_s(z,t)$	Spatially averaged WSS
TGF-β	Tumor growth factor
TNF	Tumor necrosis factor
VEGF	Vascular endothelial growth factor
VWF	Von willebrand factor
WSS	Wall shear stress

Summary

Each year, more than one million prosthetic vascular grafts are implanted. Well-over 50 % of these artificial vessels are of the small caliber variety with an inner diameter less than or equal to 10 mm. The challenge rests in implanting these synthetic substitutes into a hemodynamic environment with a high downstream resistance and low rates of flow.

Over the course of four interrelated studies, we investigated the healing properties of small caliber prosthetic vascular grafts. All of these studies were conducted using baboons (*papio cynecepahlus*). First, we documented the difference in healing response between three different types of vascular grafts: (1) autologous artery (2) allogeneic vessel (3) prosthetic ePTFE. This comparison furnished an important model of graft healing. In addition, our study presented a novel method for measuring intimal thickness and used this tool to document morphometric details of the neointima's leading edge. Proliferating endothelial cells were localized to the top 10 % of the neointima, increasing in concentration towards the leading edge, while the proliferating smooth muscle cells were identified within the lower 10 % of the neointima, increasing in concentration near the anastomosis.

Secondly, we examined the effects of changing a prosthetic graft's material properties and how that change impacts healing of the graft's surface. These ultrastructural changes were introduced by radially stretching a porous 60 μm ePTFE vascular graft. Changes to graft ultrastructure were documented with morphometric analysis of void fraction, internodal distance, graft thickness, and nodal width. Radially

stretching the graft material decreased the void fraction, reduced the potential for transmural ingrowth, and changed the healing characteristics of the implanted vessels.

Thirdly, we investigated the effect of a changing hemodynamic environment upon the healing of a vascular graft with uniform material properties. The changing hemodynamics were generated with a stenotic model rather than with a variation in the volumetric flow rate. Under sub-acute conditions, an inverse relationship failed to exist between intimal thickening and wall shear stress. The recent deposition of the shear-rate responsive endothelium explained this observation.

Lastly, the details of this hemodynamic environment were documented with computational fluid dynamics (CFD). The computational grids were constructed using three sets of geometric information: (1) incorporating the ideal material dimensions of the implanted vessel (2) utilizing contour information from pressure-perfused histologic cross-sections (3) applying geometric information form detailed MRI imaging. In the construction of the computational grids, various smoothing algorithms were applied. Pulsatile simulations were conducted using input waveforms from either pulse-transit ultrasound or Phase Contrast Magnetic Resonance Imaging. Grid reconstruction using MRI imaging information provided the best description of the vessel's hemodynamic environment. With this computational information, correlations were made between the intimal thickening of the previously harvested vascular grafts and such hemodynamic parameters as spatially averaged wall shear stress, temporally averaged wall shear stress, pulse wall shear stress, and oscillatory shear index.

Chapter I

Introduction

History of Vascular Grafts

More than one million vascular grafts are implanted each year, generating well over 1 billion dollars in sales [1,2]. Vascular grafts are needed to treat such atherosclerotic manifestations as occlusive or aneurysmal disease. Within the United States atherosclerotic disease targets one out of every four people, resulting in over 40% of all deaths [88]. This staggering percentage emphasizes the need for effective surgical repair.

Vascular graft repair of abdominal and thoracic aneurysms achieves patency rates greater than 95% after five years. Several factors contribute towards this success rate: (1) the flow environment, (2) the low downstream resistance, and (3) the large diameter of the aorta. Long-term patency rates are more challenging for smaller vessels with higher downstream resistance and lower rates of flow. For example, in the treatment of ilio-femoral-popliteal-tibial disease, five-year patency rates are less than 50% [3,89]. Unfortunately, with the inclusion of dialysis access grafts, over 70% of vascular grafts are these small caliber conduits with an inner diameter equal to or less than 10 mm [1,2].

Each year vascular surgeons implant well over 500,000 grafts into these peripheral circulatory beds [4,5]. In addition, well-over 100,000 patients on hemodialysis contend with a monthly reoccurrence of occluded access grafts. Overall, a compelling need arose to enhance the performance of surgically implanted peripheral vascular grafts and to achieve more favorable clinical outcomes [90].

There exists an array of vascular graft types: autologous, allogeneic, synthetic. The surgeon's first choice is an autologous graft such as the saphenous vein or the internal thoracic artery. Nonetheless, in approximately 30 % of patients, autologous vessels will not be used due to pre-existing disease, already utilized, or a size mismatch [6,7]. In response, physicians will usually preserve the saphenous vein for more difficult reconstructions (e.g., femoral-tibial) and use synthetic grafts for less challenging procedures such as femoral-popliteal bypass above the knee [3]. Following World War II, various allografts were implanted but encountered poor success due to robust immune rejection [8,9]. Allogeneic grafts found some renewed acceptance with the development of techniques designed to denature the vessels and remove their antigenicity [2].

Early on, researchers identified the need to engineer synthetic vascular grafts. Initially, these pioneers sought materials with as smooth a surface as possible. They attempted to investigate such materials as metal, glass, or ivory tubes. As expected these primitive attempts were quickly met with failure [10]. Things began to change in 1952 when Voorhees [12] identified a more promising alternative, a woven synthetic graft that promoted healing of its lumenal surface. In an experiment Voorhees placed a silk thread in the right ventricle of a dog's heart, only to find it covered several months later with a "glistening film of thin-fibrous endothelial-like coating." From this finding, Voorhees

concluded that the synthetic mesh of “Vinyon N” cloth promoted the formation of a non-thrombogenic flow surface composed of a tissue coating and fibrin. In 1954, Voorhees, et al., [11, 12] used the new fabric grafts to surgically repair seventeen abdominal aortic aneurysms and one popliteal aneurysm. Subsequently, efforts to develop smooth-walled grafts were abandoned in favor of textured fabric surfaces that promoted tissue ingrowth and healing of the graft surface. This design strategy persists even to today in our continuing investigation of new synthetic grafts.

The success of Voorhees encouraged engineers to develop new synthetic materials for vessel replacement, including knitted and woven Dacron and a modified version of Teflon (expanded polytetrafluoroethylene, or ePTFE). Interestingly, these two materials still comprise the most widely used synthetic vascular prostheses. For small caliber vessel reconstruction, ePTFE remains the standard. Over 30 years after the introduction of ePTFE, researchers and clinicians have achieved little improvement in overall patency rates of these synthetic grafts [3]. Obstacles continuing to limit the success of these small caliber ePTFE grafts are most noticeably (1) thrombosis and (2) pseudointimal hyperplasia. A number of anti-thrombotic agents and graft coatings are under development, although none has received widespread acceptance. Similarly, significant questions still persist with the pathogenesis of pseudointimal hyperplasia and strategies for inhibiting its growth. Until the intricacies of vascular biology are better understood, the development of a successful, small-caliber vascular graft will continue to elude researchers.

Thrombosis

Thrombosis and thromboembolic occlusion pose one of the first challenges to synthetic graft patency. A thrombosis represents an abnormal clotting of a blood vessel. The origins of a thrombus are either primary, resulting from a genetic predisposition involving the coagulation factors, or secondary, resulting from changes in either coagulation factors, blood vessels, or blood flow. As Virchow [92] noted well over 150 years ago, thrombus derives from three possible sources: (1) decreased blood flow or a change in the local hemodynamics (2) vessel injury or inflammation (3) alterations in the rheologic properties. A thrombus consists of two blood cell types: (1) platelets and (2) red blood cells (rbc). These blood cells aggregate with the help of interacting glycoproteins, plasma proteins, and fibrin. This process depends upon three platelet functions (adhesion, activation, and aggregation) and the plasma coagulation cascade. Within arterial systems, a thrombus can consist of either an accumulation of platelets with little fibrin (white thrombus) or an aggregation of red blood cells, fibrin, and relatively few platelets (red thrombus) [93].

To some extent, all synthetic vascular grafts are thrombogenic. Synthetic grafts less than 2 mm in diameter fail acutely due to thrombotic occlusion [13-15]. Even with a diameter of 4 to 6 mm, the grafts demonstrate frequent acute or sub-acute occlusion in

spite of anti-platelet or anticoagulant therapies [16-20]. The thrombosis arises from alterations in the exposed prosthetic surface, varying hematologic and hemodynamic variables, wide-ranging device configurations, and tissue injury at graft-vessel anastomoses [21].

For thrombosis studies, the baboon serves as a very useful animal model with its close rheologic similarity to humans [22]. With this animal model in hand, investigators questioned which of the two most frequently used synthetic grafts (Dacron or ePTFE) was more thrombogenic. In 1989 Schneider [23] concluded through a baboon study of ^{111}In labeled platelets that knitted Dacron was more thrombogenic than ePTFE. Even though researchers identified how the surface chemistry affected thrombosis, no relationship was yet established between the two. Investigators have tried many different approaches to reduce graft thrombogenicity: (1) seeding the grafts with endothelial cells (2) coating the grafts with select polymers (3) administering antithrombotic therapy. Despite these efforts clinical graft patency rates have not significantly improved. This reflects a still incomplete understanding of thrombosis and how it relates to intimal hyperplasia [24-26].

Intimal Hyperplasia

In 1906 Carrel and Guthrie [27] first described the intimal hyperplasia adherent to a vascular bypass anastomosis as closely resembling the endothelium. Later in 1936,

Stchelkounoff [96] reported that the predominant cell type within intimal hyperplasia was a vascular smooth muscle cell. Intimal hyperplasia results from damage to the overlying endothelium, catalyzing a series of events that transform a subset of smooth muscle cells from a contractile state to a synthetic mode. This results in smooth muscle cell proliferation and migration into the neointima. Once in the neointima, the smooth muscle cells begin a second proliferative process, followed by the final stage when they synthesize and deposit a complex extracellular matrix of collagen, elastin, proteoglycans, fibronectin, laminin, dermatan sulfate, and heparin sulfate. This process of smooth muscle cell proliferation, migration, and synthesis of complex extracellular matrix constitutes the basis of intimal hyperplasia. The endothelium, vascular smooth muscle cells, and inflammatory cells influence these sequelae through release of several growth factors and cytokines (PDGF, FGF, VEGF, TGF-β, TNF, tissue factor, thrombin, Angiotensin II, TGF-γ, endothelin, tissue plasminogen activators, metalloproteinases) [28-31, 96]. Platlet Derived Growth Factor (PDGF) and bFGF (basic Fibroblast Growth Factor) are the two growth factors most intimately involved with smooth muscle cell proliferation and migration. BFGF originates from damaged endothelial and vascular smooth muscle cells and directly stimulates proliferation of vascular smooth muscle cells. PDGF-BB derives from platelet α-granules and stimulates migration but not proliferation of smooth muscle cells. Transforming Growth Factor-β, angiotensin II, and bFGF also promote vascular smooth muscle cell migration [97]. Intimal hyperplasia can be found at many different locations within a vessel: (1) scattered throughout the vessel (2) focal to an anastomosis (3) focal to a location within the vessel body. From this intimal

hyperplasia either sub-acute or chronic failure of implanted prosthetic vascular grafts result.

It was not until 1971 that researchers and clinicians first identified that intimal hyperplasia can contribute to vascular graft failure [95]. Approximately 30% of peripheral bypass grafts develop clinically significant stenotic areas within the first year following surgery. For prosthetic vascular grafts, anastomotic intimal hyperplasia causes the overwhelming percentage of patency failures. Several factors contribute towards this troubling sequelae: (1) hemodynamic factors such as separated and disturbed flow (2) compliance mismatch between graft and native vessel (3) biomaterial incompatability with resultant foreign body response (4) mural injury (5) activation of platelets by barren ePTFE material [94].

Graft Healing

Before a vascular graft can develop intimal hyperplasia, the luminal surface must endothelialize. By virtue of its interface between the blood and the vessel wall, the endothelium occupies the important role of regulating vessel wall homeostasis. The endothelium regulates vascular tone through release of nitric oxide and prostacyclin, potentiates an anticoagulated state through the release of heparin sulfate, and recruits an immune response through the release of interleukins that attract inflammatory cells. Furthermore, the endothelium controls the structure of the vessel wall by releasing factors

such as nitric oxide, prostacyclin, and natriuretic peptides to help regulate smooth muscle cell proliferation, migration, and apoptosis. The endothelium regulates the deposition and degradation of underlying extracellular matrix through release of enzymes such as metalloproteinases. Lastly, endothelial cells function as an important physical barrier between growth factors and other circulating hematologic mediators and the underlying vascular smooth muscle cells. Overall, this discourse explains why researchers seek prosthetic materials that promote the healing of a graft surface with a confluent layer of endothelium. Ultimately, this healed surface limits thrombosis and promises to extend long-term graft patency [97-101].

Over the years, researchers documented three possible sources of graft endothelialization. The first and most well chronicled mean occurs by transanastomotic pannus ingrowth. This describes a process whereby adjoining host tissue grows across the anastomosis onto the lumenal surface of the graft. The second avenue operates through fibrous tissue and μ-vessel invasion through the interstices of the synthetic graft's porous wall. Following implantation, perigraft and adhesion tissue deposits on the outside of the graft. This tissue then migrates across the wall of the graft, resulting in growth on the inner flow surface. Interestingly, not until 1995 did researchers document such endothelial ingrowth within a vascular graft implanted into a human [37]. The last channel works through deposition of circulating endothelial or multipotential precursor cells from the circulating blood onto the luminal flow surface of the graft [32-36]. The average normal adult only has 2.6 ± 1.6 circulating endothelial cells per milliliter of blood. This sparse number makes endothelializing a graft by this means increasingly

difficult [102]. Recently, investigations of endothelial cell seeding have found renewed life, but in our discussion, we will focus our attention on the first two mechanisms.

Clowes [38] began the first baboon studies to investigate healing of a clinical, 30 μm ePTFE graft. The baboon serves as an excellent animal model to study endothelialization and general cellular healing response of implanted grafts. Through placement of carotid and aorto-iliac interposition grafts, researchers established that the baboon's healing response closely mirrored that of humans. In his first studies Clowes documented that the endothelium and smooth muscle cells within the ePTFE graft derived from the adjacent arteries' cut ends and grew at a rate of 0.2 mm/day. He showed that the endothelial and smooth muscle cells proliferated at two distinct zones: (1) neointima's leading edge (2) suture-line anastomosis. At the leading edge Clowes reported that smooth muscle cells and endothelial cells proliferated in association. At the anastomosis he concluded that the cell proliferation and the subsequent narrowing resulted from chronic endothelial injury at the surgical suture line and continued turnover of underlying cells resulting in intimal thickening. The frequent turnover of cells results from the dynamic environment of the anastomosis: (1) disturbed, non-laminar blood flow (2) compliance mismatch between host and graft vessels. Even with an intact endothelium, smooth muscle cells continued to proliferate, and extracellular matrix deposition continued [39].

This work led Clowes to ask whether at late times the endothelial cells and smooth muscle cells continued to migrate and to proliferate. Clowes found that at six and twelve months the endothelial cell ingrowth was more advanced than at three months; however, at twelve months, a significant portion of the flow surface still remained

unhealed. In fact, Clowes documented that after twelve months only 60 % of the graft's lumenal surface was endothelialized. Since the surface was not completely healed, endothelial and smooth muscle cell proliferation still persisted. These results contrasted with previous balloon injury studies of native vessels where endothelial and smooth muscle cell proliferation ceased once a confluent endothelium had been established. Once again, these results emphasized the importance of a synthetic graft that promoted confluent healing of the luminal, flow surface [40].

In addition, these studies revealed more about anastomotic healing. At the suture line the percentage of cells to extracellular matrix reached a limiting ratio of 1:4. For long-term implants, this naturally permits for increased intimal thickening and eventual occlusion of the graft lumen [40]. Concurrently, other researchers explored options to inhibit this trans-anastomotic ingrowth that Clowes described. Hanson [41] created a relatively smooth and non-textured graft surface by coating a 30 μm ePTFE vessel with a polymer coating of nonporous silicone and vapor-phase deposited fluoropolymer. This combination coating produced a smooth blood-contacting surface immune from the usual graft porosity and texture of ePTFE. As a result, the coated vessel became immune to ingrowth from adjacent native vessels and effectively prevented vascular lesion formation. While this prevented extensive ingrowth from neighboring native tissue, it also prevented the graft surface from forming a healthy, healed endothelium. Ultimately, this approach resulted in adverse surgical outcomes. In response, investigators questioned whether the solution was found in a graft that allowed for healing across its wall.

Well-established that endothelialization occurred by transanastomotic ingrowth, scientists explored whether the same process happened transmurally. In 1961

Wesolowski and Sawyer [42] concluded that porous synthetic grafts demonstrated improved patency rates through their promotion of fibrous ingrowth from perigraft tissue. In 1962 Florey [43] observed islands of endothelium along Dacron grafts implanted into nonhuman primate subjects. Florey concluded that the endothelium arose from capillary invasion of the graft material and subsequent transmural healing. With a porous 60 μm ePTFE model, Clowes later confirmed that the confluent endothelium derived from transmural capillaries linking the graft lumen to extravascular granulation tissue. Clowes showed that these porous ePTFE grafts were completely covered by one to two weeks with a confluent layer of endothelial cells. Even after three weeks, the endothelial replication rate was still elevated and at a rate that far exceeded that seen in the less porous 30 μm ePTFE. This contrasted with the failure of the transanastomotic ingrowth to completely endothelialize the surface of the 30 μm ePTFE grafts. Intrigued by this result, Clowes investigated an even more porous 90 μm ePTFE graft. Beyond the anastomosis, he observed the same results of endothelial coverage and intimal thickening; however, at focal sites, he observed endothelial loss resulting from instability of the newly deposited intima. Complicating matters further, the 90 μm ePTFE was found to be a very thrombogenic surface. On manual exam, its surface has a rough and textured feel. From these results, Clowes concluded that a 60 μm internodal distance constituted the optimum porosity for a healed ePTFE surface.

Still, uncertain about the dynamics of the vascular biology, Clowes conducted further studies. Upon closer investigation of their luminal surfaces, Clowes used cell specific immunostaining to identify how the smooth muscle cell invaded across the wall of these porous grafts. Ultimately, this cell ingrowth leads to progressive wall thickening,

intimal hyperplasia, and eventual graft failure. Clowes felt that the source of this mitogenic activity came from endothelial, smooth muscle, or perigraft inflammatory cells rather than such circulating cells as platelets. He later proved through *ex vivo* experiments that these vascular wall cells functioned as the primary source of these growth factors [42-47].

Compliance Mismatch

Early on, mechanical factors were recognized as important parameters involved in long-term graft patency. Researchers identified that one of the factors limiting success of prosthetic vascular grafts was their mechanical mismatch with the host vessel. It was long known that the patency of grafted arteries and veins surpassed the patency of prosthetic vascular grafts. Why was this trend observed? Upon physical exam, the prosthetic grafts were found to be much stiffer than the host vessels. Traditionally, investigators described this mechanical difference in terms of the ability of the vessel to dilate under pressure or the so-called compliance. A stiffer or less compliant vessel impedes the transmission of the pulsatile flow wave energy along the course of the arterial tree [148]. This interruption establishes pulsatile mechanical stresses at the anastomosis. These stresses can result in suture-line disruption, formation of a false aneurysm, and development of

subintimal hyperplasia [149]. In all, these events can either result in thrombosis and increased pannus ingrowth at the anastomosis, threatening the patency of the implanted vascular graft.

Hemodynamics

In addition to a compliance mismatch, other mechanical factors were also involved. For many years, researchers have known that hemodynamic factors function as strong regulators of vessel wall structure. Intraluminal pressure governs wall thickness through effects on wall tension [49]. Blood flow influences vessel diameter through changes in shear. With chronically reduced blood flow through a vessel, a structural modification of the arterial wall occurs, leading to a reduction in the arterial diameter [146], while elevations in blood flow culminate in an adaptive expansion of the vessel diameter [147]. This dynamic vessel response is mediated by the endothelium. The hemodynamic effect is pervasive at all points in time. Even in the earliest years of child development, increases in the hemodynamic factors of blood pressure and blood flow result in arteries developing greater wall thickness and a larger luminal caliber to help maintain wall shear stress within the physiologic range of 10 to 30 dynes/cm^2 [50-52]. Naturally, researchers began to question whether there was a relation between such hemodynamic parameters as wall shear stress and intraluminal healing. Intitially, this investigation focused upon examining the pathogenesis of atherosclerotic plaques.

In studies of the abdominal aorta, Fry [53] first postulated that elevated levels of shear stress were promoting growth of the atheroma. Fry concluded that the high shear rates were damaging the endothelium, leading to an increase in lipid permeability, and subsequent enlargement of the atherosclerotic plaque. Researchers later found that this event only occurred when wall shear stress reached an incredibly high value on the order of 400 dynes/cm^2. Other investigators offered an array of alternative theories. Fox [140] asserted flow separation promoted platelet activation and deposition, Mustard [141] contended that "local rapid flow fluctuations" or turbulence promoted atheroma, while Mitchell and Schwartz [142] identified a reduction in fatty streaking within localized areas of low wall shear rate. Many of these ideas contended that the hemodynamics exerted a causative effect upon atherosclerotic plaque formation. Counter to this thinking, Caro [54] claimed that the hemodynamics instead exercised a "controlling effect." In essence, high levels of wall shear stress (WSS) inhibit plaque formation, while low levels of WSS promote its development.

Through a series of experiments involving *in vitro* and *in vivo* work, investigators offered an ever-enlarging voice to Caro's ideas. The work of Zarins, Giddens, et al. [55] convincingly identified a relation between wall shear stress and plaque deposition in the human carotid bifurcation under steady state conditions. They concluded that plaque deposition was minimal near the flow divider (inner wall) where shear stress was high, while plaque deposition was maximal at the outer wall of the carotid sinus where low wall shear stress and separated flow occurred. Ku et al. [56] established the same results in a pulsatile model of the carotid bifurcation. Friedman conducted similar studies within the bifurcation of the abdominal aorta [143], while Friedman [144] and He [145]

examined the complicated coronary vasculature. Even today, researchers still strive to better understand this relationship between vascular biology and hemodynamics.

Graft Healing and Hemodynamics

Native arteries respond to changes in hemodynamics in many ways. As described above, that change can occur by remodeling of vascular architecture or through vasoconstriction/vasodilation of the native vessel. By introducing a model of a rigid, synthetic ePTFE graft, the effect of changes in wall shear stress can be isolated to alterations in vascular architecture. Clowes conducted a number of experiments in baboon models where he exposed the implanted grafts to varying levels of shear stress. With an *in vivo* model he observed that high wall shear stress resulted in a marked decrease in intimal thickening. Through various histologic and immunostaining profiles, he demonstrated how high shear levels decrease intimal area, intimal thickness, and smooth muscle cell proliferation. He documented these results through three different trials in baboon models [59]. In addition, the work demonstrated how an high shear environment can induce an upregulation of constitutive nitric oxide synthetase (cNOS) within the intima of implanted vascular grafts. This nitric oxide exerts a profound ability to inhibit intimal smooth muscle cell proliferation. These observations help to explain the protective benefits of high shear and elevated flow rates.

Stenotic Model

In the past, researchers have used a stenotic model to investigate a varying hemodynamic environment with changes in wall shear stress. The percent area reduction along with the length and shape of the stenosis are all involved in defining this unique hemodynamic environment. The stenotic model provides insight into how the hemodynamic behavior may influence progression of either atherosclerosis or intimal hyperplasia. To a first approximation in a straight vessel segment, WSS varies by the reciprocal of the radius raised to the third power; consequently, small changes in the radial dimension of the vessel result in large changes in wall shear stress. In the past a dog model was used to characterize flow data within different stenoses with varying degrees of a constricted band fitted around the thoracic aorta [60]. This was followed by a similar study conducted with cynomolgus monkeys fed an atherogenic diet. From this work, researchers documented the tendency of flow separation and instability to promote atherogenesis, while increased flow was identified as protecting the vessel from atheroma [149]. Later on, *In vitro* work investigated symmetric stenoses with mild, moderate, or severe occlusions (50 %, 75 %, 90 % reductions in cross luminal area). Within the 50% and 75% symmetric stenosis models, it was found that pulsatile conditions resulted in flow disturbances over a range of Reynold's numbers from 200 – 1000. These disturbances assumed the form of starting structures and puff formations, all of which impacted measured wall shear stress values [61]. Ultimately, the extent to which these

flow disturbances affected the wall shear stress values hinged on the Reynolds number and the percent area reduction of the stenosis.

Future Direction

Overall, vascular biology involves the interaction and the kinetics of many contributing factors. Our ability to design a patent vascular graft hinges on how successful we are in accomplishing two important goals. First and foremost, we need to improve our understanding of vascular biology and its many dynamics. Secondly, with this knowledge in hand, we need to engineer solutions that both limit and promote directed aspects of the vascular biology. In the following discourse, we will address many of these matters.

Chapter II

Characterization of Neointimal Growth for Vascular Grafts Implanted within a Baboon

Introduction:

Researchers continue to seek a small caliber vascular graft immune from failure due to thrombosis and pseudointimal hyperplasia. Many different sources of vascular grafts have been examined: (1) autologous, (2) allogeneic, and (3) prosthetic. Early on, studies identified the following fundamental tenet for a successfully implanted vascular graft - regardless of the vessel source, the luminal surface should heal in a way that most closely mirrors a native, healthy vessel. In 1952 Voorhees [11] paved this road with his experiments using the "Vinyon N" cloth. Soon after, investigators discovered two materials relatively well suited as prosthetic vascular grafts: (1) Dacron and (2) ePTFE (expanded polytetrafluoroethylene), a modified version of Teflon. For large caliber vessels with an inner diameter greater than 10 mm, these materials demonstrated 5-year patency rates of greater than 95 %. The challenge remained in implanting these grafts into small caliber vessels (inner diameter less than 10 mm) where low rates of flow and high downstream resistance frequently resulted in graft occlusion. Starting with Wesolowski's 1961 work [42], researchers identified the importance of fibrous ingrowth onto a graft's surface and how this leads to improved healing properties. In his studies, Wesolowski showed how Dacron grafts implanted into humans evolved a surface covered with fibroblasts, fibrin, and other circulatory cells; however these harvested

vessels failed to show an endothelialized surface. Other researchers such as Berger, Goldman, and Stratton [105-107] suggested that porous Dacron grafts implanted into humans did not develop an endothelium on their luminal surface. This later encouraged Florey and Clowes [33, 39, 40] to investigate the endothelialization of Dacron and ePTFE grafts within such animal models as baboons.

The baboon functions as a very suitable animal model to study neointima formation within an implanted vascular graft. Baboon and human subjects show very similar healing patterns in terms of where, when, and to what extent endothelial and smooth muscle cells migrate and proliferate. Researchers have long recognized a difference in vascular healing response between humans and other animal models such as canines, rabbits, and rats. These differences are not as evident in studies with baboons. The rheologic and genetic make-up of the baboons resembles that of humans better than any other animal model [108,109].

With this powerful tool in hand, Florey [33] demonstrated patchy endothelialization of a porous Dacron graft within a nonhuman primate. Florey thought that the endothelial cells derived from capillaries invading across the graft surface [33]. Much later, Sauvage [10] showed conclusive evidence of endothelialization of a Dacron vascular graft within an axillofemoral bypass of a 65-year-old man. Within this study, Sauvage corroborated Florey's conclusion that endothelialization was occurring by transmural ingrowth across the graft wall. Although Dacron was found to evolve an endothelialized surface, the healing pattern was still very incomplete. This deficient healing pattern originated from a series of sources: (1) increased thrombogenicity, (2) intimal instability during early healing, and (3) toxic product release from the underlying

material. As a result, future work focused its attention on the healing properties of the other synthetic substitute, ePTFE.

Clowes, Reidy and others [25, 39, 40, 44 – 46] investigated the healing properties of ePTFE. Healing of ePTFE grafts, much like Dacron, occurred by transanastomotic ingrowth from adjacent "cut edges" of native tissue onto the luminal surface of the barren graft. Clowes [40] documented that this ingrowth occurred at a rate of 0.2 mm/day. In their studies they compared the differences in healing between ePTFE and an arterial injury model. They created the arterial injury model by using an inflated angioballoon catheter to strip away the endothelium of an otherwise healthy artery. In the absence of an overlying endothelium, the arterial injury model experienced proliferation of smooth muscle cells. Mitogens from circulating blood cells, particularly platelets, lead to this smooth muscle cell migration and proliferation. The smooth muscle cells of a healed ePTFE vascular graft continued to proliferate even in the presence of a confluently, healed endothelial surface. There existed many explanations for this observation. Foremost, researchers believed that the surface of the healed ePTFE graft underwent a chronic "desquamating, nondenuding injury." This chronic injury resulted from several sources: (1) foreign material immunogenicity, (2) flow induced injury at the suture line, and (3) compliance mismatch between the graft and the host vessel. It was observed that the ePTFE healed differently depending upon such material properties as internodal distance. In fact, Clowes [25] documented that the more porous varieties of ePTFE with internodal distances of 60 μm and 90 μm healed by a transmural transport mechanism across the wall of the graft. As mentioned earlier, Florey [33] concluded that a similar mechanism happened with the porous Dacron grafts.

Although several studies investigated the different healing properties of vascular grafts, they failed to document the quantitative differences in intimal thickening among the three varieties: (1) allogeneic, (2) autologous, and (3) prosthetic. In this study we introduced a technique for measuring the intimal thickness as a function of distance along the surface of the three healed varities of vascular grafts. We documented the differences in healing responses of autologous, allogeneic, and prosthetic grafts. Through this investigation we hoped to generate a descriptive model of graft healing and then use that model to evaluate new vascular graft alternatives.

We were also interested in further characterizing the biology of neointima healing within a prosthetic vascular graft. Clowes and others [40, 44, 45] had investigated this topic through several earlier papers. They focused their attention on the dynamics of the neointima's leading edge. Clowes [40] demonstrated that the growing edge of the neointima contained many proliferating cells. At the anastomotic ends, he documented how, even in the presence of a confluent endothelium, the endothelial and smooth muscle cells continued to proliferate, leading to anastomotic narrowing. Clowes divided the graft into three regions for identifying proliferating cells: (1) anastomosis, (2) midzone, and (3) growing edge. Using improved spatial resolution, we wish to identify along the graft's axial direction where the larger percentage of proliferating endothelial and smooth muscle cells are found. At a given axial location, we wish to identify whether that larger percentage of proliferating cells resides near or distantly removed from the flow surface. Moreover, we plan to classify which proliferating cell type predominates at locations within the neointima's thickness.

In summary the purpose of this study was to investigate healing patterns of different vascular grafts. In so doing, we hoped to improve our understanding of early healing events so that greater insight was gained into how to prevent adverse healing outcomes.

Materials and Methods:

Animals.

In this study vascular grafts were implanted into the common carotid artery of juvenile male baboons (*papio cyncephalus / anubis*) of roughly two years of age and weighing between 13-24 kg. All animal procedures followed "Principles of Laboratory Animal Care", the "Guide for the Care and Use of Laboratory Animals" (NIH Publication No. 8023, revised 1985), and IACUC university guidelines.

Grafts.

Three different varieties of vascular grafts were implanted into the baboons. One of the grafts was composed of expanded polytetrafluoroethylene with a 4 mm inner diameter, 2 cm length, and an internodal porosity of 30 μm (Gore-Tex, non-reinforced, thin wall; provided by W.L. Gore and Associates, Inc., Flagstaff, Ariz.). For the second type of vascular graft, a 2 cm section of a baboon's common carotid artery was removed, the direction of the vessel was reversed, and then the vessel was re-implanted into the originating baboon. This variety of vascular graft was termed a (2) reversed autogenous artery. For the third variety, a 2 cm section of a baboon's common carotid artery was removed, and the vessel was then re-implanted into the common carotid artery of a different baboon. In this procedure attention was adhered to implanting the vessel into the same side of the recipient as it was explanted from the donor and into inserting the vessel so that the proximal end of the donor vessel corresponded to the proximal end of the recipient's carotid vasculature. This graft variety was termed an (3) allogeneic vessel.

Graft Placement.

One day prior to surgery, 325 mg of aspirin was administered to the baboon. On the day of surgery, blood samples were drawn to analyze such hemodynamic parameters

as platelet count, hematocrit, and white blood cell count. Under general endotracheal anesthesia with 1.5 to 2.5 % isoflurane, an approximately 1 cm section of the animal's common carotid artery was removed. All surgery was performed by the same surgeon (Changyi Chen M.D., Ph.D.). After isolation of the common carotid artery, 150 units of heparin/kg were infused. All grafts possessed a length of 2 cm, and each variety of vascular graft was implanted into the exposed common carotid artery of individual baboons. The surgical procedure was performed unilaterally. Our surgical site alternated between the right or left side of the animal so that sidedness did not impact our results. Each of the varieties of vascular grafts were implanted into a number of baboon subjects: (1) 30 μm ePTFE {n = 5}; (2) reversed autogenous artery {n = 9}; and (3) allogeneic vessels {n = 4}. Implantation of vascular grafts involved using an end-to-end anastomosis with a continuous running suture of 6.0 polypropylene (Davis & Geck, Wayne, N.J.) (Figure 2.1). An example of an implanted vessel is demonstrated in Figure 2.2.

Vessel Harvest.

All baboon subjects were sacrificed one month following graft placement. Bromodeoxyuridine (BRDU; Sigma Chemical Co., St. Louis, Mo), 50 mg/kg dissolved in 50 ml of normal saline solution, was administered subcutaneously 19, 12, and 7 hours before sacrifice. Prior to vessel harvest, blood samples were once again drawn to analyze hemodynamic parameters. Twenty minutes before sacrificing the

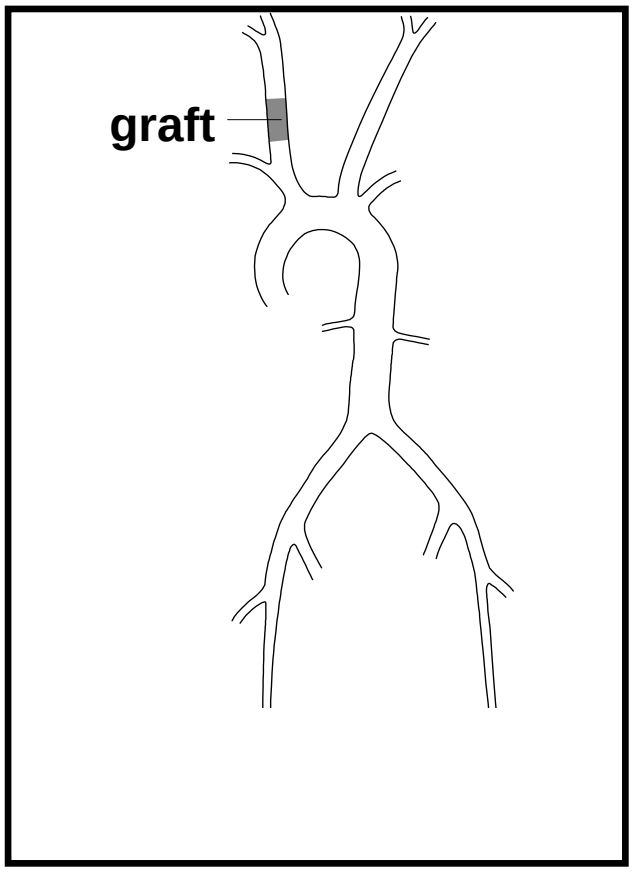

Figure 2.1: Description of Surgical Implantation. Example of isolateral, implanted vascular graft using an end-to-end anastomosis into the common carotid artery of a juvenile, male baboon. Each vascular graft possessed a length of 2 cm and an approximate inner diameter of 4 mm.

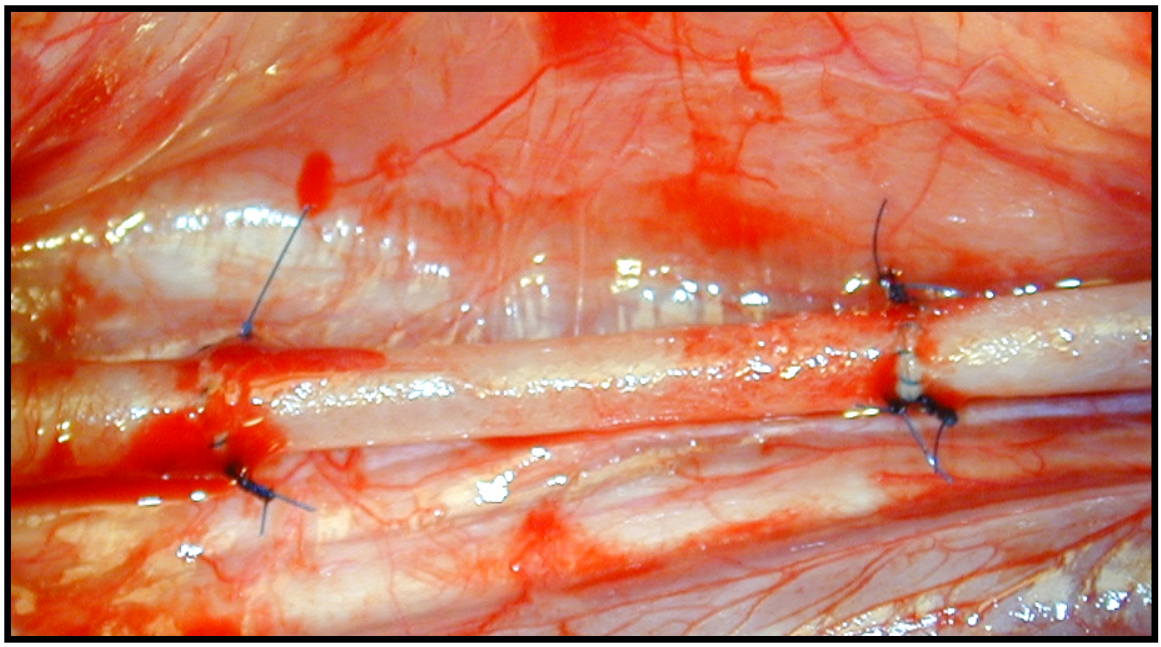

Figure 2.2: Example of an Implanted Allogeneic Vessel. Flow occurs from right to left. Note the blue prolene sutures that signify the proximal and distal anastomoses.

animal, 5000 units of heparin were administered. The animals were sacrificed by exsanguination, and the vascular grafts were harvested along with 1 cm sections of contiguous native vessel at each anastomosis. The vascular grafts were first flushed with lactated Ringer's solution, then pressure perfused with 10 % buffered formalin (Baxter Diagnostics Inc, McGraw Park, Ill) at 100 mmHg mean arterial pressure for thirty minutes, followed by submersion in 10 % buffered formalin for a 24 hour period.

Histology and Morphometry.

The vessels were prepared into longitudinal sections. The grafts were bisected perpendicular to their axial direction. Each respective proximal and distal end was then divided into four longitudinal sections, each spanning 90 radial degrees. Next, we embedded all the partitioned grafts into paraffin and microtomed the blocks parallel to the long axis of the vessel using a 5 μm slice thickness. All grafts underwent staining with Hematoxylin and Eosin (H&E). Morphometric measurements were performed to evaluate neointima thickness on the luminal surface of the 30 μm ePTFE grafts, reversed autogenous arteries, and allogeneic vessels. In the case of the 30 μm ePTFE grafts, the neointima was defined as ingrowth overlying the prosthetic graft surface. For the reversed autogenous artery and the allogeneic vessels, neointima was defined by cell proliferative tissue lying above the internal elastic lamina. All slide specimens were analyzed using a microscope with a 1x objective interfaced to a digital camera that captured all images into a TIFF format. Using the Image-Pro Plus ® Software (Media Cybernetics, Inc.; Silver Spring, Maryland), the average intimal thickness was measured in the following way. The program converted the image of the histologic specimen into a bitmap representation of pixel intensity. This bitmap representation was exported to

MATLAB ® (MathWorks Inc.) where a program called **totalconversionfinal.m** used differences in pixel intensity values to differentiate the two different borders of the overlying neointima: (1) the graft material from the overlying neointima and (2) the neointima from the empty lumen. The program then calculated the intimal thickness between these two borders as a function of axial progression along the length of the graft. The resolution of these measurements corresponded to a one-pixel width or 1/500 of a millimeter. The average intimal thickness of the vessel's four 90^{o} arcs was calculated. For each vessel, this measurement was then averaged between the proximal and distal ends. Finally, for each variety of graft the overall, average intimal thickness and standard deviation were calculated.

Immunocytochemistry and Morphometry.

The avidin-biotin complex immunoperoxidase procedure (LSAB Kit, DAKO Co., Carpenteria, Ca.) was used to differentiate proliferating cells and the different neointimal cell-types. This staining procedure was performed upon all the harvested vessels. CD-34 monoclonal antibody (DAKO Co.) identified T cells within the neointima, while HAM-56 monoclonal antibody (DAKO Co.) pinpointed infiltrating macrophages within the healed grafts. Anti-BRDU monoclonal antibody (DAKO Co.) identified proliferating cells that had uptaken the administered BRDU prior to sacrifice, while monoclonal antibodies to α-actin (DAKO) and Von Willebrand Factor (vWF; Factor VIII related antigen, DAKO) outlined smooth muscle cells and endothelial cells, respectively. Proliferating endothelial and smooth muscle cells were located by identifying cells that simultaneously stained positive for BRDU and VWF or α-actin. Morphometric measurements were performed using stained sections from only the 30 μm ePTFE grafts.

Since both the reversed autogenous artery and the allogeneic vessel evolved very little neointima, this procedure was not performed for these graft types. For the 30 μm ePTFE, the location of the proliferating endothelial and smooth muscle cells was determined within the neointima. As with the measurements of intimal thickness, the slide specimens were analyzed using a microscope with a 1x objective, interfaced to a digital camera that captured all images into a TIFF format. Using the Image-Pro Plus ® Software, a bitmap representation of pixel intensity was made of the histologic specimen. This bitmap representation was exported to MATLAB ® (MathWorks Inc.) where a program called **AOI.M** used the difference in pixel intensity to determine the borders of the neointima and to measure the neointimal area (mm^2). The program then calculated four areas of interest (AOI) within the neointima: (1) top 10 % near the adluminal, flow surface; (2) lower 90 % near the graft surface; (3) lower 10 % near the graft surface; and (4) top 90 % near the adluminal, flow surface. The outlines of these four AOIs were imported into the Image-Pro Plus ® Software. Within Image-Pro a macro called **graft** identified the immunostained cells based on colorimetric and intensity analysis and then used the imported macros to identify the location of the cells within the neointima. Concurrently, the Image-Pro macro calculated several other parameters within each AOI: (1) the total number of cells; (2) the total number of endothelial cells; and (3) the total number of smooth muscle cells. Analyzing the sequential immunostains for BRDU, vWF, and α-actin, the Image-Pro macro distinguished which of the endothelial cells were proliferating and where within the neointima that they were located. Using this table of information, a series of immunostaining index markers were calculated for each AOI: (1) BRDU immunostaining index reflecting the number of proliferating cells divided by the total

number of cells; (2) the proliferating endothelial cell immunostaining index indicating the number of proliferating endothelial cells divided by the number of endothelial cells; and (3) the proliferating smooth muscle cell immunostaining index signifying the number of proliferating smooth muscle cells divided by the total number of smooth muscle cells. These indices were calculated from either the proximal or distal anastomotic junction along the axial length of the graph up to the leading edge of the neointima. These markers were averaged between the proximal and distal locations of each respective vessel.

Statistics.

Statistical analysis was performed on a Pentium IV P.C. with the use of either MATLAB or Excel 2000 statistical software (Microsoft Co.). Comparisons of intimal thickness between the various grafts were made using a Student *t* test (two-tailed). The documented values are given as the mean ± the standard deviation. The results were considered significant if the p value was less than 0.05.

Results:

Patency Rates.

The different vascular grafts demonstrated a range of patency rates (Table 2.1). When grafts occluded, there existed evidence of both red and white thrombi, occluding the entire implanted vessel along with adjacent regions of native vessel distal to the vascular graft.

Table 2.1: Table of Patency Rates for the Various Implanted Vascular Grafts.

Vascular Grafts	**Patency Rates**
Reversed Autogenous Artery	6/9 = 66.7 %
30 μm ePTFE	4/5 = 80.0 %
Allogeneic Vessels	4/4 = 100%

Healing in Harvested Grafts.

In order to understand the different healing responses of implanted vascular grafts, a qualitative analysis of a healthy, native vessel was conducted. Figure 2.3a displays the outlined regions for the biology of a healthy native vessel. The vessel demonstrated a very thin layer of intima (**Int**), comprised almost entirely of endothelial cells. The media (**Med**) consisted of a composite of smooth muscle cells, fibroblasts, and deposited extracellular matrix. The outlying adventitia (**Adv)** was composed of mainly extracellular matrix. For the reversed autogenous artery (Figure 2.3b) the healing pattern differed little from the healthy, native vessel. The only noteworthy difference was found in its slightly accentuated pannus ingrowth at the

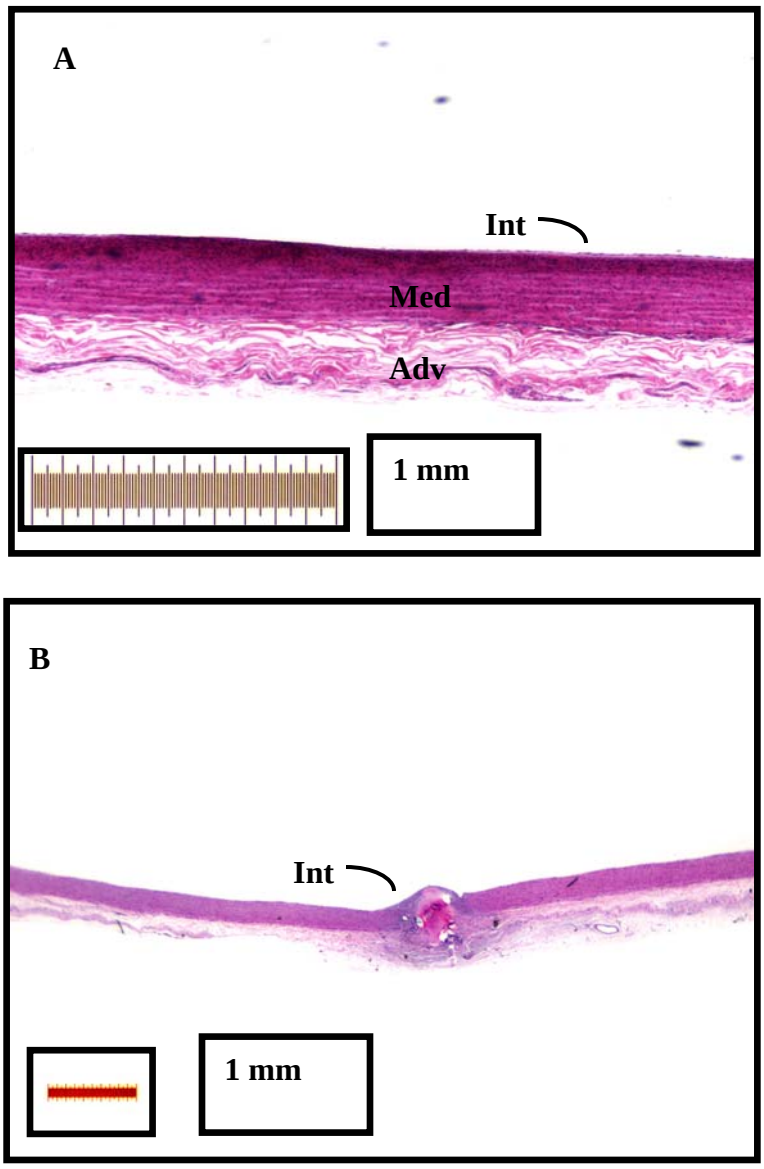

Figure 2.3: H&E Staining of Healthy Native Vessel and Reversed Autogenous Artery. Flow occurs from right to left. (A) Longitudinal cross-section of a healthy, native vessel. (B) Longitudinal cross-section of a reversed autogenous artery.

anastomotic junction. Figure 2.4a displays a quantitative description of average intimal thickness, progressing from the anastomotic junction along the axial length of the vessel. We observed that this pannus ingrowth at the anastomotic end reached a peak value of 0.15 mm. Moving away from the anastomotic end, the average intimal thickness decreased to a plateau of 0.024 mm.

In contrast, the H&E staining of the allogeneic vessel demonstrated more pronounced intimal thickening not only at the anastomosis but also at the mid-vessel point (Figure 2.5a). Its quantitative description of intimal thickening showed a larger amount of neointima at the anastomosis (0.20 mm) and an even higher level of intimal thickening once removed from the suture line (0.06 mm) (Figure 2.4b).

For the 30 μm ePTFE grafts qualitative examination of the H&E slide showed even greater levels of intimal thickening both at the anastomosis and distantly removed from the suture line (Figure 2.5b). In comparison to the other vascular grafts, quantitative examination of the 30 μm ePTFE witnessed the highest anastomotic intimal thickening (0.36 mm) and the highest level of intimal deposition at mid-vessel (0.084 mm) (Figure 2.6).

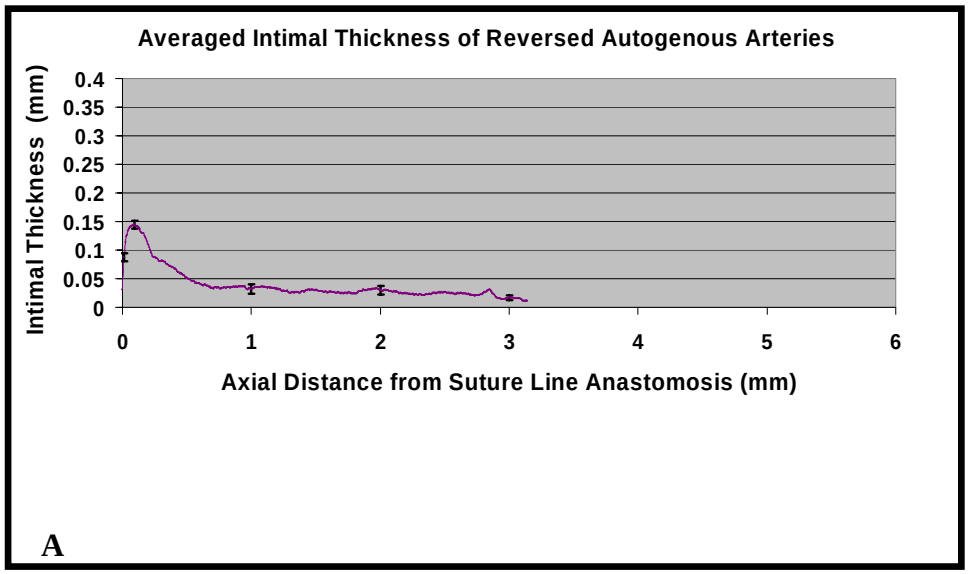

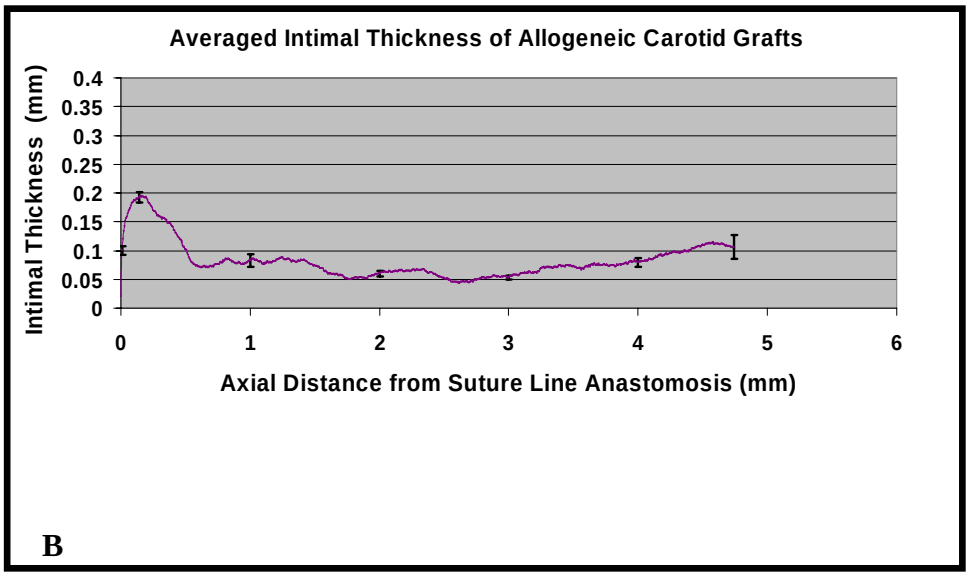

Figure 2.4: Quantitative Description of Intimal Thickening for Reveresed Autogenous Arteries and Allogeneic Vessels. Average intimal thickness as a function of axial distance removed from the anastomotic end of (A) reversed autogenous arteries (B) allogeneic vessels.

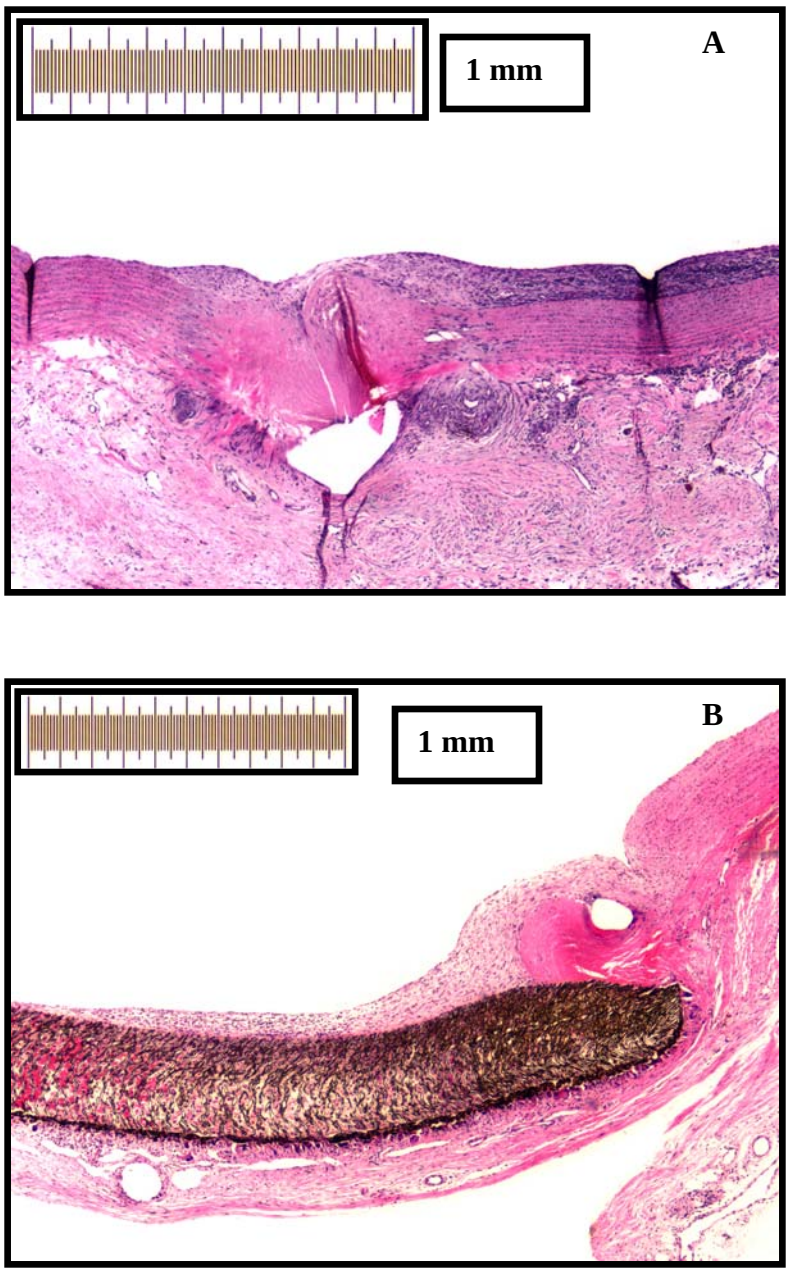

Figure 2.5: H&E Staining of Allogeneic Vessel and 30 μm ePTFE Vascular Graft. Flow occurs from right to left. (A) Longitudinal Cross-Section of an Allogeneic Vessel (B) Longitudinal Cross-Section of a 30 μm ePTFE vascular graft.

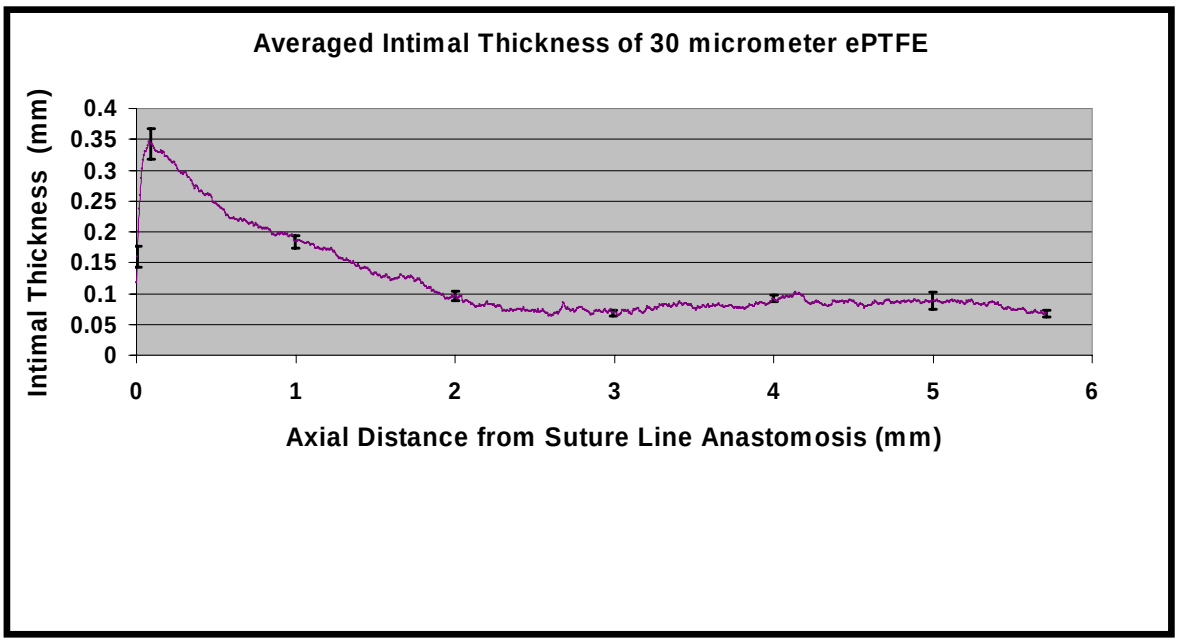

Figure 2.6: Quantitative Desciption of Intimal Thickness for 30 μm ePTFE Vascular Graft.

A statistical comparison was made of the three vascular grafts ((1) reversed autogenous artery, (2) allogeneic vessels, (3) 30 μm ePTFE) and their respective intimal thickenings (Figure 2.7). First, a comparison was made of intimal thickness at the anastomotic junction. The 30 μm ePTFE vascular grafts demonstrated not only the greatest amount of intimal thickening (0.3584 ± 0.003), but they also showed a statistically significant difference in intimal thickening when compared to the other two classes of vascular grafts ($p < 0.05$). Although the reversed autogenous artery evolved the least amount of intimal thickening (0.11 ± 0.002), it failed to demonstrate a stastically significant difference in intimal thickening when compared to the allogeneic vessels ($p = 0.19$). Secondly, a comparison was made of intimal thickening at the mid-vessel location of the vascular grafts (Figure 2.8). Once again, the 30 μm ePTFE vascular grafts demonstrated not only the greatest amount of intimal thickening (0.084 ± 0.002) at the mid-vessel point, but they also showed a statistically significant difference in intimal thickening when compared to the other two classes of vascular grafts ($p < 0.05$). At this mid-vessel point, the reversed autogenous arteries showcased the least amount of intimal thickening (0.024 mm ± 0.003). Furthermore, its intimal thickening was statistically different than the other two classes of vascular grafts (p-value < 0.05).

Media Thickness and Inflammatory Response.

The allogeneic vessels experienced a statistically significant increase in the thickness of the media (0.38 ± 0.022 mm, p-value < 0.05) in comparison to a native, healthy vessel (0.32 ± 0.009 mm) or to a reversed autogenous artery (0.28 ± 0.009 mm) (Figure 2.9). There existed no statistically significant difference between the reversed autogenous arteries and the healthy, native vessels (p-value = 0.11).

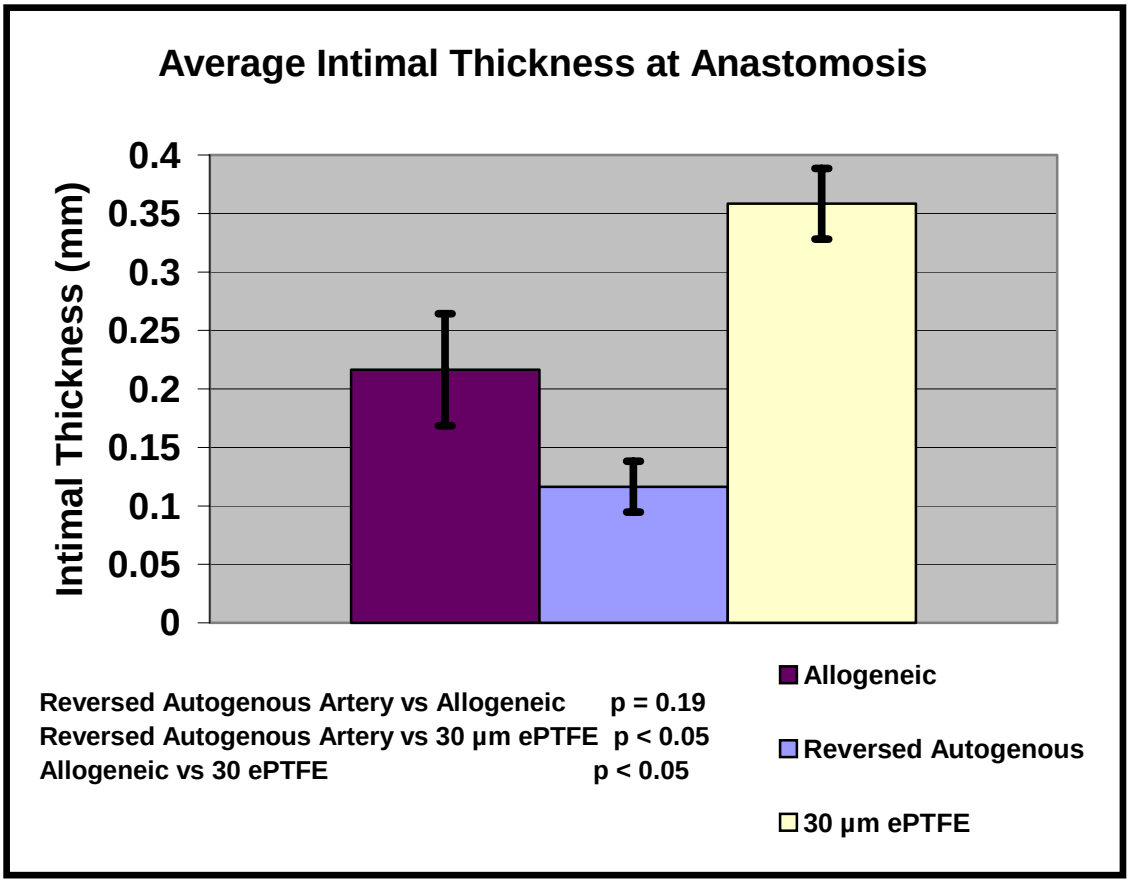

Figure 2.7: Average Intimal Thickness at the Anastomotic Junction. This figure displays the average intimal thickness at the anastomotic junction for the allogeneic vessels, the reversed autogenous arteries, and the 30 µm ePTFE vascular grafts. At this location the 30 µm ePTFE exhibited the largest intimal thickening. There existed no statistically significant difference in the intimal thickening between the allogeneic vessels and the reversed autogenous arteries.

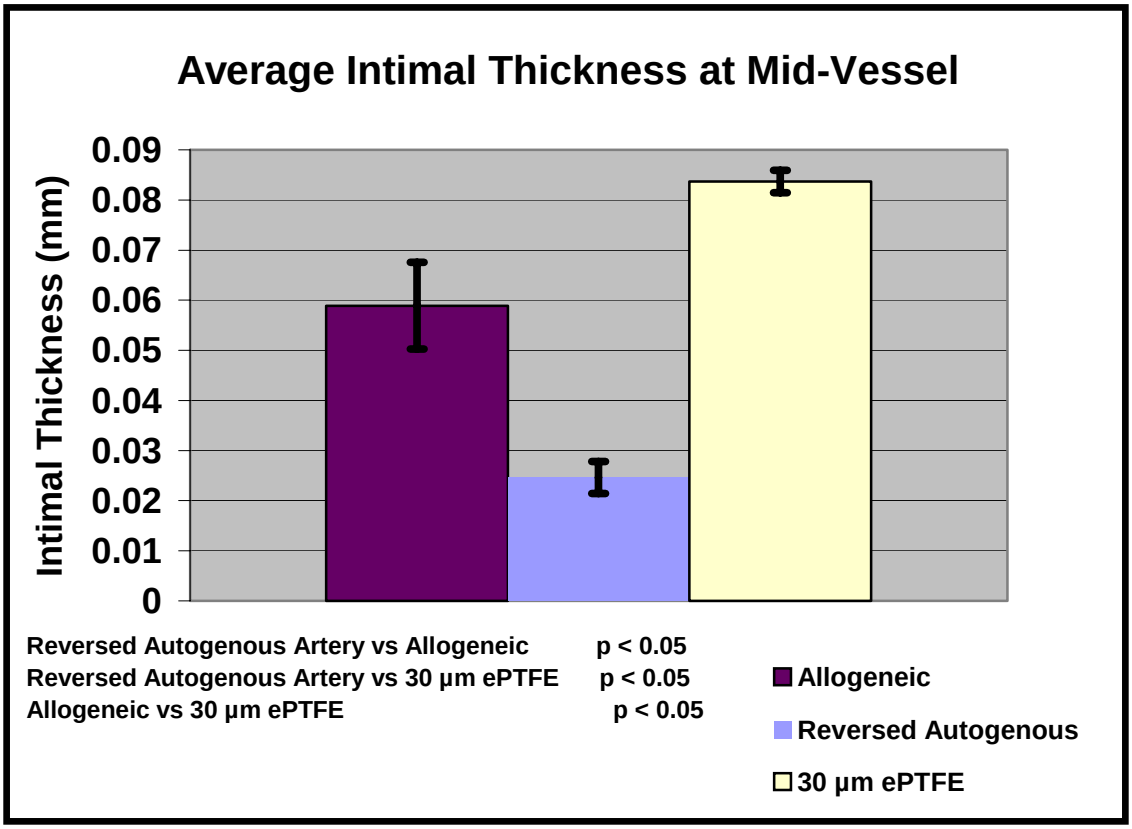

Figure 2.8: The Average Intimal Thickness at Mid-Vessel. This figure displays the average intimal thickness at mid-vessel for the allogeneic vessels, the reversed autogenous arteries, and the 30 µm ePTFE vascular grafts. At this location, the reverse autogenous artery possessed the smallest intimal thickening, and this was statistically different from the other two vessel types. The allogeneic vessel demonstrated a smaller intimal thickness than the prosthetic 30 µm ePTFE vascular grafts.

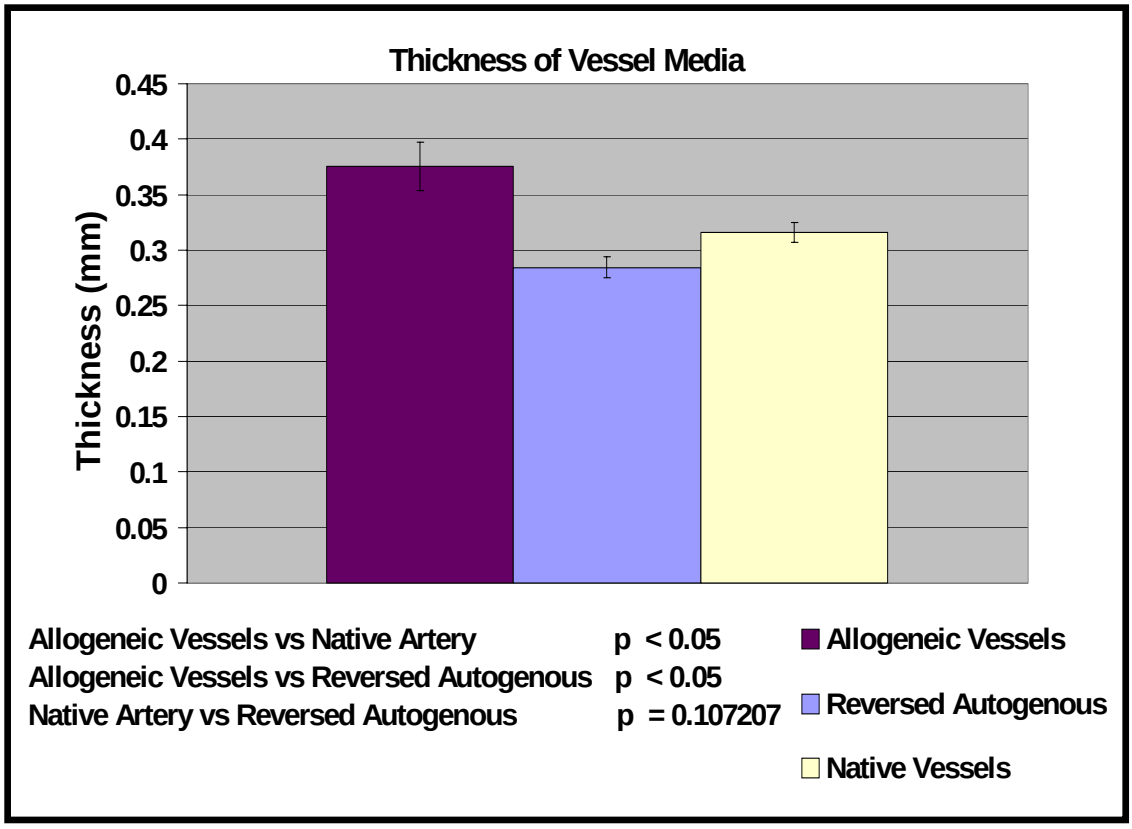

Figure 2.9: Thickness of Vessel Media. The media of the allogeneic vessel demonstrated a thickness that was statistically greater than either the reversed autogenous artery or the native vessels. The difference in media thickness between the reversed autogenous artery and the native vessels was not statistically significant.

CD34 immunostaining was performed to demonstrate the presence or absence of lymphocyte infiltration into the healed vascular grafts. CD34 immunostaining of the reversed autogenous arteries demonstrated a media relatively devoid of an inflammatory response (Figure 2.10a), while CD34 immunostaining of 30 μm ePTFE grafts illustrated a distinct response to the prosthetic graft material (Figure 2.10b). In the case of the allogeneic vessels (Figure 2.10c), a very well identified inflammatory response was elicited within its large media. HAM-56 immunostaining of the allogeneic vessels spotlighted macrophage infiltration into the media (Figure 2.11).

Location of Proliferating Cells.

For the 30 μm ePTFE vascular grafts, BRDU, VWF, and α-actin immunostains determined the location of proliferating cells by providing information for the quantitative immunostaining index. BRDU identified proliferating cells of every origin (Figure 2.12). The overwhelming majority of proliferating cells were localized to the upper 10 % of the neointimal area, whereas very few proliferating cells were found within the lower 90 % of the neointimal area (Figure 2.13). Within the upper 10 % of the neointimal area, the number of proliferating cells progressively increased towards the leading edge, yet within the lower 90 % of the neointimal area, the number of proliferating cells decreased away from the anastomotic junction.

Using the BRDU results alongside sequential VWF and α-actin immunostaining results (Figure 2.14, Figure 2.16), the immunostaining index differentiated where the proliferating endothelial and smooth muscle cells (Figure 2.15, Figure 2.17) were concentrated. The proliferating endothelial cells resided within the upper 10 % of the

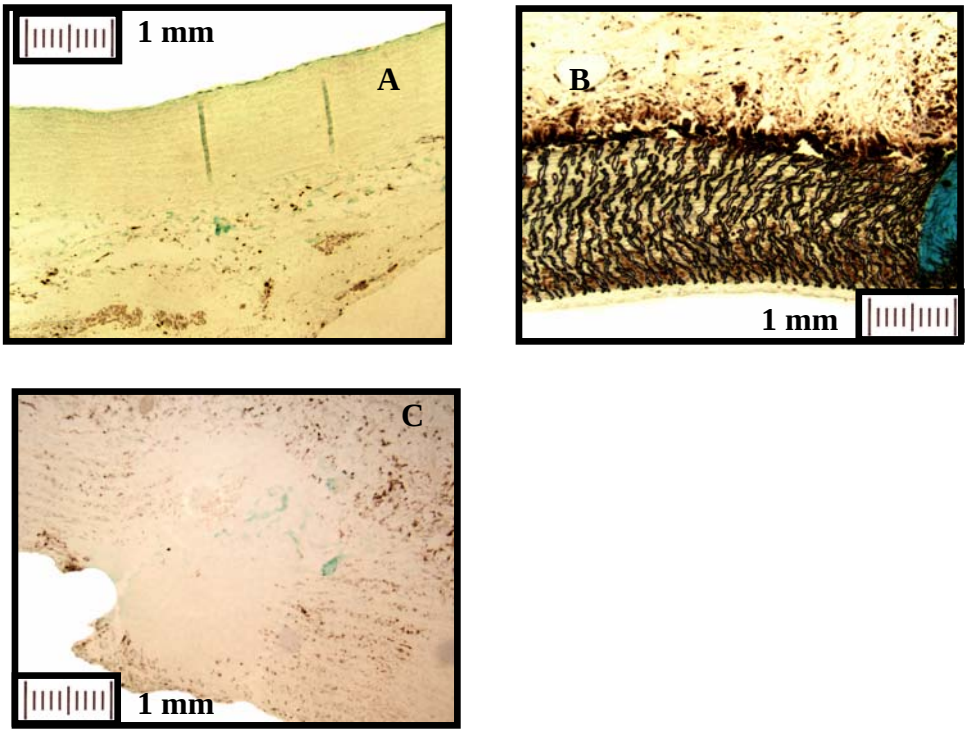

Figure 2.10: CD34 Immunostaining of Vascular Grafts. (A) CD34 immunostaining of a reversed autogenous artery. Observe the lack of inflammatory cells within the media. (B) CD34 immunostaining of a 30 μm ePTFE. Note the presence of inflammatory cells near the prosthetic material. (C) CD34 immunostaining of an allogeneic vessel. Notice the presence of inflammatory cells throughout the media.

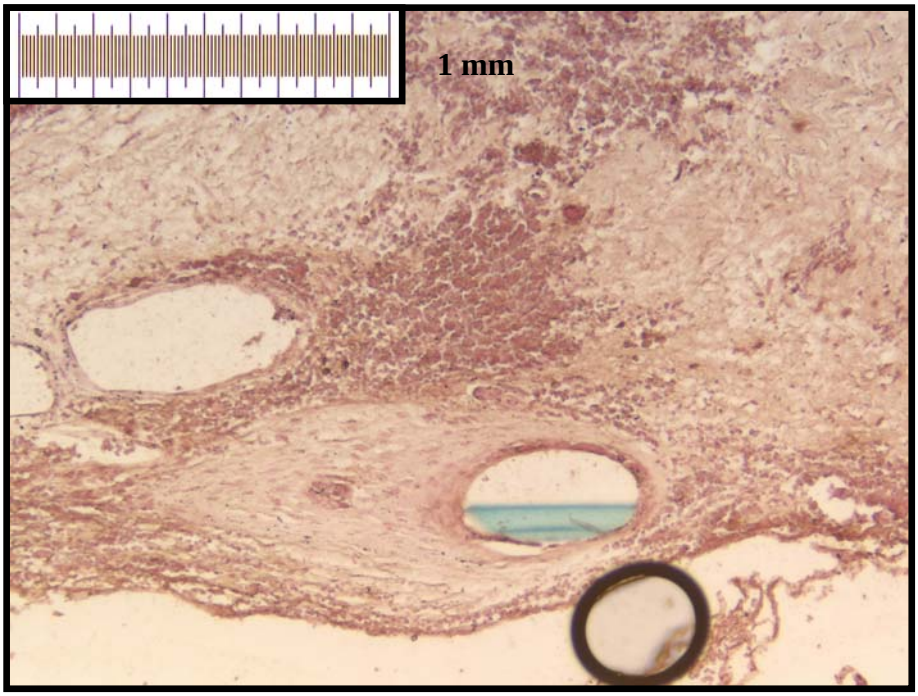

Figure 2.11: HAM-56 Immunostaining of an allogeneic vessel. Observe the presence of labeled macrophages within the media of the allogeneic vessel.

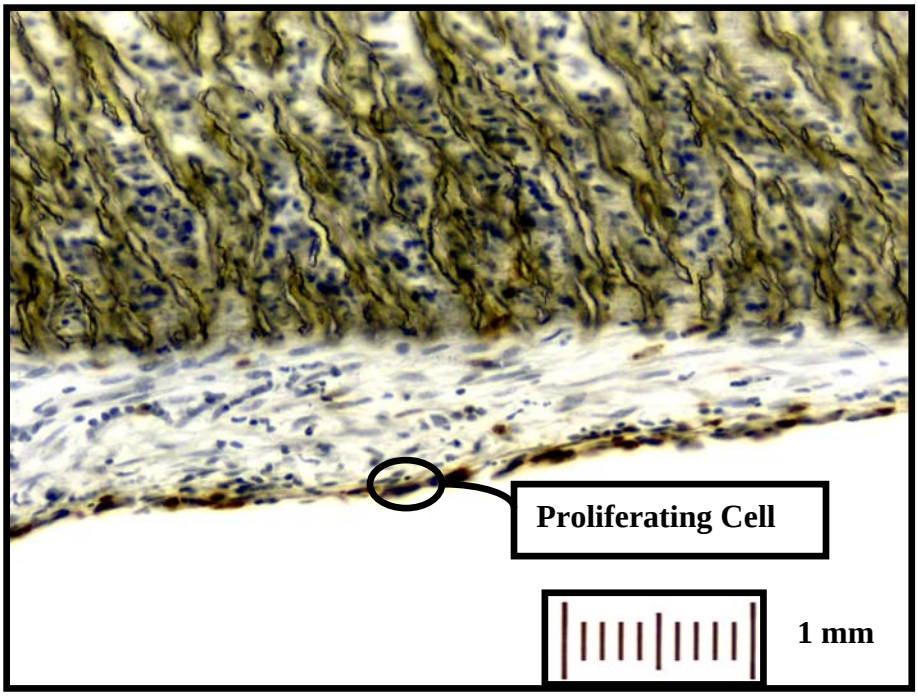

Figure 2.12: BRDU Immunostaining of 30 μm ePTFE Vascular Graft. BRDU labeled or proliferating cells are stained brown. These proliferating cells (endothelial, smooth muscle, etc.) are localized to the luminal, flow surface.

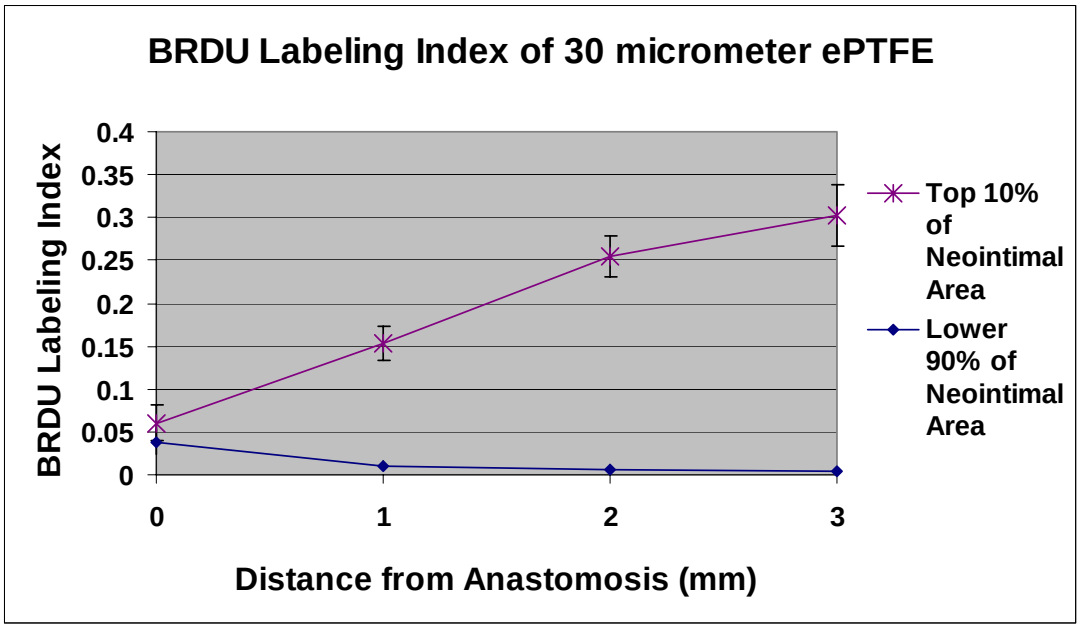

Figure 2.13: BRDU Labeling Index of 30 μm ePTFE. The majority of proliferating cells (enodothelial cells, smooth muscle cells, etc.) are localized to the upper 10 % of the neointimal area, increasing in number with approach towards the leading edge.

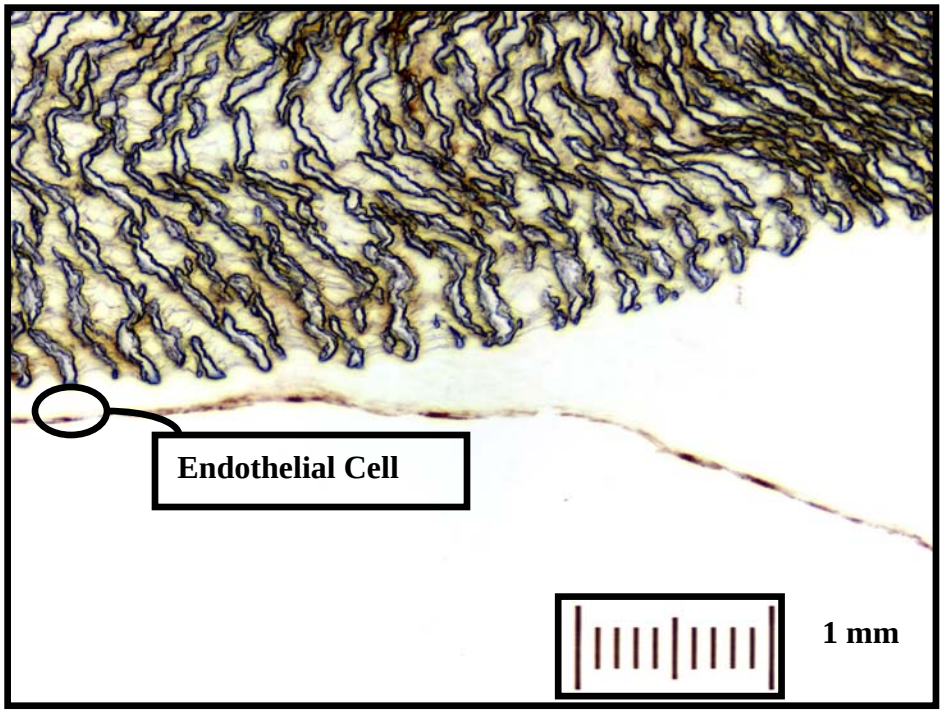

Figure 2.14: VWF Immunostaining of 30 μm ePTFE Vascular Graft. The darkly stained endothelial cells are located on the adluminal flow surface.

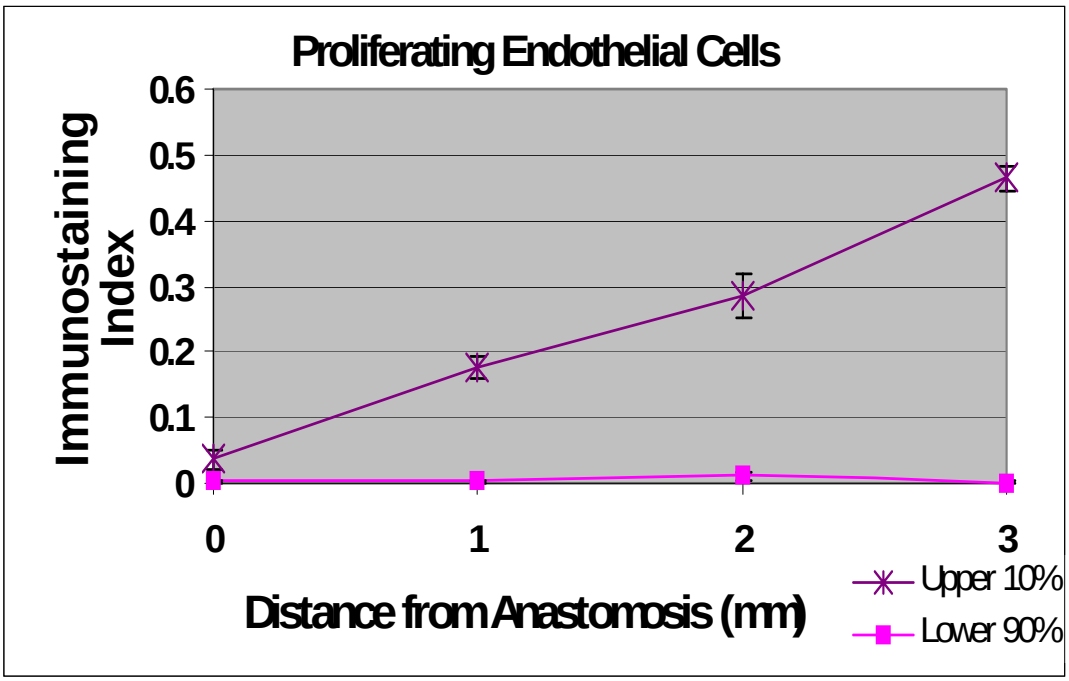

Figure 2.15: Location of Proliferating Endothelial Cells. The proliferating endothelial cells are concentrated within the upper 10 % of the neointimal area, increasing in value towards the leading edge.

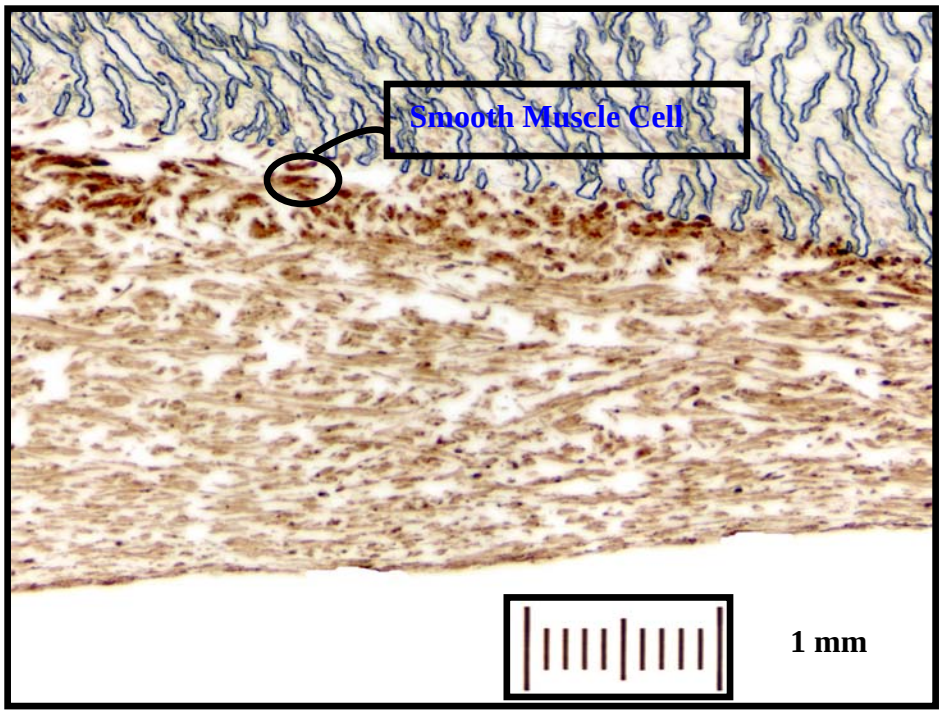

Figure 2.16. α-Actin Immunostaining of 30 μm ePTFE. The smooth muscle cells are concentrated near the prosthetic graft surface and are stained an intense brown.

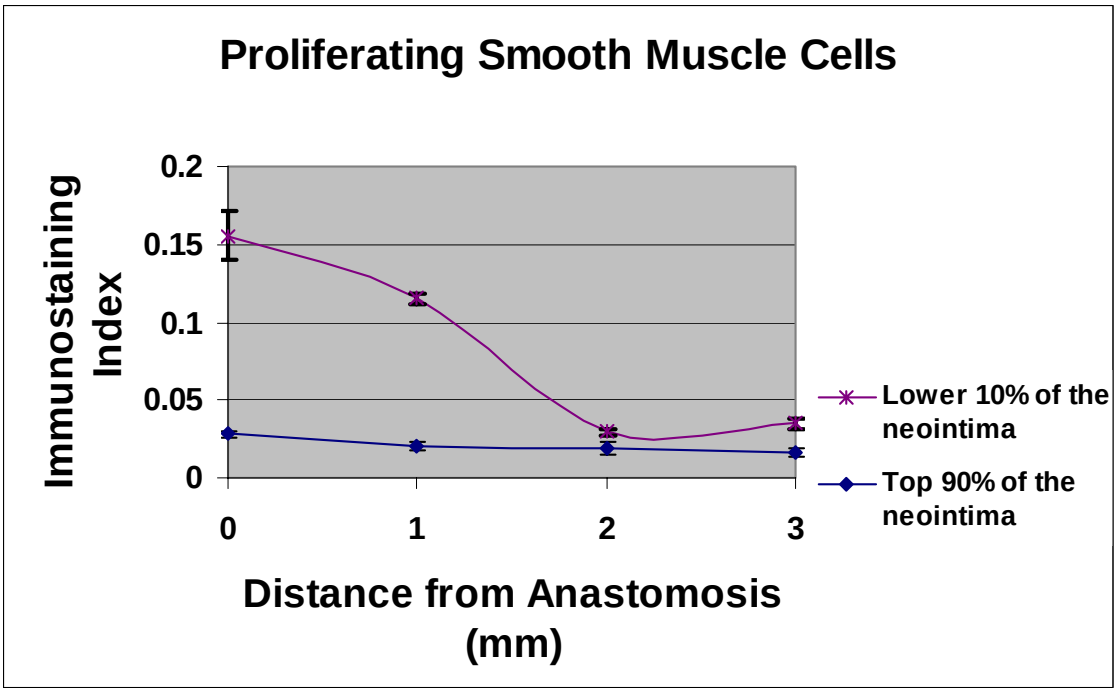

Figure 2.17: Location of Proliferating Smooth Muscle Cells within Healed ePTFE. The proliferating smooth muscle cells are concentrated within the lower 10 % of the neointimal area, reaching a maximum at the anastomosis and decreasing away from the suture line.

neointimal area and increased in number as the leading edge is approached. A negligible number of proliferating endothelial cells were found within the lower 90 % of the neointimal area. In contrast, the proliferating smooth muscle cells clustered within the lower 10 % of the neointima and decreased in number away from the anastomotic junction towards the leading edge. Very few proliferating smooth muscle cells resided within the top 90 % of the neointima.

Discussion:

In an attempt to better understand some of the encountered problems associated with revascularization, researchers investigated the healing response of vascular grafts. Still today, incomplete understanding of this healing process persists. For example, there exists an unfavorable complication rate of 44 % at 10 years following aortocoronary bypass grafting with an autologous artery, while repair of femoropopliteal occlusion develops surgically adverse results using both autologous and synthetic grafts [110,111]. In the past, investigators dealt with these issues in a very qualitative way. Recently, attempts have been made to quantify such parameters as intimal area and intimal thickness at specific locations within the vascular graft [44-46]. Unfortunately, these studies focused their attention upon the histology and immunochemistry at specific locations such as mid-vessel, neglecting the remainder of the graft [25,26,39]. The present study represents the first attempt to quantify intimal thickness as a function of axial distance from the proximal to the distal anastomosis. Furthermore, our approach to measuring intimal thickness provides a mathematically more rigorous method than previous attempts. Past studies had quantified intimal thickness by measuring the intimal area of a circular cross-section and dividing that value by the circumference of the vessel [40,45,46]. This method suffers from at least two shortcomings. First, confusion exists whether to use the circumference of the unhealed luminal surface before implantation or of the healed luminal surface after implantation. Regardless, this approach estimates and does not measure the value of the intimal thickness. Our approach calculates the distance between the luminal flow surface and the original graft surface. This reflects the actual thickness of the deposited neointima. Furthermore, our intimal thickness measurements claim a resolution of 0.005 mm. This resource assumes greater importance when

conducting one-month subacute studies where the intimal thickness may not be that pronounced. This tool will be used in our later sub-acute studies of aortic interposition grafts.

Model of Graft Healing.

We investigated the differences in healing patterns among the three different choices of vascular grafts: autologous, allogeneic, and prosthetic. Since all three of these varieties find clinical use, we attach even greater importance to deciphering their healing differences. The reverse autogenous artery mirrors the use of the internal thoracic artery, while the allogeneic vessel finds use as a glutaraldehye treated cadaver vessel. The reversed autogenous artery or autologous vessel exhibited the least amount of intimal thickening in comparison to the other vascular grafts. Less intimal thickening was measured not only at the anastomosis but also at the mid-vessel location. The reversed autogenous artery showed this healing pattern for several reasons. First, the vessel was not introduced into a new flow environment. Unlike such vessels choices as the saphenous vein, the reversed autogenous artery represented an arterial conduit accustomed to a high flow, high-pressure environment. Secondly, issues of immunogenicity did not arise since the vessel came from the same animal. The surgical trauma of implanting and re-suturing the vessel constituted the only new parameter. From this trauma and the foreign prolene sutures, intimal thickening occurred at the anastomotic junctions. With these results in mind, the reversed autogenous artery

functioned as our gold standard of comparison when evaluating the healing of the other two graft varieties.

While the allogeneic vessel produced less intimal thickening than the 30 μm ePTFE vascular grafts, it failed to perform as well as the reversed autogenous artery. At the mid-vessel location, the reversed autogenous artery possessed statistically less intimal thickening than the allogeneic vessels. Although both vessel types derived from baboons, the allogeneic vessel introduced more of an immunogenic response due to the donor and the recipient vessels coming from different animals. Our immunostaining with CD34 and HAM-56 distinctly outlined the infiltration of the allogeneic graft with lymphocytes and macrophages. This immune response contributed to the observed increase in media thickness. Due to its difference in antigenicity, the allogeneic vessel recruited inflammatory cells into the media. These inflammatory cells release such growth factors as b-FGF, PDGF-AA, PDGF-BB, TGF-β, and an assortment of cytokines leading to both smooth muscle cell migration and proliferation [97]. With these dynamics in mind, we were surprised to witness that all of the allogeneic vessels remained patent. This outcome was unexpected given previous work documenting alloimmune-mediated vascular rejection in an arterial transplantation model [114]. These studies examined the ability of allograft endothelium to recruit T lymphocytes and antigen-presenting macrophages by releasing vascular adhesion molecules, chemokines, MHC molecules, and other proinflammatory vasoactive chemokines. Within this work, they were limited by the use of inferior animal models such as rats and mice. This constraint becomes important when one considers the interspecies differences in endothelial expression and how that relates to clinical human responses. For example, unlike primates, rodents do not constitutively

express both class I and II MHC molecules or the co-stimulatory molecule, lymphocyte fuction antigen LFA-3 [115]. Why then did all of our allogeneic vessels remain patent? The answer may relate to the length of time that the vessels were implanted. At a one month time period an immunogenic response had begun, yet it still failed to generate as strong of a reaction as seen several months later. This rejection process is more likely to occur under chronic and not the sub-acute conditions created by this study. Our observed increase in media size and the surrounding infiltration by lymphocytes and macrophages may have foretold the eventual cascade of events leading towards possible chronic rejection of the vessels.

The 30 μm ePTFE vascular grafts exhibited the largest increase in intimal thickness. There existed a statistically significant difference not only at the anastomotic ends but also at sites distantly removed from the suture line at the mid-vessel point. This increase in intimal thickening originated from many sources. First, the prosthetic graft generated an immune response based on its material interaction as a foreign body. The CD34 immunostaining illustrated this point well. On the underside of the vessel, there existed an immune infiltration into the perigraft tissue surrounding the vascular graft. Through well-documented studies, the ePTFE has been shown to be thrombogenic [97]. As the internodal porosity of the ePTFE enlarges, the thrombogenicity of the prosthetic material increases. Although less thrombogenic than 60 μm ePTFE, the 30 μm ePTFE still resulted in acute thrombotic occlusion (one out of the five clotted). Even if a thrombogenic material does not clot, the activation of platelets and other inflammatory mediators promotes the process of intimal hyperplasia. Over time, this results in failure of the implanted grafts under chronic conditions. The compliance mismatch between the

cut, native vessel and the ePTFE manifests as a flow disturbance at the suture line. This difference in vessel stiffness creates a wall stress disturbance that interferes with arterial pulse wave transmission. These stresses can result in suture-line disruption, formation of a false aneurysm, and development of subintimal hyperplasia [148, 149]. Researchers have clearly shown how these flow disturbances result in increases in anastomotic intimal thickening [112].

Overall, we documented the differences in healing between the three clinically used varieties of vascular grafts. In the future, alternative designs to vascular grafts will emerge. Ideally, a graft that mimics the biology of a healthy, native vessel represents the most desirable approach. Such a vascular graft heals much like a reversed autogenous artery with minimal intimal thickening at the anastomosis and at sites distantly removed from the suture line. Such a possible alternative is a prosthetic vascular graft seeded with endothelial and smooth muscle cells [113]. The use of porous, prosthetic grafts such as 60 μm ePTFE represents another potential choice. As Clowes [25] documented, the porous ePTFE acquires confluent healing of its luminal surface within two weeks. This rapid healing by transmural ingrowth inhibits the ability of transanastomotic or pannus ingrowth to cover the unhealed graft surface with a thick layer of neointima. By healing rapidly, the porous prosthetic material benefits from the many protective effects of a confluent endothelium. Lastly, work is being conducted on developing a prosthetic vascular graft with a local drug infusion system that inhibits pannus formation at the distal anastomosis [62 – 65]. The drug is stored within a local infusion pump and then continuously infused for up to one month into the boundary layer of the flowing blood. Through local drug delivery, high concentrations of otherwise very expensive

pharmacologic agents can be administered, and in so doing, we can avoid the production of either drug tolerance or damaging systemic effects [63]. Hanson and Chen [68, 69, 72] have investigated the pharmacologic effect of locally administering such drugs as nitric oxide donors, bFGF conjugated to saporin, and heparin. In all cases they observed a decrease in intimal area and in the number of proliferating cells [70-72].

Proliferating Cells within the Neointima.

In this work we characterized the location of proliferating cells within the growing neointima. These proliferating cells function in two different capacities; one that is beneficial and one that threatens graft patency. First, they help to heal barren, prosthetic graft material that is potentially thrombogenic, and if left unhealed, it may lead to acute occlusion. Secondly, they produce damaging neointima that threatens to occlude the graft. In the past Clowes had identified that the proliferating endothelial cells were localized to the leading edge of the neointima [44-45]. Our work further refined this study by identifying that the proliferating endothelial cells were localized to the top 10 % of the neointima, increasing in concentration from the anastomotic junction until reaching their maximum at the leading edge. This result reveals how proliferating endothelial cells receive their stimulus to grow from blood borne elements within the lumen. In contrast to Clowes' work, we quantified the number of proliferating endothelial cells as we progressed along the axial length of the vessel and differentiated where within that growing neointima that the proliferating cells resided. By isolating the proliferating

endothelial cells to the upper 10 % of the neointima, we provide strong evidence for their growth being humoral-mediated.

We were also interested in characterizing the location of proliferating smooth muscle cells. We observed that the proliferating smooth muscle cells were concentrated within the lower 10 % of the neointima, reaching a peak value at the anastomosis and then decreasing in value with distance away from the suture line. Unlike the endothelial cells, the proliferating smooth muscle cells appear to receive more stimuli for growth from the prosthetic graft surface rather than from blood borne elements. This helps to explain the vigorous healing response to a foreign material and the subsequent intimal thickening. One potential source for this mitogenic activity is the already documented inflammatory response in and outside the prosthetic graft material. This conclusion contrasts with the governing thought that the mitogenic source of smooth muscle cells derives predominantly from platelets and such released growth factors as PDGF-AA and PDGF-BB. Our observation that the underlying graft material so significantly affects healing emphasizes the importance in careful selection of the prosthetic material. Furthermore, this result now helps to better explain why we saw such a wide-range of healing responses depending upon whether the graft variety was autologous, allogeneic, or prosthetic. Ultimately, this difference in healing response influences our decision for which variety of vascular graft to use when the need for revascularization arises.

Chapter III

Graft Healing of Stretched ePTFE Implanted within a Baboon

Introduction:

Within the United States atherosclerotic disease affects one out of every four people, resulting in over 40% of all deaths [88]. Frequently, this occlusive disease localizes to the peripheral vasculature, resulting in such problems as claudication of the legs. To treat this clinical situation, surgeons construct bypass vascular grafts using such prosthetic materials as Dacron and ePTFE. For peripheral vascular disease, ePTFE serves as the preferred prosthetic material. To achieve high patency rates, ePTFE vascular grafts need to exhibit two properties: a flow surface with reduced thrombogenicity and reduced intimal thickening. One way to accomplish this goal is to promote rapid and confluent healing of the graft surface.

For well over thirty years, researchers focused their attention upon the healing properties of graft materials. Their studies determined that prosthetic vascular grafts healed by the following three mechanisms: (1) transanastomotic ingrowth, (2) seeding from circulating blood borne cells, and (3) transmural ingrowth. Through the years, transanastomotic ingrowth has been well characterized, while investigators still debate the role of “humoral seeding”. Early on, they identified the potential for vascular grafts to heal by the migration of surrounding perigraft tissue across its wall, so-called transmural ingrowth. Beginning with Wesolowski’s 1961 work [42], researchers

concluded that porous synthetic grafts achieved better healing properties. The fibrous ingrowth of fibroblasts, fibrin, and blood-borne cells improved graft patency rates. Clowes [25] later detailed the ability of ePTFE grafts to heal by transmural ingrowth. Clowes documented that the more porous varieties of ePTFE, internodal distances of 60 μm and 90 μm, healed by ingrowth across the graft wall. In fact, these more porous varieties of ePTFE showcased a confluent endothelium, a uniformly distributed pseudointimal growth, and an improved intimal stability. These results contrasted to what was found when porosity was decreased. Even as far as one year after implantation, ePTFE with internodal porosities of 10 μm and 30 μm exhibited patchy and incomplete healing.

While these results established the importance of graft porosity, the question evolved as to whether changes in the ePTFE ultrastructure affected graft healing. Since porosity reflects a structural characteristic of the material, researchers expected to see changes with additional material alterations. In 1986 McClurken [48] defined the standards for examining the physical properties of ePTFE vascular grafts. He explained how the ePTFE grafts must be evaluated for both static (inside diameter, wall thickness, internodal distance) and dynamic (hysteresis following mechanical stretch) physical properties. With the development of medical devices, ePTFE ultrastructure assumed greater importance in the design and choice of prosthetic vascular grafts. The endovascular stent graft represents an example of such a challenging innovation. The stent graft consists of a metallic and alloy stent surrounded by 30 μm prosthetic vascular graft material. In order to deploy this device, an angio-balloon catheter inflates within its lumen, stretching out the metallic infrastructure and subsequently altering the adjoining

prosthetic graft material. Williams [48] questioned what happened to the healing properties of this material once stretched. In 1995 Palmaz [103] first addressed this subject. His work suggested that balloon dilatation of stent grafts failed to alter such material properties as internodal distance. Williams' results [48] extended upon this study. By radially stretching sections of 30 μm ePTFE, he corroborated that there were no changes in internodal distance, but unlike Palmaz, he observed additional changes within other material properties. Such static physical properties as wall thickness, nodal thickness, interfiber distance, and fiber width became altered. Williams concluded that radially stretching the graft material permanently altered the structure of the ePTFE [48].

In a later animal study of 30 μm ePTFE implanted into the subcutaneous and adipose tissue of Sprague-Dawley rats, Williams [150] observed a greater inflammatory response within stretched grafts versus unstretched grafts. This inflammatory response became important in its ability to affect cell recruitment and matrix deposition. A chronic inflammatory response concentrates macrophages and foreign body giant cells within an area of interest. These cells then direct fibroblasts, blood vessels, and other inflammatory cells. It would seem then that Williams observed a distinct change in healing outcomes; however, his conflicting results regarding adipose and subcutaneous implants made it difficult to draw any definitive conclusions regarding how changes in graft ultrastructure impact neovascularization or cellular ingrowth. These results emphasized the need to study the healing characteristics of mechanically altered graft material within an animal model with a pulsatile flow environment.

In this study we will investigate how radially stretching a porous synthetic graft, such as 60 μm ePTFE, will change the healing characteristics of the implanted vessel. We

will document the ultrastructural changes and how those results relate to the observed histopathologic measurements. Furthermore, we will introduce a complicated model of a stenotic graft where there will exist both distortion and preservation of the material ultrastructure. This model will allow us to investigate how the healing response changes as the material properties are progressively altered. In addition, the stenotic throat will establish an altered hemodynamic environment with high levels of wall shear stress. Based on published literature [54-56], we expect a mechanism to evolve within the stenotic throat that inhibits progressive intimal thickening.

Material and Methods:

Animals.

In this study vascular grafts were implanted into juvenile male baboons (*papio cyncephalus / anubis*) of roughly two years of age and weighing between 13-24 kg. All animal procedures followed "Principles of Laboratory Animal Care", the "Guide for the Care and Use of Laboratory Animals" (NIH Publication No. 8023, revised 1985), and IACUC university guidelines.

Grafts.

Three different vascular grafts constructed of 60 μm expanded polytetrafluoroethylene (Gore-Tex, non-reinforced, thin wall; provided by W.L. Gore and Associates, Inc., Flagstaff, Ariz.) were used in this study. The first type of vascular graft, the so-called unstretched control, possessed a length of approximately 4 cm and an inner diameter of 6 mm. The next two varieties of vascular grafts were constructed from the same starting material with an inner diameter of 3 mm. The first of these vascular grafts, the so-called stretched control, was uniformly stretched in a radial direction from a 3 mm inner diameter to a 6 mm inner diameter. The second of these vascular grafts, the so-called stretched stenosis, consisted of a 75 % reduction in its cross-luminal area. The stretched stenosis was constructed by fitting the ePTFE over an aluminum mandrel that began with an inner diameter of 6 mm, symmetrically contracted down to 3 mm, and then symmetrically expanded back out to 6 mm. The aluminum mandrel was lathed according to the following mathematical equation:

$Z = 6.0 \text{ mm} \quad \text{for } 0 \leq x < 1.25 \text{ and for } 2.75 < x \leq 4.0$

$Z = 1-.25(1+\cos(\pi((x-2)/0.75)) \text{ for } 1.25 \leq x \leq 2.75$ (**Equation 1)**

The aluminum mandrel was separable in the middle, allowing for easy separation and removal of the graft prior to surgery. A schematic of the stretched stenosis illustrates this design (Figure 3.1).

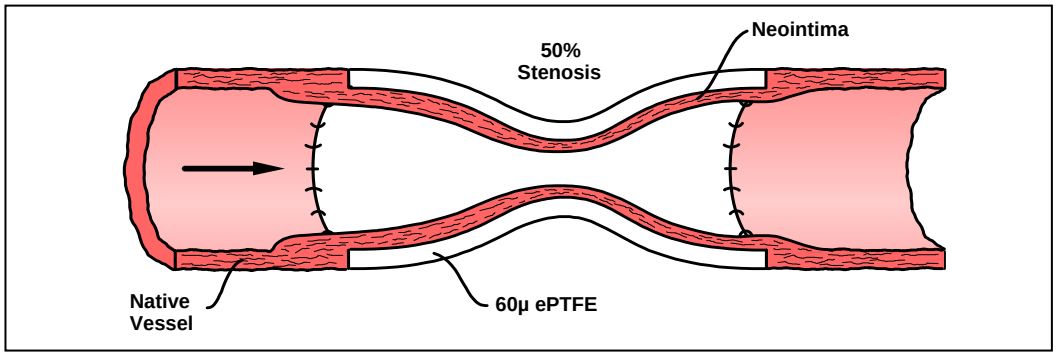

Figure 3.1: The Stretched Stenosis. The stenotic graft was constructed from 60 μm ePTFE with an initial inner diameter of 3mm. By fitting the graft material over the separable mandrel, the proximal and distal ends were stretched to an inner diameter of 6 mm.

Surgery.

One day prior to surgery, 325 mg of aspirin was administered to the baboon. Blood samples were drawn to analyze such hemodynamic parameters as platelet count, hematocrit, and white blood cell count. Under general endotracheal anesthesia with 1.5 to 2.5 % isoflurane, a mid-line incision was made, followed by exposure of the retroperitoneum. Following isolation of the distal abdominal aorta, 150 units of heparin/kg were infused. The volumetric flow rate of the baboon was measured by fitting

a perivascular flow probe (Transonic Inc.) around the exposed aorta, just distal to the bifurcation of the renal arteries. The transonic flowmeter was connected to a PC computer using an Analog/Digital card. On the PC, Labview recorded the volumetric flow rate for thirty cardiac cycles (Figure 3.2). Twenty ePTFE grafts were implanted into the distal abdominal aortas of individual baboons. Implantation of vascular grafts involved using an end-to-end anastomosis with a continuous running suture of 6.0 polypropylene (Davis & Geck, Wayne, N.J.) (Figure 3.3). An example of an implanted vessel is demonstrated in Figure 3.4. Changyi Chen M.D., Ph.D performed all of the surgeries.

Vessel Harvest.

All baboons were sacrificed one month following graft placement. Bromodeoxyuridine (BRDU; Sigma Chemical Co., St. Louis, Mo), 50 mg/kg dissolved in 50 ml of normal saline solution, was administered subcutaneously 19, 12, and 7 hours before sacrifice. Prior to vessel harvest, blood samples were once again drawn to analyze hemodynamic parameters. Twenty minutes before sacrificing the animal, 5000 units of heparin were administered. The distal abdominal aorta was once again exposed. Using the perivascular flow probe, we acquired the volumetric flow rate just distal to the renal arteries for thirty cardiac cycles. The animals were sacrificed by exsanguination. The implanted grafts were fixed *in vivo* by implanting a 14-gauge angiocatheter into the abdominal aorta and infusing the fixative from a 60 cc syringe. Before infusing the fixative, the grafts were first flushed with 0.1 M phosphate buffered saline (PBS) at pH 7.4 and 37° Celsius. Next, Evan's Blue Dye (50mg/kg) was administered, followed by another flushing of the distal aortic tree with 0.1 M PBS. A 14-gauge angiocatheter was

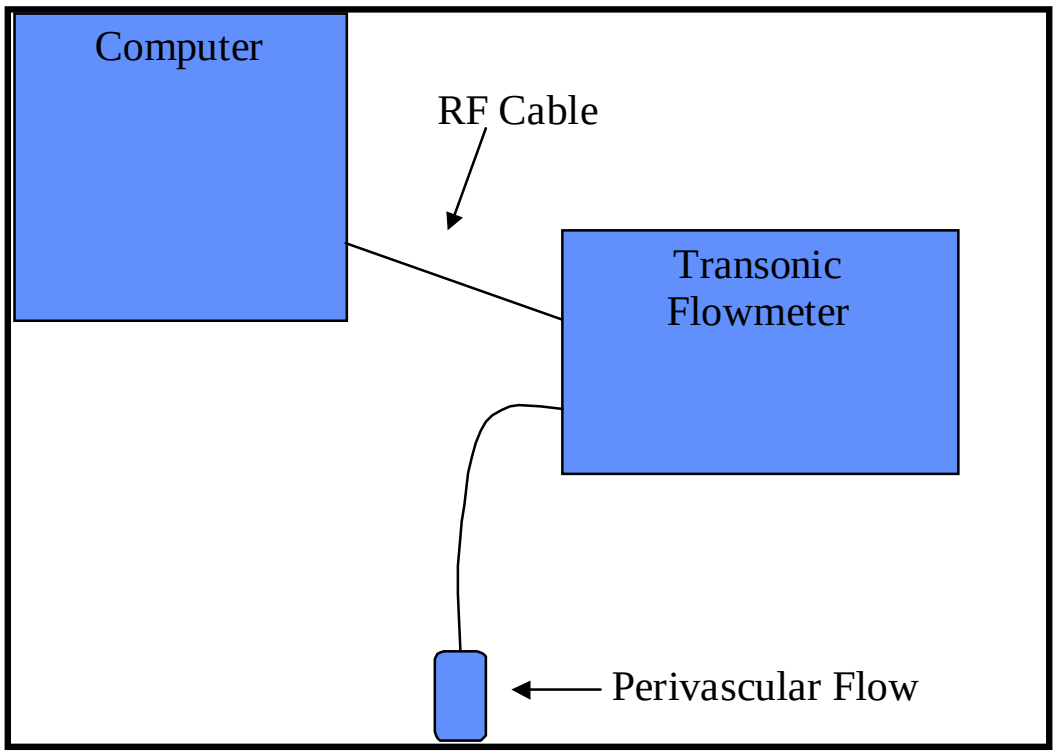

Figure 3.2: Data Acquisition for the Volumetric Flow Rate. The perivascular flow probe connected to the pulse-transit ultrasound flowmeter that interfaced with an analog to digital card installed on the PC. The computer captured the volumetric flow rate for thirty cardiac cycles.

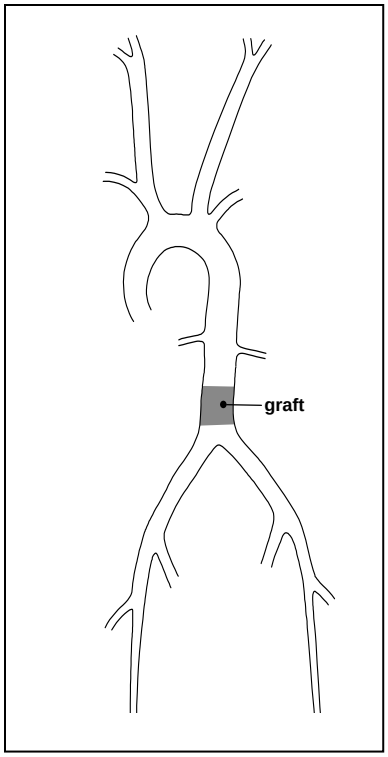

Figure 3.3: Illustration of Implanted Vascular Graft. The vascular graft was implanted into the distal abdominal, aorta using an end-to-end anastomosis.

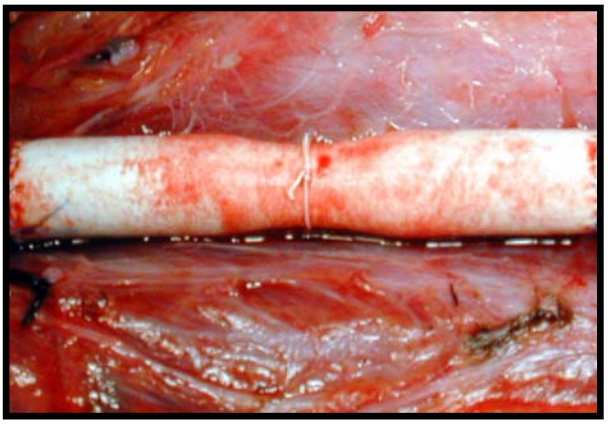

Figure 3.4: Implanted Stretched Stenosis. Photograph of implanted prosthetic vascular graft.

inserted into the right common iliac to control the rate at which perfusate drained, while another 14-gauge angiocatheter was fed into the left common iliac up to the level of the aorta's bifurcation to measure mean arterial pressure (MAP) using a sphygmomanometer. The vessels were perfused at a MAP of 100 mmHg for at least thirty minutes with either 10 % buffered formalin (Baxter Diagnostics Inc, McGraw Park, Ill), accomodating a protocol for immunohistochemistry, or 2.5 % glutaraldehye (Sigma Inc), accommodating a protocol for scanning electron microscopy (SEM). Figure 3.5 illustrates the set-up for the *in vivo* pressure perfusion of the grafts. Following fixation, the grafts were harvested along with 1 cm sections of contiguous native vessel at each anastomosis and then submersed in fixative for a 24-hour period.

Histology and Morphometry.

All harvested grafts were divided into 5 mm long segments with circular cross sections, embedded into paraffin, and microtomed perpendicular to the long axis of the vessel using a 5 μm slice thickness. At the proximal anastomosis, the center of the graft, and the distal anastomosis, microscope sections were cut every millimeter from the embedded blocks, while elsewhere in the vessel, only one representative set of sections was taken from each embedded block. As a result, greater resolution was obtained at the anastomotic ends and at the center of the vessels. All grafts underwent staining with Hematoxylin and Eosin (H&E). Morphometric measurements were performed to evaluate neointimal thickness and area. Neointima was defined as ingrowth overlying the prosthetic graft surface. All slide specimens were analyzed using a microscope with a 1x objective interfaced to a digital camera that captured all images into a TIFF format. Using the Image-Pro Plus ® Software (Media Cybernetics, Inc.; Silver Spring, Maryland), the

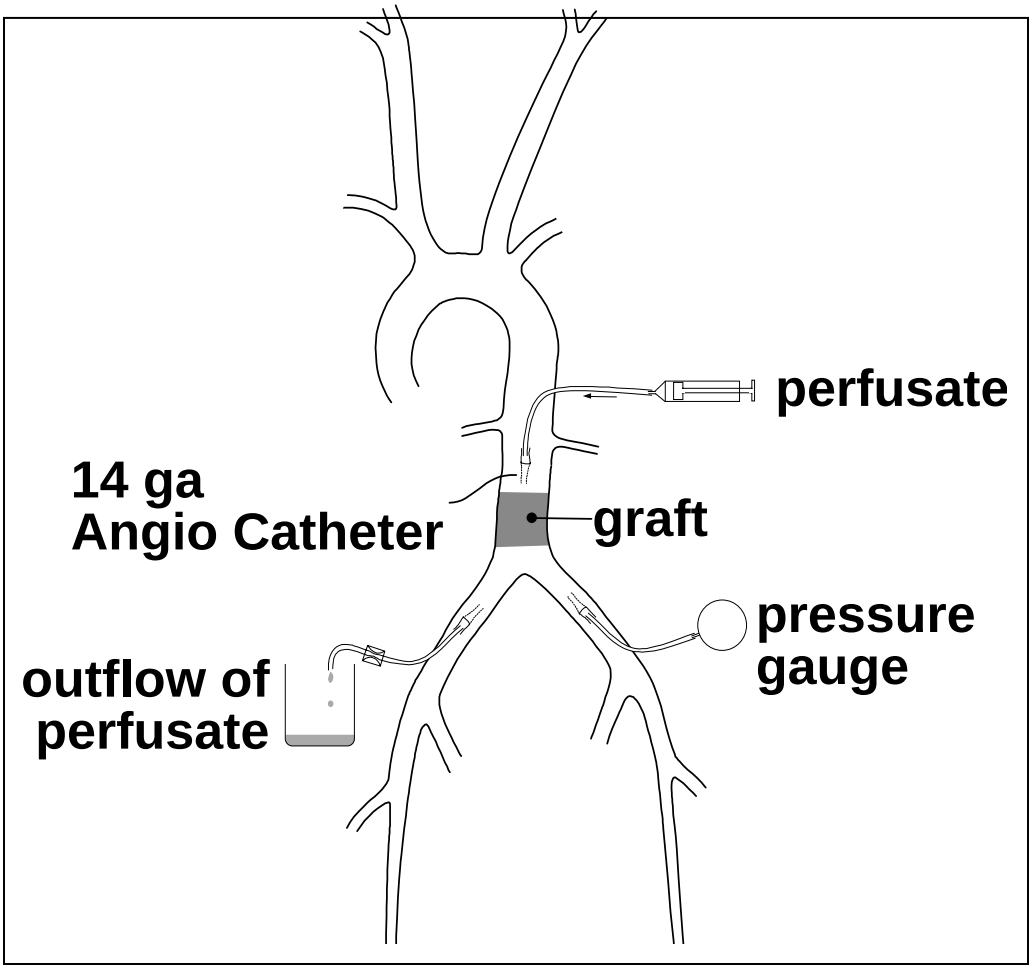

Figure 3.5: *In Vivo* Pressure Perfusion of Implanted Vascular Graft. The perfusate consisted of either 10 % buffered formalin allowing for immunohistochemistry or 2.5 % glutaraldehyde allowing for Scanning Electron Microscopy. The angiocatheter in the right common iliac was fed up to the aorta's bifurcation. This allowed the sphygmomanometer to measure the MAP within the aorta.

average intimal thickness was measured in the following way. A macro within Image-Pro called **graft1** identified the two borders of the neointima defined by the surface of the ePTFE graft and the adluminal surface of the neointima. The software then calculated the distance between these two borders, progressing with a one-pixel resolution (0.005 mm) around the circumference of the vessel. For each cross-section an average intimal thickness was calculated. A macro called **area** measured the intimal area between these two borders. Since the length of harvested vascular grafts varied by 12 %, the axial locations were normalized to a scale from 0 to 1. This adjustment allowed for comparison of intimal thickness and area measurements at the same relative location within vascular grafts of different lengths. For each particular graft type the intimal thickness and area measurements were processed using an autoregressive moving average (ARMA). The ARMA technique generates a representative measurement of intimal thickness by incorporating measurements that precede, follow, and occur at a location of interest. At 0.1 normalized distances along the vascular graft, standard deviations were calculated. For each vascular graft type, a comparison of intimal thickness at the proximal and distal anastomoses was performed. Furthermore, a comparison of intimal thickness measurements at the mid-vessel point of the different graft varieties was conducted.

Immunocytochemistry and Morphometry.

The avidin-biotin complex immunoperoxidase procedure (LSAB Kit, DAKO Co., Carpenteria, Ca.) was used to differentiate proliferating cells and the different neointimal cell-types. This staining procedure was performed upon all the harvested vessels. Anti-BRDU monoclonal antibody (DAKO Co.) identified proliferating cells that had uptaken the administered BRDU prior to sacrifice, while monoclonal antibodies to α-

actin (DAKO) and Von Willebrand Factor (vWF; Factor VIII related antigen, DAKO) outlined smooth muscle cells and endothelial cells, respectively.

Scanning Electron Microscopy.

Two different sets of scans were performed using a Topcon-ISI DS-130 operated with a LaB6 electron source at 9 kV. First, an analysis of the graft ultrastructure was performed upon vascular grafts that were not implanted. For three of the respective control and stenotic models, a longitudinal strip with a width of 5 mm was analyzed. Secondly, healing patterns were observed by analyzing implanted vascular grafts. From the harvested vascular grafts, two longitudinal sections with a width of 5 mm were taken from each of the respective control and stenotic models. The SEM protocol required fixation of the sample in 2.5 % electron microscopy grade glutaraldehyde diluted in cacodylate. The samples were then dehydrated with graded alcohol, critical point dried, and then sputter coated with gold palladium with a deposited thickness of 20 Δ. Both the anastomotic ends and the middle of the vascular grafts were interrogated and digital images captured.

Graft Ultrastructure.

With the SEM images described above, the vascular grafts' material properties were measured. For each of the vascular graft types, internodal distance (distance between nodes of ePTFE) and nodal width (width of a node of ePTFE) were measured (Figure 3.6). Using the H&E stained circular cross-sections, the ultrastructural properties of graft thickness and void volume were measured (Figure 3.7). Using Image-Pro, the graft thickness was measured by calculating the distance between the outer and inner borders of the prosthetic graft at each radial location around the vessel's circumference,

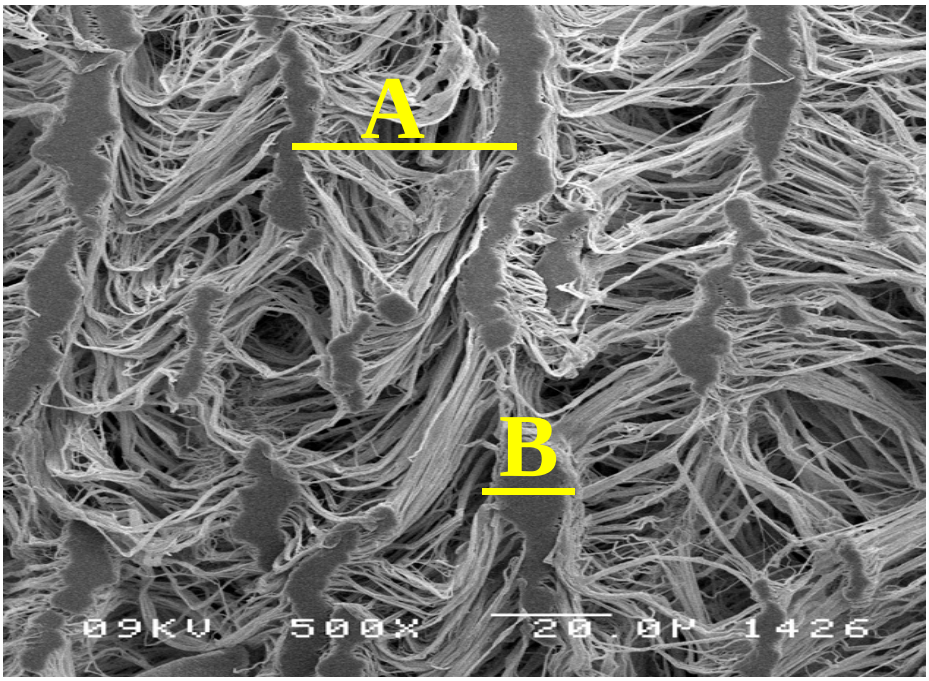

Figure 3.6: Scanning Electron Microscopy of Unstretched 60 μm ePTFE. (A) designates the internaodal distance, while (B) designates the nodal width.

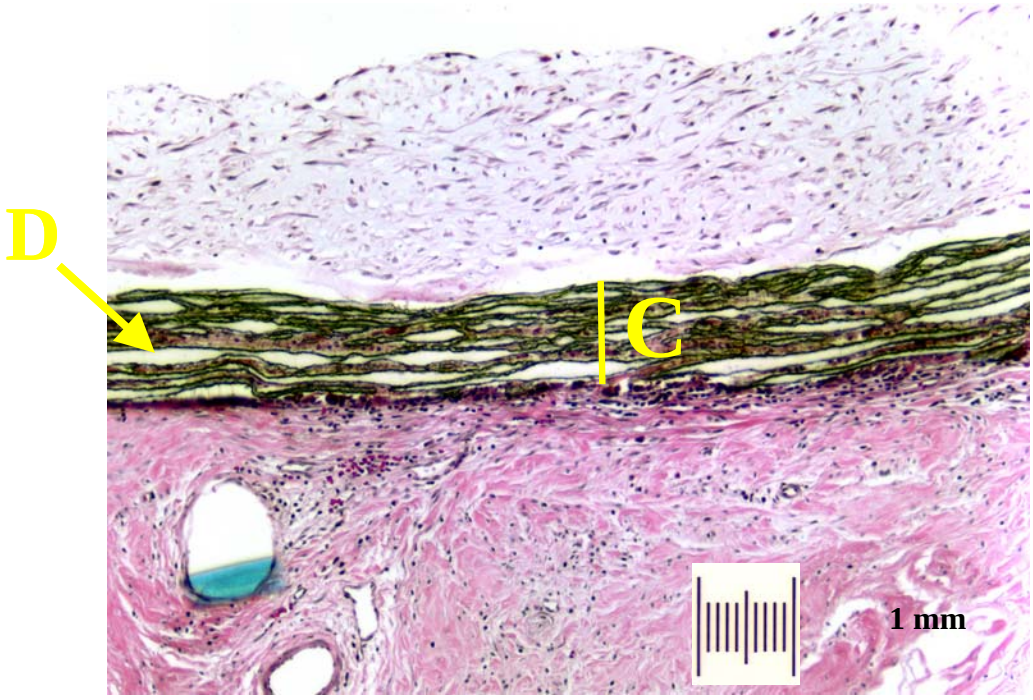

Figure 3.7: H&E Staining of a Circular Cross-Section of a Harvested 60 μm ePTFE Vascular Graft. (D) illustrates void volume, while (C) designates graft thickness.

and then the average was calculated. Void Fraction reflected the percentage of empty space within the prosthetic graft that permitted for transmural ingrowth across its wall. A macro within Image-Pro called **Void** evaluated void fraction by calculating the area of empty space unoccupied by ePTFE material and dividing it by the total area of the graft material. For each control graft, the average of these parameters was taken between the anastomotic and mid-vessel location. For the stretched stenosis, these parameters were individually evaluated at the mid-vessel and anastomotic location. Since the material properties of the graft changed from the anastomosis to the stenotic throat, their measurements were not averaged as with the control grafts.

Fluid Mechanics.

Computational fluid mechanics characterized the flow field within the vascular grafts. Chapter V describes in detail how this was accomplished. Briefly, computational grids were constructed of the control and stenotic grafts. The grids were constructed using contours outlined from the harvested, circular cross-sections of the vascular grafts. A best-fit line calculated from an MRI analysis of an implanted vascular graft determined the orientation of these contours in space. The Gambit software (Fluent Inc) helped construct the computational grids. An ensemble average of the measured volumetric flow rates at harvest was calculated to obtain a representative description of blood flow for both the control and stenotic grafts. This ensemble averaged volumetric flow rate was then applied to a Womersley solution [151] to derive velocity values for the flowing blood at the vessel inlet. This velocity profile then functioned as the boundary condition at the inlet of the vascular graft. Using Fidap (Fluent Inc), pulsatile simulations were run for three cardiac cycles. From these simulations, wall shear stress within the vascular

graft was calculated. Wall shear stress is defined as the dynamic viscosity of the fluid times the gradient of the velocity, evaluated at the wall. The dynamic viscosity of blood was assumed to be 0.04 Poise. The hemodynamic data were compressed into a description of wall shear stress as a function of distance along the axial direction of the vascular graft. This was accomplished by averaging the WSS measurements around the circumference of the vessel. This term is referred to as spatially averaged WSS or $\tau_s(z,t)$ (Equation 3.2).

$$\tau_s(z,t) = \left| 1/S \int_0^S \tau ds \right|$$

Equation 3.2

At each axial location along the graft, the pulse spatially averaged WSS (Pulse WSS) was calculated. Over a cardiac cycle, the Pulse WSS measures the difference between the maximum spatially averaged WSS and the minimum spatially averaged WSS. Lastly, the temporal mean of the spatially averaged WSS was calculated. This manipulation produced the spatially averaged, temporal mean wall shear stress {τavg(z)} (Equation 3.3).

$$\tau avg(z) = \left| (1/(T*S)) \int_0^S \int_0^T \tau dt ds \right|$$

Equation 3.3

Statistics.

Statistical analysis was performed on a Pentium IV P.C. with the use of either MATLAB or Excel 2000 statistical software (Microsoft Co.). Comparisons of intimal

thickness between the various grafts were made using a Student *t* test (two-tailed). The documented values are given as the mean ± the standard deviation. The results were considered significant if the p value was less than 0.05.

Results:

Graft Ultrastructure.

In this study stretching the vascular graft altered the material properties of the ePTFE. A qualitative comparison of the SEM and H&E pictures best illustrated this point. The SEM picture of the unstretched ePTFE (Figure 3.8a) showed empty space or void fraction within the graft material, while the SEM picture of the stretched ePTFE (Figure 3.8b) highlighted the dense and compact nature of the graft material with its noted absence of void fraction. The H&E stained cross-sections (Figure 3.7) further demonstrated how stretching the vascular graft made the material more compact and reduced its thickness. The morphometric measurements of the graft material attempted to quantify these mechanically induced changes in the graft ultrastructure. First, the void fraction of the material was analyzed (Figure 3.9). The void fraction of the unstretched 60 μm ePTFE (74.1 ± 1.8 %) notably exceeded the void fraction of the stretched 60 μm ePTFE (45.8 ± 1.7 %) and of the 30 μm ePTFE (39.3 ± 6 %). Furthermore, the difference in void fraction between the unstretched 60 μm ePTFE and the other two graft varieties was statistically significant. Secondly, the thickness of the graft material was investigated (Figure 3.10). The thickness of the stretched 60 μm ePTFE (0.25 ± 0.05 mm) was notably smaller than the graft thickness of the unstretched 60 μm ePTFE (0.46 ± 0.02 mm) and of the 30 μm ePTFE (0.41 ± 0.02 mm). Also, there existed a statistically significant difference between the graft thickness of the stretched 60 μm ePTFE and the other two graft varieties. Thirdly, the internodal distance of the ePTFE varieties was measured (Figure 3.11). The internodal distance of the stretched 60 μm ePTFE (33.8 ± 2.1 μm) was markedly greater than the internodal distance of the unstretched 60 μm ePTFE (25.5 ±

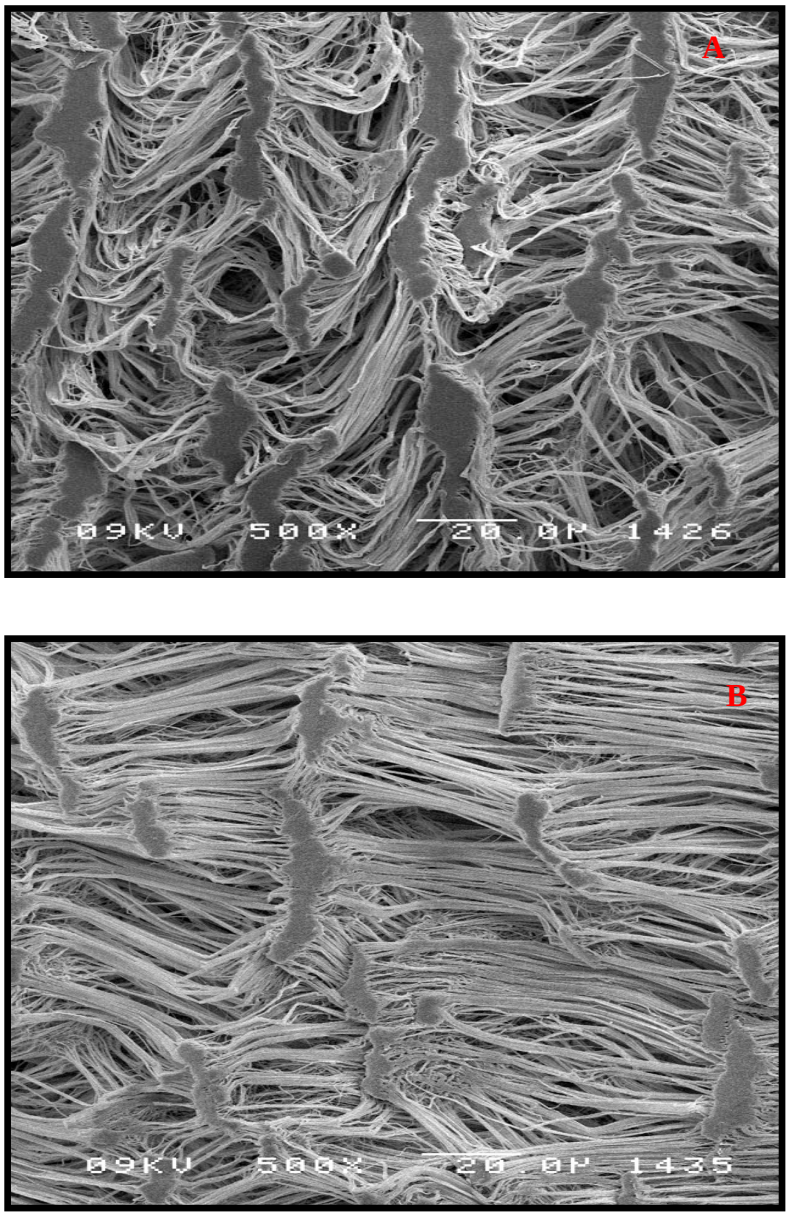

Figure 3.8: SEM Pictures of Unstretched and Stretched ePTFE. (A) Unstretched ePTFE demonstrating the empty space within the graft material. (B) Stretched ePTFE illustrating the dense and compact nature of the mechanically deformed material.

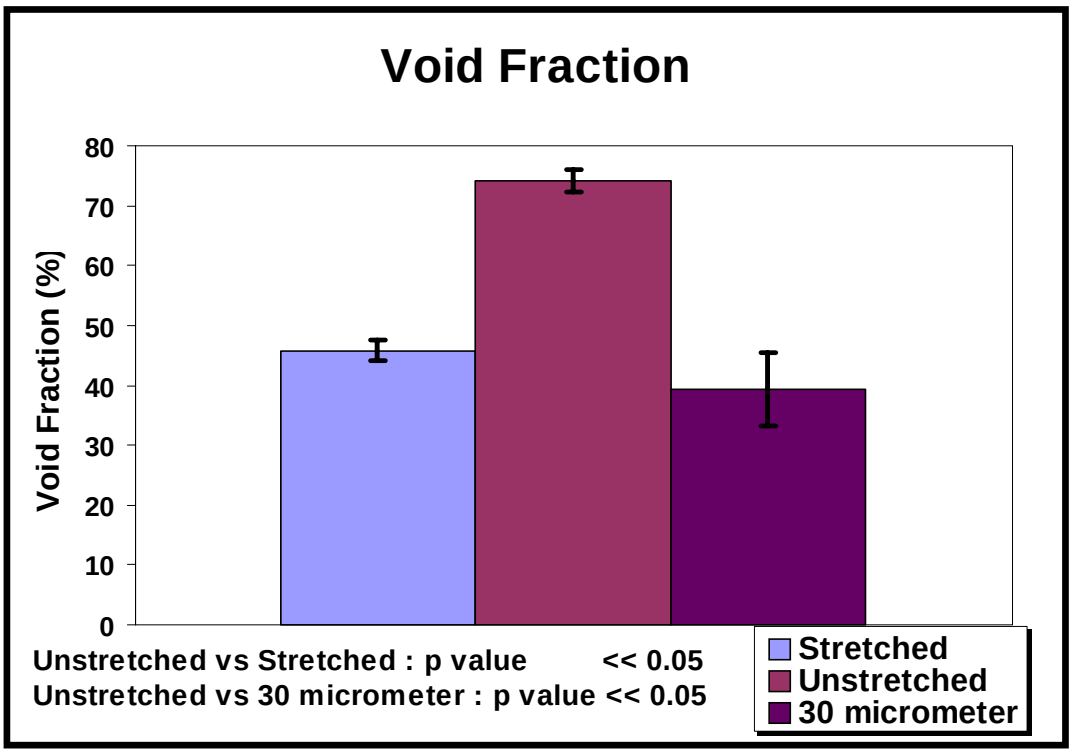

Figure 3.9: Void Fraction of Stretched 60 μm ePTFE, Unstretched 60 μm ePTFE, and 30 μm ePTFE. The void fraction of the unstretched 60 μm ePTFE significantly exceeded the void fraction of the stretched 60 μm ePTFE and the 30 μm ePTFE, while there was no statistical difference between the stretched 60 μm ePTFE and the 30 μm ePTFE.

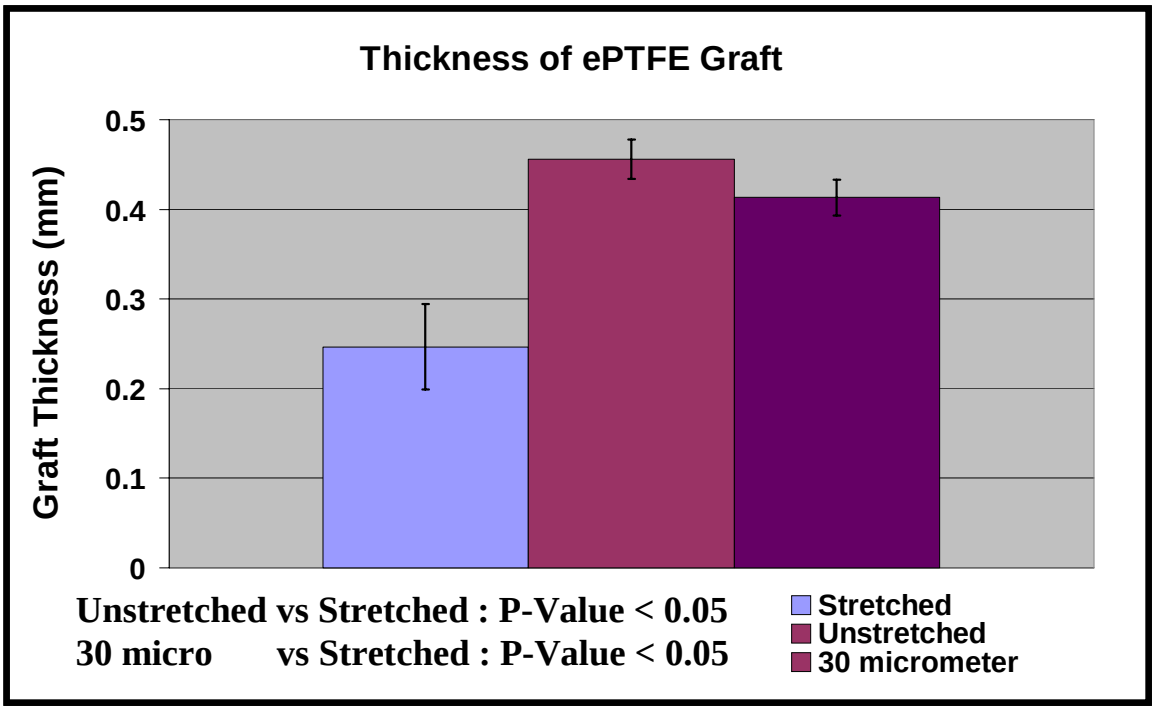

Figure 3.10: The Thickness of the Different ePTFE Vascular Grafts. The stretched 60 μm ePTFE possessed a notably smaller thickness than the other two varieties of vascular grafts. The difference in graft thickness between the stretched and unstretched 60 μm ePTFE was statistically significant.

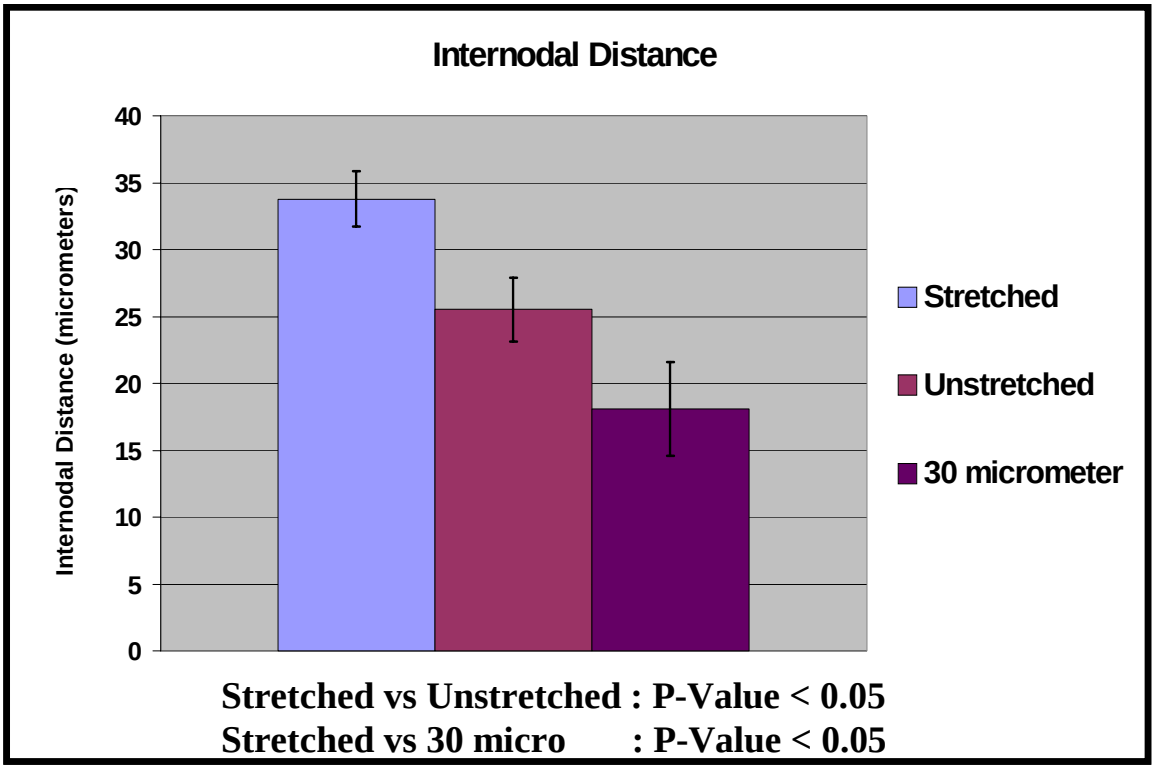

Figure 3.11: The Internodal Distance of the Different Varieties of ePTFE. The internodal distance of the stretched 60 μm ePTFE vascular graft exceeds that of the other two graft types. The difference in internodal distance between the stretched 60 μm ePTFE and the other two graft varieties was statistically significant.

2.4 μm) or the 30 μm ePTFE (18.1 ± 3.5 μm). Once again, this difference was found to be statistically significant. Lastly, the nodal width was measured (Figure 3.12). There existed no statistically significant difference between the nodal width of the stretched 60 μm ePTFE (5.58 ± 0.6 μm) and the unstretched 60 μm ePTFE (5.5 ± 0.7 μm).

Graft Healing.

On gross examination, the implanted vascular grafts appeared to have undergone healing of their flow surface (Figure 3.13). The H&E stained sections better explained the extent of the luminal healing. First, we examined the stained circular cross-sections of the unstretched controls (Figure 3.14). At the anastomotic ends there existed very distinct pannus ingrowth. At the mid-vessel point the surface had healed by transmural ingrowth from the surrounding perigraft tissue across the wall of the vascular graft. The Evan's blue dye qualitatively indicated that the graft surface possessed a confluent layer of endothelium (Figure 3.15). Before administering the Evan's blue dye, an angioballoon catheter was fed up to the level of the graft's proximal anastomosis and then inflated. The catheter was gradually withdrawn, stripping the endothelium off the native vessel. This region of native vessel, devoid of endothelium, uptook the Evan's blue dye, while the healed graft surface excluded it. At the mid-vessel section, the VWF immunostain (Figure 3.16) further outlined how the graft surface healed with a confluent endothelium. The intimal thickening of the unstretched control grafts was quantified (Figure 3.17). At the anastomotic ends the intimal thickness reached an average of 0.43 mm. There existed no significant difference in intimal thickening between the proximal and distal anastomosis (Figure 3.18). The intimal thickness decreased towards the mid-point, reaching a minimum value of 0.08 ± 0.02 mm.

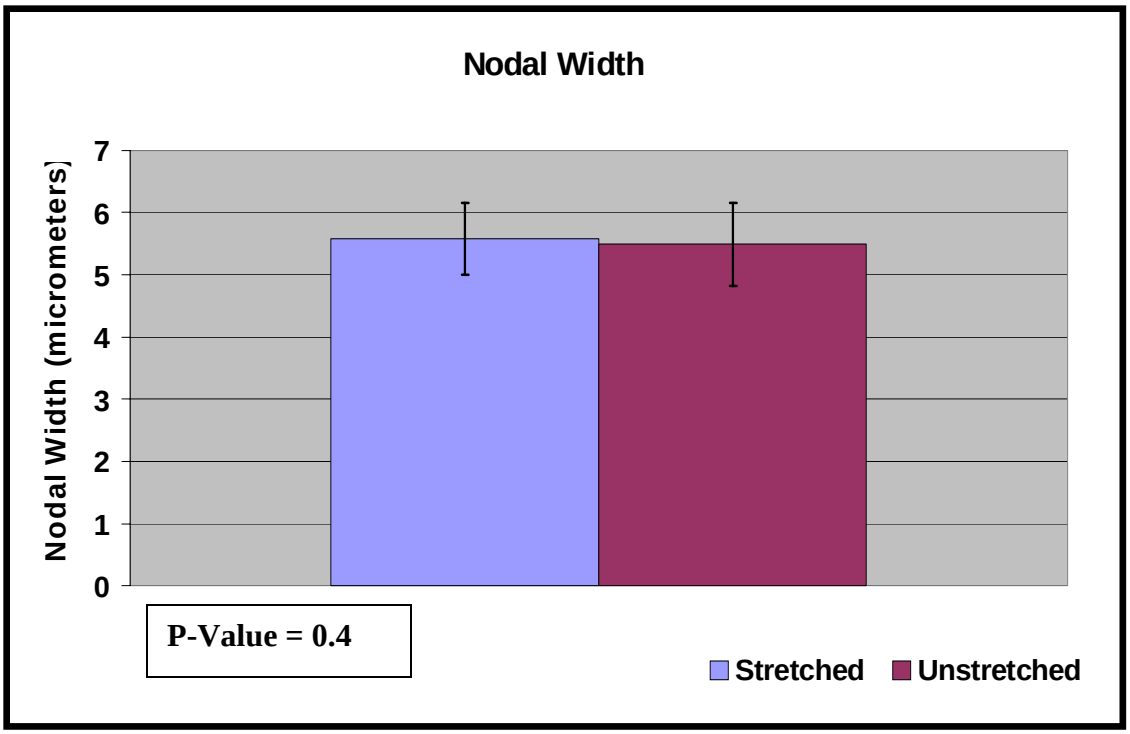

Figure 3.12: The Nodal Width of the Stretched and Unstretched 60 μm ePTFE. There existed no statistically significant difference in the nodal width between the stretched and unstretched 60 μm ePTFE.

Figure 3.13: Photograph of a Harvested, Stretched Stenotic Graft. Flow occurs from right to left. On initial observation the graft surface has undergone some healing. The question persists as to how complete and confluent a healed surface is present.

.

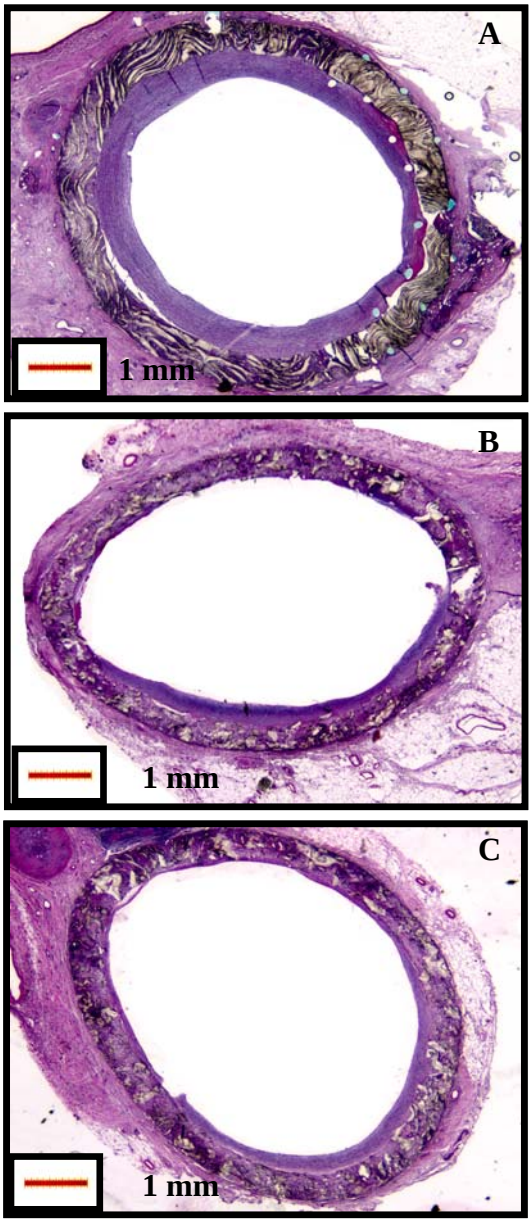

Figure 3.14: H&E Staining of Circular Cross-Sections from the Unstretched Control. (A) Proximal Anastomosis (B) Mid-Vessel (C) Distal Anastomosis.

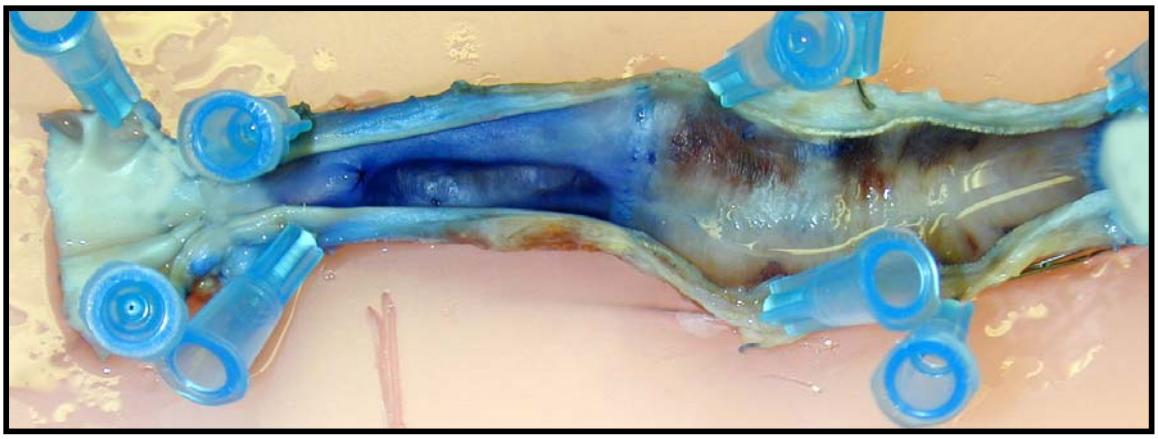

Figure 3.15: Evan's Blue Dye Stain of Harvested, Unstretched Control Graft. The Evan's Blue Dye (50 mg/ml) was administered through an angioballoon catheter into the vessel's lumen. The inflated angioballoon catheter stripped away the endothelium of the native vessel, resulting in uptake of blue dye. Note the absence of dye uptake upon the surface of the healed graft. This experiment qualitatively shows that the graft surface was healed.

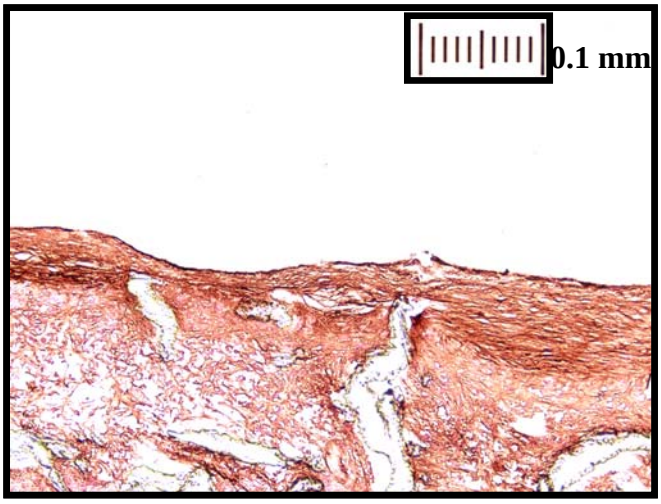

Figure 3.16: VWF Immunostain of Unstretched Control. The positive staining on the luminal surface demonstrates a confluent endothelium.

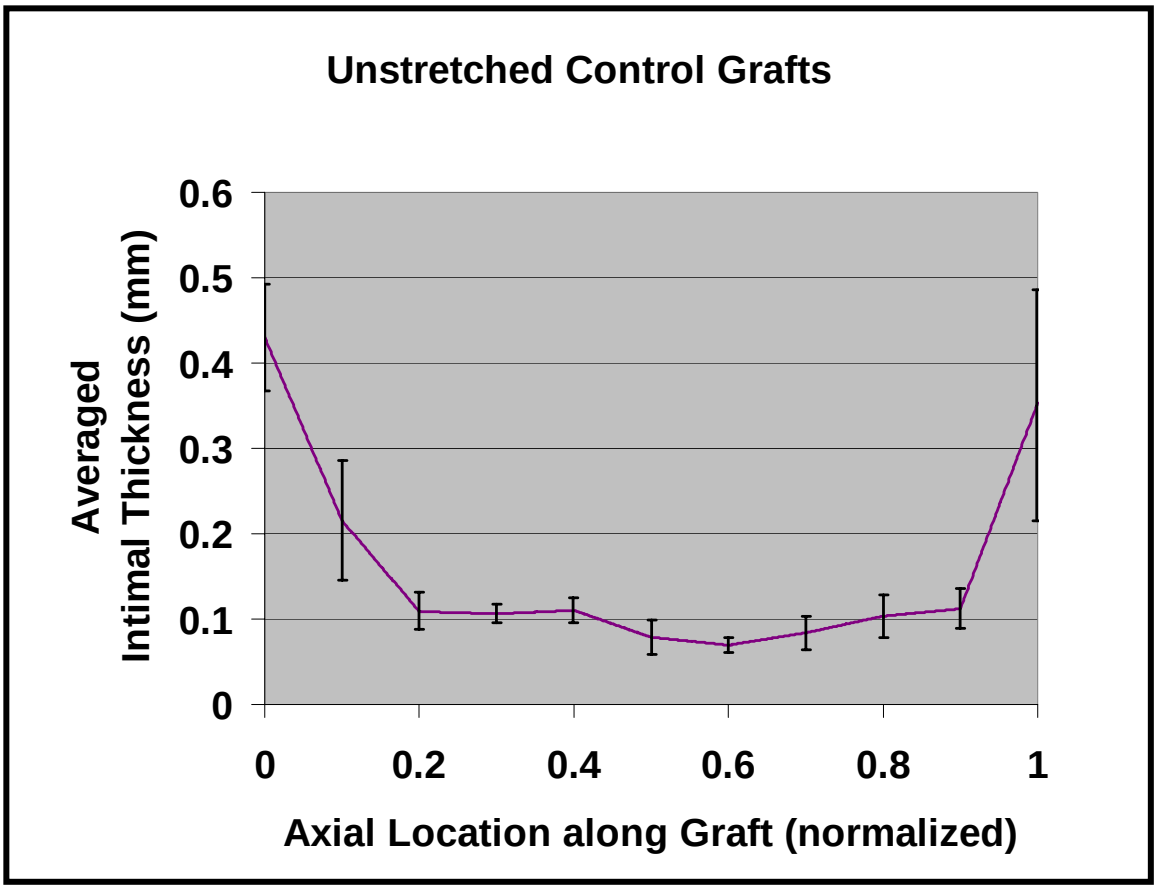

Figure 3.17: A Quantitative Description of Intimal Thickness along the Axial Length of an Unstretched Control Graft. The pannus ingrowth resulted in the pronounced thickening at the anastomotic junction. Once removed from the suture line, the intimal thickness assumed a baseline level.

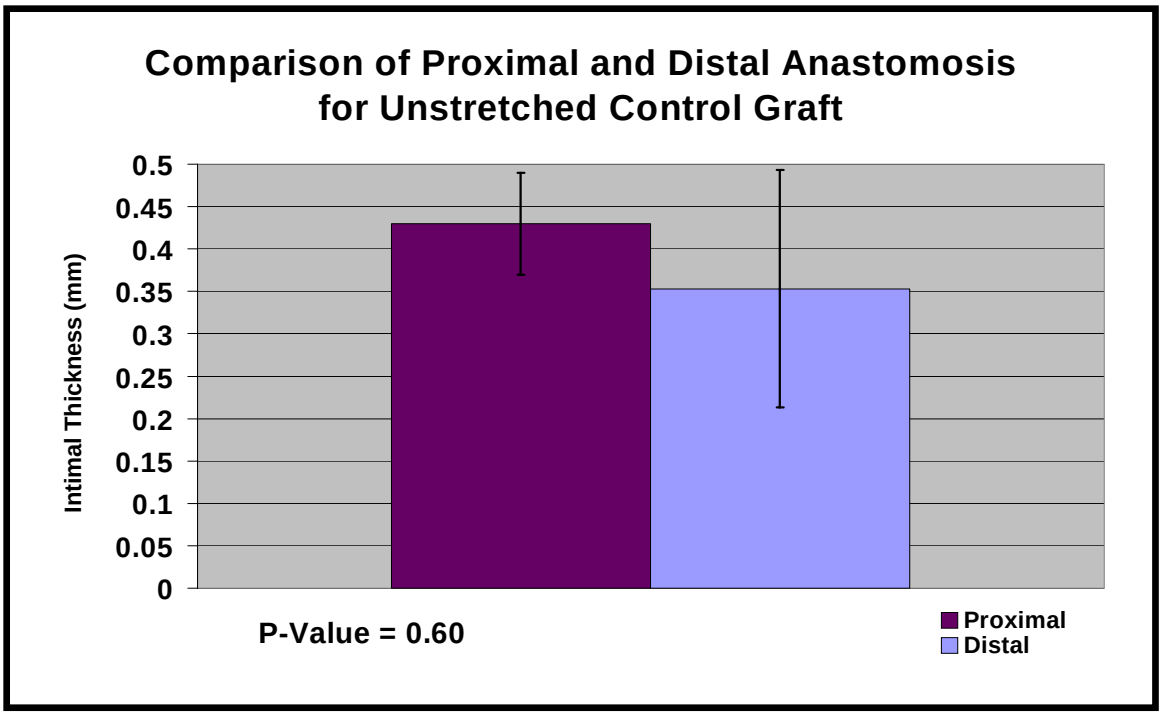

Figure 3.18: Comparison of Proximal and Distal Anastomosis for Unstretched Control Graft. There existed no statistically significant difference between the proximal and distal ends.

Secondly, we investigated the stained circular cross-sections of the stretched controls (Figure 3.19). In comparison to the unstretched controls, the graft material appeared compressed and very compact. Pannus ingrowth was observed at the anastomotic ends while very little, if any ingrowth, was observed at the mid-vessel location. The intimal thickening of the stretched control grafts was quantified as a function of distance along the axial length of the vascular graft (Figure 3.20). At the anastomotic ends the intimal thickness reached an average value of 0.25 mm, while at the mid-vessel point the intimal thickness was 0.09 ± 0.06 mm. At the proximal and distal anastomosis, there existed no difference in intimal thickening (Figure 3.21). Lastly, we examined the stained circular cross-sections of the stretched stenosis (Figure 3.22). As with the controls, pannus ingrowth was observed at the anastomoses, but there existed no difference in intimal thickening between the proximal and distal ends (Figure 3.23). Unexpectedly, an increase in intimal thickening was recorded at the mid-vessel point. Quantitative exam revealed that at the stenotic throat the intimal thickness increased to 0.34 ± 0.06 mm (Figure 3.20). To ensure that the intimal thickness measurements were reflecting the healing pattern accurately, the deposited intimal area was measured as a function of axial distance (Figure 3.24). The figure displays the results for the stretched control and stretched stenotic grafts. The intimal area results mirrored the earlier discussion for intimal thickness.

Graft Healing at Mid-Vessel.

The intimal thickness measurements at the mid-vessel location were compared between the different vascular graft types. First, we examined the unstretched and stretched controls (Figure 3.25). There existed no

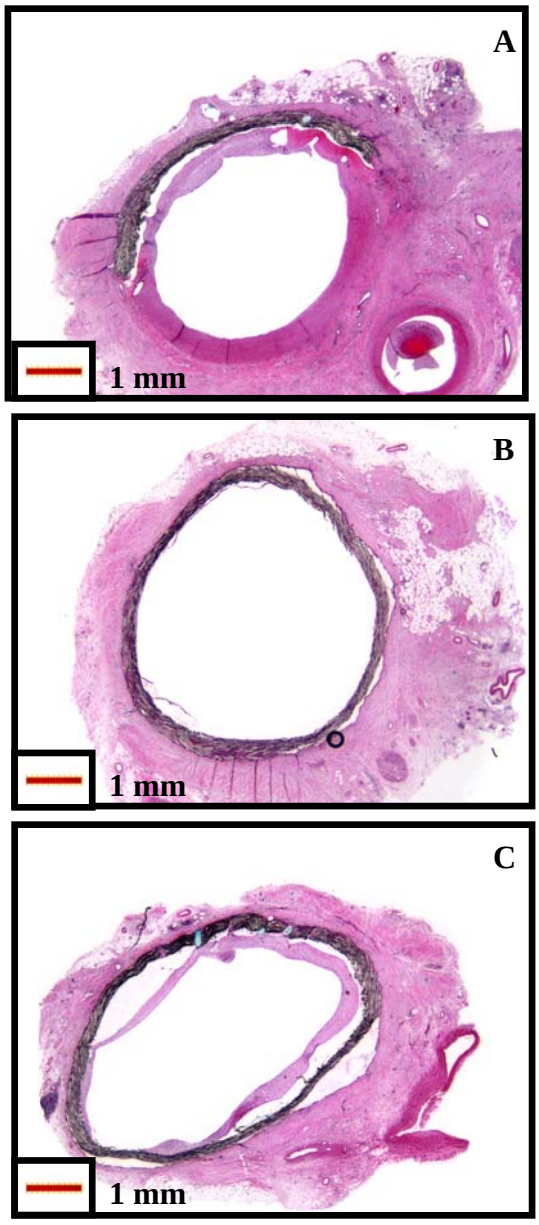

Figure 3.19: H&E Staining of Circular Cross-Sections from the Stretched Control. (A) Proximal Anastomosis (B) Mid-Vessel. Note the absence of intimal thickening (C) Distal Anastomosis.

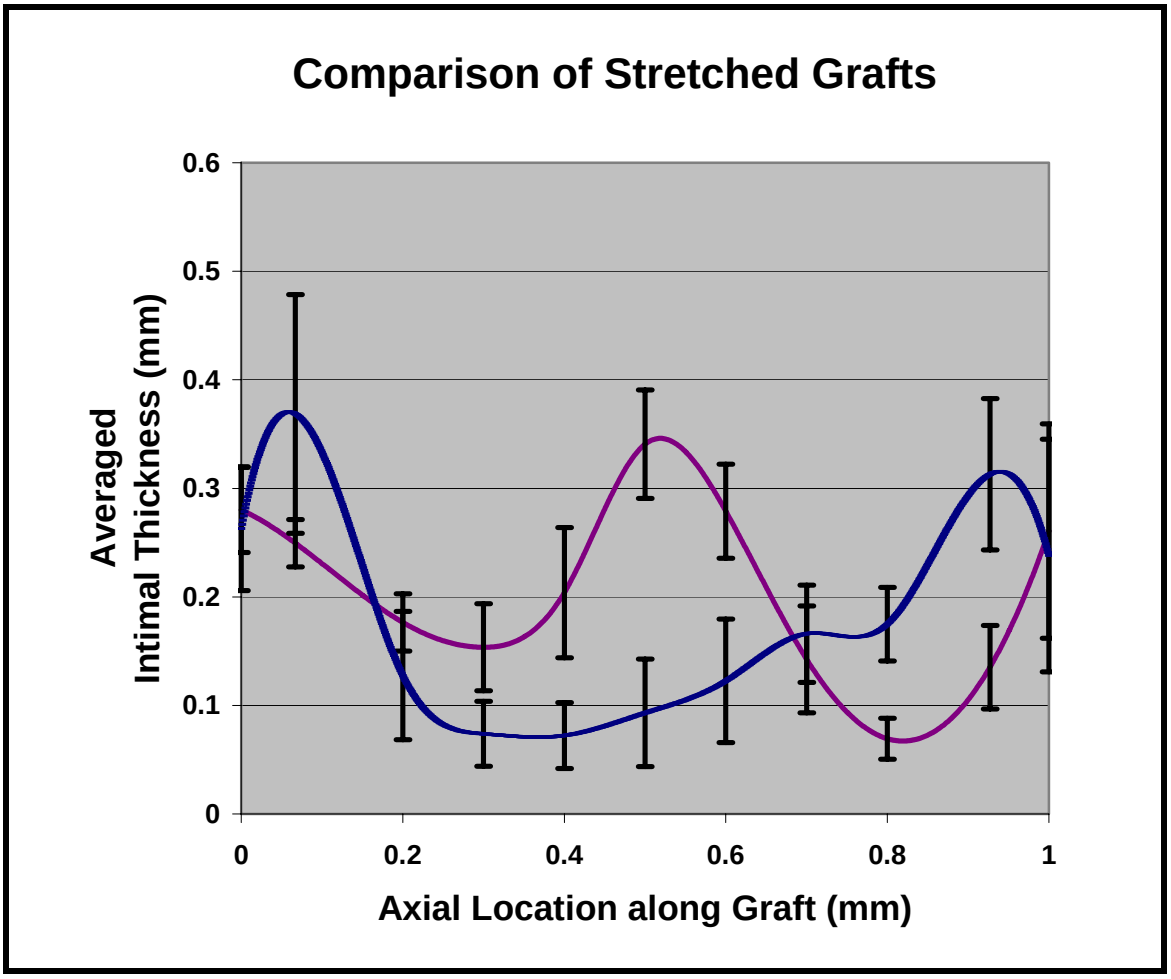

Figure 3.20: A Quantitative Description of Intimal Thickness along the Axial Length of the Stretched Control and the Stretched Stenosis. The raw intimal thickness data was processed using an ARMA, producing the above waveforms. The increase in intimal thickening at the stenotic throat was very unexpected. Several contributing factors helped to explain this observation.

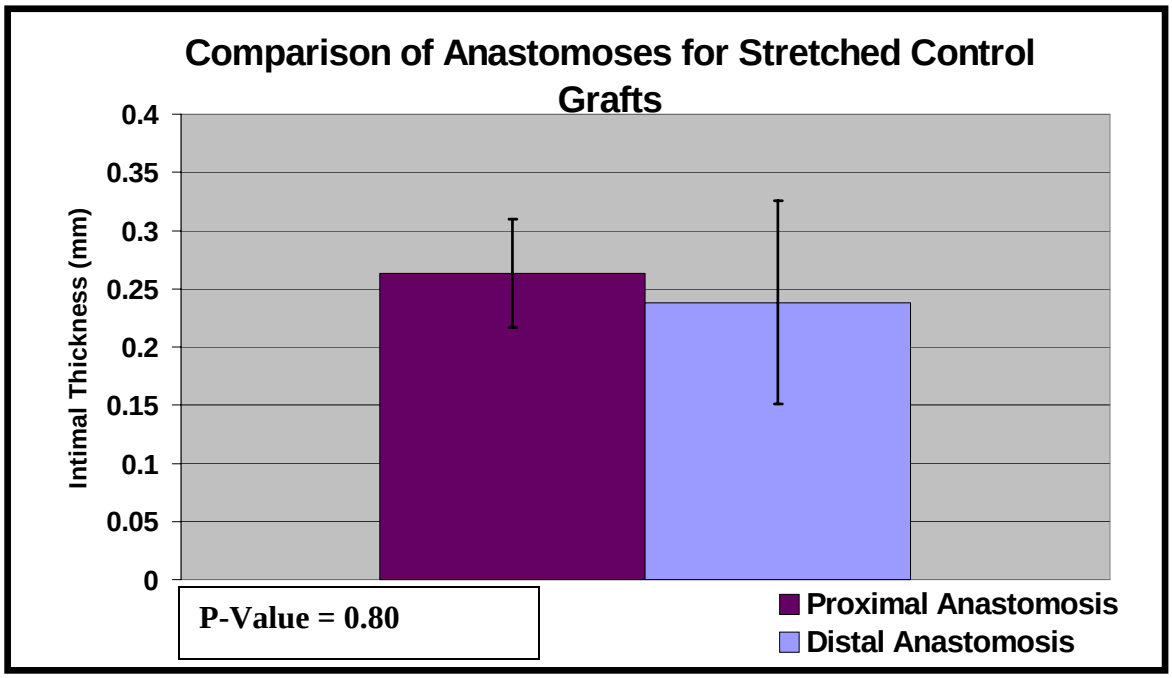

Figure 3.21: Comparison of Intimal Thickening at the Proximal and Distal Anastomoses of the Stretched Control Grafts. There existed no statistically significant difference in intimal thickening between the proximal and distal ends of the vascular graft.

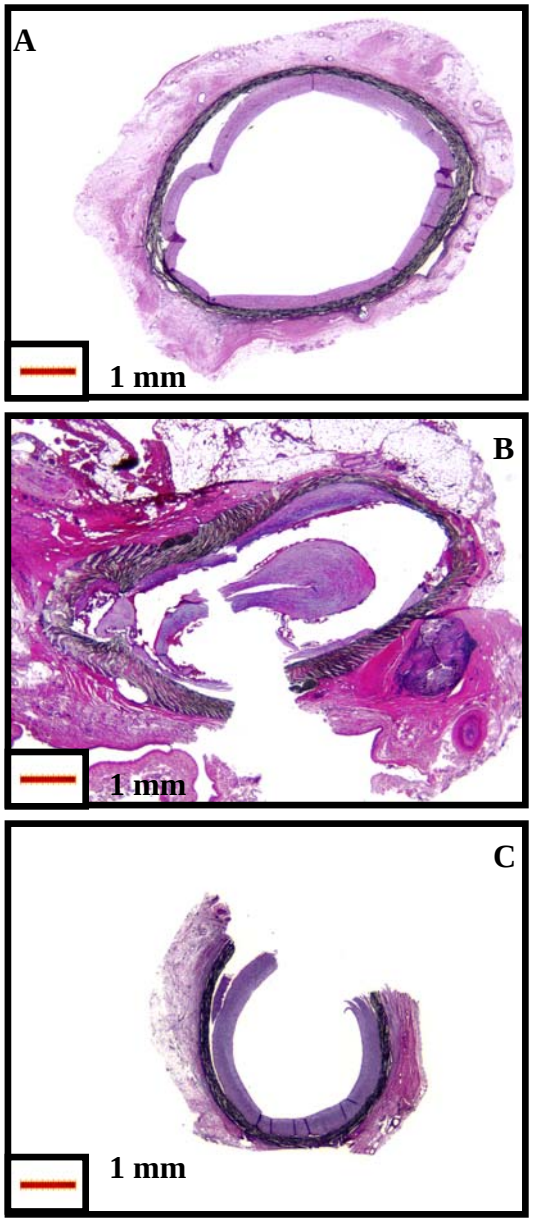

Figure 3.22: H&E Staining of Circular Cross-Sections from the Stretched Stenosis. (A) Proximal Anastomosis (B) Mid-Vessel. Observe the very distinct intimal thickening (C) Distal Anastomosis.

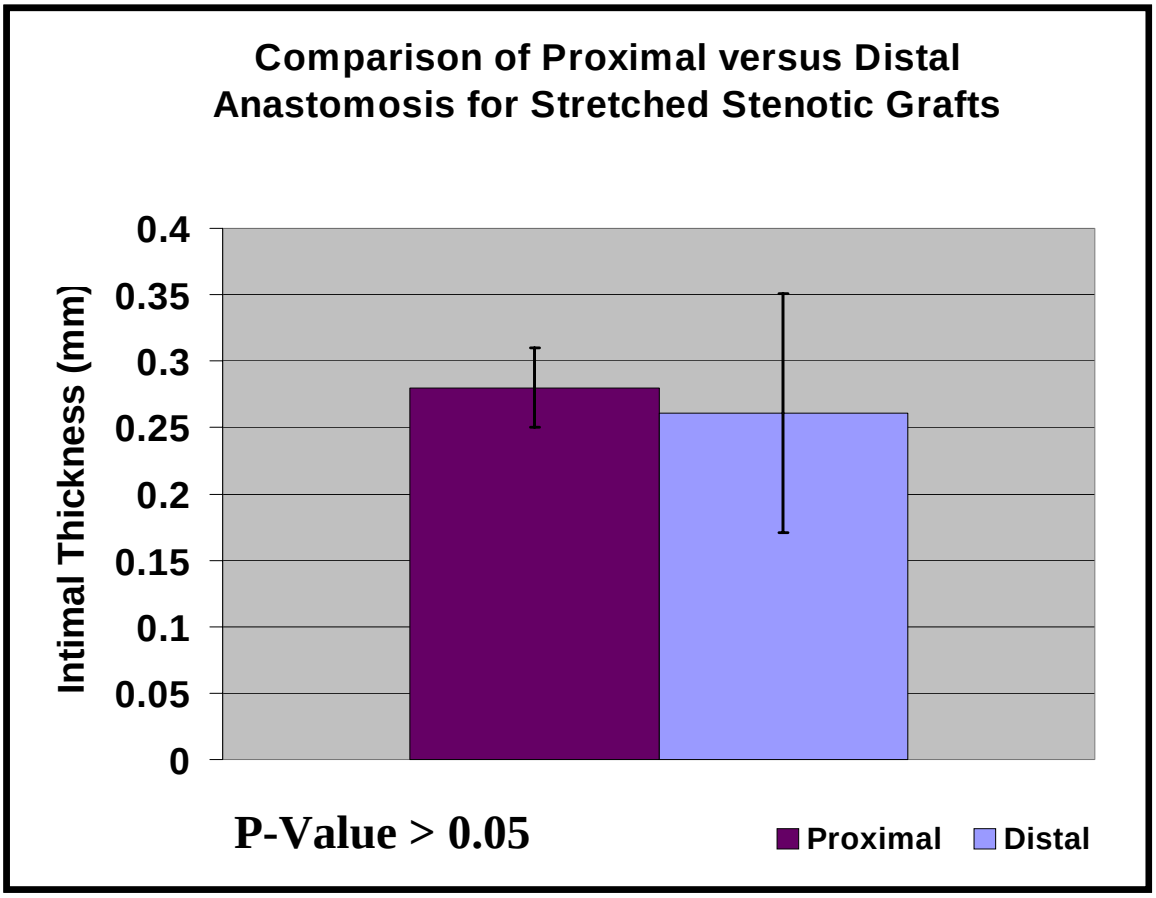

Figure 3.23: Comparison of Intimal Thickening at the Proximal and Distal Anastomoses of the Stretched Stenotic Grafts. There existed no statistically significant difference in intimal thickening between the proximal and distal ends of the vascular graft.

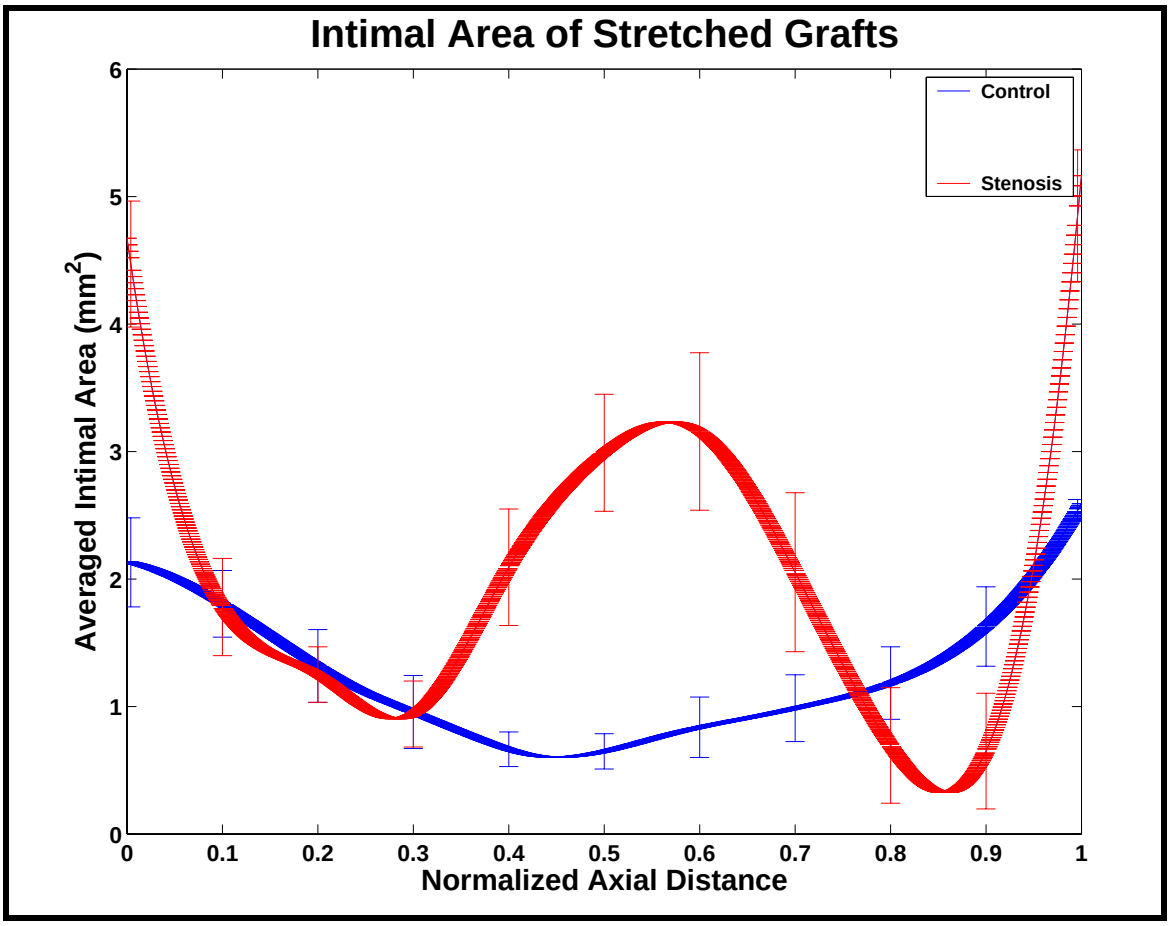

Figure 3.24: Intimal Area of Stretched Control and Stretched Stenotic Grafts. This description mirrors what was described earlier with the intimal thickness results.

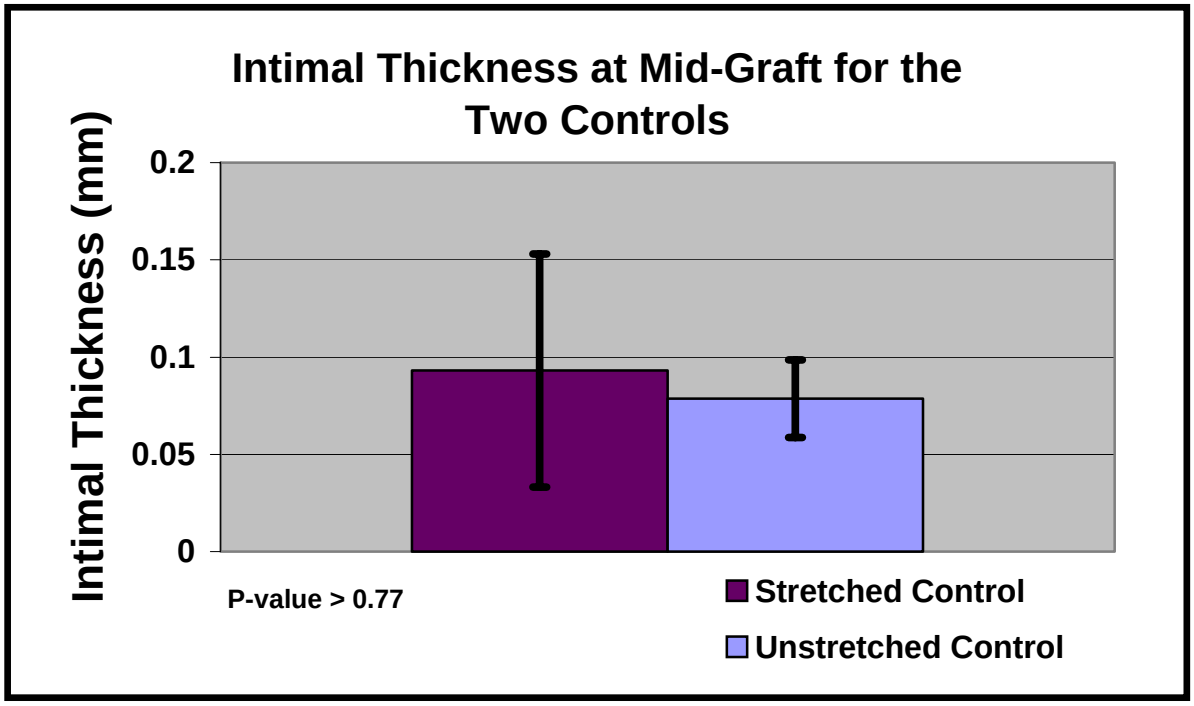

Figure 3.25: Comparison of Intimal Thickening at Mid-Vessel Between Stretched and Unstretched Control. No statistically significant difference was observed between the intimal thickenings of the two different types of control grafts.

statistically significant difference between the unstretched control (0.08 ± 0.02 mm) and the stretched control (0.09 ± 0.06 mm). When comparing the controls to the stretched stenosis, different results evolved. There emerged a statistically significant difference between the unstretched control (0.08 ± 0.02 mm) and the stretched stenosis (0.34 ± 0.06 mm) (Figure 3.26), as well as between the stretched control and the stretched stenosis (Figure 3.27).

BRDU at Mid-Vessel.

BRDU immunostains were performed on cross-sections at the stenotic throat and up to 0.5 cm upstream and downstream of this location (Figure 3.28). Qualitatively, the number of proliferating cells was concentrated at the stenotic throat and decreased with translation from this region.

Hemodynamics.

Based on the CFD simulations, WSS values under harvest conditions were obtained for the control and stretched stenosis grafts. For the control grafts the $\tau avg(z)$ averaged 4 dynes/cm^2. For the stretched stenotic grafts, the proximal and distal graft segments with a 6 mm internal diameter had a $\tau avg(z)$ of 3 dynes/cm^2 , while the stenotic throat had a $\tau avg(z)$ of 18 dynes/cm^2. Within the stenotic throat, the Max WSS equaled 82 dynes/cm^2, while the Pulse WSS exceeded 47 dynes/cm^2. Additional CFD results will be discussed in Chapter V.

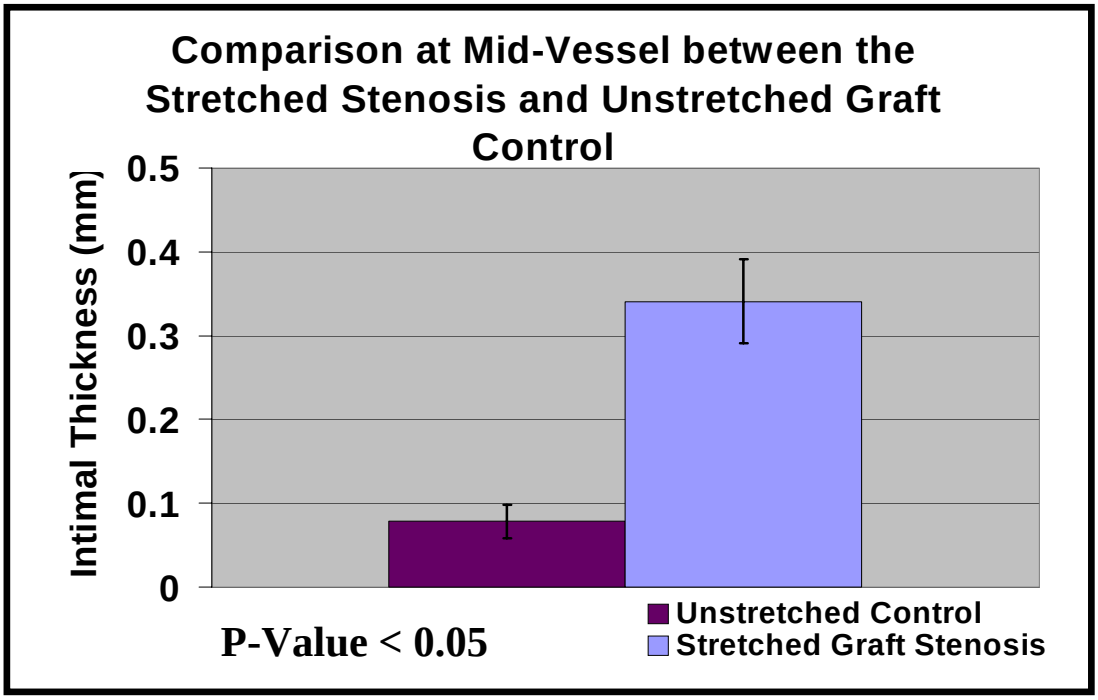

Figure 3.26: Comparison of Intimal Thickness at Mid-Vessel Between Unstretched Control Graft and Stretched Stenotic Graft. There existed a statistically significant difference between the intimal thickening of the unstretched control graft and the stretched stenotic graft.

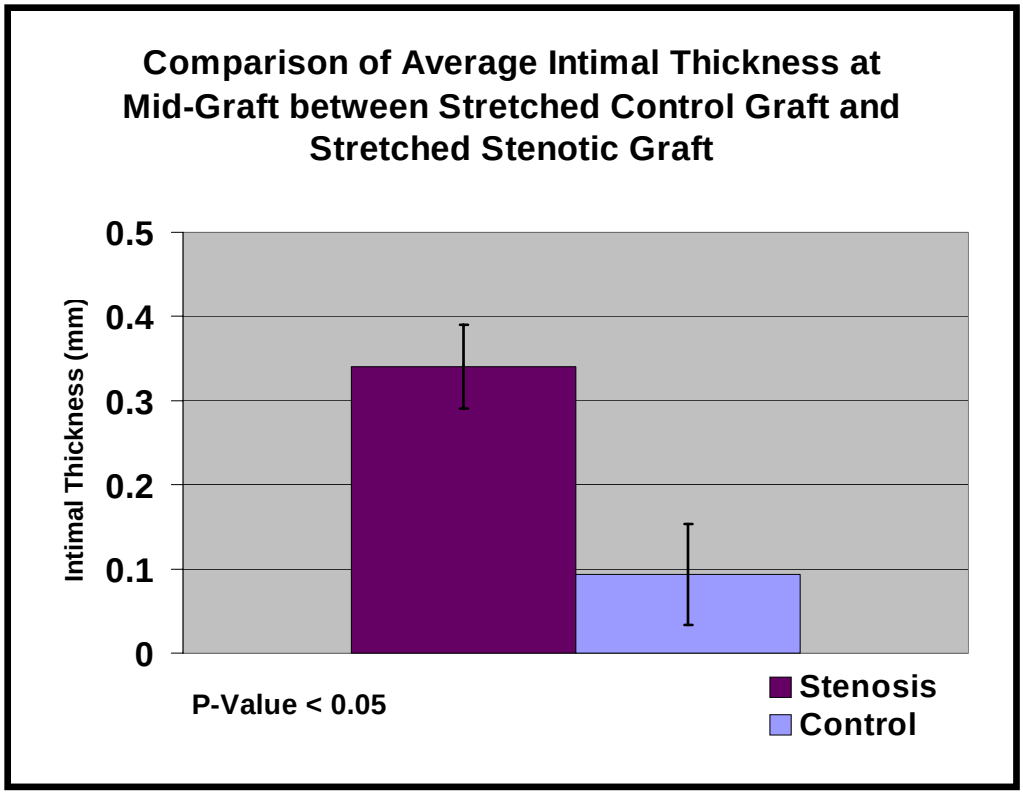

Figure 3.27: Comparison of Intimal Thickening at Mid-Vessel Between Stretched Control Graft and Stretched Stenotic Graft. There existed a statistically significant difference between the intimal thickening of the Stretched Control Graft and the Stretched Stenotic Graft.

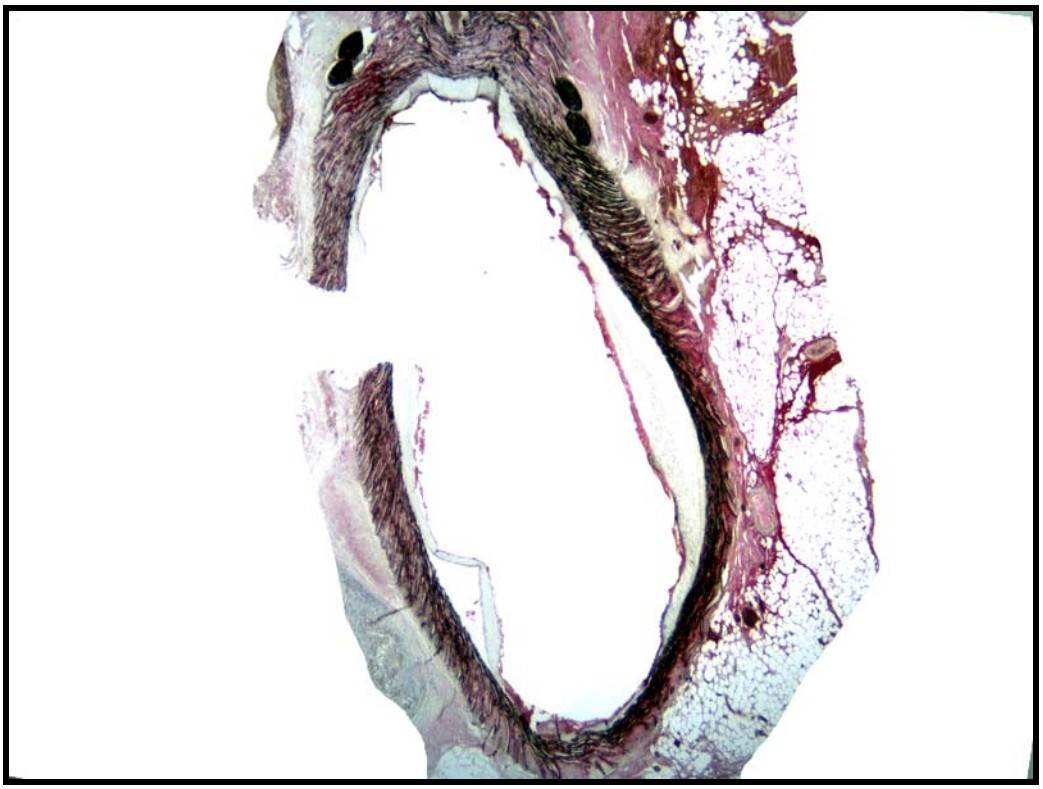

Figure 3.28: BRDU Immunostaining of the Stretched Stenosis. The proliferating cells are located near the adluminal flow. Based on their location nearthe flow surface, they are predominantly endothelial cells.

Discussion:

Our study documented how changes in the material ultrastructure affected healing of a prosthetic vascular graft. We investigated this topic using two different models. Before discussing how the grafts healed, we will begin by documenting how the vessel ultrastructure was altered.

Graft Ultrastructure.

The radial stretching of the 60 μm ePTFE induced a definitive change in the initial material properties. First and foremost, the stretching reduced the void fraction of the graft material. Without empty space within the graft material, there existed no avenue for tissue to migrate from outside the vessel into its inner lumen. The void fraction reflects the ability of the graft to heal by transmural ingrowth. Without transmural ingrowth, the ePTFE grafts fail to evolve a confluently healed surface. Nonporous grafts such as 30 μm ePTFE do not heal by transmural ingrowth. Even one year following implantation, 30 μm ePTFE still demonstrates patchy and incomplete healing [39]. In a study of porous grafts, the void fraction distinguishes itself as the most informative parameter regarding how quickly and how completely the graft will heal. While Palmaz [103] and Williams [48] evaluated many structural properties within their studies, they did not investigate this very important parameter since their studies only focused upon 30 μm ePTFE. While they investigated the effect of material deformation on graft healing, they began with a material that did not permit for transmural ingrowth even in its native, unstretched state [47,103]. 30 μm ePTFE heals primarily by transanastomotic ingrowth. Any stretching and mechanical deformation will exert little change upon this mechanism of healing. This

helps to explain why both Palmaz and Williams reported inconclusive findings in their animal studies with healed, stretched grafts.

In contrast to their studies, our work began with the porous 60 μm ePTFE that healed completely within two weeks. Unlike 30 μm ePTFE, the 60 μm ePTFE graft heals both by transanastomotic ingrowth and by transmural ingrowth [25]. The radial stretching of the 60 μm ePTFE mechanically deformed the material so that the void fraction was reduced by nearly 38 %. Even before quantitatively measuring the void fraction, the SEM images illustrated how stretching made the grafts very compact and dense (Figure 3.8b). The SEM images displayed the luminal graft surface parallel to the vessel's axial direction. From this angle, we observe a very distorted graft material that appears devoid of any empty space. This picture contrasts with Figure 3.8a that shows a relaxed, unstretched 60 μm ePTFE that is receptive to tissue ingrowth. The H&E stained cross sections illustrated this point from an alternative perspective. These stained cross sections highlighted the empty space perpendicular to the vessel's axial length. The unstretched control graft showed empty space that was inviting to tissue ingrowth and was unoccupied by surrounding graft material. By stretching the porous 60 μm ePTFE, the void fraction was reduced to a level commensurate with the 30 μm ePTFE. The process of stretching removed a distinguishing property of the porous material. The void fraction between stretched, 60 μm ePTFE and unstretched 30 μm ePTFE only differed by 10 %, and this difference was not found to be statistically significant. Based on this result, we expected the stretched 60 μm ePTFE and the unstretched 30 μm ePTFE to heal in a very similar fashion. In the end, our results with the 60 μm ePTFE mirrored previously published observation with 30 μm ePTFE [25,39,40].

The radial stretching reduced the thickness of the vascular graft material. The thickness of the stretched graft material decreased by 45 % and was statistically different than the unstretched graft material. There existed no statistically significant difference in graft thickness between unstretched, 60 μm ePTFE and unstretched, 30 μm ePTFE. By stretching the graft material, the distance between the outside of the vessel and its luminal lining was reduced. In essence, tissue now had to travel less distance to heal the intraluminal surface. A very interesting question emerged from this observation. By stretching the graft material, we reduced the void fraction that facilitates transmural ingrowth, but we also reduced the distance that tissue now needed to migrate to heal the intraluminal surface. As far as graft healing was concerned, stretching the ePTFE material reduced void fraction in an unfavorable way, while it decreased graft thickness in a beneficial way. In the end did we alter the ability of these stretched porous ePTFE vascular grafts to heal? The results from the harvested grafts answered this question.

The other two parameters of internodal distance and nodal width were also measured. Unlike Williams [48], we observed that stretching lengthened the internodal distance by 36 %. Doubt surrounds whether this lengthening of the internodal distance impacts graft healing to any degree. If nothing else, any effect that it exerts has already been incorporated into our evaluation of graft thickness and void fraction. A similar line of thought applies to our evaluation of nodal width and the lack of any appreciable difference in the measurements between stretched and unstretched graft.

Healing of the Stretched and Unstretched Control Grafts.

First, we examined the healing patterns of the two different varieties of control grafts. The unstretched control graft demonstrated confluent healing of its intraluminal surface. This was verified through several different methods. The H&E stained sections displayed complete healing at every examined cross-section. Furthermore, tissue migration across the graft wall was revealed from ingrowth laden within its interstices. The Evan's Blue Dye was noticeably excluded from the vessel's intraluminal lining. This exclusion only occurs in the presence of a confluent layer of endothelium that shields the vessel from dye uptake. On exam with SEM, we observed a healed surface with healthy and "cobble-stone" endothelium. Lastly, immunostaining with VWF illustrated a healed endothelial layer. This picture was consistently observed in any examined section. In comparison, the stretched control graft failed to evolve a completely healed graft surface. This was evident just on observation of the H&E staining. On some of the circular cross-sections, there appeared very little if any tissue migration across the graft wall; consequently, some of these cross-sections showed no healing at all. The Evan's blue dye was uptaken by the graft, resulting in a distinct blue staining. This dye uptake hinted at the absence of an endothelium. The SEM demonstrated very incomplete healing with sections of graft covered only by an occasional platelet or other blood-borne cell. Most importantly, the VWF immunostain was conspicuously absent on many of the examined cross-sections.

Clearly, the unstretched control was more healed than the stretched control. As expected, there existed no difference in intimal thickening at the anastomotic ends of the two grafts types. At this location both varieties healed by the same mechanism of pannus ingrowth. Next, we examined the mid-vessel regions that are immune from healing by

transanastomotic ingrowth. Surprisingly, there existed no statistically significant difference in the quantitative measurements between the two graft varieties. At the mid-graft both types of grafts evolved the same amount of average intimal thickening. With the preservation of graft ultrastructure in the unstretched control, we expected to observe greater average intimal thickening. This peculiar healing process occurred for several reasons. First, the unstretched control grafts heal very quickly with an established layer of protective endothelium. This protective endothelial layer shields the underlying tissue from potentially mitogenic and chemogenic mediators within the flowing blood. In addition, the endothelium releases such vasodilatory products as nitric oxide and vascular endothelial growth factor (VEGF) that inhibit smooth muscle cell proliferation. By healing very rapidly, the unstretched control graft stymied several of the processes that lead to pronounced intimal thickening. On the other hand, the stretched control failed to evolve this confluent and protective endothelium. As a result, some of the examined cross-sections developed very significant intimal thickening with large amounts of extracellular matrix, while other cross-sections evolved little to no intimal thickening at all. Even with its incomplete healing, the stretched control grafts developed on average the same amount of intimal thickening as the unstretched control grafts. The marked thickening at some locations compensated for its absence in other regions. This trend was best reflected by a comparison of standard deviations between the stretched (0.06 mm) and unstretched (0.02 mm) control grafts. The standard deviation of the stretched control grafts was three times as large as that for the unstretched control grafts. In conclusion, the amount of intimal thickening fails to function as the most reflective parameter of graft

healing. Instead, the ability of the graft to heal quickly and to evolve a confluent endothelium has assumed that ever-important role.

Healing of the Stenotic Grafts.

The stretched stenotic graft introduces a very interesting model, for within its borders there exists both preservation and distortion of the graft ultrastructure. At each of the anastomotic ends the graft material has been stretched from an inner diameter of 3 mm to an inner diameter of 6 mm. As we progress toward the stenotic throat, the graft material has also been stretched, albeit not to the same extent since its size progressively approaches the starting diameter of 3 mm. At the stenotic throat the material properties are identical to those of unaltered 60 μm ePTFE. Since both the starting 60 μm ePTFE and the stenotic throat have an inner diameter of 3mm, no stretching occurs at this location. As a result, surrounding tissue can migrate across the wall of the stenotic throat, depositing on the luminal surface. The animal experiments revealed significant intimal thickening at the stenotic throat. In fact, the average intimal thickness at the stenotic throat was statistically different than either control. On average the intimal thickness at the stenotic throat exceeded that of the control grafts' mid-vessel value by nearly 300 %. This observation was all the more surprising because it happened in the stenotic throat where there exists an elevation of wall shear stress values (WSS). As many investigators have documented through animal experiments, elevations in WSS furnish a mechanism to inhibit intimal thickening. Through several studies examining the carotid arteries, coronary arteries, and abdominal aorta, these *in vivo* experiments presented results where high levels of WSS led to decreased intimal thickening. Conversely, they have shown

that low and oscillatory levels of WSS promote pronounce and progressive thickening [54-56,60].

The explanation for the stenotic throat's intimal thickening probably involves several interacting factors. First, the preservation of the original graft ultrastructure encourages transmural ingrowth. Transmural ingrowth fails to occur either upstream or downstream of the stenotic throat where the inner diameter is stretched from its starting 3 mm internal diameter. At these locations the material has been too mechanically altered. As a result, the stenotic throat then functions as an origin for healing to spread upstream and downstream of this infiltrated location. If the stenotic throat operates in this capacity, there must exist a population of proliferating cells prepared to migrate. Through BRDU immunostaining, we identified a large number of proliferating endothelial cells and some proliferating smooth muscle cells. In many respects, the healed surface of the stenotic throat resembled the leading edge of the neointima. Just as the leading edge attempts to cover unhealed graft surfaces away from the anastomotic junctions, this neointima attempts to migrate towards adjacent areas of unhealed graft that have been stretched and mechanically altered, making them impermeable to transanastomotic ingrowth. Still, a certain caveat must be heeded with this analogy. While the throat's neointima demonstrates some resemblance to a leading edge, we cannot definitively conclude that it functions in that capacity. In order to empirically draw that conclusion, the vessels need to be processed into longitudinal sections rather than the present circular cross-sections. While circular cross-sections visualize proliferating cells, they fail to illustrate the shape or progression of the leading edge. Future studies will be needed to elucidate this mechanism.

At the stenotic throat there exists an elevation of WSS; however the WSS values still reside within high physiologic limits. Over the 0.5 cm length of the stenotic throat, the τavg(z) hovered near a mean value of 18 dynes/cm^2. Although this value exceeded the 2 - 3 dynes/ cm^2 seen either upstream or downstream, its magnitude failed to achieve a sufficient range to exert its inhibitory effect upon intimal thickening [117-121]. In their work researchers often correlated the WSS measurements to the measured intimal thickness, hoping to reveal a causative relationship between these biologic measurements and the mechanical forces. In this study altering the material ultrastructure obviated any future ability to isolate the effect of changing hemodynamics upon such biologic variables as intimal thickness; consequently, no correlative studies were conducted. Another possible explanation for the increased intimal thickening may derive from humoral-mediated factors. At the stenotic throat an elevation of blood velocity occurs. This faster velocity can result in damaging of such blood-borne elements as platelets. While the τavg(z) did not exceed 30 dynes/cm^2, other parameters such as the Pulse WSS and Max WSS did. The Pulse WSS exceeded 47 dynes/cm^2, while the Max WSS was greater than 87 dynes/cm^2. These values represented transiently high levels of WSS. While they were not sustained for a long enough period to inhibit intimal thickening, their magnitude was sufficient enough to damage the blood-borne platelets. Once damaged, platelets release such potent mediators as PDGF-AA, PDGF-BB, thromboxane A_2, b-FGF, and many other cytokines. These mediators and growth factors can lead to smooth muscle cell migration, proliferation, and deposition of extracellular matrix, all contributing factors to increased intimal thickening. In the end, a combination of all these contributing influences may have led to the observed intimal thickening. Since these

models incorporated several parameters, it becomes difficult to distill which was the most important or exerted the most pervasive effect. In the future we would like to conduct a study of graft ultrastructure where we alter the void fraction but where we do not change the thickness of the graft material. This modification simplifies an analysis of graft ultrastructure and its subsequent effects on healing. Furthermore, we would like to isolate the effect of a changing hemodynamic environment on graft healing but without any concordant changes in graft ultrastructure.

Chapter IV

Graft Healing of Unstretched ePTFE Implanted within a Baboon

Introduction:

Since its inception, expanded polytetrafluoroethylene (ePTFE) has functioned as the preferred prosthetic vascular graft for repair of occlusive, peripheral vascular disease. Clinically, physicians use a rigid ePTFE with an internodal porosity of 30 μm and with reinforced rings that ensure material integrity. In the absence of an available autologous vessel like the saphenous vein, ePTFE is frequently used in femoropopliteal reconstruction. Clinicians prefer ePTFE because of its smooth and relatively nonthrombogenic surface, its ease of use, and its lack of pre-clotting. Interestingly, when used for surgical repair of femoropopliteal arteries, the patency rates of Dacron and ePTFE are indistinguishable, and quite often, a physician's choice of ePTFE is governed by an allegorical feel rather than a well-established scientific basis. An even more surprising fact is that both of these synthetic substitutes were developed in the 1950s, and even in the technologically advanced world of today, they still function as the only available choices for a prosthetic vessel [115,116]. A possible alternative to both of these clinically used synthetic substitutes can be found with a more porous, prosthetic material such as 60 μm ePTFE. Unlike the less porous 30 μm ePTFE, 60 μm ePTFE allows for tissue migration across its wall and subsequent transmural ingrowth onto its luminal lining. As a result, researchers have documented how these more porous grafts heal with

a well-identified confluent endothelium within two weeks following implantation; however, further investigation of these prosthetic grafts is required before they can be used clinically.

Prosthetic vascular grafts occlude because of two reasons: (1) thrombosis and (2) pseudointimal hyperplasia. Hemodynamic factors modulate both of these causative factors. For quite some time, published literature has investigated the ability of hemodynamics to affect vessel wall structure and healing. We have long known how intraluminal pressure or wall tension regulates the vessel wall thickness. Furthermore, we have recognized how changing blood flow influences the vessel's vasodilatory reaction and vascular remodeling. Much work has documented the ability of such hemodynamic parameters as wall shear stress to affect atherosclerotic plaque formation. Early researchers such as Fry [53] proposed that high wall shear stress leads to increased plaque formation. Fry reasoned that the high wall shear stress damaged the endothelium and promoted subsequent thickening of the vessel wall. In a canine model, Fry identified that the endothelium possessed a critical shear threshold of 380 dynes/cm^2 at which point the integrity of the endothelium became compromised. In contrast, studies conducted by Taylor and Zarins [117-119] in primates demonstrated that high wall shear stress resulted in little to no disruption of the endothelial integrity. With this context in mind, researchers soon began to investigate the role of low and oscillatory wall shear stress in the pathogenesis of atherosclerotic disease.

Caro et al. [54] were the first to suggest that the location of arterial plaques coincides with regions of low wall shear rate. Unlike Fry, Caro interpreted such hemodynamic parameters like high wall shear stress as exercising a "controlling or

inhibiting" influence on plaque formation rather than a causative role [54,120]. Investigators confirmed this theory through a series of experiments. In an investigation of the human carotid bifurcation, Zarins et al. [56] showed that under steady state conditions an inverse relationship existed between wall shear stress and intimal thickening. Ku et al. [55] later extended this study by identifying the same relationship under pulsatile conditions. Friedman [143] found similar results in his investigation of the abdominal aorta, while He [145] studied the same relationship within the coronary arteries. Overwhelmingly, we see a uniform message relating hemodynamics and atherosclerotic plaque formation. Now, we ask how does a changing hemodynamic environment affect healing and intimal thickness within an implanted prosthetic, vascular graft.

The prosthetic vascular graft presents an interesting model to investigate the effect of changing wall shear stress upon neointimal thickening. The synthetic substitute is a rigid material, immune from vasconstriction or vasodilation; consequently, variations in the neointimal expansion can be directly related to the changing hemodynamic environment. Early on, Bassiouny et al. [121] investigated the contribution of local hemodynamics upon intimal thickening at the distal junction of an end-to-side anastomosis. Flow visualization studies revealed a stagnation point on the anastomosis' arterial floor coincident with low and oscillating shear along with increased intimal thickening. Furthermore, Bassiouny reconfirmed an earlier suspicion that the compliance mismatches between native vessel and prosthetic graft resulted in disturbed and separated flow that lead to increased intimal thickening at the suture-line anastomosis. Loth [122] later confirmed these conclusions using laser Doppler anemometry to measure wall shear

stress values within a transparent model of a canine end-to-side anastomosis involving a 30 μm ePTFE vascular graft.

Clowes [57] used the porous 60 μm ePTFE to examine the effect of wall shear stress upon intimal area. Since these porous grafts heal rapidly, the effects of changing hemodynamics upon wall thickening can be more easily discerned. With an *in vivo* model, he attempted to extend the thinking that wall shear stress can "inhibit and control" more than just atherosclerotic plaque formation. Through various histologic and immunostaining profiles, he demonstrated that within a porous, prosthetic vascular graft high wall shear stress levels decrease intimal area and smooth muscle cell proliferation. He documented these results through three different trials in baboon models. First, he implanted 60 μm ePTFE grafts into a high wall shear stress environment of the abdominal aorta, and then he concurrently implanted two ePTFE grafts into the lower wall shear stress environment of an aorta-iliac bypass [57]. Second, he implanted 60 μm ePTFE vascular grafts into aorta-iliac bypasses and induced a high shear stress environment by distally creating an AV fistula between the femoral artery and the superficial femoral vein. He then removed the fistula to normalize the shear stress levels and to observe any subsequent changes on the intimal area. Lastly, he performed a variant of the above procedure by first implanting the grafts into a low shear stress environment and then by imposing higher shear level with an AV fistula. [57-59]. While drawing some interesting conclusions, there were limitations to Clowes' work. First, within all the experiments, the hemodynamic environment was altered by changing the volumetric flow rate through the vessels. Temporarily, this alters the wall shear stress incident upon the vessel wall, but the circulation compensates and reduces the level of blood flow through

the vessels. Furthermore, Clowes chronicled the hemodynamic effect by using a very simplified assumption of Poiseuille steady state flow. As researchers have explained, this greatly simplifies an otherwise complicated and dynamic system.

In this work we propose to investigate the effect of a changing hemodynamic environment on the intimal thickening of an implanted porous, 60 μm ePTFE vascular graft. We will alter the hemodynamic environment not through a change in the volumetric flow rate but through a stenotic geometry. We will measure the hemodynamic environment through a combination of magnetic resonance imaging (MRI) and computational fluid dynamics (CFD). We will then attempt to correlate this hemodynamic information to our detailed measurements of intimal thickness along the length of the prosthetic vascular graft.

Material and Methods:

Animals.

In this study vascular grafts were implanted into juvenile male baboons (*papio cyncephalus / anubis*) of roughly two years of age and weighing between 13-24 kg. All animal procedures followed “Principles of Laboratory Animal Care”, the “Guide for the Care and Use of Laboratory Animals” (NIH Publication No. 8023, revised 1985), and IACUC university guidelines.

Grafts.

Two different vascular grafts constructed of 60 μm expanded polytetrafluoroethylene (Impra ©, non-reinforced, thin wall) were used in this study. The first type of vascular graft, the so-called unstretched control, possessed a length of approximately 4 cm and an inner diameter of 6 mm. The Impra Corporation constructed the second type of vascular graft, the so-called unstretched stenosis. In the center of the graft the cross-luminal area reduced by 75 %. The vascular graft consisted of a central stenotic section with a 3 mm internal diameter and a length of 1.5 cm melded to two separate segments with an inner diameter of 6 mm and a length of 2 cm. The artistic configuration of Figure 4.1 best describes this design.

Surgery.

One day prior to surgery, 325 mg of aspirin was administered to the baboon. Blood samples were drawn to analyze such hemodynamic parameters as platelet count, hematocrit, and white blood cell count. Under general endotracheal anesthesia with 1.5 to

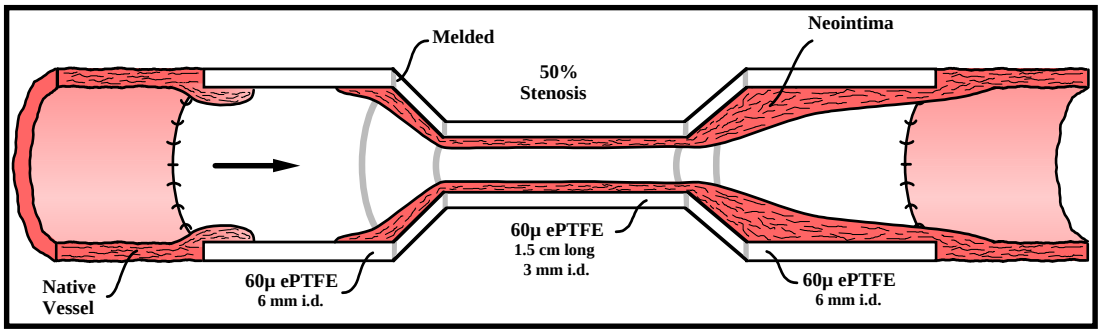

Figure 4.1: The Unstretched Stenosis. This artistic configuration describes the design of the vascular graft constructed with 60 μm ePTFE. A central stenotic portion with an inner diameter of 3 mm and a length of 1.5 cm was melded to two separate 2 cm lengths of graft with an inner diameter of 6 mm.

2.5 % isoflurane, a mid-line incision was made, followed by exposure of the retroperitoneum. Following isolation of the distal abdominal aorta, 150 units of heparin/kg were infused. The volumetric flow rate of the baboon was measured by fitting a perivascular flow probe (Transonic Inc.) around the exposed aorta, just distal to the bifurcation of the renal arteries. The perivascular flow probe was attached to a

Transonic© pulse-transit ultrasound flow meter that was connected to a PC computer using an Analog/Digital card. On the PC, Labview® recorded the volumetric flow rate for at least thirty cardiac cycles (Figure 4.2). Fifteen ePTFE grafts were implanted into the distal abdominal aortas of individual baboons. Implantation of vascular grafts involved using an end-to-end anastomosis with a continuous running suture of 6.0 polypropylene (Davis & Geck, Wayne, N.J.) (Figure 4.3). An example of an implanted vessel is demonstrated in Figure 4.4. Changyi Chen M.D., Ph.D performed all of the surgeries.

MRI Imaging.

Two weeks following surgery, the implanted vascular grafts were imaged using a 1.5 Tesla mobile MRI (Phillips Inc.). The animal was sedated with a combination of 70 mg of telazol and 0.1 mg/kg of ketamine. With the help of 15 cc of a Gadolinium contrast marker, the vasculature was visualized. Coronal sections were recorded to evaluate the overall position of the graft within the arterial tree (Figure 4.5). Axial cross-sections were acquired using a slice thickness from 1 to 2 millimeters. The recorded axial cross-sections started 0.5 cm upstream of the graft's proximal anastomosis and extended downstream to the bifurcation of the iliac arteries. Phase Contrast Magnetic Resonance Imaging measured the velocity of flowing blood at three separate locations: (1) proximal anastomosis, (2) mid-vessel, and (3) distal anastomosis. Cardiac gating facilitated acquisition of the blood velocity. The cardiac gating involved placing an electrocardiogram (ECG) upon the sedated animal and marking the p-wave as the start of the cardiac cycle. This procedure provided the MRI processing software with very valuable information in regards to the beginning and end of the cardiac cycle.

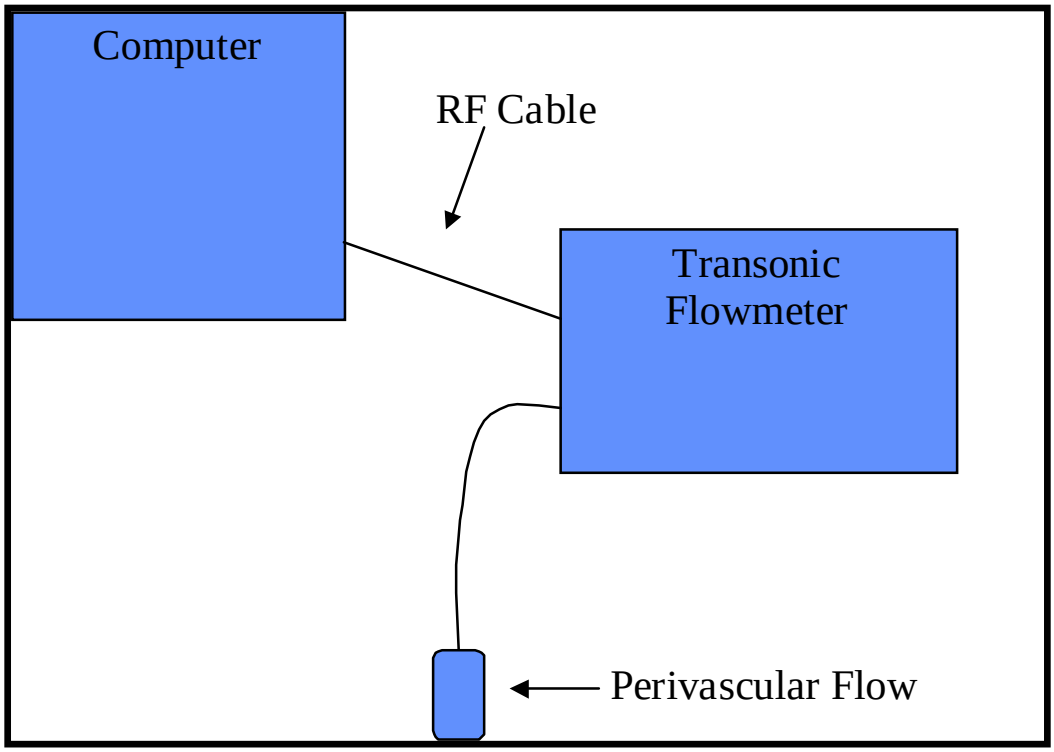

Figure 4.2: Data Acquisition for Volumetric Flow Rate. The perivascular flow probe connected to the pulse-transit ultrasound flow meter that interfaced with an analog to digital card installed on the PC.

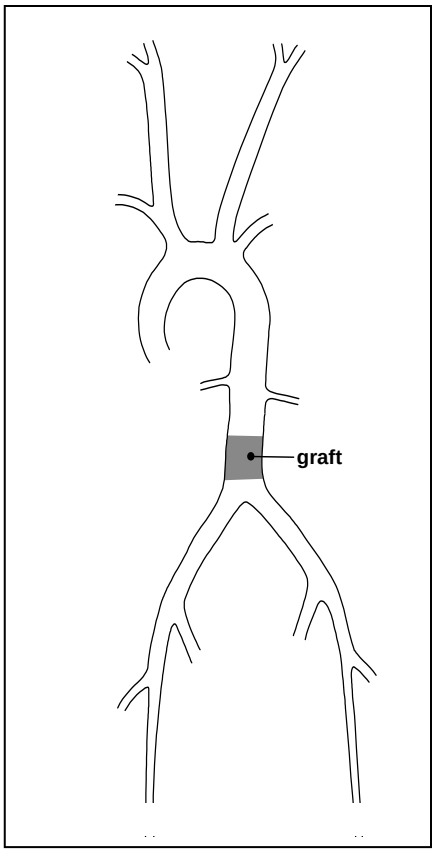

Figure 4.3: Illustration of an Implanted Vascular Graft. The graft was implanted into the abdominal aortic tree, just distal to the bifurcation of the renal arteries, using an end-to-end anastomosis.

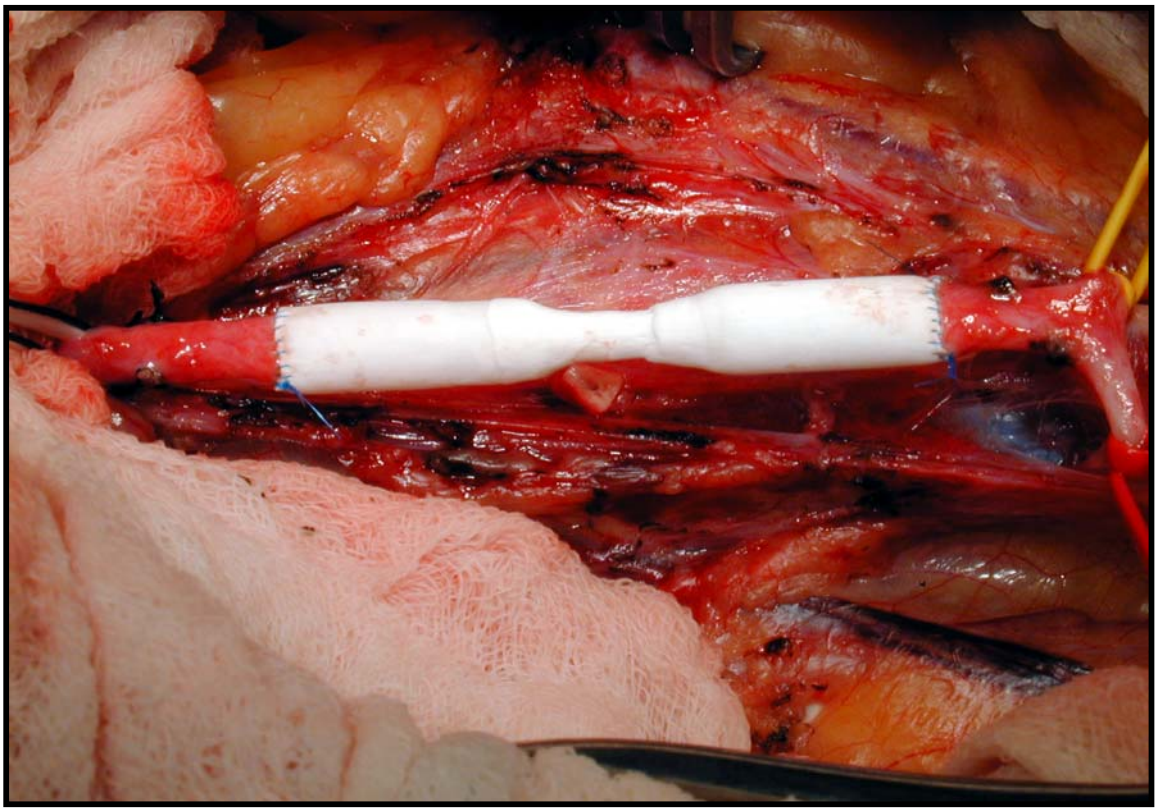

Figure 4.4: A Gross Illustration of an Implanted Unstretched Stenosis. This picture shows an implanted vascular graft shortly after suturing. Observe the central stenotic portion with a 75 % reduction in cross-luminal area and an inner diameter of 3 mm.

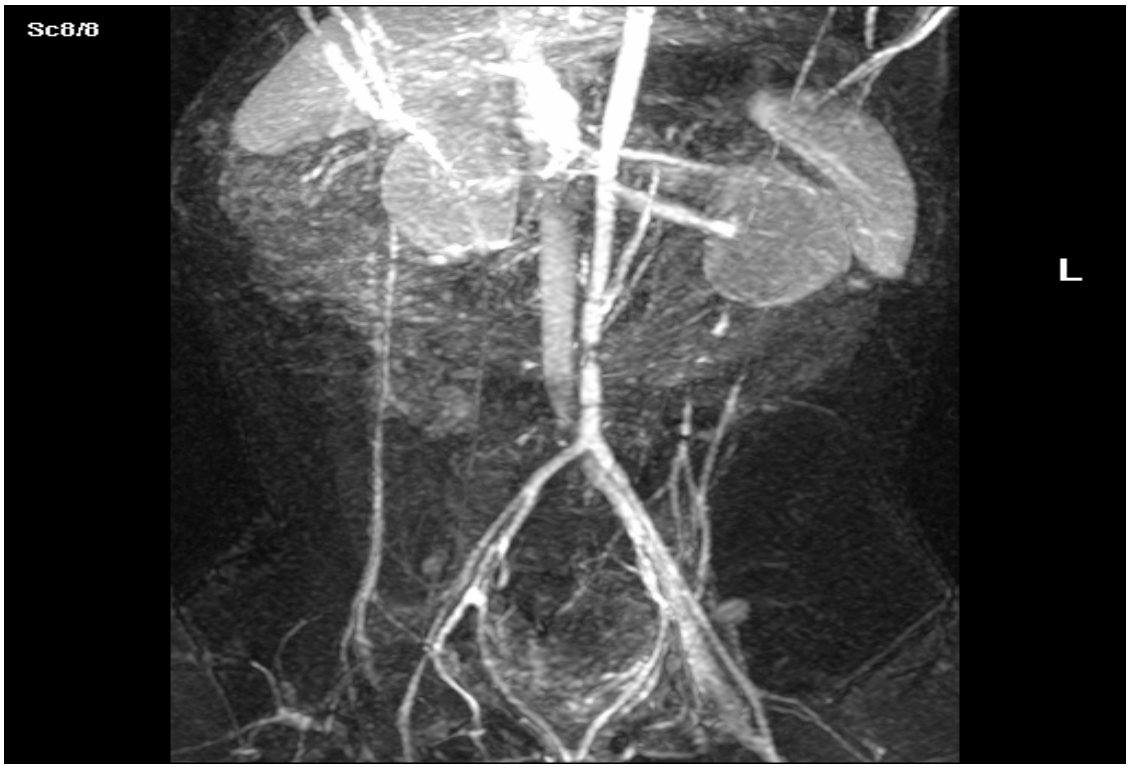

Figure 4.5: MRI Coronal Cross-Section of an Implanted Stenotic Graft. The stenotic throat is easily observed at the center of the vascular graft.

Vessel Harvest.

All baboons were sacrificed one month following graft placement. Bromodeoxyuridine (BRDU; Sigma Chemical Co., St. Louis, Mo), 50 mg/kg dissolved in 50 ml of normal saline solution, was administered subcutaneously 19, 12, and 7 hours

before sacrifice. Prior to vessel harvest, blood samples were once again drawn to analyze hemodynamic parameters. Twenty minutes before sacrificing the animal, 5000 units of heparin were administered. The distal abdominal aorta was once again exposed. Using the perivascular flow probe, the volumetric flow rate was acquired just distal to the renal arteries for thirty cardiac cycles. The animals were sacrificed by exsanguination. The implanted grafts were fixed *in vivo* by implanting a 14-gauge angiocatheter into the abdominal aorta and infusing the fixative from a 60 cc syringe. Before infusing the fixative, the grafts were first flushed with 0.1 M phosphate buffered saline (PBS) at pH 7.4 and 37° Celsius. Next, Evan's blue dye (50mg/kg) was administered, followed by another flushing of the distal aortic tree with 0.1 M PBS. A 14-gauge angiocatheter was inserted into the right common iliac to control how quickly the perfusate drained, while another 14-gauge angiocatheter was fed into the left common iliac up to the level of the aorta's bifurcation to measure mean arterial pressure (MAP) using a sphygmomanometer. The vessels were perfused at a MAP of 100 mmHg for at least thirty minutes with either 10 % buffered formalin (Baxter Diagnostics Inc, McGraw Park, Ill), accommodating protocols for immunohistochemistry, or 2.5 % glutaraldehye (Sigma Inc), accomodating protocols for scanning electron microscopy (SEM). Figure 4.6 illustrates the set-up for the *in vivo* pressure perfusion of the grafts. Following fixation, the grafts were harvested

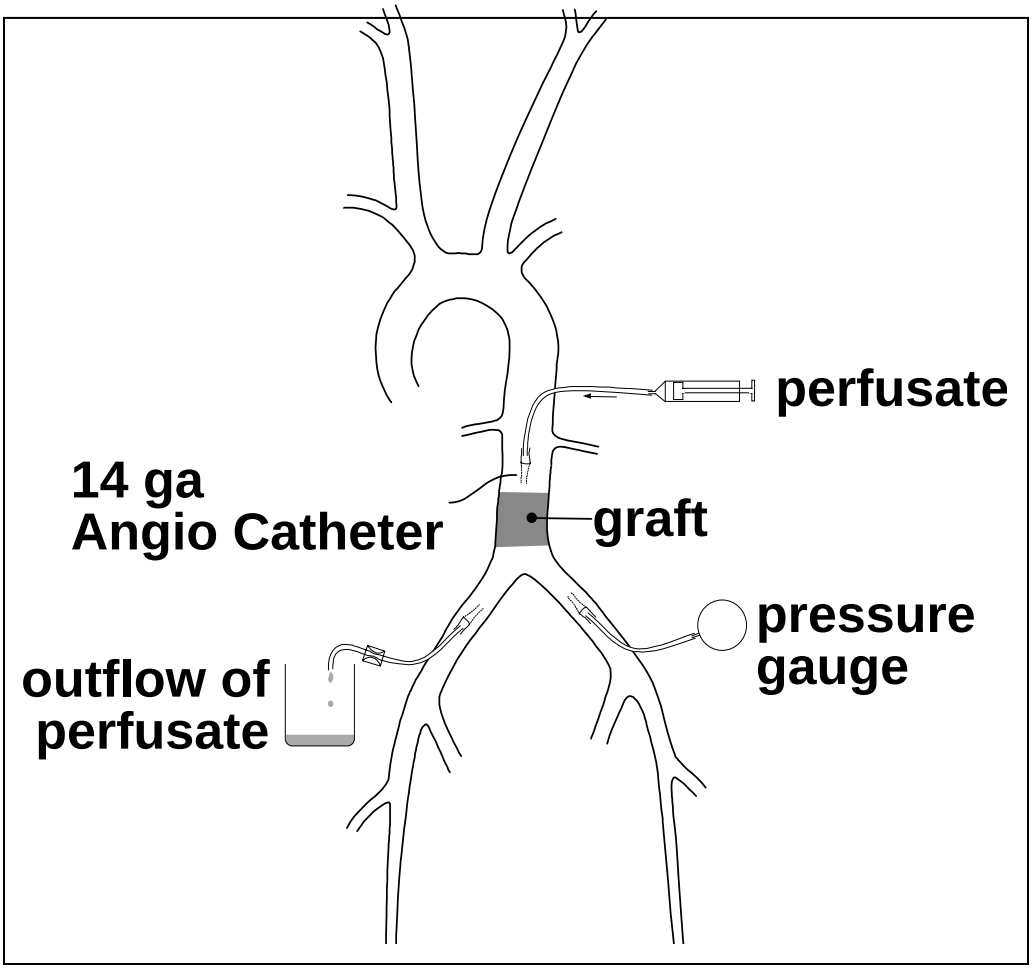

Figure 4.6: *In Vivo* Pressure Perfusion of Implanted Vascular Graft. The perfusate consisted of either 10 % buffered formalin allowing for immunohistochemistry or 2.5 % glutaraldehyde allowing for Scanning Electron Microscopy.

along with 1 cm sections of contiguous native vessel at each anastomosis and then submersed in fixative for a 24-hour period.

Histology and Morphometry.

All harvested grafts were divided into 5 mm long segments with circular cross sections, embedded into paraffin, and microtomed perpendicular to the long axis of the vessel using a 5 μm slice thickness.

At the proximal anastomosis, the center of the graft, and the distal anastomosis, microscope sections were cut every millimeter from the embedded blocks, while elsewhere in the vessel, only one representative set of sections was taken from each embedded block. As a result, greater resolution was attained at the anastomotic ends and at the center of the vessels. All grafts underwent staining with Hematoxylin and Eosin (H&E). Morphometric measurements were performed to evaluate neointimal thickness and area. Neointima was defined as ingrowth overlying the prosthetic graft surface. All slide specimens were analyzed using a microscope with a 1x objective, interfaced to a digital camera that captured all images into a TIFF format. Using the Image-Pro Plus ® Software (Media Cybernetics, Inc.; Silver Spring, Maryland), the average intimal thickness was measured in the following way. A macro within Image-Pro called **graft1** identified the two borders of the neointima as defined by the surface of the ePTFE graft and the adluminal surface of the neointima. The software then calculated the distance between these two borders, progressing with a one-pixel resolution (0.005 mm) around the circumference of the vessel. For each cross-section an average intimal thickness was calculated. A macro called **area** measured the intimal area between these two borders. Since the length of harvested vascular grafts varied by 12 %, the axial locations were

normalized to a scale from 0 to 1. This adjustment allowed for comparison of intimal thickness and area measurements at the same relative location within vascular grafts of different lengths. For each particular graft type the intimal thickness and area measurements were processed using an autoregressive moving average (ARMA) method. The ARMA technique generates a representative measurement of intimal thickness by incorporating measurements that precede, follow, and occur at a location of interest. At 0.1 normalized distances along the vascular graft, standard deviations were calculated. For each vascular graft type, a comparison of intimal thickness at the proximal and distal anastomoses was performed. Furthermore, a comparison of intimal thickness measurements at the mid-vessel point of the different graft varieties was performed.

Immunocytochemistry and Morphometry.

The avidin-biotin complex immunoperoxidase procedure (LSAB Kit, DAKO Co., Carpenteria, Ca.) was used to differentiate proliferating cells and the different neointimal cell-types. This staining procedure was performed upon all the harvested vessels. Anti-BRDU monoclonal antibody (DAKO Co.) identified proliferating cells that had uptaken the administered BRDU prior to sacrifice, while monoclonal antibodies to α-actin (DAKO) and Von Willebrand Factor (vWF; Factor VIII related antigen, DAKO) outlined smooth muscle cells and endothelial cells, respectively.

Scanning Electron Microscopy.

Two different sets of scans were performed using a Topcon-ISI DS-130 operated with a LaB6 electron source at 9 kV. First, an analysis of the ultrastructure was performed on unimplanted vascular grafts. For three of the respective control and stenotic models, longitudinal strips with a width of 5 mm and a length of 0.5 cm were sectioned from three

different locations within the vessel: (1) proximal, (2) mid-vessel (3) distal. Secondly, healing patterns were observed by analyzing implanted vascular grafts. From the harvested vascular grafts, two longitudinal sections with a width of 5 mm were taken from each of the respective control and stenotic models. The SEM protocol required fixation of the sample in 2.5 % electron microscopy grade glutaraldehyde, diluted in cacodylate. The samples were then dehydrated with graded alcohol, critical point dried, and then sputter coated with gold palladium with a deposited thickness of 20 Å. Both of the anastomotic ends and the mid-vessel regions were interrogated, and digital images captured.

Graft Ultrastructure.

With the SEM images described above, the vascular grafts' material properties were measured. For each of the vascular graft types, internodal distance (distance between nodes of ePTFE) and nodal width (width of a node of ePTFE) were measured (Figure 4.7). The ultrastructural properties of graft thickness and void volume were measured using the H&E stained circular cross-sections (Figure 4.8). Using Image-Pro, the graft thickness was measured by calculating the distance between the outer and inner borders of the prosthetic graft at each radial location around the vessel's circumference, followed by calculating their average. Void Fraction reflected the percentage of empty space within the prosthetic graft that permitted for transmural ingrowth across its wall. A macro within Image-Pro called **Void** evaluated void fraction by calculating the area of empty space unoccupied by ePTFE material and dividing it by the total area of the graft material. For the control graft, the average of these parameters was taken between the anastomotic and mid-vessel locations. For the unstretched stenosis, these parameters were

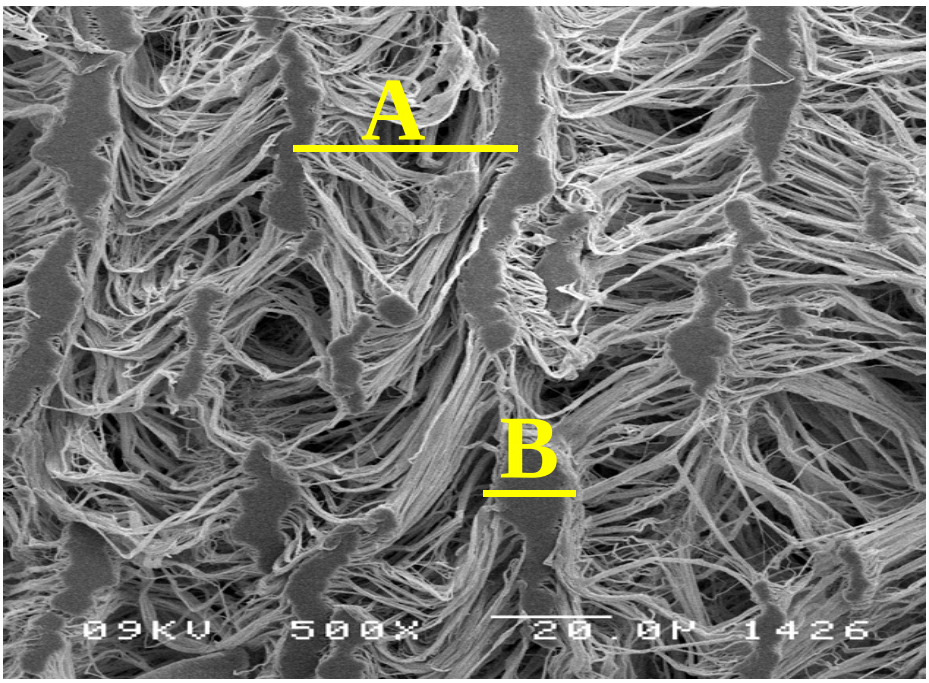

Figure 4.7: Scanning Electron Microscopy of Unstretched 60 μm ePTFE. (A) designates the internaodal distance, while (B) designates the nodal width.

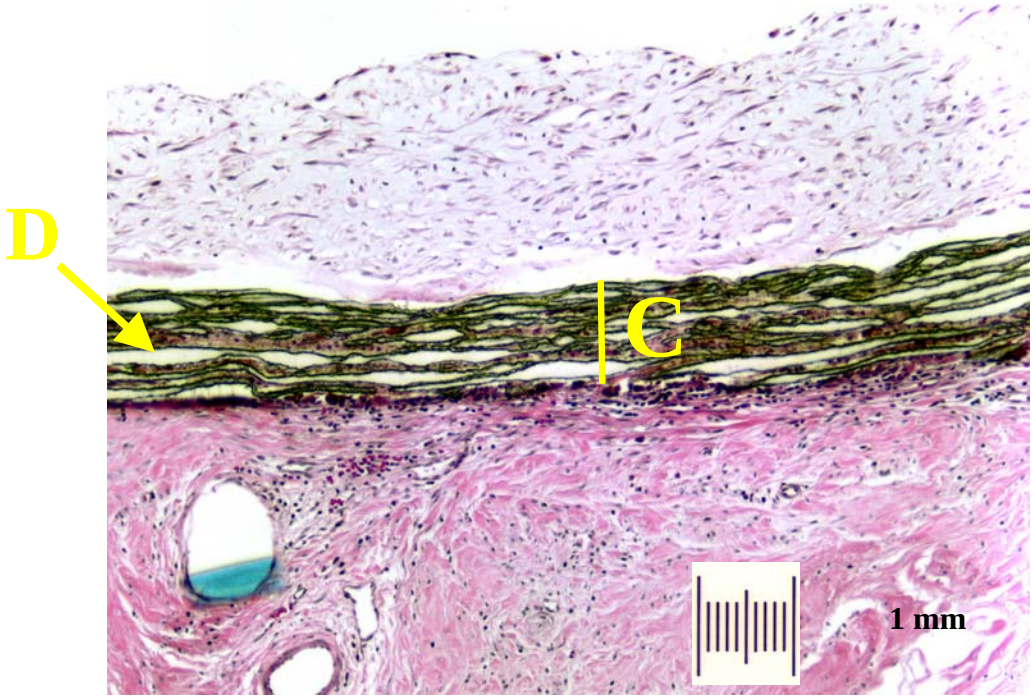

Figure 4.8: H&E Staining of a Circular Cross-Section of a Harvested 60 μm ePTFE Vascular Graft. (D) illustrates void volume, while (C) designates graft thickness.

individually evaluated at the mid-vessel and anastomotic location. Since the material properties of the graft changed from the anastomosis to the stenotic throat, their measurements were not averaged as with the control graft.

Fluid Mechanics.

Computational fluid mechanics characterized the flow field within the vascular grafts. Chapter V describes in detail how this was accomplished. Briefly, using the MRI axial images, a computational grid was constructed of the control and stenotic grafts. The grid was composed of luminal contours outlined from the MRI axial images. The Gambit software (Fluent Inc.) took the information extracted from these contours

and helped construct the computational grids. With all pulsatile simulations, boundary conditions at the inlet were needed. A representative description of blood flow at implant and at harvest for both the control and stenotic grafts was calculated by ensemble averaging the volumetric flow rates. These waveforms were then applied to a Womersley solution [151] to derive velocity values for the flowing blood at the vessel inlet. Using Fidap (Fluent Inc), pulsatile simulations were run for three cardiac cycles. From these simulations, wall shear stress within the vascular graft was calculated. Wall shear stress is defined as the dynamic viscosity of the fluid times the gradient of the velocity, evaluated at the wall. The dynamic viscosity of blood was assumed to be 0.04 poise. The hemodynamic data were compressed into a description of wall shear stress as a function of distance along the axial direction of the vascular graft. This was accomplished by averaging the WSS measurements around the circumference of the vessel. This term is referred to as spatially averaged WSS or $\tau_s(z,t)$ (Equation 4.1).

$$\tau_s(z,t) = \left| 1/S \int_0^S \tau ds \right|$$

Equation 4.1

At each axial location along the graft, the pulse spatially averaged WSS (Pulse WSS) was calculated. Over a cardiac cycle, the Pulse WSS measures the difference between the maximum spatially averaged WSS and the minimum spatially averaged WSS. Lastly, the temporal mean of the spatially averaged WSS was calculated. This manipulation produced the spatially averaged, temporal mean wall shear stress {τavg(z)} (Equation 4.2).

$$\tau avg(z) = \left| (1/(T*S)) \int_0^S \int_0^T \tau dt ds \right|$$

Equation 4.2

These different descriptions of WSS were then correlated with the measured histologic data. The three dimensional oscillatory shear index was calculated (Equation 4.3).

$$OSI = 0.5\left(1 - \frac{\left| \int_0^T \tau dt \right|}{\int_0^T |\tau| dt}\right)$$

Equation 4.3

Statistics.

Statistical analysis was performed on a Pentium IV P.C. with the use of either MATLAB or Excel 2000 statistical software (Microsoft Co.). Comparisons of intimal thickness between the various grafts were made using a Student *t* test (two-tailed). The documented values are given as the mean ± the standard deviation. The results were considered significant if the p value was less than 0.05.

Results:

Graft Ultrastructure.

The material properties of the unstretched stenosis were investigated (Figure 4.9). Corroboration was needed that the ultrastructure of the stenotic throat was identical to those parameters within the straight, 6mm internal diameter (id) sections of the vessel. First, the void fraction was examined (Figure 4.10). The 3 mm id stenotic throat had a void fraction of 78.3 ± 4.8 %, while the 6 mm id regions had a void fraction of 73.0 ± 4.8 %. There existed no statistically significant difference in the void fraction between these two investigated areas. Secondly, the graft thickness was investigated (Figure 4.11). The 3 mm id stenotic throat had a graft thickness of 0.44 ± 0.03 mm, while the 6 mm id regions had a graft thickness of 0.34 ± 0.06 mm. There existed no statistically significant difference in the graft thickness between these two examined regions. Lastly, the internodal distance was measured. The 3 mm id stenotic throat had an internodal distance of 20.4 ± 8 μm, while the 6 mm id regions had an internodal distance of 19.8 ± 8 μm. There existed no statistically significant difference in the internodal distance between the two investigated areas.

Graft Healing.

On gross-inspection of the harvested stenotic graft, the intraluminal surface appeared healed (Figure 4.13). Within the lumen, a “glistening” and healed surface was observed. Over the next several experiments confirmation was gathered that the graft surface had confluently healed. The infused Evan’s Blue Dye was selectively excluded from the surface of the unstretched, 60 μm ePTFE control graft (Figure 4.14). The absence of Evan’s blue staining hints at the presence of a deposited endothelial surface within the

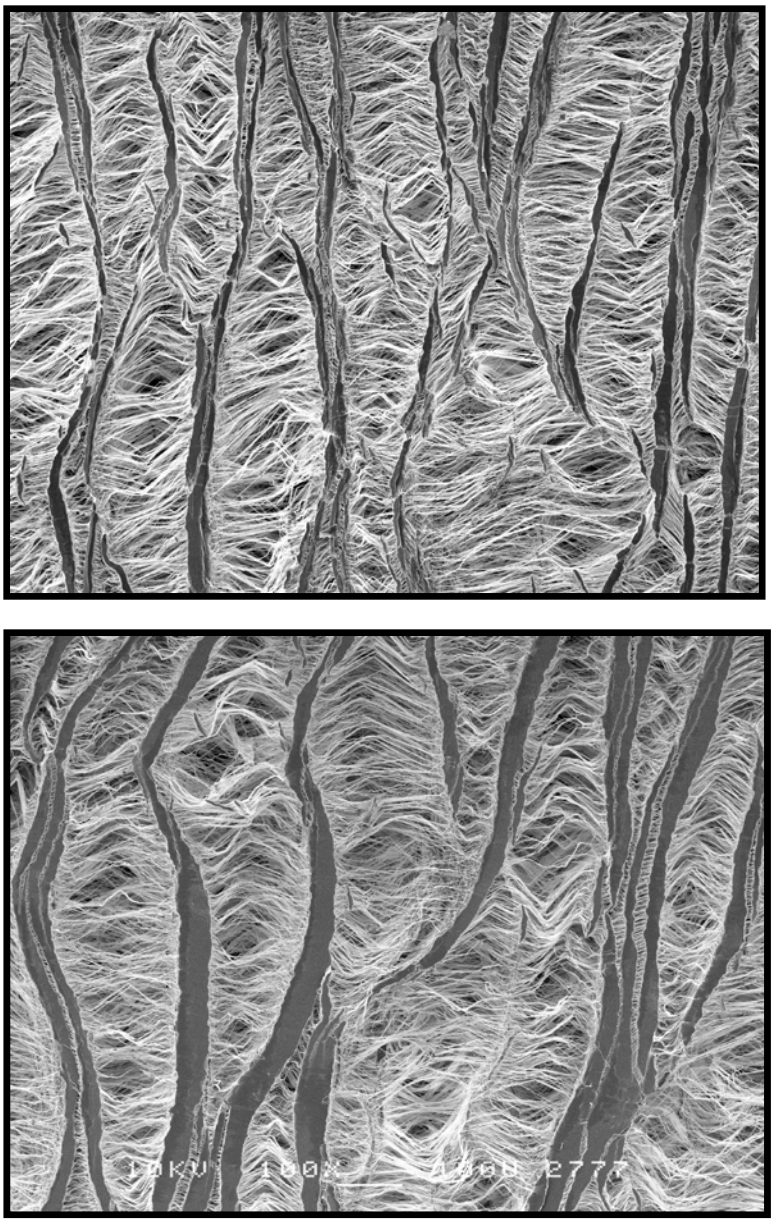

Figure 4.9: Scanning Electron Microscopy of 60 μm ePTFE Sampled from the Proximal and Throat Regions of the Unstretched Stenosis. The ultrastructure of the two graft regions is nearly identical, indicative of very similar material properties.

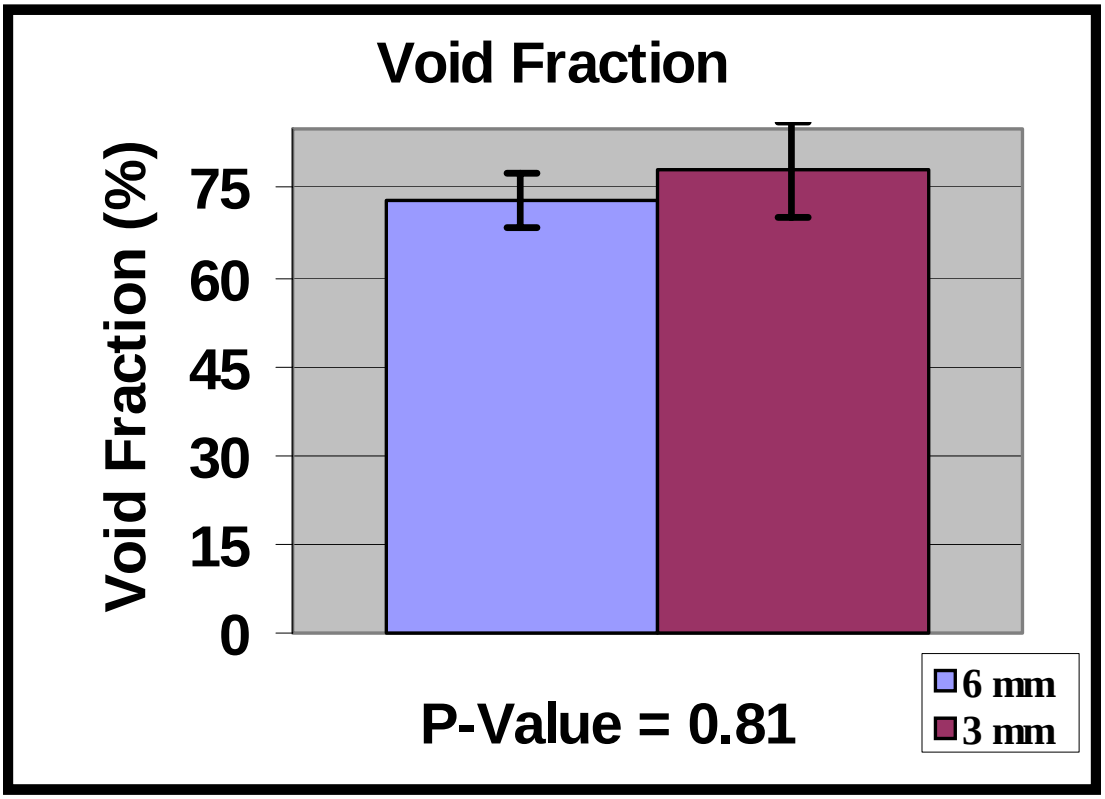

Figure 4.10: Void Fraction for the Proximal and Throat Regions of the Stenotic Graft. There existed no statistically significant difference in the void fraction between the two different locations of the unstretched stenosis.

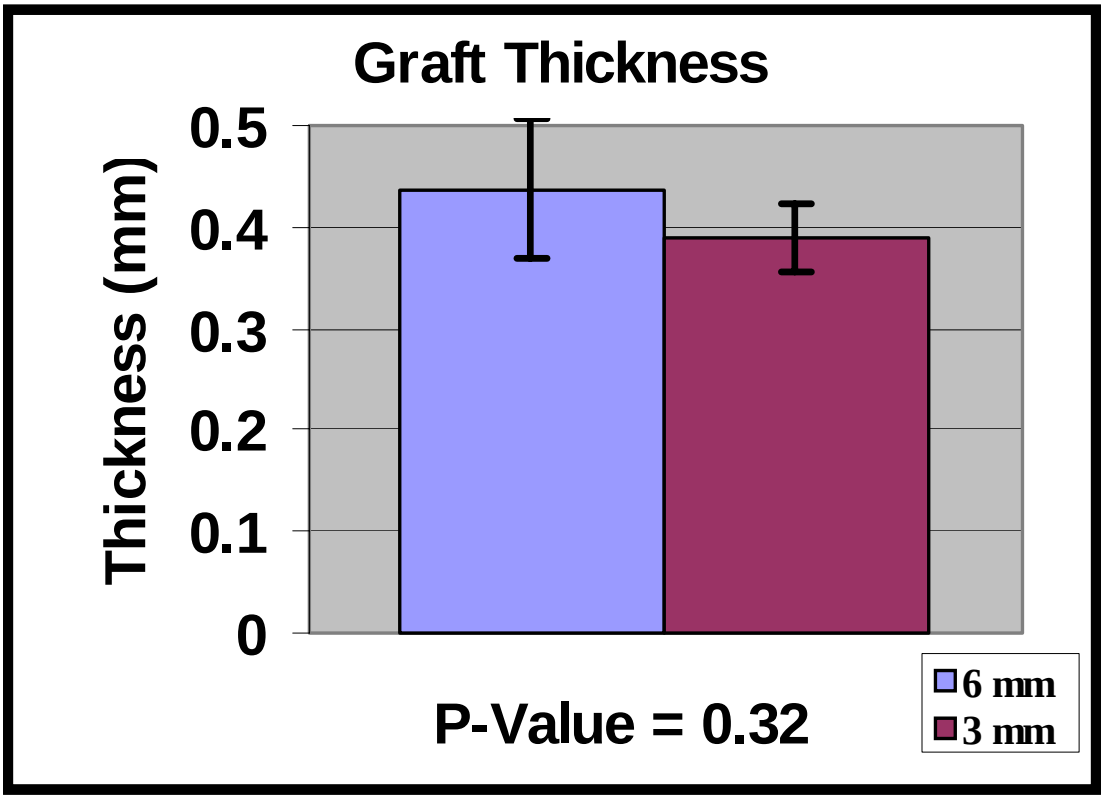

Figure 4.11: The Graft Thickness for the Proximal and Throat Regions of the Stenotic Graft. There existed no statistically significant difference between the two examined locations of the unstretched stenosis.

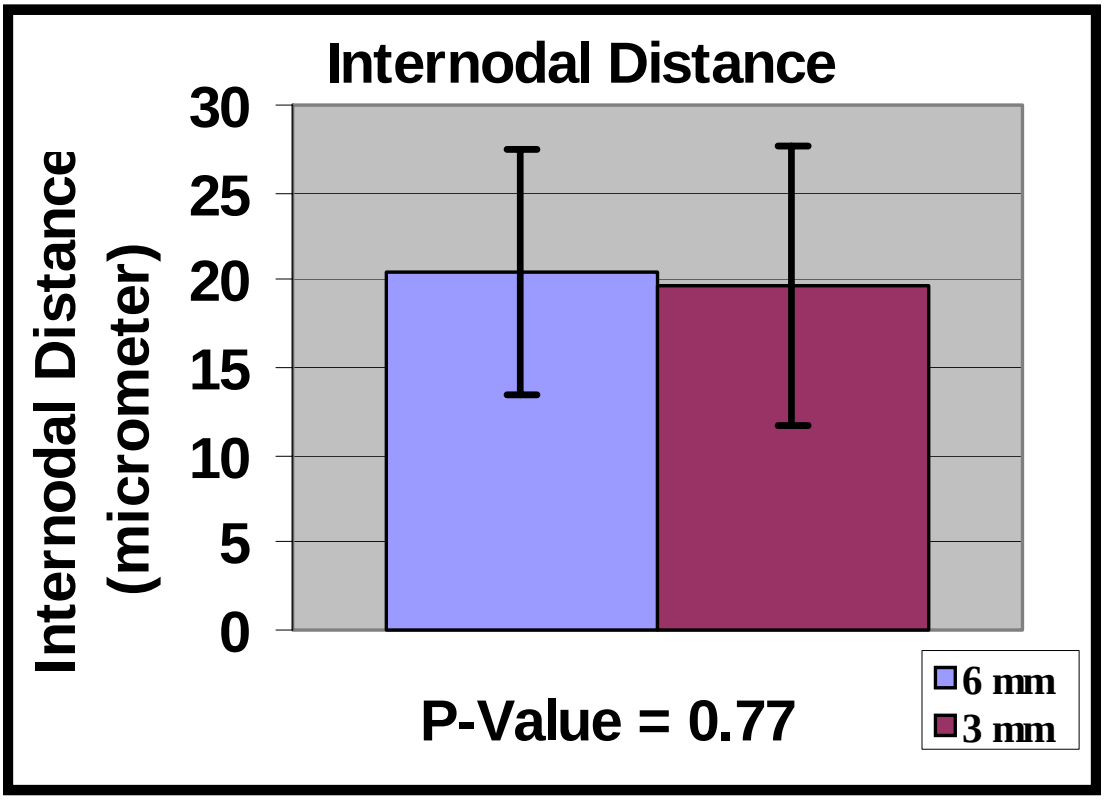

Figure 4.12: The Internodal Distance for the Proximal and Throat Regions of the Stenotic Graft. There existed no statistically significant difference between the two regions of the unstretched stenosis.

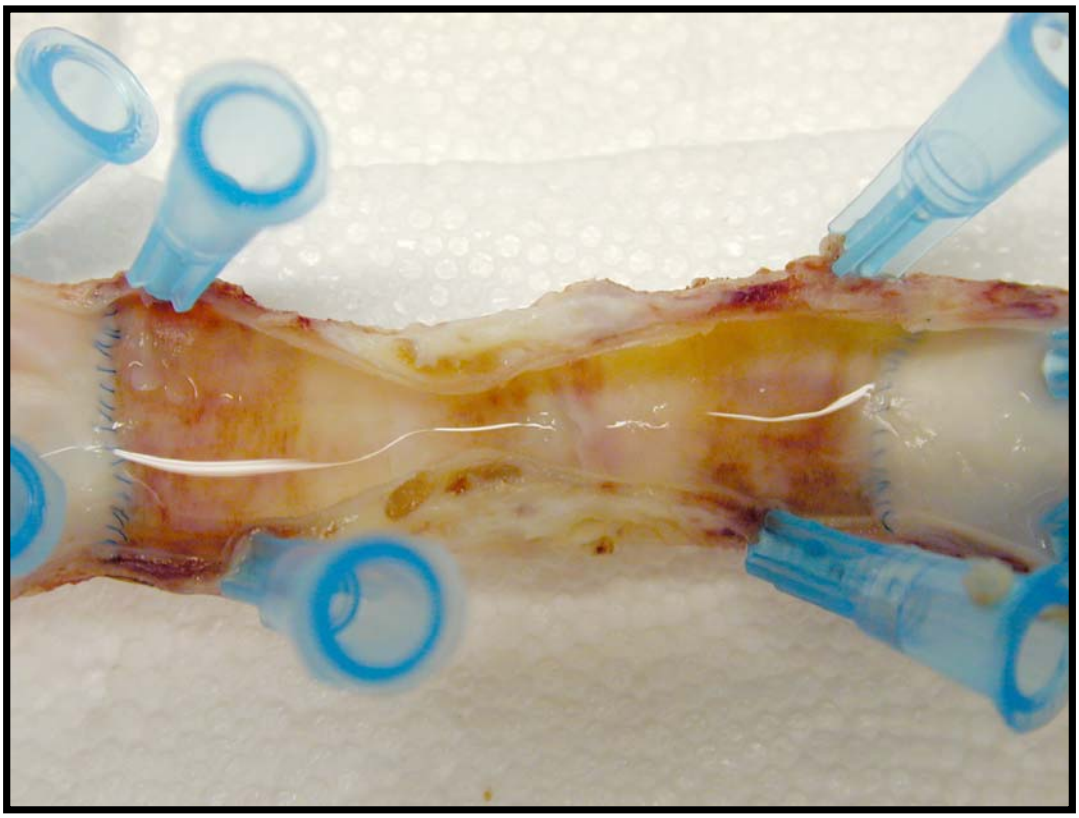

Figure 4.13: Gross Examination of Unstretched Stenosis. A “glistening”, healed surface was observed within the lumen of the harvested vessel. Blood flows from right to left.

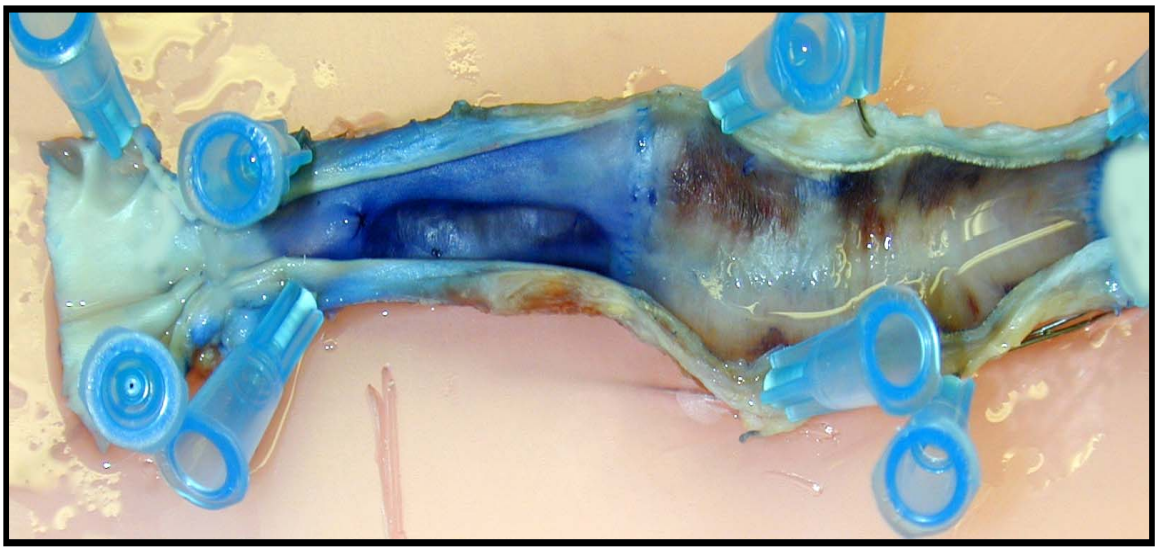

Figure 4.14: Evan's Blue Dye Injection of Healed, 60 μm ePTFE Control Graft. The Evan's Blue Dye (50 mg/ml) was administered through an angiocatheter into the vessel's lumen. Note the absence of dye uptake upon the surface of the healed graft. Dye was uptaken by the native tissue stripped of its endothelium by the inflated angioballoon catheter. This experiment qualitatively shows how the graft surface was healed.

prosthetic graft. A complete endothelial layer blocks the uptake of the infused dye, unlike the upstream vessel where the endothelium was stripped away using an angioballoon catheter. Endothelium was also observed on examination with SEM (Figure 4.15). Within the stenotic throat an endothelial surface was observed. Due to the high velocity at this location, the endothelial cells are not “cobble-stone” shaped, but instead, they are elongated and oriented in the blood flow direction. Finally, the presence of a complete endothelium was confirmed by VWF immunostaining. For the control vessel, positive immunostaining was observed around the circumference of every examined cross-section (Figure 4.16). For the unstretched stenosis, positive immunostaining was observed everywhere within the graft except for the 0.25 cm transition regions where the graft material was melded. Within the stenotic throat, staining of the confluent endothelium was observed (Figure 4.17).

The H&E stained cross-sections illustrated the amount of intimal thickening deposited upon the graft surfaces. First, the healed control grafts were examined (Figure 4.18). The proximal and distal anastomosis demonstrated the expected pannus ingrowth. The midpoint of the control graft showed a healed surface with some intimal thickening. Next, the healed, unstretched stenosis was investigated (Figure 4.19). As with the controls, intimal thickening was documented at the suture line. At the stenotic throat, the graft surface was healed with a well-identified neointima. The intimal thickening of the control and stenotic grafts was quantified (Figure 4.20). On examination, the intimal thickening at the anstomotic ends of both the control and stenotic grafts did not differ between their respective proximal and distal ends (Figures 4.21 and 4.22). At the Mid-vessel point, the average intimal thickening of the stenotic throat (0.132 ± 0.03 mm).

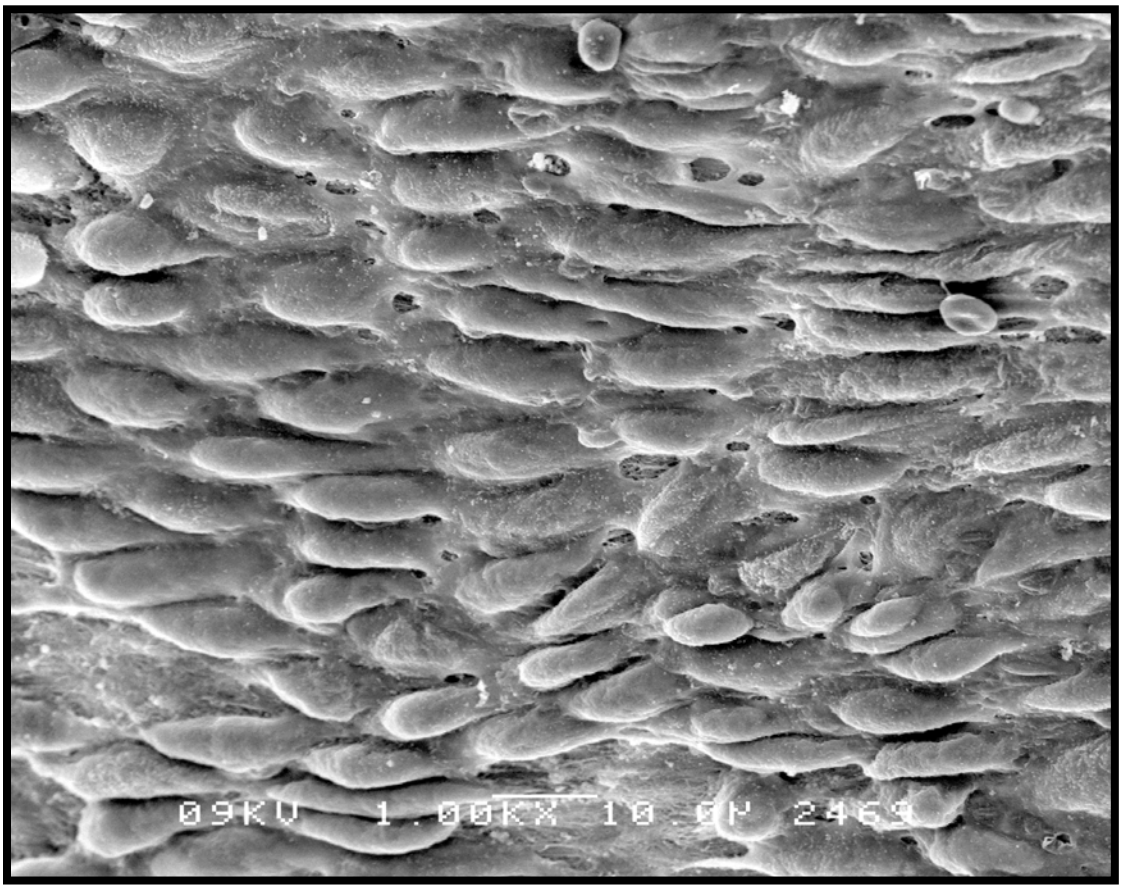

Figure 4.15: Scanning Electron Microscopy of Healed Surface at the Stenotic Throat. Elongated and flow-oriented endothelial cells are observed.

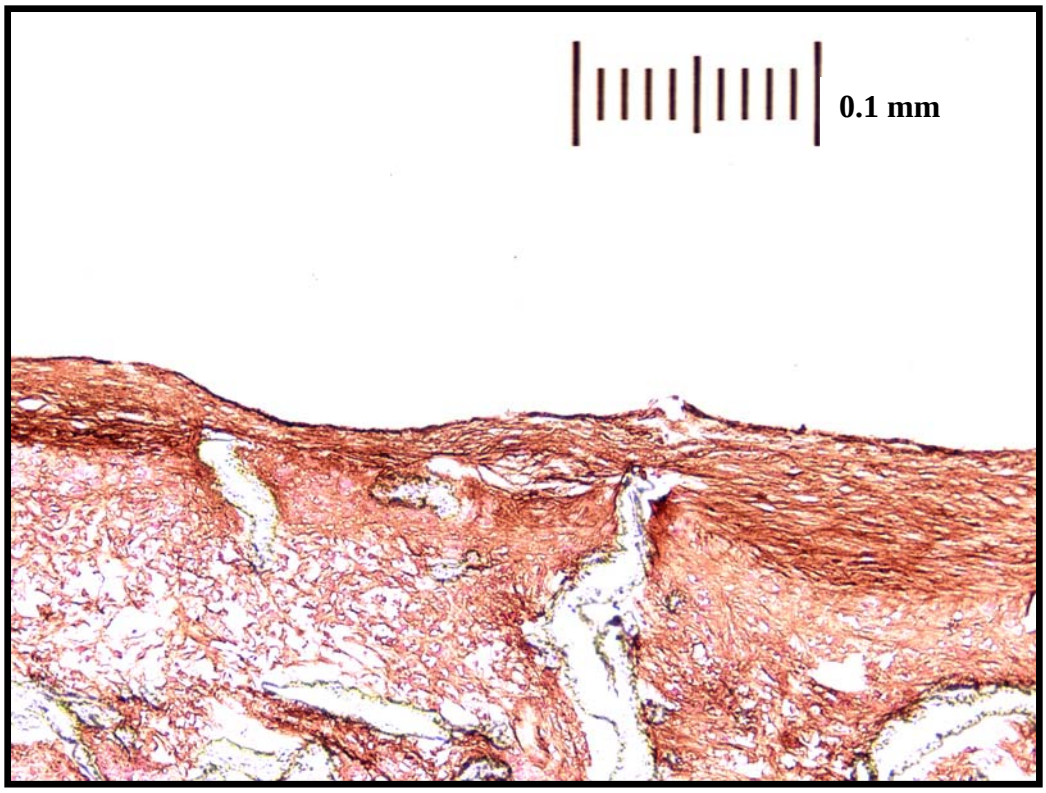

Figure 4.16: VWF Immunostaining of Straight and Unstretched Control. Positive staining was identified around the circumference of every examined cross-section.

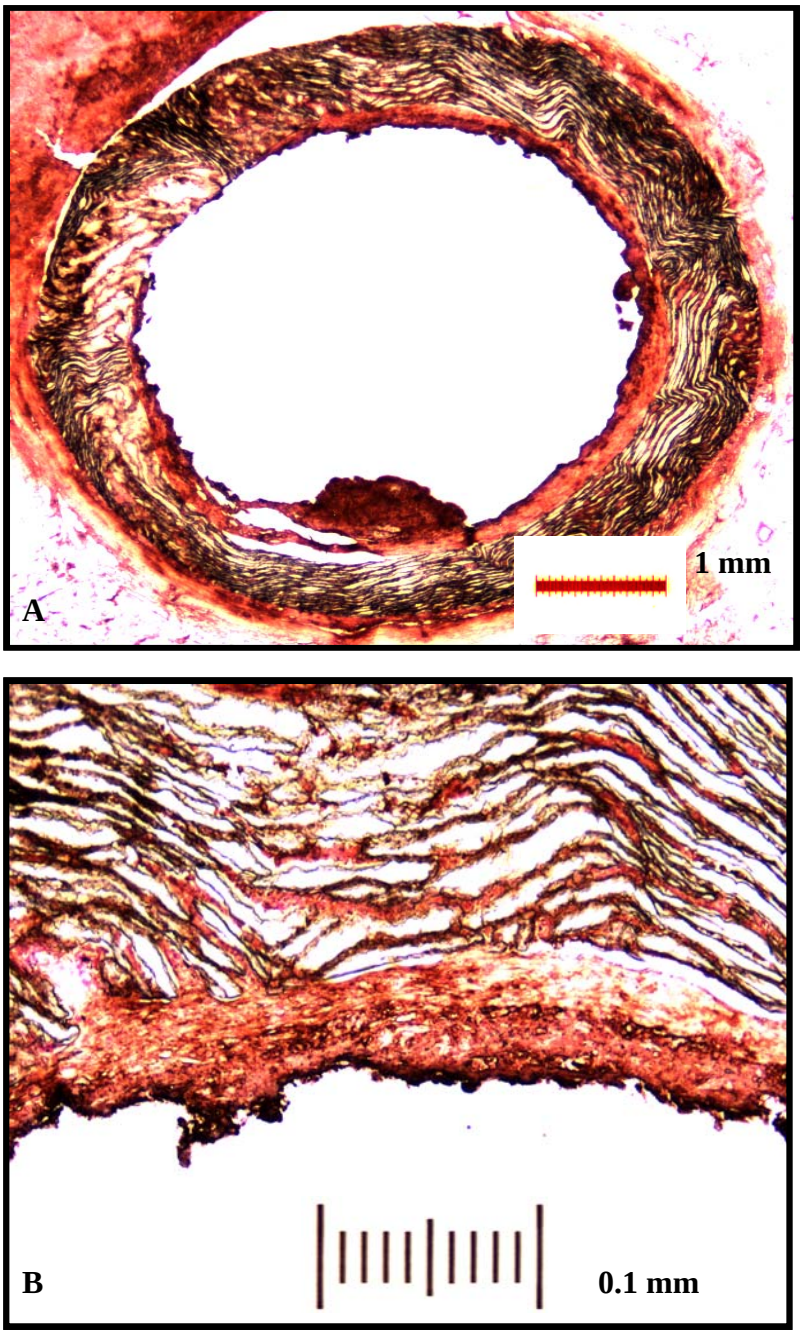

Figure 4.17: VWF Immunostaining of Unstretched Stenosis. (A) Cross-section of the stenotic throat demonstrating the healed endothelium. (B) Magnified view highlighting the stained endothelial cells.

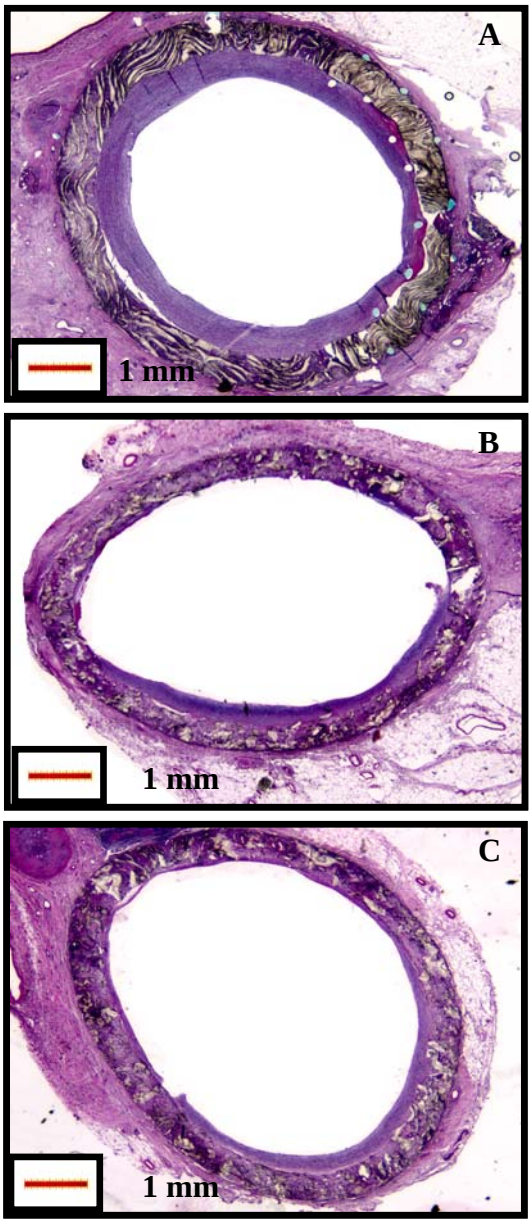

Figure 4.18: H&E Staining of Circular Cross-Sections from the Unstretched Control. (A) Proximal Anastomosis (B) Mid-Vessel (C) Distal Anastomosis.

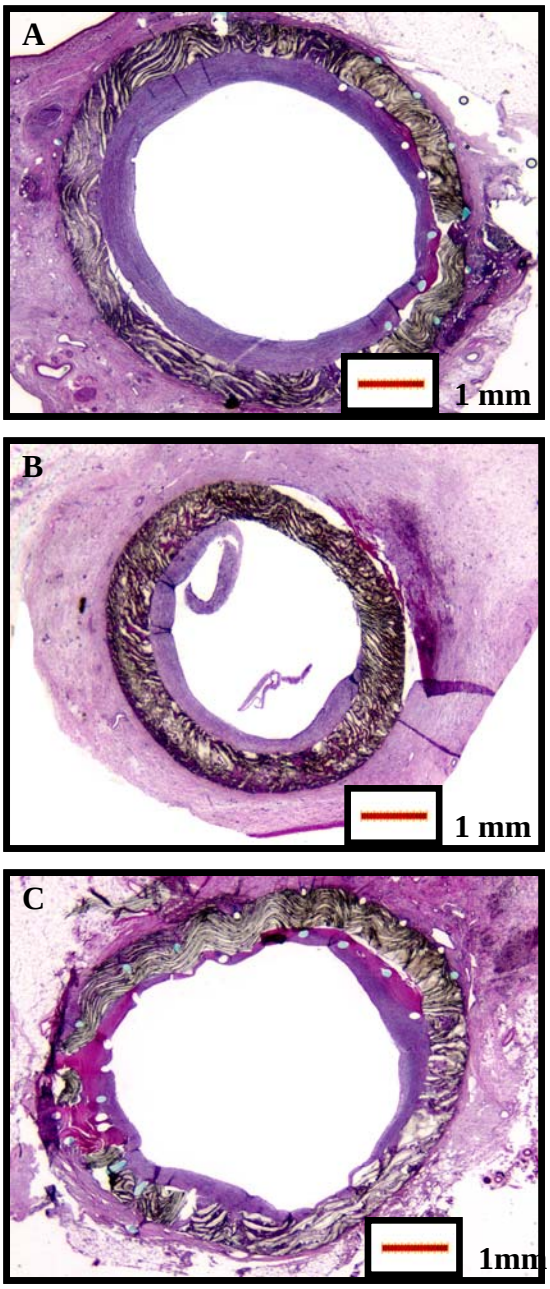

Figure 4.19: H&E Staining of Circular Cross-Sections from the Unstretched Stenosis. (A) Proximal Anastomosis (B) Stenotic Throat (C) Distal Anastomosis.

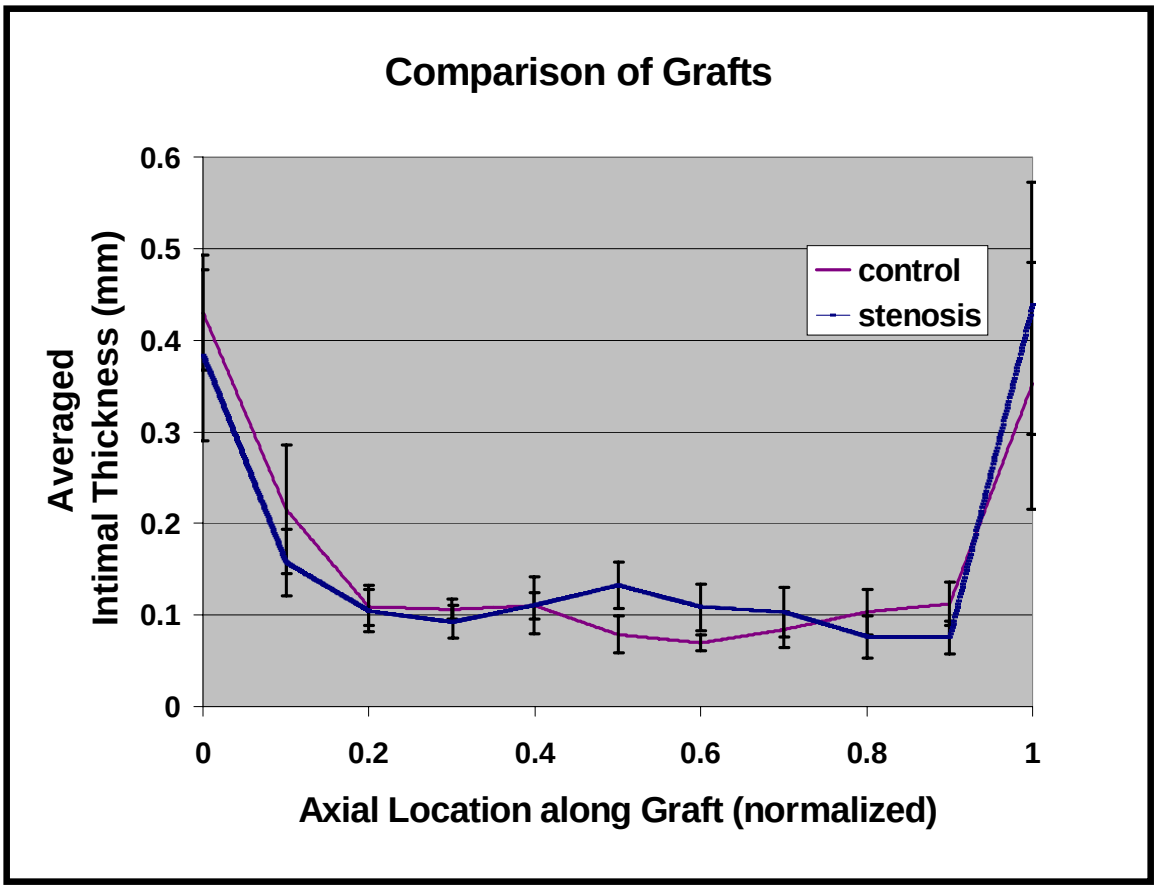

Figure 4.20: Quantitative Description of Intimal Thickening for the Unstretched Control and Stenotic Grafts. Pannus ingrowth was observed at the anastomotic ends of the control and stenotic grafts. At the vessel mid-point the stentotic throat demonstrated a modest increase in intimal thickening.

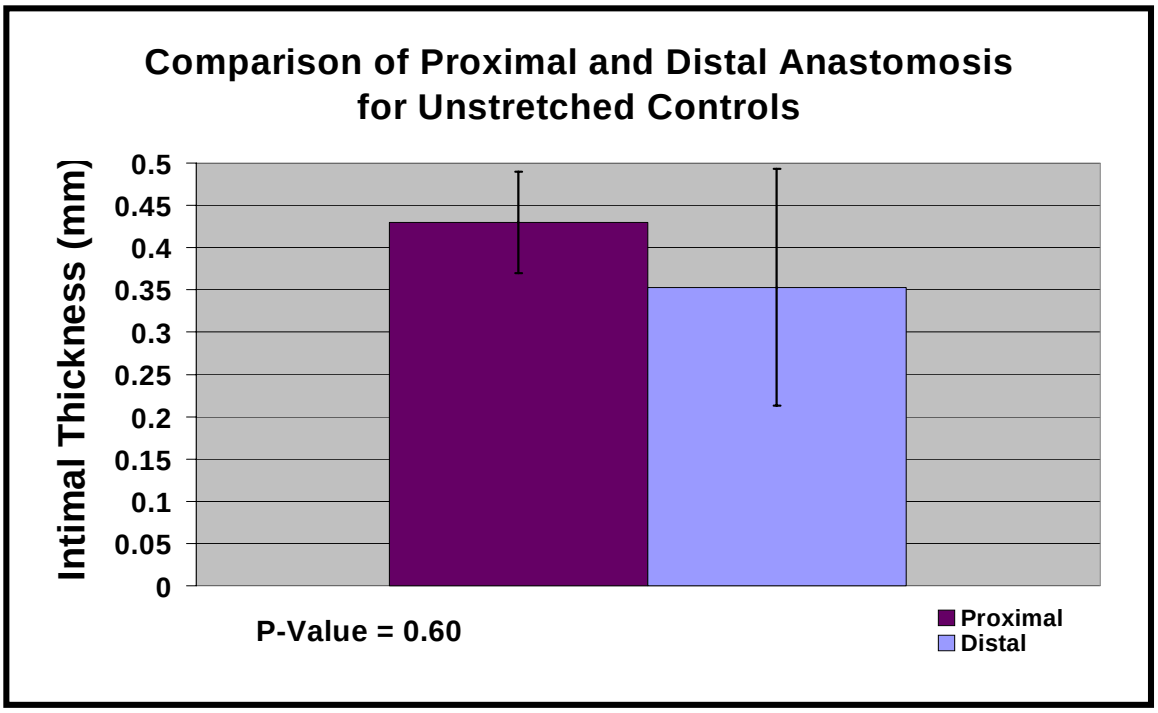

Figure 4.21: Comparison of Intimal Thickening at the Proximal and Distal Anastomosis of the Unstretched Control Grafts. There existed no statistically significant difference between the two ends.

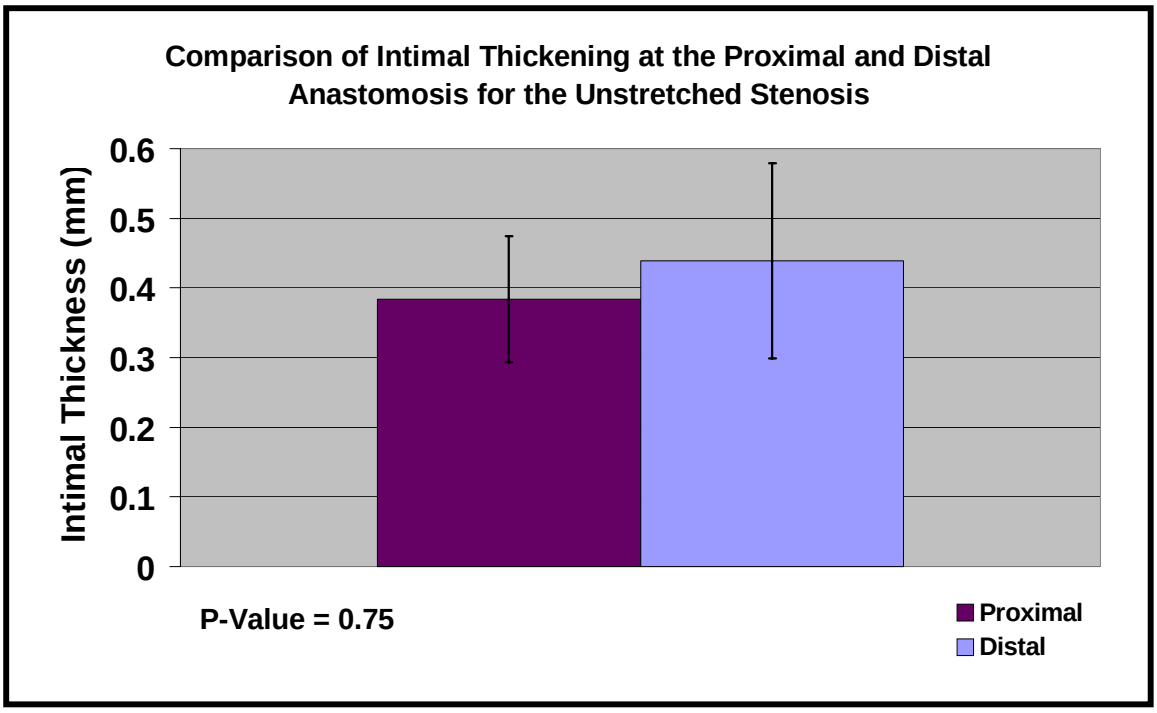

Figure 4.22: Comparison of Intimal Thickening at the Proximal and Distal Anastomosis of the Unstretched Stenosis. There existed no statistically significant differences between the two respective ends.

exceeded the average intimal thickening of the control's mid-vessel region (0.08 ± 0.02 mm) (Figure 4.23). Upon statistical comparison, a p-value of 0.10 was calculated. The intimal area of the control and stenotic grafts was also compared (Figure 4.24). This illustration told a very similar story to what was seen with our comparison of intimal thickening. With increased intimal thickening and area at the stenotic throat we suspected that a large number of proliferating cells were concentrated in this region. The BRDU immunostaining revealed very few proliferating cells (Figure 4.25).

Hemodynamics.

The CFD simulations calculated WSS measurements in both the unstretched control and the unstretched stenosis. The results for the control grafts gave low WSS values of 2 to 4 dynes/cm^2. These results differed markedly from the unstretched stenosis. For the stenotic grafts, two different boundary conditions were applied to the computational grid. The first boundary condition derived from the ensemble averaged volumetric waveform at harvest. The spatially averaged temporal mean WSS (τavg) was calculated along the length of the vascular graft (Figure 4.26). At the stenotic throat, the τavg intitally increased to over 42 dynes/ cm^2. Further within the stenotic throat, the τavg values returned to a baseline level near 27 dynes/cm^2. Within the stenotic throat, the Pulse WSS went as high as 100 dynes/cm^2 with a baseline level near 60 dynes/cm^2 (Figure 4.27). Furthermore, excluding any averaging algorithms, the maximum WSS within the stenotic throat reached a ceiling of 130 dynes/cm^2 during systole and 93 dynes/cm^2 during diastole. The second boundary condition originated from the PCMRI data. Once again, the spatially averaged temporal mean WSS (τavg) was calculated along

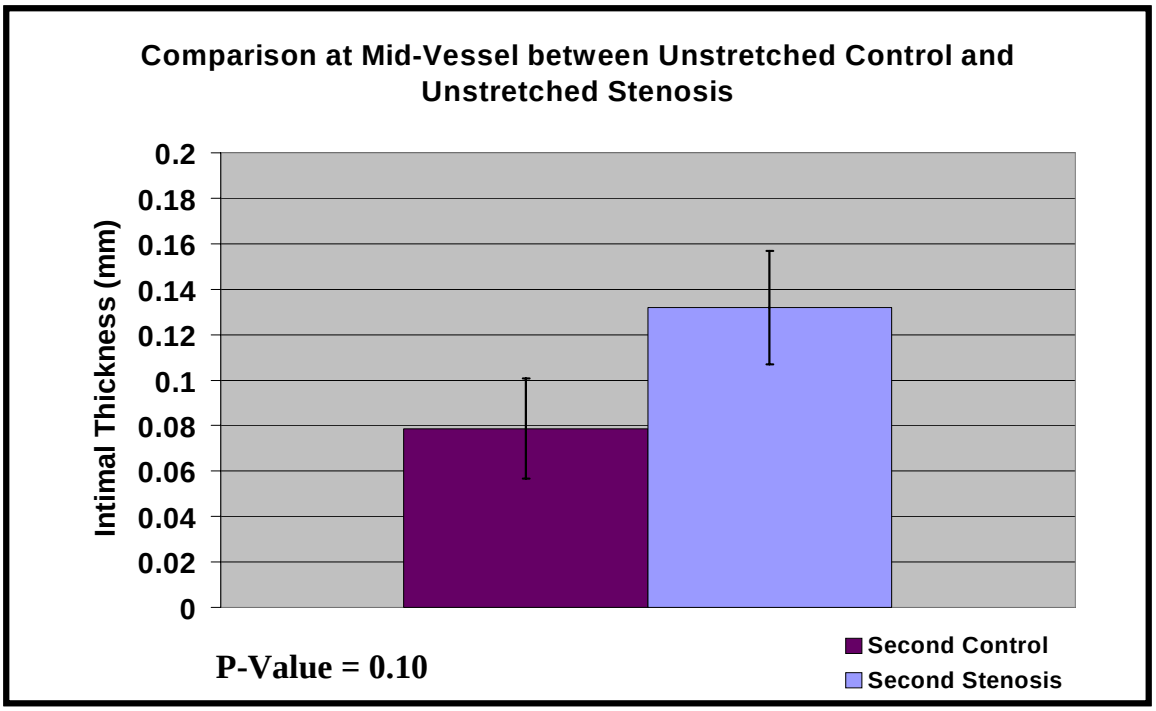

Figure 4.23: Comparison of Intimal Thickening at the Mid-Point of the Unstretched Control and the Unstretched Stenosis. Although the stenotic throat had a higher average intimal thickness than the mid-point of the control, the p-value was not less than 0.05.

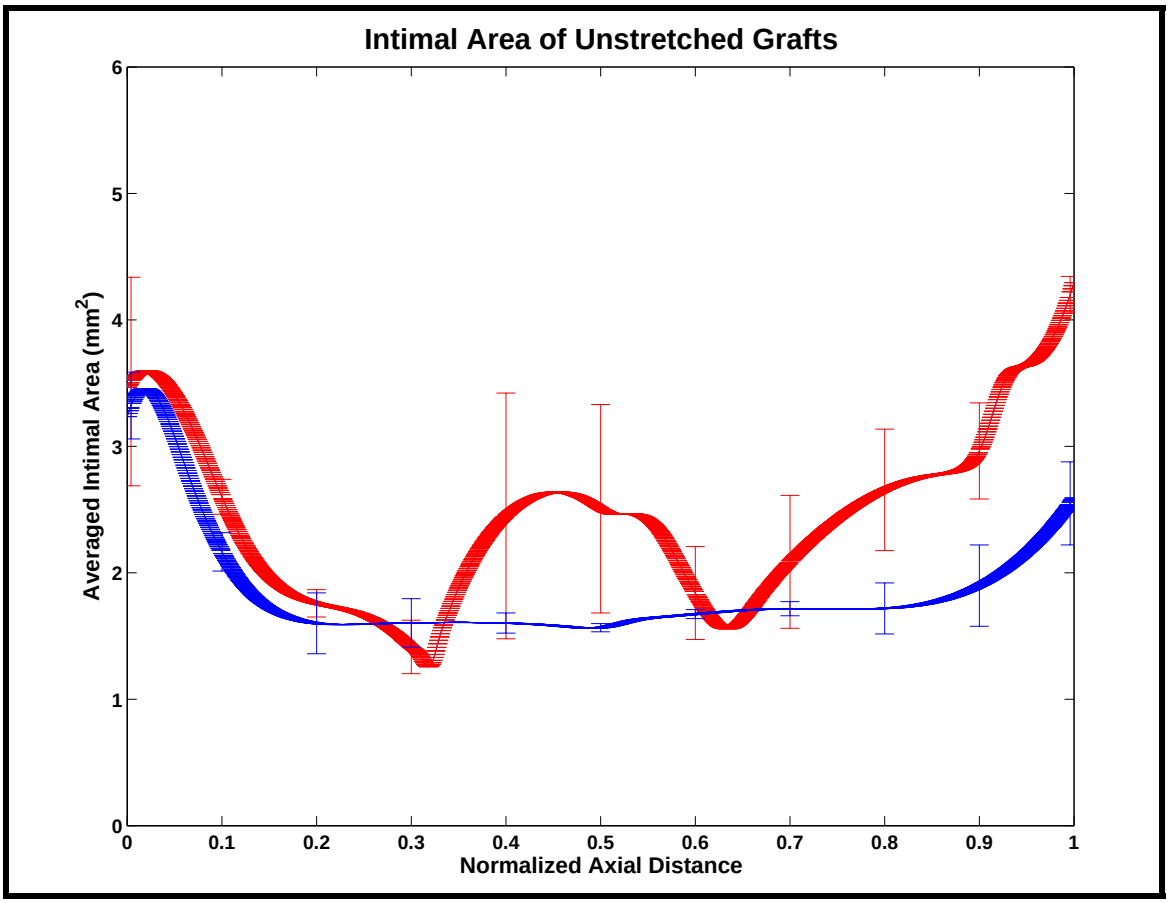

Figure 4.24: The Intimal Area of the Unstretched Control and Unstretched Stenosis. The red line describes the unstretched stenosis, while the blue line details the unstretched control. As with the intimal thickness description, the intimal area within the stenotic throat demonstrates a modest increase in comparison to the mid-vessel of the control.

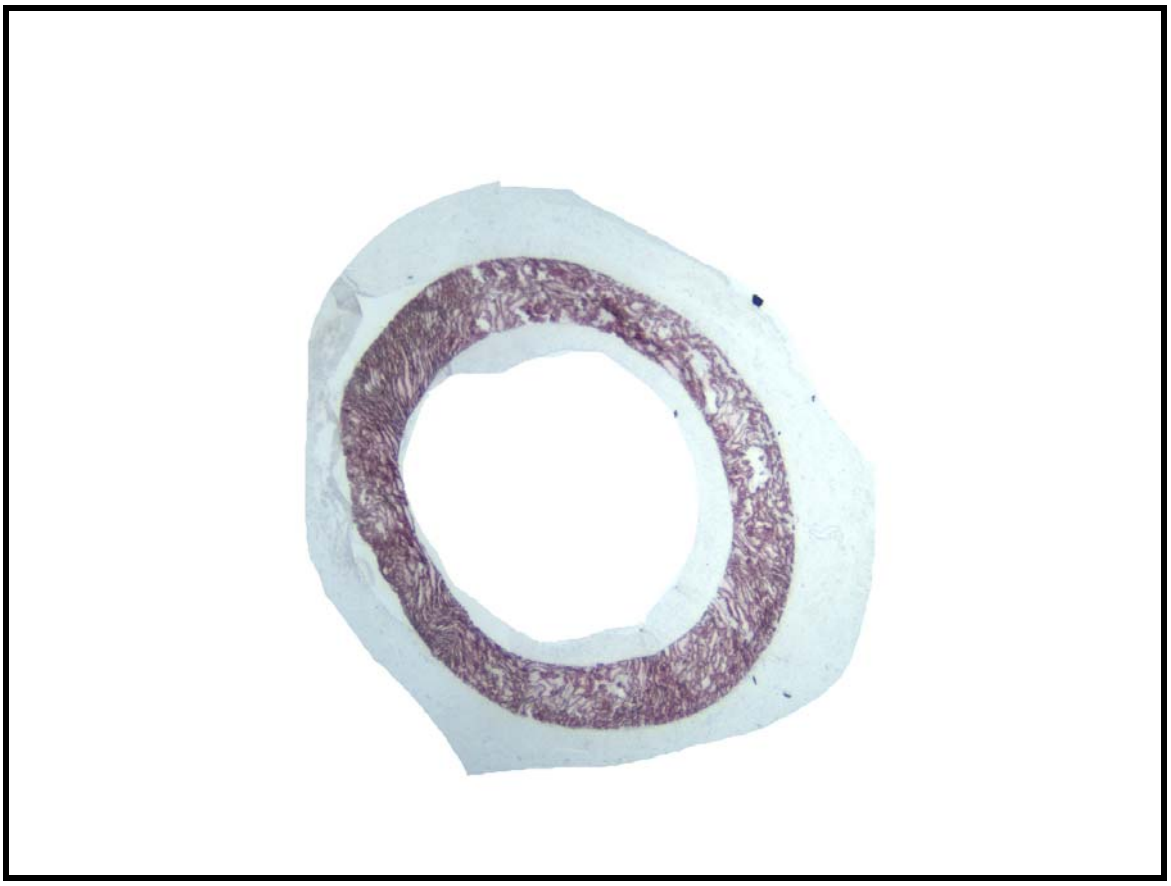

Figure 4.25: BRDU Immunostaining at the Throat of the Unstretched Stenosis. There existed an absence of proliferating cells at the throat of the Unstretched Stenosis. Only one or two positively, stained cells are identified within the neointima.

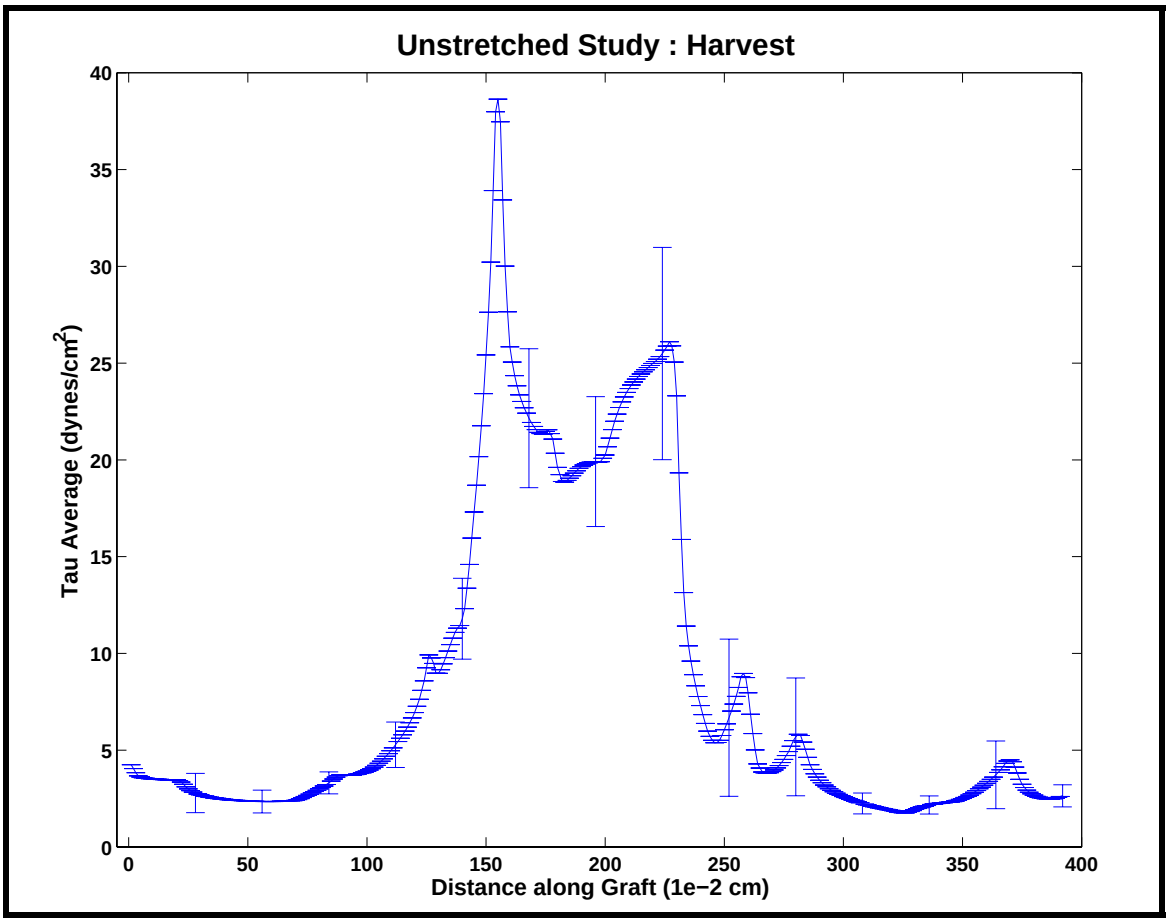

Figure 4.26: τavg(z) with an Applied Boundary Condition from the Ensemble Averaged Volumetric Flow Rate at Harvest.

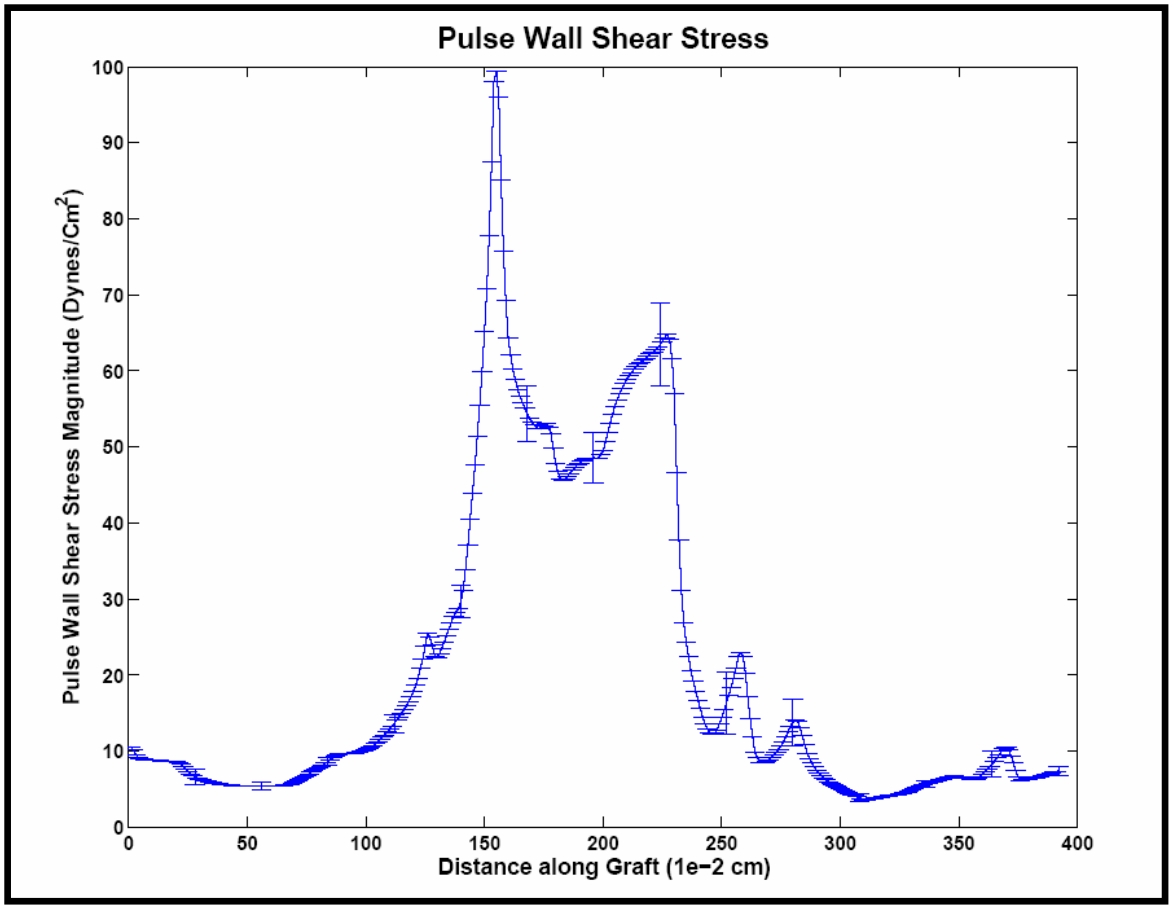

Figure 4.27: Pulse Wall Shear Stress with an Applied Boundary Condition from the Ensemble Averaged Volumetric Flow Rate at Harvest.

the length of the vascular graft (Figure 4.28). At the stenotic throat, the WSS initially increased to a little less than 40 dynes/ cm^2. Further within this expanse, the WSS values returned to a baseline level near 24 dynes/cm^2. Within the stenotic throat, the Pulse WSS went as high as 80 dynes/cm^2 with a baseline level of 45 dynes/cm^2 (Figure 4.29). Furthermore, excluding any averaging algorithms, the maximum WSS within the stenotic throat reached a ceiling of 122 dynes/cm^2 during systole and 83 dynes/cm^2 during diastole.

For the unstretched stenosis, correlation coefficients were calculated between the intimal thickness data and the hemodynamic data. For the harvest volumetric flow rate boundary condition, the correlation coefficient between the reciprocal of τavg and intimal thickness was r = -0.77 with a p-value less than 0.05. In addition, the correlation coefficient between the reciprocal of the Pulse WSS and the intimal thickness was r = -0.79 with a p-value less than 0.05. Lastly, the correlation coefficient between the reciprocal of the Max WSS and the intimal thickness was r = -.80 with a p-value less than 0.05. For the PCMRI boundary condition, the correlation coefficient between the reciprocal of τavg and intimal thickness was r = -0.78 with a p-value less than 0.05. In addition, the correlation coefficient between the reciprocal of the Pulse WSS and the intimal thickness was r = -0.80 with a p-value less than 0.05. Lastly, the correlation coefficient between the reciprocal of the Max WSS and the intimal thickness was r = -0.80 with a p-value less than 0.05. For the two simulations, the oscillatory shear index detailed transient flow separation distal to the stenotic throat (Figure 4.30 and 4.31).

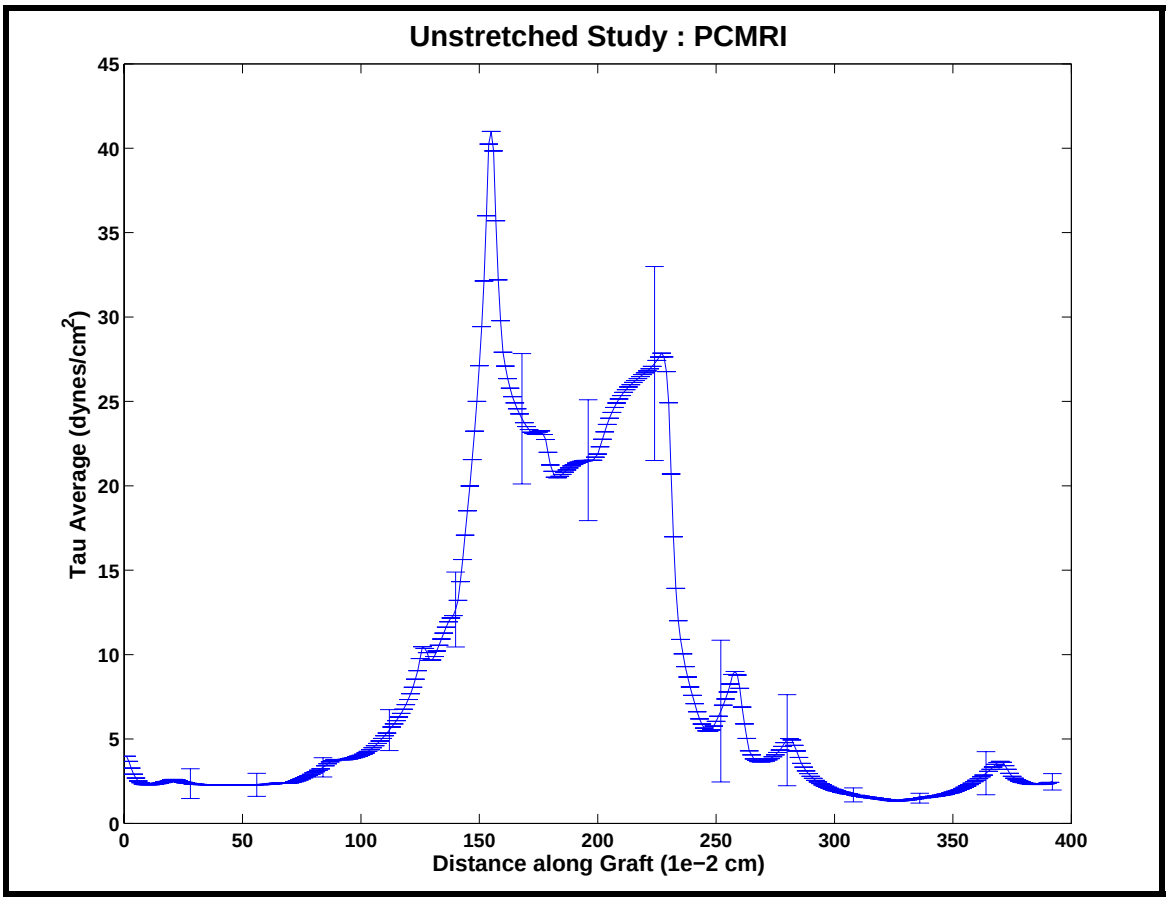

Figure 4.28: τavg(z) with an Applied Boundary Condition from the Phase Contrast Magnetic Resonance Imaging.

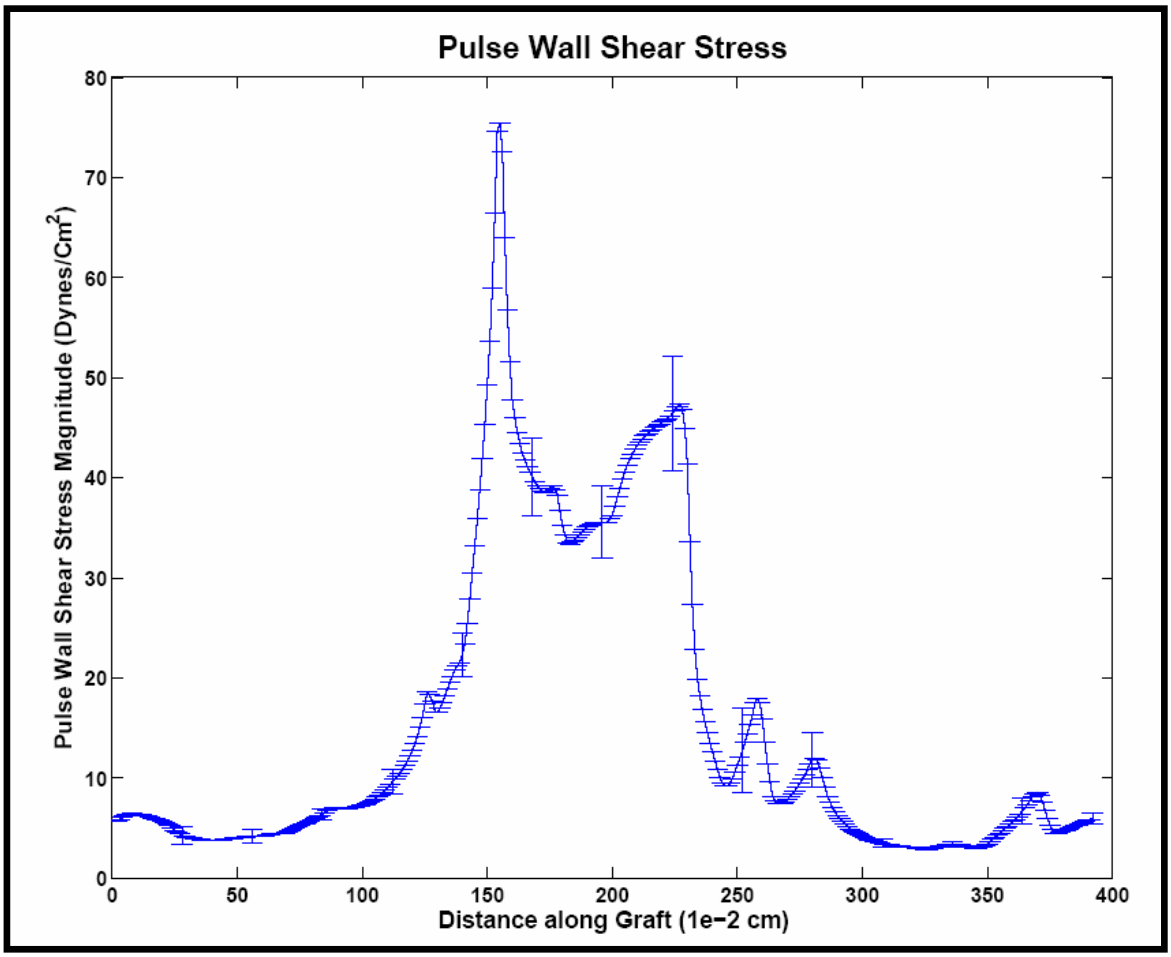

Figure 4.29: Pulse Wall Shear Stress with an Applied Boundary Condition from the Phase Contrast Magnetic Resonance Imaging.

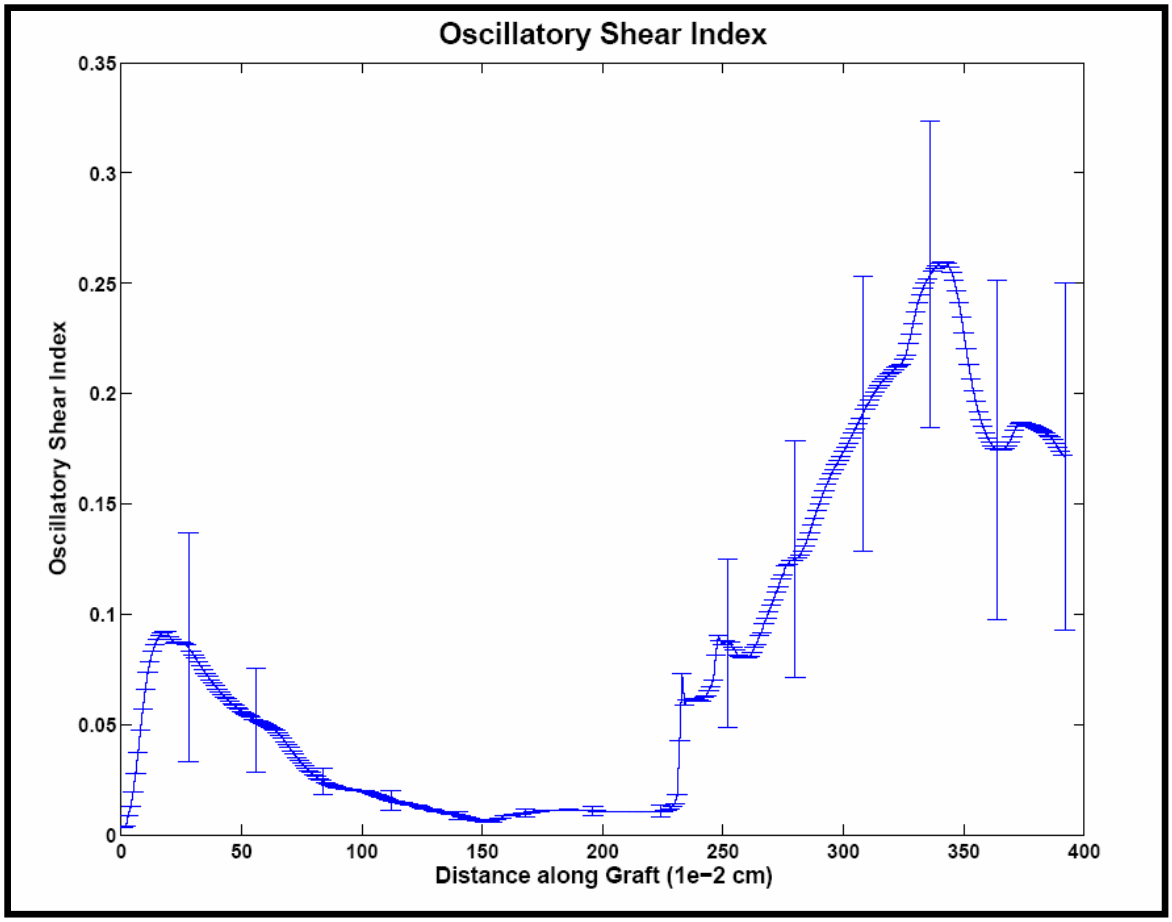

Figure 4.30: Oscillatory Shear Index With An Applied Boundary Condition from the Ensemble Averaged Volumetric Flow Rate At Harvest.

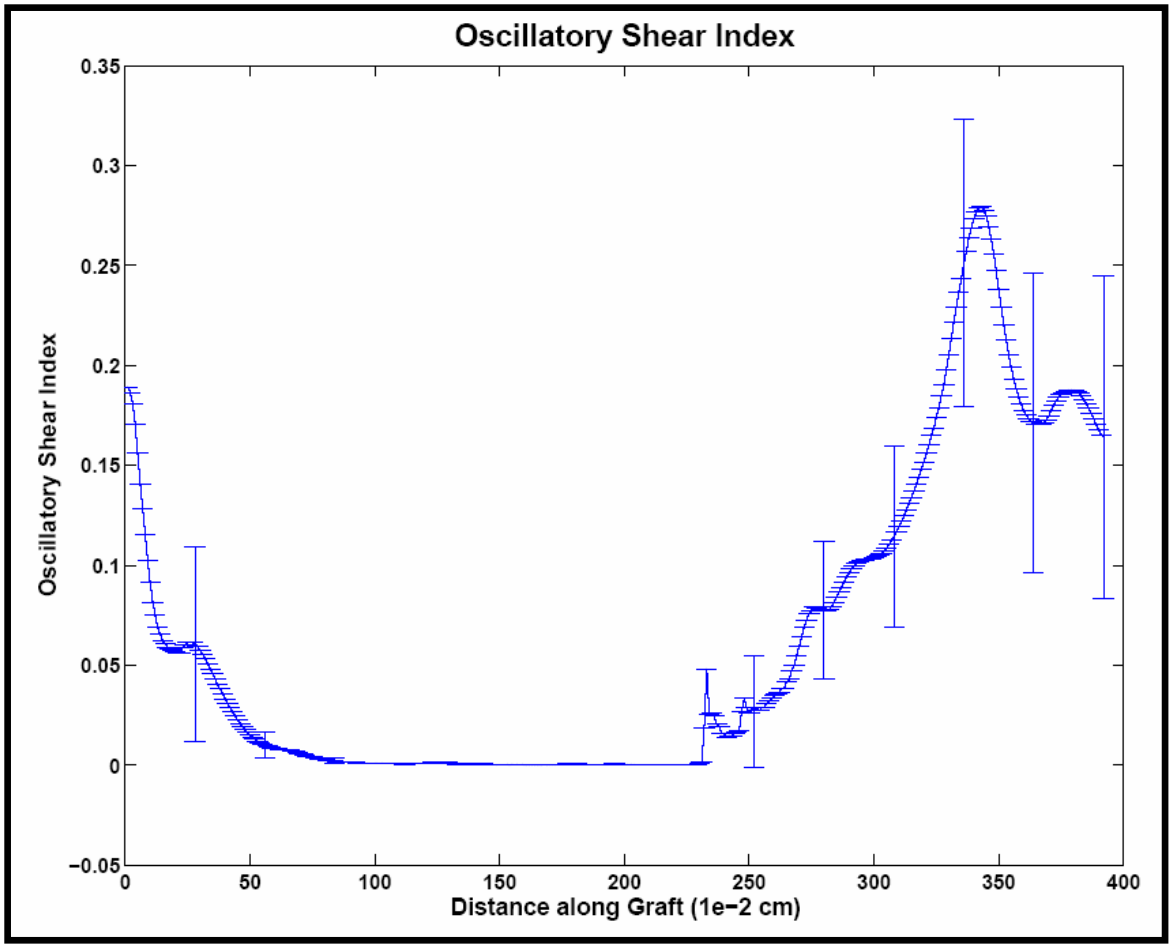

Figure 4.31: Oscillatory Shear Index With An Applied Boundary Condition from the Phase Contrast Magnetic Resonance Imaging.

Discussion:

This study focused upon the effect of a changing hemodynamic environment upon intimal thickening within a porous ePTFE vascular graft. Before discussing any conclusions, we first needed to establish that the material properties of the graft were uniform in both the 3 mm stenotic throat and the 6 mm upstream and downstream graft regions.

Graft Ultrastructure.

Our material analysis revealed that the ultrastructure of the 3 mm stenotic throat and the 6 mm straight expanses were relatively consistent. More specifically, there existed no statistically significant difference in their respective void fraction and graft thickness. The transition regions between the 3 mm stenotic throat and the 6 mm straight expanses signified the only locations where any material variations arose. Upon examination of the H&E cross-sections, these transition regions showed an overlap of the two adjoining graft materials. Due to this material inconsistency, the intimal thickness within these rather short 0.25 cm sections were ignored. Our detailed method of measuring intimal thickness easily accommodated this method.

The Stenotic Model.

Overall, the unstretched stenosis furnished a valuable model to investigate the effect of changing hemodynamics on intimal healing. This model altered the wall shear stress levels through a change in the flow geometry. This differed from Clowes' method [58] of adjusting the volumetric flow rate through an adjustment of the downstream resistance. Clowes [57,58] modulated the downstream resistance by inserting and removing an AV

fistula between the femoral artery and the superficial femoral vein. Temporarily, this arrangement furnished elevated wall shear stress levels within the prosthetic graft. The animal compensated for this elevated blood flow by adjusting its vascular resistance downstream of the graft. Over the course of months, this adjustment led to significant variation in the measured volumetric flow rate. In Clowes study he even documented that during the first week that the volumetric flow rate reduced by over 60 %. As expected, this variation in volumetric flow rate resulted in changes of the wall shear stress levels. These results contrasted markedly with our stenotic model. The unstretched stenosis maintains the same hemodynamic environment for an extended period of time. The stenotic model was constructed of prosthetic ePTFE that rigidly kept its original shape. Unlike an autologous vessel, the synthetic substitute is immune from any vasoconstrictive or vasodilatory response. Previously, researchers had investigated stenotic models by imposing a coarctation upon the abdominal aorta of animal models. This model consisted of fitting a constrictive band around the artery [123]. Over time, this model changed. The native vessel adjusted its diameter in an attempt to reduce the wall shear stress levels.

Previous attempts to characterize the hemodynamic environment were limited by this adaptive change in the volumetric flow rate. Our protocol assured some level of consistent hemodynamic measurements by evaluating the dynamics of the flowing blood at two different time points. The volumetric flow rate was measured at sacrifice, while the PCMRI velocity profile was gathered two weeks following surgery. The simulations at these two time points produced very similar estimates of vessel wall shear stress. Between the two time points, the τ_{avg} differed by only 12 %, while the Pulse WSS varied

by only 20 %. This fluctuation was significantly less than what other researchers had reported.

Graft Healing.

Within our unstretched stenosis, confluent healing of the graft surface was verified using several different tools. Researchers documented that the surface of the 60 μm ePTFE heals within two weeks [25]. With a confluently, healed surface, the porous graft provides a good model for discerning the effect of hemodynamics upon graft healing. At the anastomotic junctions, pannus ingrowth occurred within all the harvested vessels. This transanastomotic ingrowth occured at a maximum rate of 0.2 mm/day [39]. For a graft implanted for thirty days, this pannus ingrowth progressed up to 6 mm into each respective graft end. The rate and extent of the transanastmotic ingrowth was governed by factors other than just the hemodynamic environment. At the anastomosis, a compliance mismatch between the synthetic substitute and the native vessel resulted in intimal thickening. This mismatch caused disturbed flow patterns and pulsatile mechanical stresses that affected pannus ingrowth. Moreover, the perianastomotic ends healed by a steadily progressing leading edge. At the leading edge, the neointima advanced with the help of proliferating endothelial and smooth muscle cells. As detailed in an earlier study, the dynamics of these proliferating cells were regulated by a combination of humoral factors and interaction with the immunogenic graft surface. Transmural ingrowth was not impacted by these same parameters; and therefore, it provided a better medium to investigate the effect of changing hemodynamics on graft healing. With these factors in mind, we choose to ignore those regions that were healed

by transanastomotic ingrowth and to focus our attention upon how hemodynamics impact transmural ingrowth.

The mid-point of the unstretched control and the unstretched stenosis furnished the best insight into the hemodynamic's effect. At this location the stenotic throat (0.13 mm) demonstrated greater intimal thickening than the corresponding mid-point within the unstretched control (0.08 mm). This difference in average thickening was not statistically significant. Using a two-sided student t-test, a p-value of 0.10 was generated. While this value does not demonstrate a statistically significant difference, the result does suggest that other factors are influencing healing within the stenotic throat that are absent within the unstretched control graft. This thinking was strengthened by our correlative results between intimal thickening and the computational estimates of wall shear stress. An inverse relationship was defined between intimal thickening and the reciprocals of three wall shear stress estimates: (1) $\tau avg(z)$ (2) Pulse WSS (3) Max WSS. These results were consistent between the simulations using the two different boundary conditions of PCMRI and harvest volumetric flow rate. For all of the comparisons, the correlation coefficients were statistically significant. This inverse relationship suggests that an elevation in wall shear stress assists the thickening of the healed prosthetic vascular graft. The question then arises as to why this result emerges?

Over the past forty years researchers have published results [54-56] contending that elevations in WSS "inhibit and control" intimal thickening. This inverse relationship has been well documented through *in vivo* and *in vitro* studies; however, our examined results assert quite the opposite relationship [54-56]. Several distinguishing features help to explain this phenomenon. First, this study investigates the healing of prosthetic

vascular grafts and not the pathogenesis of atherosclerotic plaque. Much of the published literature deals with wall shear stress and its relationship to atheroma. While very similar, the pathology of atherosclerotic plaques differs from that of neointima deposition. An atherosclerotic plaque never constitutes a desirable outcome. Billions of dollars are expended each year attempting to prevent this damaging result, and even more money and time are spent in treating its sequelae. On the other hand, prosthetic vascular grafts respond best when a healed flow surface evolves. The most successful vascular grafts mirror the native state of an autologous vessel with its confluent layer of thin endothelium. When a prosthetic vascular graft heals quickly, the possibility of an acute, thrombotic episode reduces significantly. The healed surface possesses a healthy endothelium that provides many protective benefits. First and foremost, it functions as a border between the underlying synthetic material and the flowing blood. This prevents platelets from becoming activated by the rough prosthetic surface. Secondly, the endothelium protects the underlying smooth muscle from such reactive factors within the blood as PDGF-AA, PDGF-BB, b-FGF, TGF-β, IL-3, IL-5, IL-6, and many others intermediates. The endothelium functions not only as a physical barrier, but it also inhibits underlying smooth muscle proliferation through the release of prostacyclin, nitric oxide, and heparin sulfate.

Neointima growth becomes undesirable when it progresses to a point that occludes the graft. How the graft heals during the initial stages frequently dictates how it performs under chronic conditions and whether it remains patent. This study provides valuable insight into how the vascular graft heals during the first month and how the hemodynamic environment alters that behavior. Our observations suggest that different

dynamics are at work under these sub-acute conditions. All other published studies limited their investigation to chronic conditions [39,40,44,57,58]. The studies of atherosclerotic plaque involved measuring the intimal thickness of harvested cadaver vessels that were from patients ranging between eighteen and forty-five years of age or canines fed a cholesterol rich diet [55,56,147,119,121]. In Clowes' study involving the AV fistula [39,40], the grafts were implanted for at least four months, while in Bassiouny's study [121], ePTFE grafts were harvested at two months. During such a nascent study held under subacute conditions, hemodynamics fail to function as the critical mediator of intimal growth. In order for elevated levels of WSS to inhibit intimal thickening, a vascular graft needs a prolonged and chronic exposure spanning several months.

In this study, the vessel experienced high levels of WSS. To some degree, the pulse WSS and τavg measurements were misleading. Within the stenotic throat, the instantaneous WSS values exceeded 130 dynes/cm^2 during systole and 93 dynes/cm^2 during diastole. These were several reasons for these selectively high WSS values. First, the pulsatile flow temporarily leads to high levels at peak systole. Second, the vascular graft assumed a curved shape at the stenotic throat. The curvature was produced by the animal's lumbar lordosis. This curvature produced higher velocities on the posterior surface of the graft. Variations in graft shape can produce these large fluctuations in wall shear stress. Third, with elevations in velocity the WSS increased in value too. This effect was very apparent within the stenotic throat.

Our post-processing of computing the temporal and spatial averages obscured these instantaneous levels. These instantaneous measurements highlight the benefits of

performing pulsatile simulations using computational fluid dynamics. Steady state measurements fail to reveal these important dynamics. While useful for a quick assessment, Poiseuille flow overlooks many of the details inherent to a pulsatile flow environment. This trend is further suppressed if the vessel is treated as an axi-symmetric pipe devoid of any three-dimesional artifacts like vessel curvature.

Reconstruction of the computational grid provided a very good representation of the vessel *in vivo*. The MRI axial cross sections preserved very good information concerning the vessel's three-dimensional shape. The MRI images did suffer from some problems associated with image artifacts, contrast, and resolution. These obstacles were easily overcome through image processing. With its noninvasive means of analyzing vessel geometry, MRI imaging provided the best investigative modality. With our computational grid and the appropriate boundary conditions, we possessed all the necessary tools to thoroughly interrogate the vessel's hemodynamics.

CFD has long been recognized as a reliable means for furnishing this exquisite flow information. In comparison to experimental approaches such as laser Doppler anemometry, CFD accommodates intricate three-dimesional shapes and different input flow waveforms. CFD generates a wealth of hemodynamic information. Unfortunately, its potential use extends only as far as the resolution of the biologic data. In this study, there existed no preservation of how the circular cross sections were oriented in three-dimensional space. As a result, no potential existed for specifying intimal thickness values around the vessel's circumference such as its anterior, posterior or lateral walls. The intimal thickness could only be described as a function of distance along the axial

length of the graft. In the future, the use of such tools as molecular beacons and immunofluorescent dyes may preserve this information.

In our results we identified very disturbed and separated flow distal to the stenotic throat. The transient flow separation was evaluated by measuring the three-dimensional oscillatory shear index. Post-stenotically, the oscillatory shear index reflected pronounced transient flow separation, particularly at end-systole and the beginning of diastole. The flow separation possesses the potential to thicken the graft surface downstream of the stenotic throat. In our results, there was no observed difference in intimal thickening between the regions proximal or distal to the stenotic throat. Even in this disturbed flow environment, the graft had not been exposed to altered hemodynamics for a long enough period of time. A certain caveat must be heeded in this conclusion. At these regions upstream and downstream of the stenotic throat, the transition areas of altered graft ultrastructure resided. Still, when these 0.25 cm regions were excluded from the analysis, the same conclusions held true. Furthermore, the area of post-stenotic transient flow separation extended as far as the distal anastomosis; therefore, there were ample regions with consistent ultrastructure to perform the analysis.

In the end this study investigated the healing response of prosthetic vascular grafts under sub-acute conditions. The changing hemodynamic environment failed to exert a pervasive effect upon intimal thickening. The elevated WSS neither promoted nor inhibited intimal thickening. Ultimately, the graft was not exposed to the WSS conditions for a period of time long enough to change its pattern of healing. In the future, a comparative study must be conducted where the stenotic model is implanted under more chronic conditions.

Chapter V

Computational Fluid Dynamics of an Implanted ePTFE Vascular Graft within a Baboon

Introduction:

There has been a growing body of knowledge related to hemodynamics in vascular grafts. Intially, studies involved using qualitative tools such as flow visualization techniques to describe the hemodynamic environment. Soon after, they progressed to more quantitative methods such as Laser Doppler Anemometry (LDA). Researchers applied these techniques in their investigation of how the prosthetic vascular grafts healed. Bassiouny et al. [121] conducted a study where polymer casts were made from 30 μm ePTFE vascular grafts implanted within the aorto-iliac circulation of mongrel dogs using an end-to-side anastomosis. From these polymer casts, transparent silicone models were constructed that allowed for flow visualization studies using helium-neon laser illuminated particles. Through this study, these investigators qualitatively examined the dynamics within the distal end-to-side anastomotic geometry. Loth et al. [125, 126] later attempted to quantify this hemodynamic environment by investigating flow in a polysiloxane cast first under steady flow conditions and subsequently under pulatile flow. LDA provided detailed information concerning the near-wall velocity gradients and the wall shear stress distribution. Loth et al. identified a region of low wall shear stress near a stagnation point on the floor of the distal anastomotic junction. This area of low wall shear stress extended to the sidewalls and the suture lines [125,126].

Another way of studying detailed hemodynamics is through numerical simulations of pulsatile flow. Perktold et al. [127] documented the dynamics of an arterial T- bifurcation model by solving the Navier-Stokes equations within a finite element field. Taylor and Zarins [128] later attempted a three-dimensional pulsatile simulation of the abdominal aorta. The computational grid was based on an idealized abdominal aorta derived from averaged measurements. They attempted to correlate this hemodynamic data to sudanophilic lesions reported by Cornhill [129]. Lei et al. [130-132] later performed computational studies of pulsatile flow through an end-to-side vascular graft model. In these and later studies, Lei et al. investigated the behavior of temporal and spatial wall shear stress gradients. Some researchers believed that these hemodynamic parameters helped predict distortion of the healed graft surface along with future locations of intimal hyperplasia. Lei et al. later compared the computational results to Loth's [125,126] LDA measurements of the wall shear stress environment. Lei et al. concluded that the computational approach functioned an effective tool for a quantitative assessment of graft hemodynamics.

While these studies provided useful information, there still exist many additional details to investigate. From the published litrerature, most of the measurements of biologic data were frequently qualitative, lacking rigorous measurements of intimal thickness. Other studies derived their hemodynamic models from idealized arterial geometries. With sensitive variables such as wall shear stress, slight variations in velocity values produce large variations in the velocity gradient. An attractive alternative involves computationally modeling the blood flow using geometric grids constructed from three-dimensional *in vivo* medical images. Moore et al. [133-136] used time-of-flight MRI

imaging sequences to model the hemodynamics of the carotid arterial bifurcation. Phantom models of the carotid bifurcation were imaged with MRI and then processed with various smoothing algorithms. These investigators concluded that the smoothing algorithms eliminated many of the problems associated with the MRI images (resolution detail, flow artifacts, non-unifrom lumen signals, partial volume effects) without compromising the anatomic detail. As opposed to past attempts using direct surface triangulation, Moore outlined the cross-sectioned arterial profiles from axial images. When attempting to reconstruct models of *in vivo* carotid bifurcations, smoothing of the cross-sections and created surfaces was absolutely critical. With a representative *in vivo* model in hand, calculated wall shear stress measurements varied little from the accepted "gold standards." This established MR arterial reconstruction as an acceptable means for investigating *in vivo* hemodynamics. Later, Moore compared the differences in arterial geometry preservation between *in vivo* medical imaging and post-mortem tissue preparation. She investigated the post-mortem tissue techniques of *in situ* casting and *ex situ* pressure fixation. Computational simulations were then conducted using these different information sets. She concluded that *in vivo* MRI provided the best overall model for replicating vessel geometry.

In this study we explore different approaches to modeling the hemodynamic environment of 60 μm ePTFE vascular grafts implanted within the abdominal aortic tree of juvenile, male baboons. The vascular graft incorporates a stenotic shape with a 75 % reduction in luminal area. The vessel geometry is reconstructed into a series of computational grids using three different sources: (1) the geometric parameters of the graft prior to implantation, (2) *in vivo* pressure-perfused histologic cross-sections, and (3)

MRI imaging of the implanted grafts. Pulsatile simulations will be run using boundary conditions from two different sources: (1) the measured ensemble averaged volumetric flow rate and (2) phase contrast magnetic resonance imaging of the inlet velocity. The computational results from all the generated grids will be presented and their estimates of wall shear stress compared. In the end, we hope to discern which of these computational grids best represents the graft geometry; but moreover, which one provides the best description of the *in vivo* vascular graft flow environment. Towards this end, we will compare the CFD simulation results with PCMRI velocity measurements made at selected downstream locations. Furthermore, we will evaluate the accuracy of the volumetric flow rate as an inlet condition by comparing its results to simulations using PCMRI.

Material and Methods:

Animals.

In this study vascular grafts were implanted into juvenile male baboons (*papio cyncephalus / anubis*) of roughly two years of age and weighing between 13-24 kg. All animal procedures followed "Principles of Laboratory Animal Care", the "Guide for the Care and Use of Laboratory Animals" (NIH Publication No. 8023, revised 1985), and IACUC university guidelines.

Grafts.

Four different vascular grafts constructed of 60 μm expanded polytetrafluoroethylene (Gore-Tex, non-reinforced, thin wall; provided by W.L. Gore and Associates, Inc., Flagstaff, Ariz.) were used in this study. The first type of vascular graft, the so-called unstretched control, possessed a length of approximately 4 cm and an inner diameter of 6 mm. The next two varieties of vascular grafts were constructed from the same starting material with an inner diameter of 3 mm. The first of these vascular grafts, the so-called stretched control, was uniformly stretched in a radial direction from a 3 mm inner diameter to a 6 mm inner diameter. The second of these vascular grafts, the so-called stretched stenosis, consisted of a 75 % reduction in its cross-luminal area. The stretched stenosis was constructed by fitting the ePTFE over an aluminum mandrel that began with an inner diameter of 6 mm, symmetrically contracted down to 3 mm, and then symmetrically expanded back out to 6 mm. The aluminum mandrel was lathed according to the following mathematical equation:

$Z = 6.0 \text{ mm} \quad \text{for } 0 \leq x < 1.25 \text{ and for } 2.75 < x \leq 4.0$

$Z = 1-.25(1+\cos(\pi((x-2)/0.75)) \text{ for } 1.25 \leq x \leq 2.75$ (**Equation 5.1)**

The aluminum mandrel was separable in the middle, allowing for easy separation and removal of the graft prior to surgery. A schematic of the stretched stenosis illustrates this design (Figure 5.1).

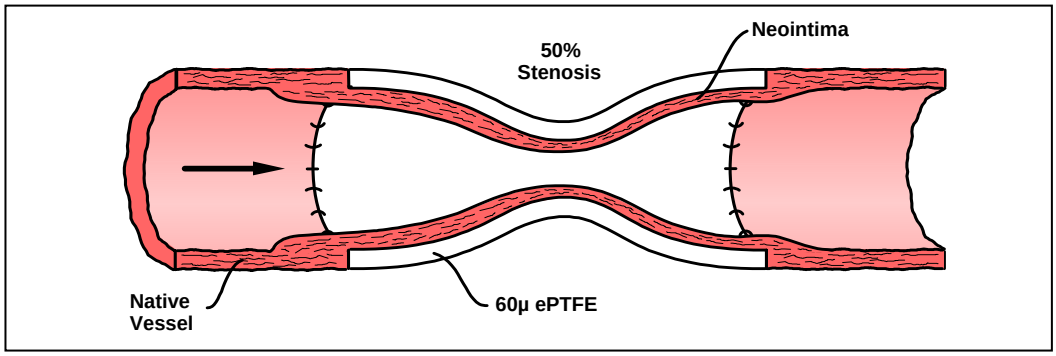

Figure 5.1: The Stretched Stenosis. The stenotic graft was constructed from 60 μm ePTFE with an initial inner diameter of 3mm. By fitting the graft material over the separable mandrel, the proximal and distal ends were stretched to an inner diameter of 6 mm.

The Impra Corporation constructed the fourth type of vascular graft, the so-called unstretched stenosis. In the center of the graft the cross-luminal area was reduced by 75 %. The vascular graft consisted of a central stenotic section with a 3 mm internal diameter and a length of 1.5 cm melded to two separate segments with an inner diameter of 6 mm and a length of 2 cm. All material used in this construction was unstretched 60 μm ePTFE. The artistic configuration of Figure 5.2 describes this design.

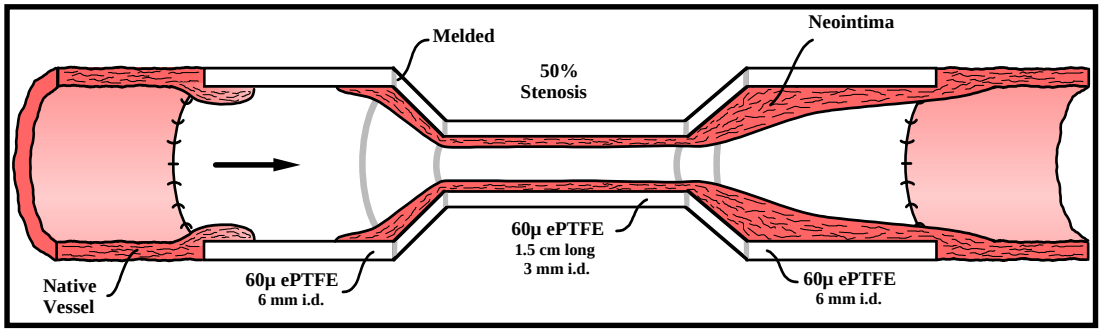

Figure 5.2: The Unstretched Stenosis. This artistic configuration describes the design of the vascular graft constructed with 60 μm ePTFE. A central stenotic portion with an inner diameter of 3 mm and a length of 1.5 cm was melded to two separate 2 cm lengths of graft with an inner diameter of 6 mm.

Surgery.

One day prior to surgery, 325 mg of aspirin was administered to the baboon. Blood samples were drawn to analyze such hemodynamic parameters as platelet count, hematocrit, and white blood cell count. Under general endotracheal anesthesia with 1.5 to 2.5 % isoflurane, a mid-line incision was made, followed by exposure of the retroperitoneum. Following isolation of the distal abdominal aorta, 150 units of heparin/kg were infused. The volumetric flow rate of the baboon was measured by fitting a perivascular flow probe (Transonic Inc.) around the exposed aorta, just distal to the

bifurcation of the renal arteries. The transonic flowmeter was connected to a PC computer using an Analog/Digital card. On the PC, Labview® recorded the volumetric flow rate for thirty cardiac cycles. The volumetric flow rate was again measured at sacrifice. Twenty ePTFE grafts were implanted into the distal abdominal aortas of individual baboons. Implantation of vascular grafts involved using an end-to-end anastomosis with a continuous running suture of 6.0 polypropylene (Davis & Geck, Wayne, N.J.). An example of an implanted vessel is demonstrated. Changyi Chen M.D., Ph.D performed all of the surgeries.

MRI Imaging.

Two weeks following the surgery, two of the animals were imaged using a 1.5 Tesla Phillips Mobile scanner with a time of flight imaging sequence. The imaging parameters were TR = 20 ms, TE = 6 ms, FOV = 190 mm, 256 x 256 acquisition, 2 mm slice thickness, flip angle = 40 degrees. After placing three EKG leads upon the animal, cardiac gating was used during image acquisition. Two animals were imaged, one with an unstretched control and the other with an unstretched stenosis. The animals were sedated with a combination of ketamine (0.1mg/kg) and telazol (5 mg/kg). The sedative effect lasted about forty-five minutes. Once within the scanner, the animal's abdomen was placed within a head coil. In order to visualize the vessels, a radio-opaque contrast marker of 15 cc of gadolinium was infused. At first, coronal sections were taken to visualize the vessels within the animal (Figure 5.3). Next, the vessels were interrogated using a sequence of axial slices acquired 2 cm upstream of the proximal anastomosis and extending up to 2 cm downstream of the distal anastomosis. This process captured the shape of the implanted vessels. The MRI images were converted into a 256 x 256

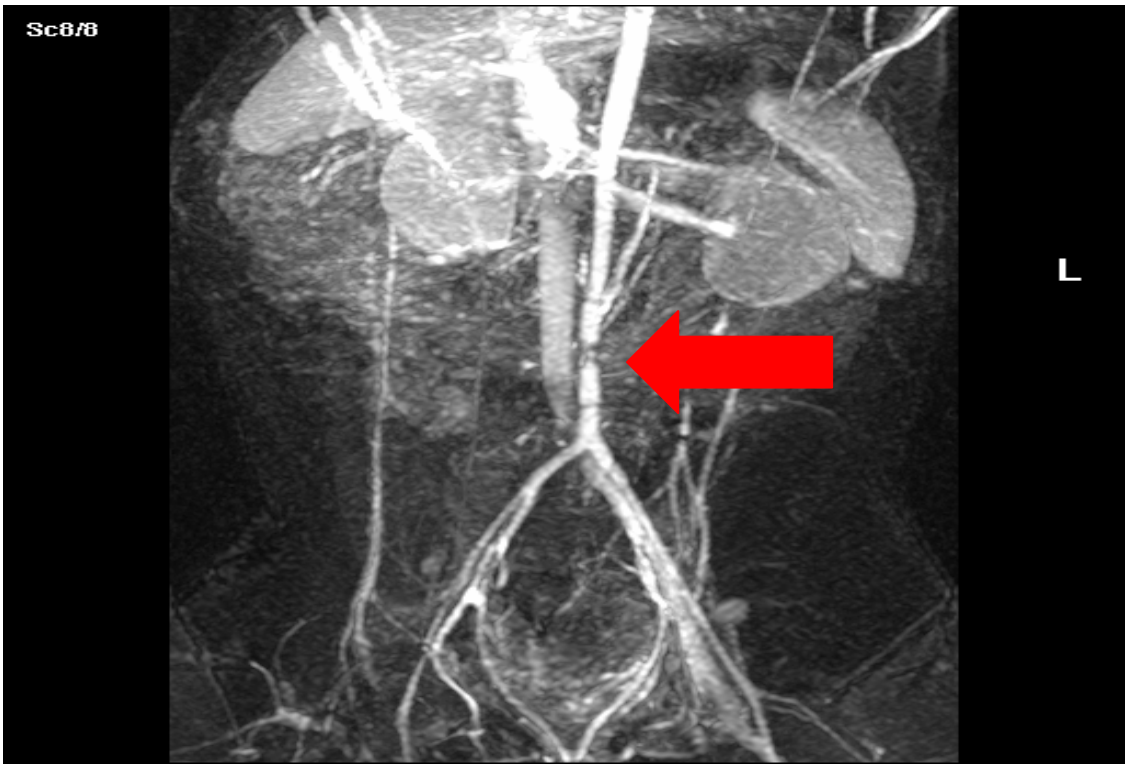

Figure 5.3: Coronal Cross-Section of an Implanted Unstretched Stenosis within a Baboon. The image shows the proximal and distal anastomosis. The stenotic throat of the graft was well visualized.

unsigned 16-bit format with the aid of a MATLAB generated program (Marijn Brummer, Ph.D., Emory University Department of Radiology). Next, phase contrast magnetic resonance imaging (PCMRI) velocity data were collected at three different locations within the analyzed grafts: (1) proximal anastomosis, (2) mid-vessel, and (3) distal anastomosis. Additionally, using a black-blood imaging sequence, the captured pixel intensity reflected blood velocity within the vascular graft.

MRI Contours.

With the MRI axial images, the outlines of the graft luminal surfaces were captured (Figure 5.4 and 5.5). First, the location of the vessel wall was defined (program **mricontmain.m**). The captured images were converted to pixel intensity values from 0 to 1 (program **pixtocm.m**). A scale was input that helped to define the inside of the vessel as a white entity. If the pixel value was above the scale, its value was redefined as equaling 1, while if the pixel value was below the scale, its value was redefined as equaling 0. The edges of the vessel posed a significant challenge. A binary dilation and erosion procedure helped to differentiate the inside from the outside of the graft (program **edgedetect.m**). Based on the value of the input parameter, this signal processing helped either to expand or to contract the vessel edge until the wall was defined. A contour line was then fit to the analyzed vessel borders. This line was then smoothed using an algorithm that calculated an average value based on values that preceded and followed the location of interest (program **smoothfil.m**). From the contour's location within the MRI image, the pixel values were then converted to a scale of centimeters.

The contour specified the location of the vessel wall within a Cartesian coordinate frame. This information was then further smoothed based on an algorithm

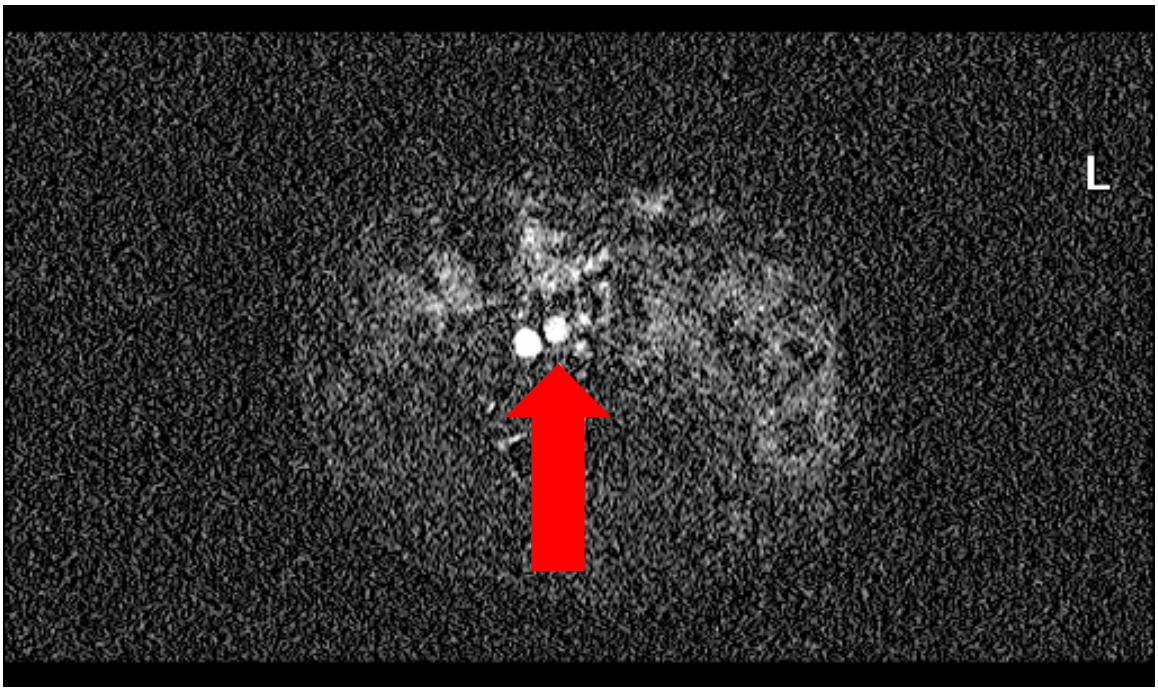

Figure 5.4: Axial Cross-Section of an Implanted Prosthetic Vascular Graft. The red arrow highlights the vascular graft. Next to the graft is the Inferior Vena Cava.

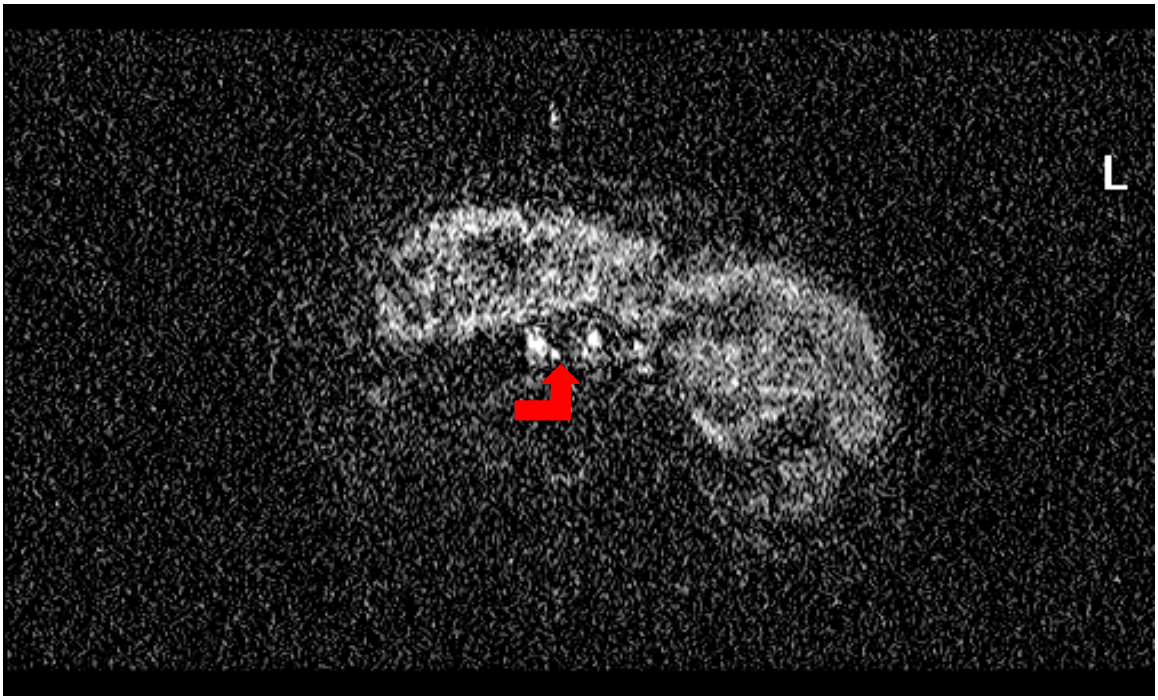

Figure 5.5: Axial Cross-Section of an Implanted Prosthetic Vascular Graft at the Level of the Stenotic Throat. The red arrow highlights the stenotic throat.

introduced by Moore [137]. First, along the length of the vessel each captured contour was smoothed using a fifth order smoothing spline. Secondly, a cubic spline was used to smooth the resulting vector that connected the centroids of all the slice contours. Lastly, the square root of each contour's cross-sectional area was smoothed using a cubic spline (program **loop2.m**). The last two steps adjusted the coordinates of the slice contour according to equation 5.2.

$$(x_{new}, y_{new}) = [(x, y) - (x_{cen}, y_{cen})] * \sqrt{area_{smoothed} / area} + (x_{cen,smoothed}, y_{cen,smoothed})$$

(**Equation 5.2)**

Histologic Contours.

The contours of the harvested vessels were captured from vascular grafts fixed by *in vivo* pressure perfusion. All baboons were sacrificed one month following graft placement. The distal abdominal aorta was exposed, and the animals were sacrificed by exsanguination. The implanted grafts were fixed *in vivo* by implanting a 14-gauge angiocatheter into the abdominal aorta and infusing the fixative from a 60 cc syringe. Before infusing the fixative, the grafts were first flushed with 0.1 M phosphate buffered saline (PBS) at pH 7.4 and 37° Celsius. A 14-gauge angiocatheter was inserted into the right common iliac to control the rate at which perfusate drained, while another 14-gauge angiocatheter was fed into the left common iliac up to the level of the aorta's bifurcation to measure mean arterial pressure (MAP) using a sphygmomanometer. The vessels were perfused at a MAP of 100 mmHg for at least thirty minutes with 10 % buffered formalin (Baxter Diagnostics Inc, McGraw Park, Ill). Figure 5.6 illustrates the

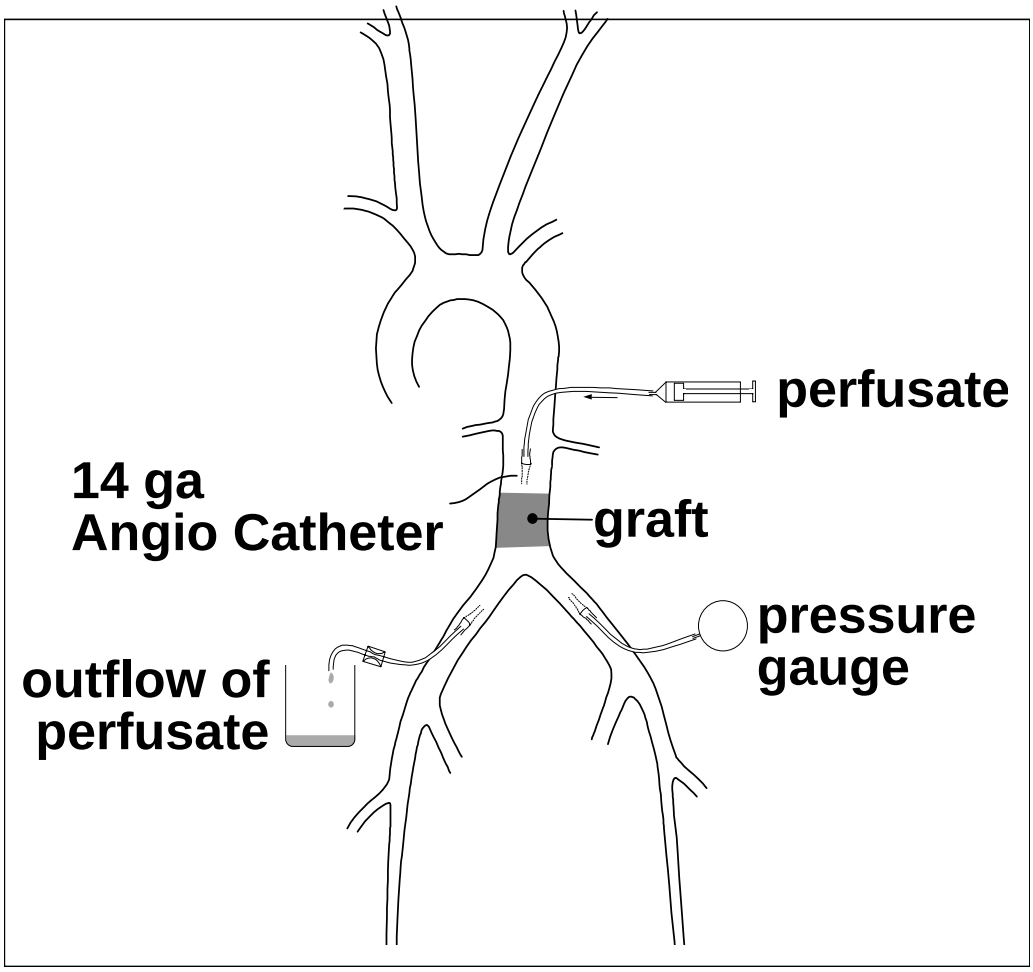

Figure 5.6: *In Vivo* Pressure Perfusion of Implanted Vascular Graft. The perfusate consisted of either 10 % buffered formalin for immunohistochemistry or 2.5 % glutaraldehyde for Scanning Electron Microscopy. The angiocatheter in the right common iliac was fed up to the aorta's bifurcation. This allowed the sphygmomanometer to measure the MAP within the aorta.

set-up for the *in vivo* pressure perfusion of the grafts. Following fixation, the grafts were harvested along with 1 cm sections of contiguous native vessel at each anastomosis and then submersed in fixative for a 24-hour period. All harvested grafts were divided into 5 mm circular cross sections, embedded into paraffin, and microtomed perpendicular to the long axis of the vessel using a 5 μm slice thickness. The entire axial length of the vessel was interrogated. At the proximal anastomosis, the center of the graft, and the distal anastomosis, microscope sections were cut every millimeter from the embedded blocks, while elsewhere in the vessel, only one representative set of sections was taken from each embedded block. As a result, greater resolution was obtained at the anastomotic ends and at the center of the vessels.

All grafts underwent staining with Hematoxylin and Eosin (H&E) (Figure 5.7). All slide specimens were analyzed using a microscope with a 1x objective interfaced to a digital camera that captured all images into a TIFF format. Using the Image-Pro Plus ® Software (Media Cybernetics, Inc.; Silver Spring, Maryland), the vessel contour was outlined. The vessel contours were obtained for all four different vascular graft varieties. These contours were then processed using the Moore [137] smoothing algorithm as discussed in the MRI grid construction section; however, one important adjustment was introduced. The histologic cross-sections lacked information that connected them to the graft's position within three-dimensional space. This problem was addressed in two different ways. In the first approach, all the contours were aligned along the same z-axis (program **loophistreorgflat.m**). An alternative approach was explored in which the three-dimensionsal information from the MRI scans was combined with the histologic

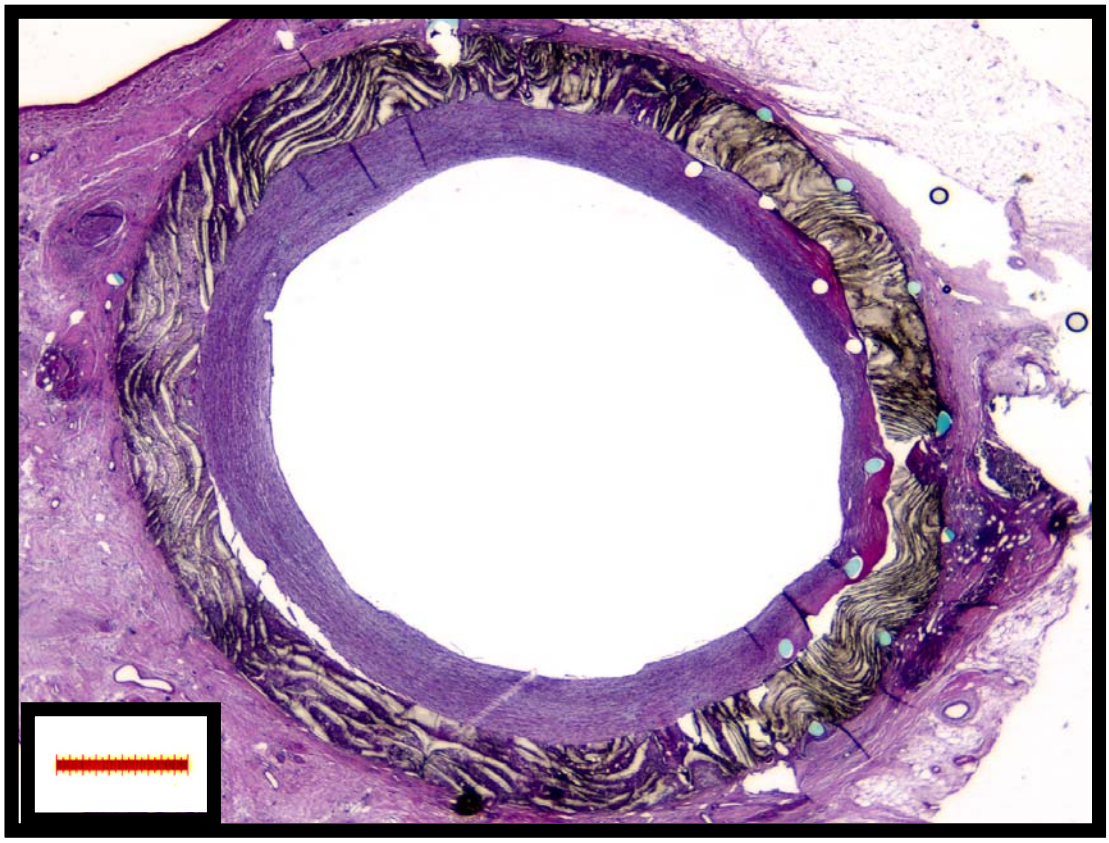

Figure 5.7: H&E Stained Circular Cross-Section.

contours in the following way. From our processing of the MRI contours, a smoothed vector passing through each image centroid was generated. This information was then used to reorient the histologic contours within three-dimensional space (program **loophistreorg.m**).

Ideal Contours.

Contours were outlined based on the pre-implantation geometry of the vascular grafts. For the stretched and unstretched controls, this process was based on their straight shapes. For the stentoic grafts, the mathematical definitions of their shapes helped to define their cross-sectional contours.

Grid Construction.

With the contour information from these three different approaches, three-dimensional computational grids were next created. This step was completed within the preprocessor software GAMBIT (Fluent Inc., Lebanon, NH). A wire frame of the vascular graft was constructed from these contours using a combination of connecting spline functions. From this wire frame or computational volume, a mesh was generated using a cooper scheme with a grid spacing of 0.025. A total of thirteen different grids were constructed from the MRI, histologic, and ideal contours with approximately 90000 nodes (Tables 5.1, 5.2, 5.3, 5.4, 5.5). For the purposes of demonstrating grid independence, three additional grids were constructed of the ideal control graft. These grids contained 90 %, 80 %, or 70 % of the number of nodes within the original ideal control graft. In the case of the MRI stenosis and the histologic unstretched stenosis, two extended grids were constructed by extending their outlet lengths by 3 diameter distances (1.8 cm).

Table 5.1: Table of Ideal Computational Grids for Grid Independence and Applied Inlet Boundary Conditions. Executed simulations show Reynolds number based on the boundary condition's mean flow rate.

	Implant	Harvest	PCMRI	Nodes
Ideal Control 0.9		**Re (mean Q) =141**		**90000**
Ideal Control 0.8		**Re (mean Q) =141**		**80000**
Ideal Control 0.7		**Re (mean Q) =141**		**70000**

Table 5.2: Table of Ideal Computational Grids and Applied Inlet Boundary Conditions. Executed simulations show Reynolds number based on the boundary condition's mean flow rate.

	Implant	Harvest	PCMRI	Nodes
Ideal Control	**Re (mean Q) =134**	**Re (mean Q) =141**	**Re (mean Q) =115**	**100000**
Ideal Stretched Stenosis	**Re (mean Q) =132**	**Re (mean Q) =113**		**93000**
Ideal Unstretched Stenosis	**Re (mean Q) =132**	**Re (mean Q) =113**	**Re (mean Q) =115**	**91000**

Table 5.3: Table of MRI Computational Grids and Applied Inlet Boundary Conditions. Executed simulations show Reynolds number based on the boundary condition's mean flow rate.

	Implant	Harvest	PCMRI	Nodes
MRI Unstretched Control	**Re (mean Q) =125**	**Re (mean Q) =134**	**Re (mean Q) =109**	**88000**
MRI Unstretched Stenosis	**Re (mean Q) =125**	**Re (mean Q) =108**	**Re (mean Q) =109**	**92000**
Extended MRI Unstretched Stenosis		**Re (mean Q) =108**	**Re (mean Q) =109**	**150000**

Table 5.4: Table of Histologic Stretched Computational Grids and Applied Inlet Boundary Conditions. Executed simulations show Reynolds number based on the boundary condition's mean flow rate.

	Implant	Harvest	PCMRI	Nodes
Histologic Stretched Control	**Re (mean Q) =118**	**Re (mean Q) =127**		**86000**
Histologic Stretched Control Flat	**Re (mean Q) =118**	**Re (mean Q) =127**		**87000**
Histologic Stretched Stenosis	**Re (mean Q) =118**	**Re (mean Q) =103**		**94000**
Histologi Stretched Stenosis Flat	**Re (mean Q) =118**	**Re (mean Q) =103**		**94000**

Table 5.5: Table of Histologic Unstretched Computational Grids and Applied Inlet Boundary Conditions. Executed simulations show Reynolds number based on the boundary condition's mean flow rate.

	Implant	**Harvest**	**PCMRI**	**Nodes**
Histologic Unstretched Control	**Re (mean Q) =132**	**Re (mean Q) =141**	**Re (mean Q) =115**	**86000**
Histologic Unstretched Control Flat	**Re (mean Q) =132**	**Re (mean Q) =141**		**87000**
Histologic Unstretched Stenosis	**Re (mean Q) =132**	**Re (mean Q) =113**	**Re (mean Q) =115**	**91000**
Extended Histologic Unstretched Stenosis		**Re (mean Q) =113**	**Re (mean Q) =115**	**147000**
Histologic Unstretched Stenosis Flat	**Did not converge**	**Did not converge**		**90000**

Inlet Boundary Condition.

In order to conduct pulsatile simulations with these computational grids, boundary conditions at the inlet were required. The boundary conditions came from two different sources: (1) the measured volumetric flow rate and (2) PCMRI velocity measurements.

The volumetric flow rate was obtained from the abdominal aorta just distal to the bifurcation of the renal arteries at the time of surgery and at sacrifice. The waveforms acquired at surgery and at sacrifice were ensemble averaged for the two control and two stenotic grafts to obtain representative descriptions (program **ensembleinit1.m**). These ensemble averaged waveforms were then input into a Womersley solution (Equation 5.3 and 5.4) with an $\alpha = 4.8$ to derive velocity values at the inlet (program **nodefinalyep.m**).

$$\frac{\partial^2 w}{\partial r^2} + \frac{1}{r}\frac{\partial w}{\partial r} - \frac{1}{\nu}\frac{\partial w}{\partial t} = \frac{A}{\rho}e^{\text{int}}$$

Equation 5.3

$$w = \frac{AR^2}{\mu}\frac{1}{i^3\alpha^2}\left\{1 - \frac{J_0(\alpha i^{\frac{3}{2}} y)}{J_0(\alpha i^{\frac{3}{2}})}\right\}e^{\text{int}} \bullet\bullet\bullet$$

Equation 5.4

In order to define the velocity values, a description of the nodes at the inlet was required. At the walls the velocity was set equal to 0. A linear interpolation scheme was then used to define velocity values at each node as a function of time.

The PCMRI collected information concerning the blood velocity moving across an interrogated region of interest as a function of time (Figure 5.8). The intensity of the pixel values within the vessel's lumen reflected the velocity of the blood. In order to convert the intensity values, the maximum velocity over the cardiac cycle was needed. The maximum velocity was determined from an in house program (Marijn Brummer, Ph.D., Emory University Department of Radiology). With this value in hand, the intensity values were then converted to units of cm/sec. In order to define the velocity values, a description of the nodes at the inlet was required. At the walls the velocity was set equal to 0. A linear interpolation scheme was then used to define velocity values at each node as a function of time.

FIDAP Simulations.

With the computational grids and the boundary conditions, CFD simulations were run using FIDAP (Fluent Inc., Lebanon, NH). All simulations were executed with certain established parameters: (1) no slip boundary conditions at the wall; (2) zero traction boundary condition at the outlet; (3) three-dimensional non-moving geometry; (4) laminar flow conditions; (5) non-linear Navier-Stokes equations; (6) isothermal conditions; (7) fluid dynamic viscosity was assumed to be 0.04 Poise; and (8) fluid density of 1.081 g/cm^3. The convergence criteria specified a tolerance value of 0.0001 for the pressure and all three-velocity components. First, simulations were run under steady-state conditions. A blunt inlet profile was assumed, and its average velocity was specified as the axial boundary condition. The average velocity for the measured ensemble averaged flow rates were as follows: (1) control at implantation = 8.25 cm/sec; (2) control at harvest = 8.83 cm/sec; (3) stenosis at implantation = 8.25 cm/sec; and (4)

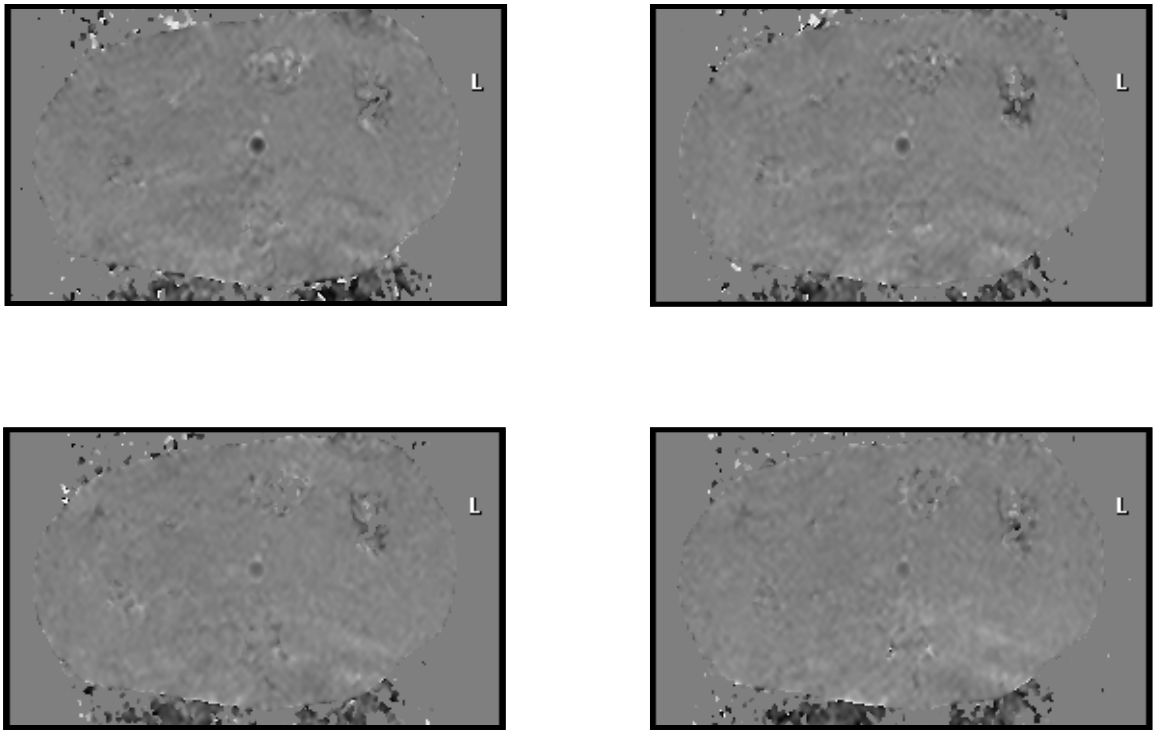

Figure 5.8: PCMRI Images as a Function of Time. The intensity of the black pixels within the vessel lumen reflects the velocity of the blood. We observe that the velocity within the vessel changes as a function of time.

stenosis at harvest = 7.10 cm/sec. A segregated interative solver was used. Secondly, simulations were run under pulsatile conditions. As described earlier, the boundary conditions were specified by both the ensemble averaged flow rates and the PCMRI. For all the computational grids, pulsatile simulations were run using the ensemble averaged volumetric flow rates at implantation and at sacrifice, while the PCMRI was only used for the computational grids describing the unstretched control and the unstretched stenosis (Tables 5.1, 5.2, 5.3, 5.4, 5.5). In order to eliminate any start-up effects, the pulsatile simulations ran for three cardiac cycles. Once again, a segregate interative solver was used. The simulations were executed with a Backward Euler algorithm involving a variable time step with a window of 0.3 normalized units. Initial conditions were imported from the previously run steady state simulations.

Once the simulations converged, the datafiles for each simulation were concatenated into one file (program **concatenate1.m**). The velocity vectors and pressure at each node were exported to text files for post-processing. The WSS values were generated within FIDAP by decomposing the total fluid stress into its viscous and tangential components. These three-dimensional WSS values were then exported into text files (program **fidapconversion2.m**). These exported text files were then converted into a file format readable by Tecplot 9.0 (Amtec Engineering, Bellevue, WA) (program **testmod.m**). Within Tecplot, the computational grid was decomposed into circular cross-sections every 0.1 mm. At these locations, the velocity and WSS values were exported to text files. These files were then processed by a MATLAB program designed to describe the various hemodynamic parameters along the axial length of the graft (programs **testfinal.m** and **spatial1.m**). The hemodynamic data were compressed into a description

of wall shear stress as a function of distance along the axial direction of the vascular graft. Along the graft's axial length, this was accomplished by averaging the WSS measurements around the circumference of the vessel. This term is referred to as spatially averaged WSS or $\tau_s(z,t)$ (Equation 5.5).

$$\tau_s(z,t) = \left| 1/S \int_0^S \tau ds \right|$$

Equation 5.5

At each axial location along the graft, the pulse spatially averaged WSS (Pulse WSS) was calculated. Over a cardiac cycle, the Pulse WSS measures the difference between the maximum spatially averaged WSS and the minimum spatially averaged WSS. Furthermore, the temporal mean of the spatially averaged WSS was calculated. This manipulation produced the spatially averaged, temporal mean wall shear stress (τavg) (Equation 5.6).

$$\tau avg(z) = \left| (1/(T*S)) \int_0^S \int_0^T \tau dt ds \right|$$

Equation 5.6

The three-dimensional oscillatory shear index was also calculated (Equation 5.7).

$$OSI = 0.5\left(1 - \frac{\left| \int_0^T \tau dt \right|}{\int_0^T |\tau| dt}\right)$$

Equation 5.7

These different descriptions of WSS and OSI were then correlated with the measured histologic data. The histologic data described intimal thickness (mm) as a function of axial distance along the length of the vascular graft as described in Chapter III and IV.

CFD Code Validation.

In order to validate the accuracy of the FIDAP simulations, the velocity values generated by the simulations were compared to the PCMRI measurements at the distal anastomosis of the unstretched stenosis. At this distal site, a program was generated that calculated the average velocity within the inner 70 % of the lumen's cross-sectional area (program **average.m**). The average velocities of the core flow were then statistically compared between the PCMRI measurement and the FIDAP simulations.

Statistics.

Statistical analysis was performed on a Pentium IV P.C. with the use of either MATLAB or Excel 2000 statistical software (Microsoft Co.). The documented values are given as the mean ± the standard deviation. The correlations coefficients between the various hemodynamic parameters and the intimal thickness were considered significant if the p value was less than 0.05.

Results:

Computational Grids.

A selection of different computational grids was constructed. The various computational grids reflected the different investigational modalities used to model their borders. First, the ideal grids were created (Figure 5.9, 5.10, 5.11). These grids were based upon the original design parameters of the vascular grafts. Secondly, the computational grids based on the MRI images were generated (Figures 5.12 and 5.13). Thirdly, the computational grids based on the histologic contours were made. Some of the grids imposed the best-fit line passing through the centroids of the MRI generated grids (Figures 5.14, 5.16, 5.18). These computational grids assumed a natural shape for a vascular graft implanted within the distal abdominal aortic tree. The remaining grids imposed a common parallel z-axis throughout the axial length of the vessel (Figures 5.15, 5.17). These computational grids appeared distorted as though they were not implanted within *in vivo* conditions. Lastly, the extended grids were created for the unstretched stenosis (Figures 5.19).

Boundary Conditions.

The ensemble averaged volumetric flow rates were generated for both the control and the stenotic grafts at implantation and at sacrifice (Figures 5.20, 5.21). The velocity profiles were then created for the ensemble averaged flow rates and for the PCMRI (Figure 5.22).

Node Independence.

Node independence was demonstrated by comparing wall shear stress calculations within a straight control graft with varying number of nodes. These simulations were performed under pulsatile conditions Between the four different computational grids of 70,000, 80000, 90000, and 100000 nodes, the wall shear stress

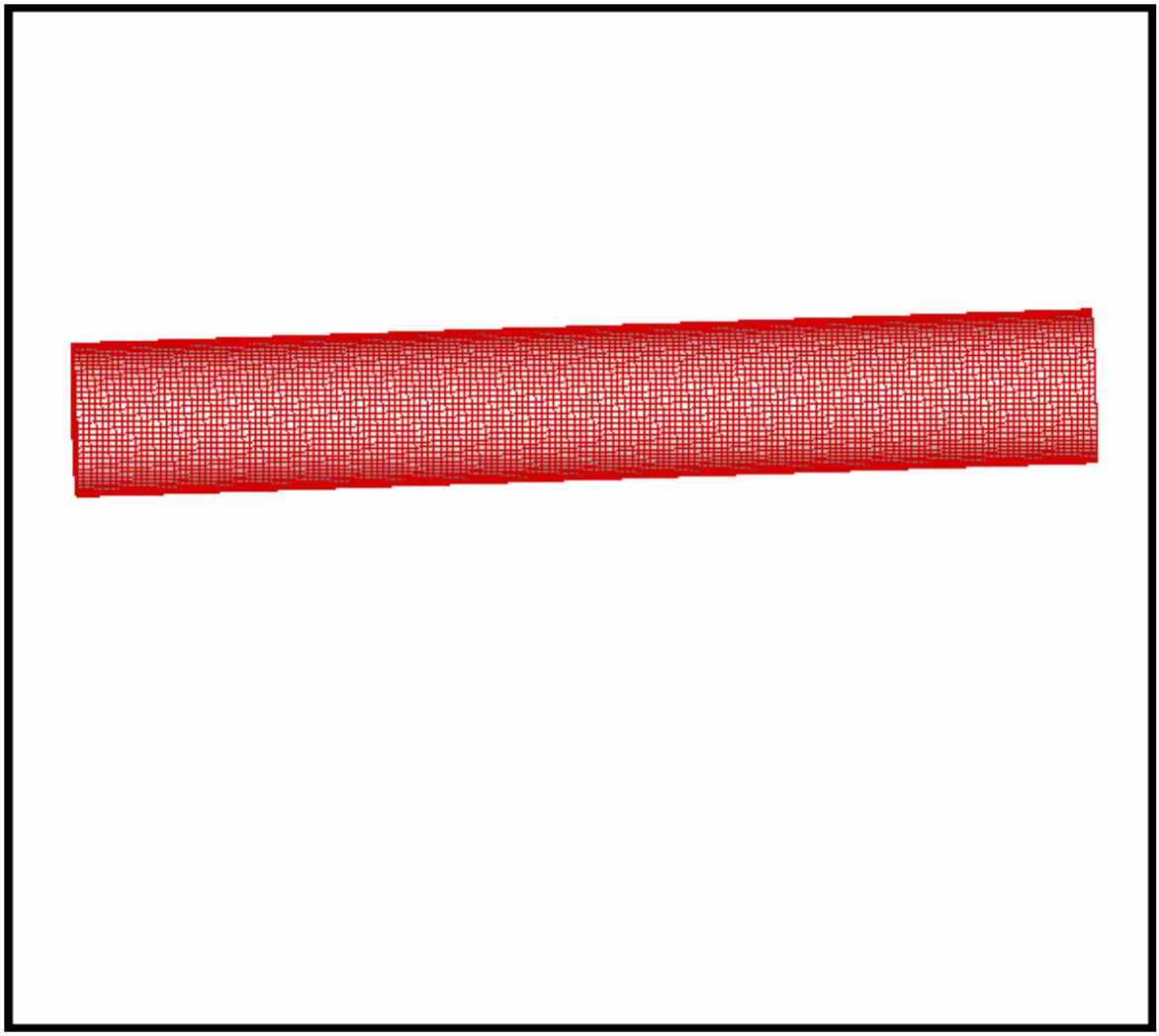

Figure 5.9: Ideal Control Computational Grid.

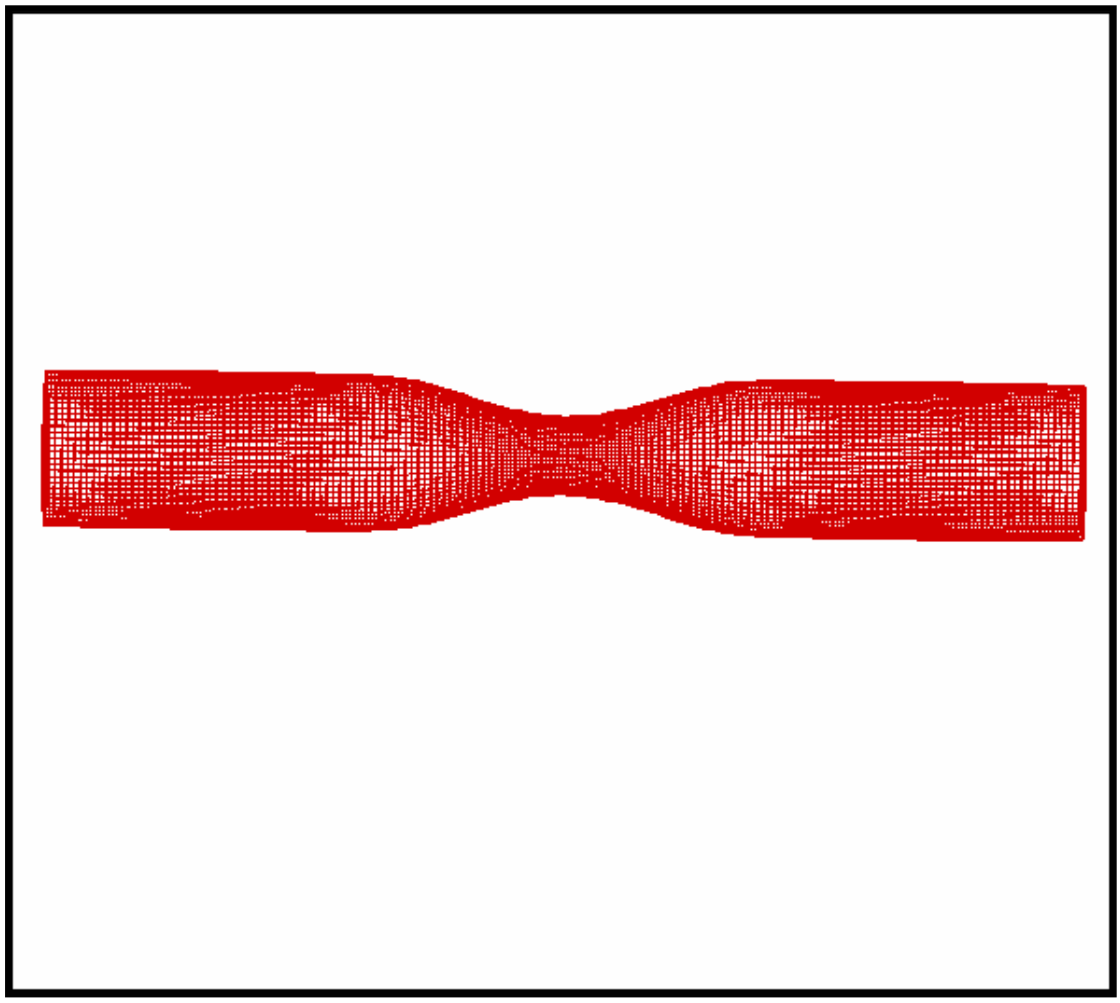

Figure 5.10: Ideal Stretched Stenosis.

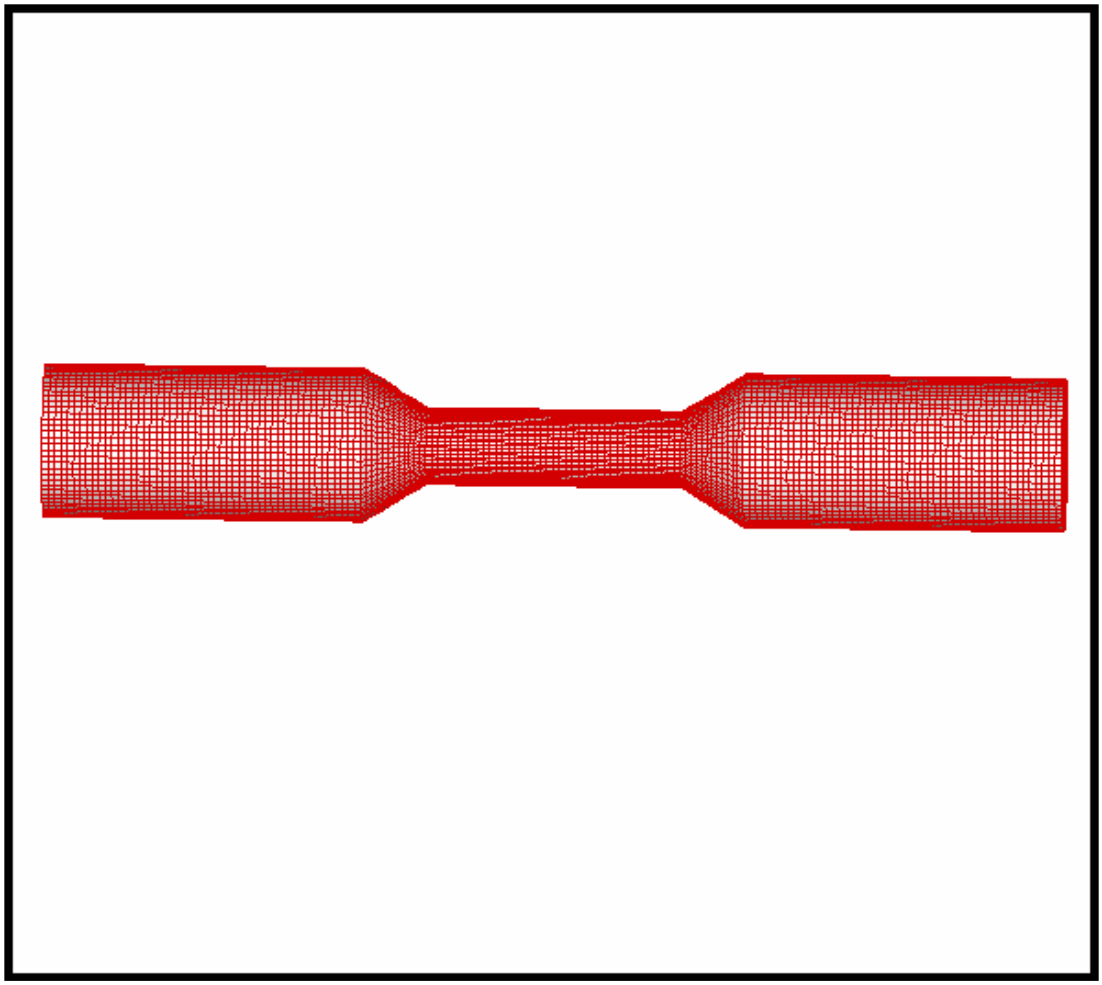

Figure 5.11: Ideal Unstretched Stenosis.

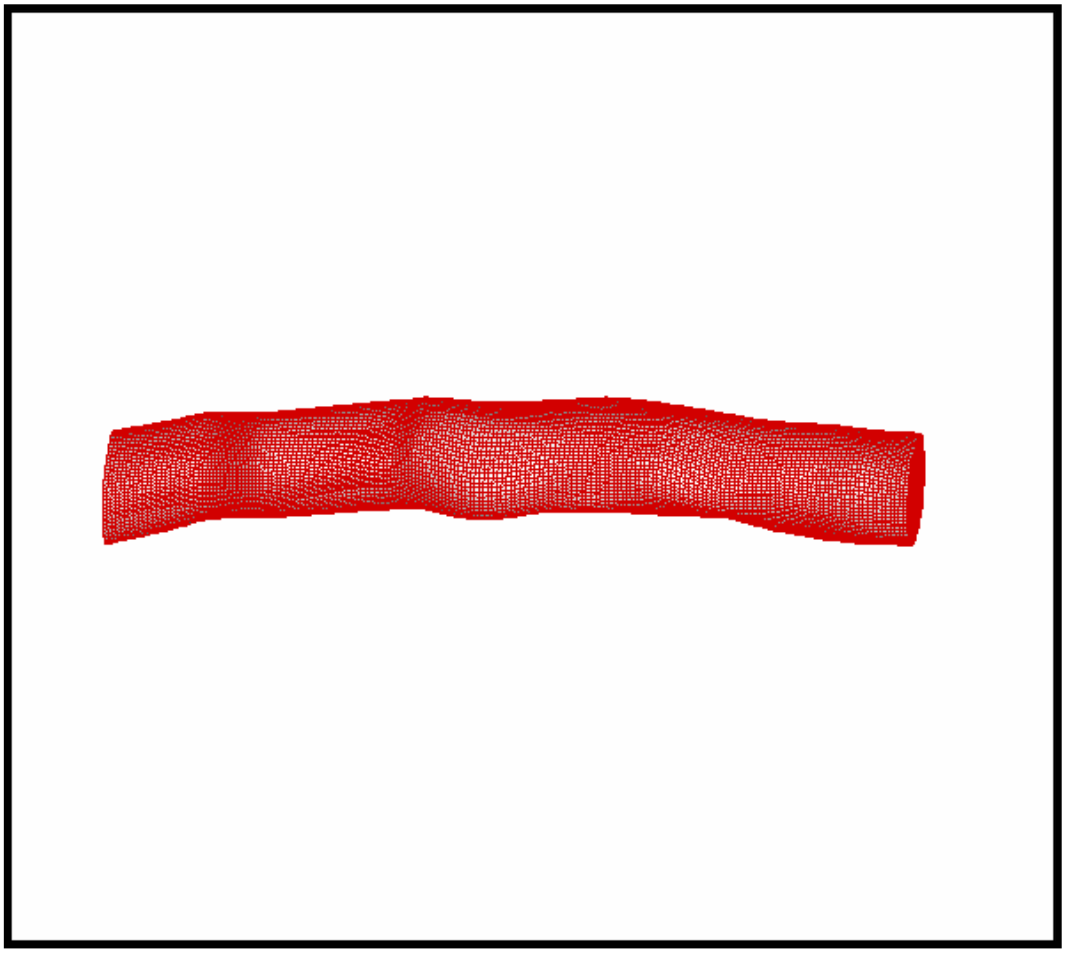

Figure 5.12: Unstretched Control Based on the MRI Image. This computational grid is referred to as the MRI Unstretched Control.

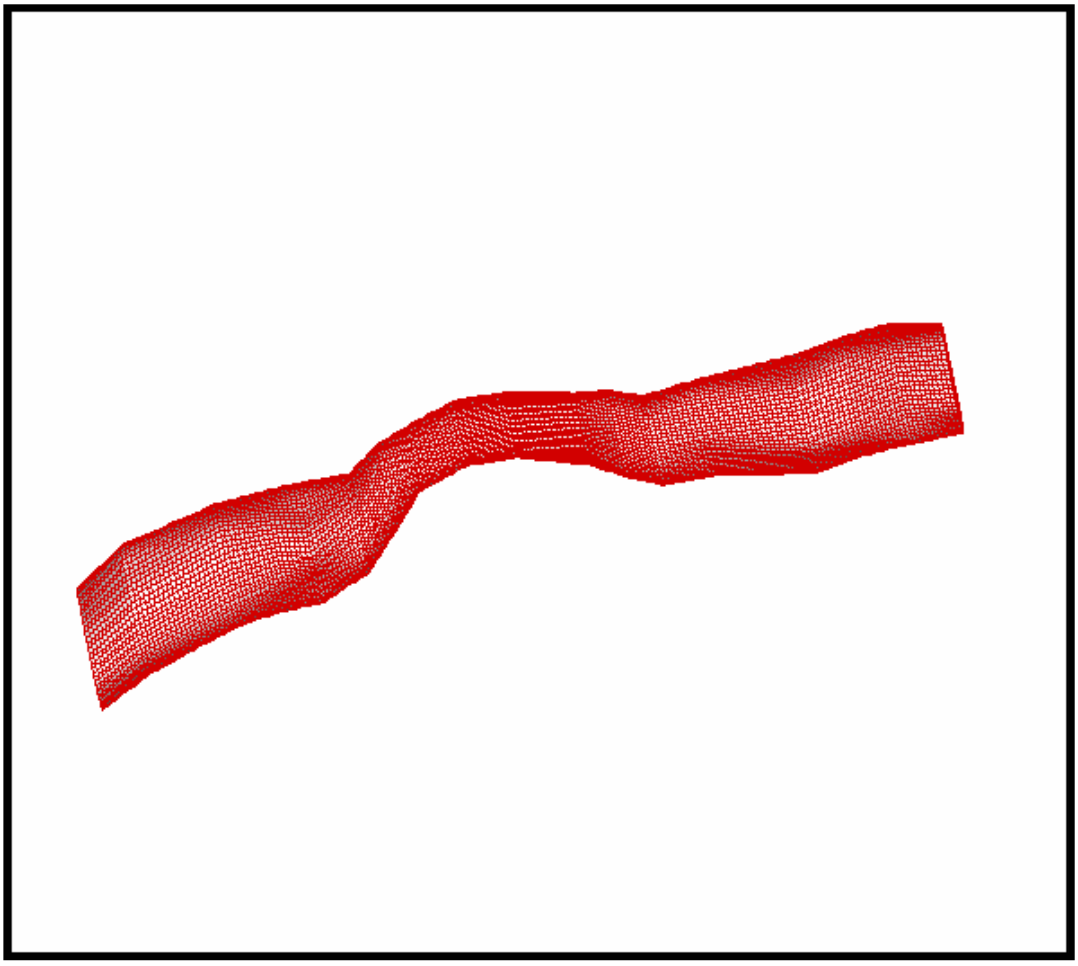

Figure 5.13: Unstretched Stenosis based on the MRI Images. This computational grid is referred to as the MRI Unstretched Stenosis.

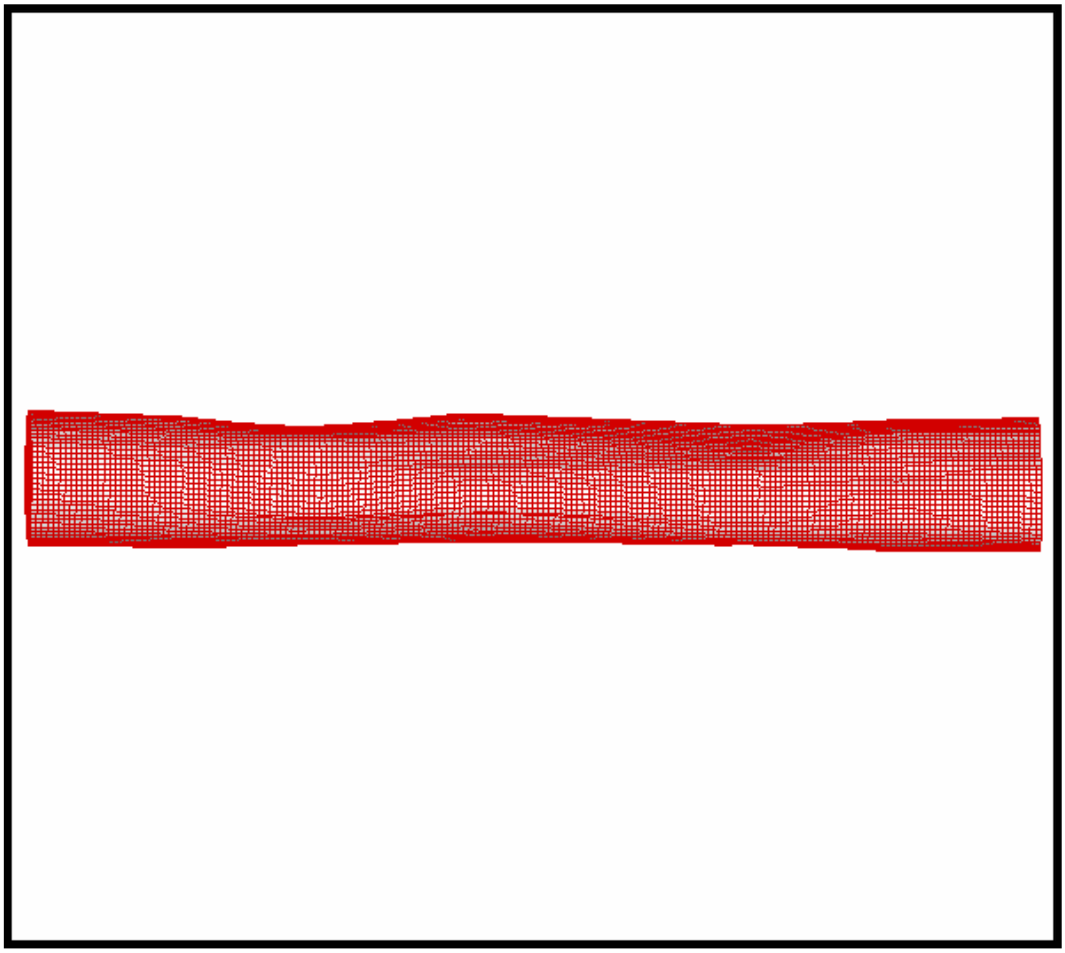

Figure 5.14: Control Based on Histologic Contours and MRI Center Line. The best fit line through the centroids of the MRI control was imposed. This computational grid is referred to as the Histologic Control.

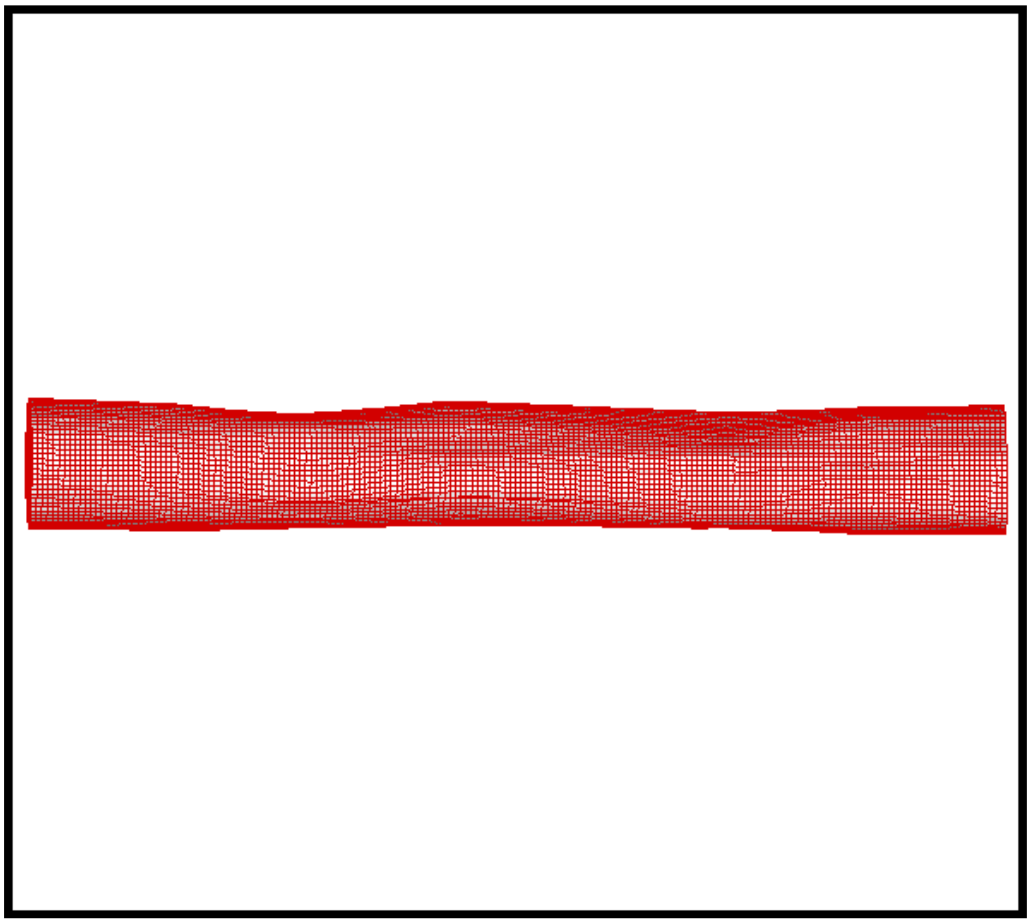

Figure 5.15: Control Based on Histologic Contours and Parallel Z- Axis. This computational grid is referred to as the Flat Histologic Control.

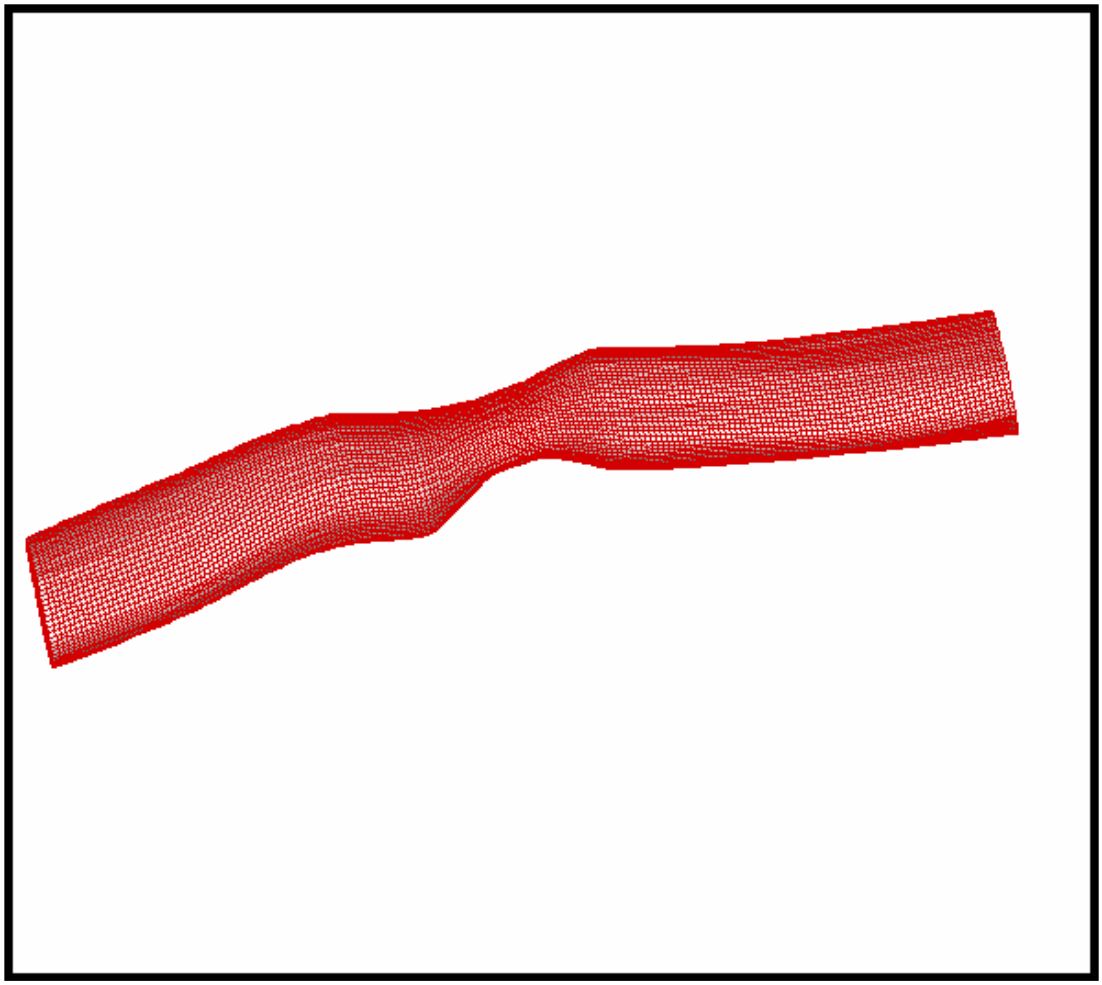

Figure 5.16: Stretched Stenosis Based on Histologic Contours and MRI Center Line. The best-fit line through the centroids of the MRI Stenosis was imposed. This computational grid is referred to as the Histologic Stretched Stenosis.

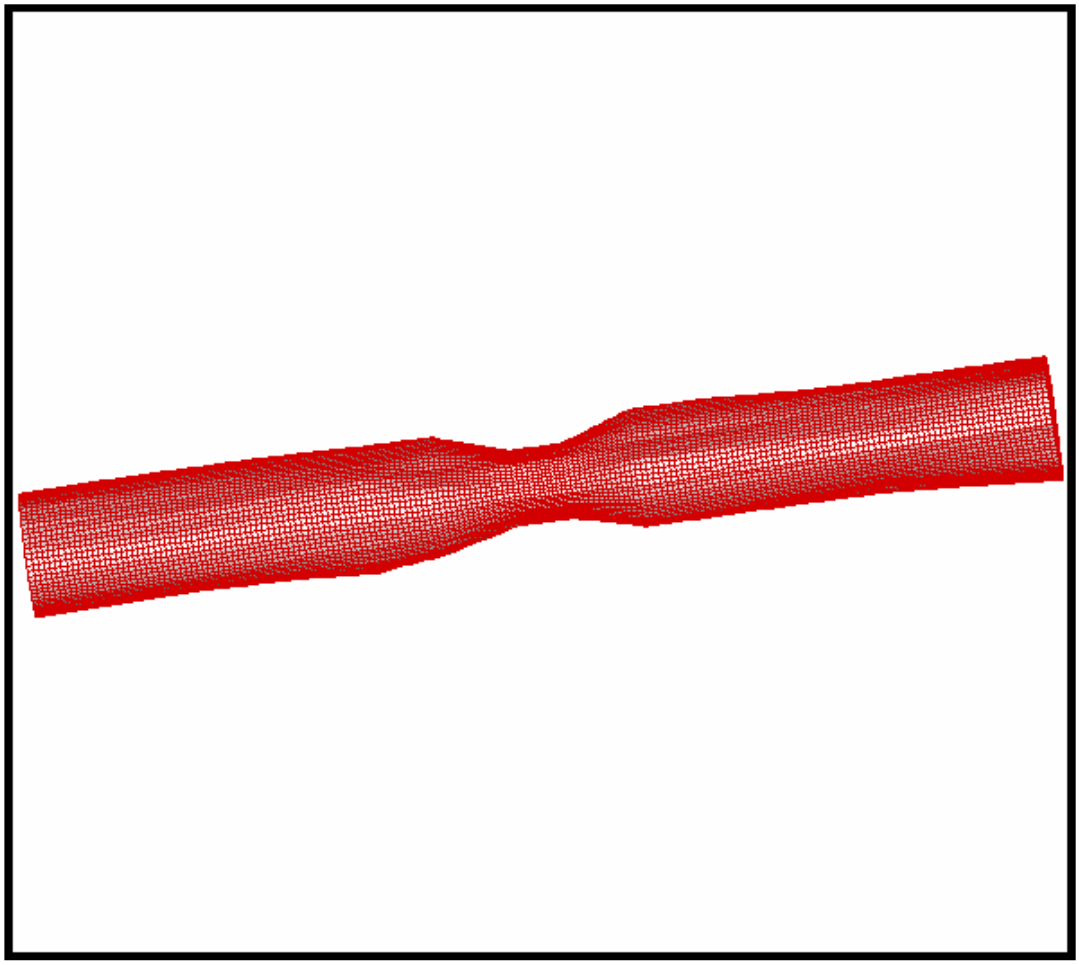

Figure 5.17: Stretched Stenosis Based on Histologic Contours and a Parallel Z-Axis. This computational grid is referred to as the Flat Histologic Stretched Stenosis.

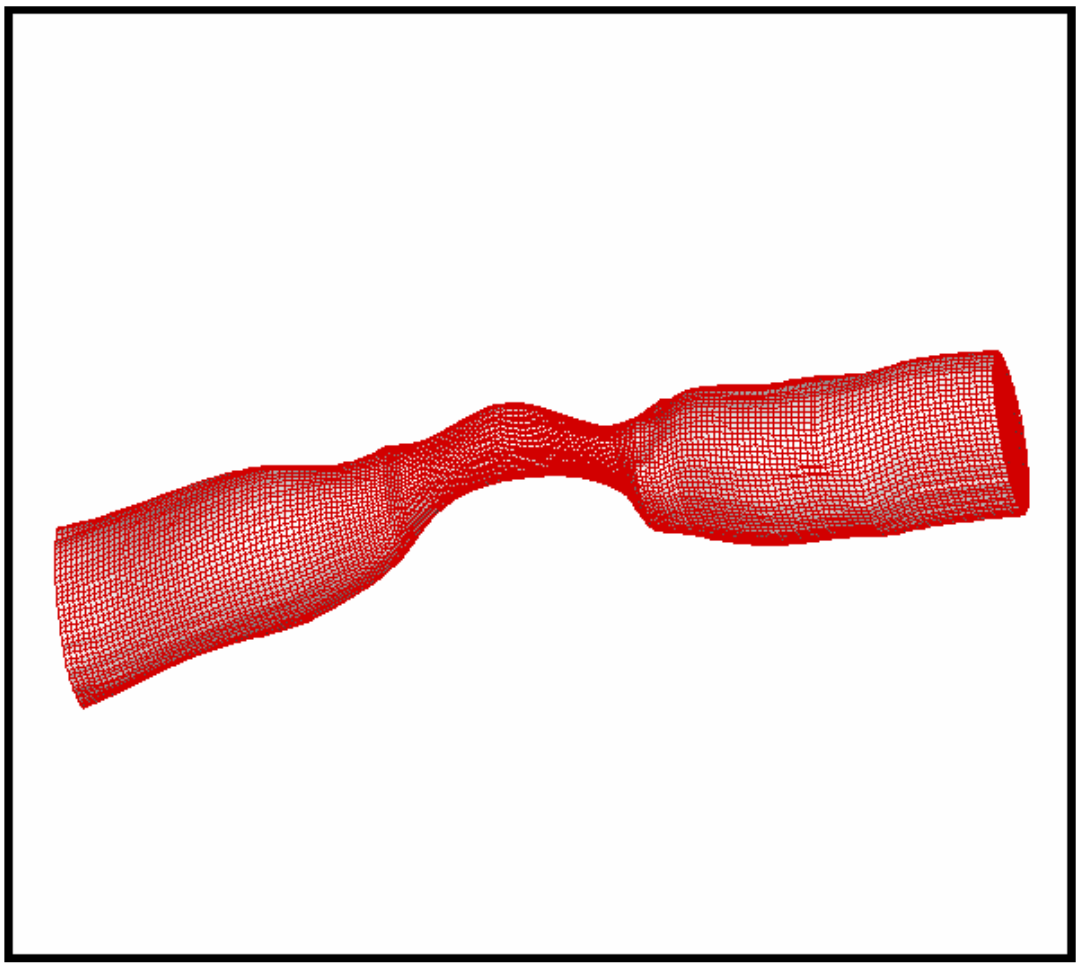

Figure 5.18: Unstretched Stenosis Based on the Histologic Contours and the MRI Center Line. The best fit line through the centroids of the MRI Stenosis was imposed. This computational grid is referred to as the Histologic Unstretched Stenosis.

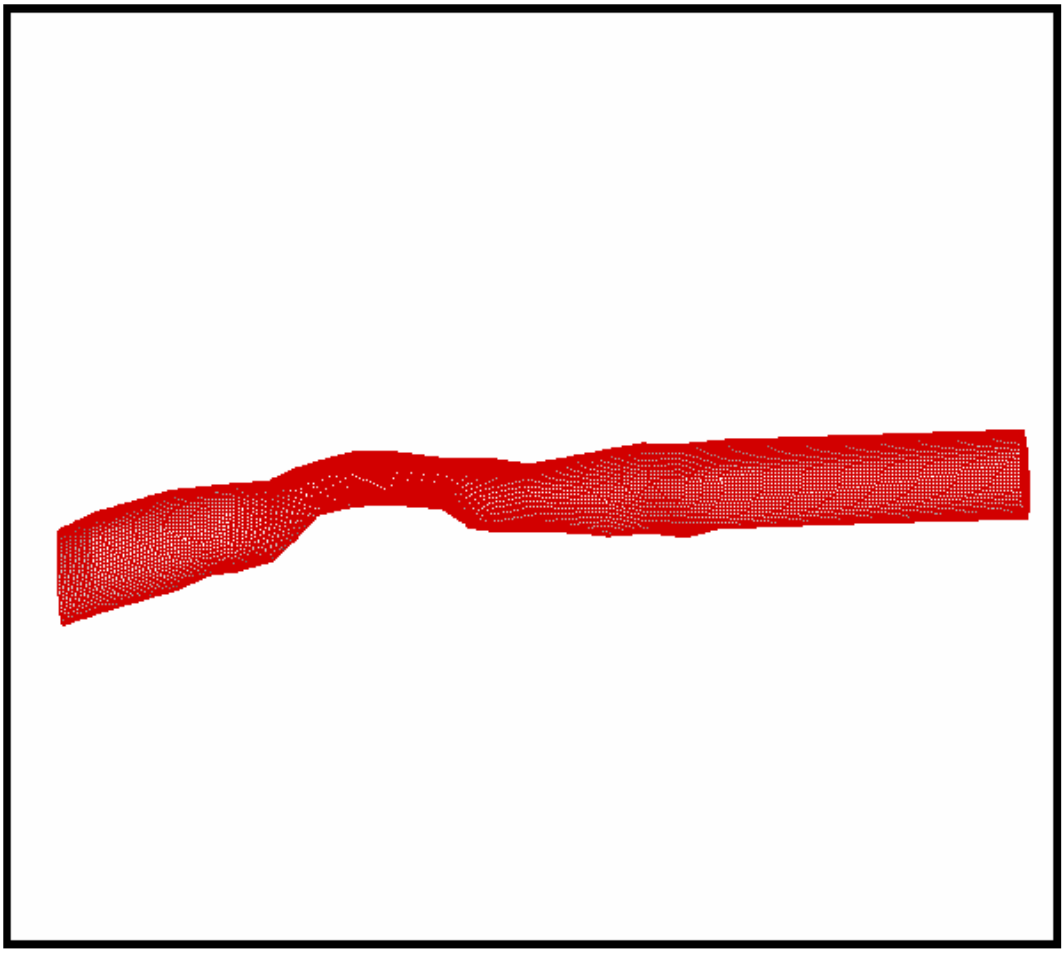

Figure 5.19: Extended Unstretched Stenosis Based on MRI Images.

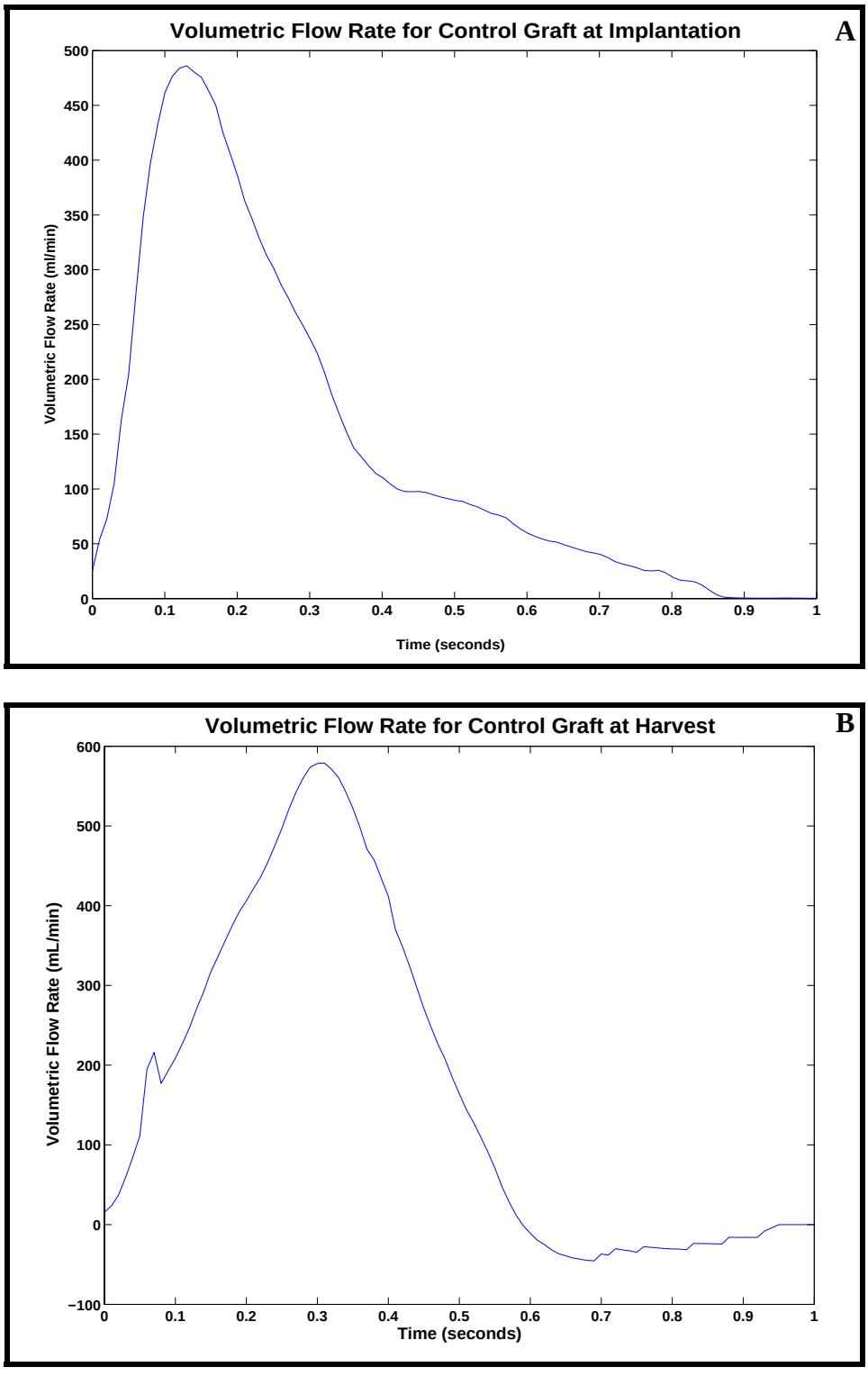

Figure 5.20: Ensemble Averaged Volumetric Flow Rates for the Control Grafts. (A) Implantation (B) Sacrifice.

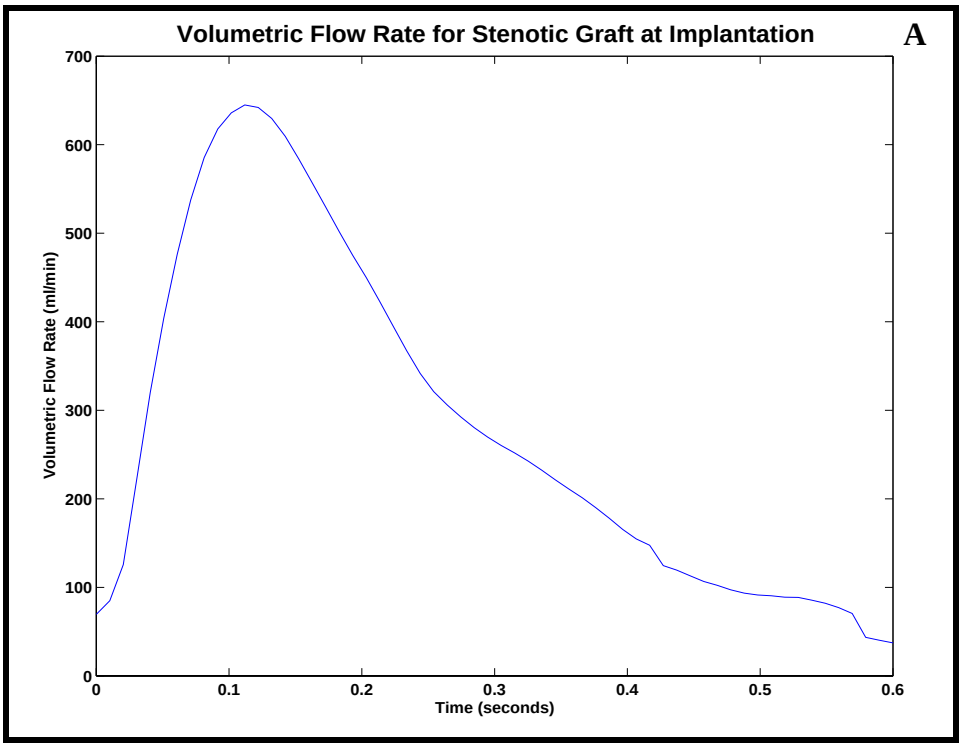

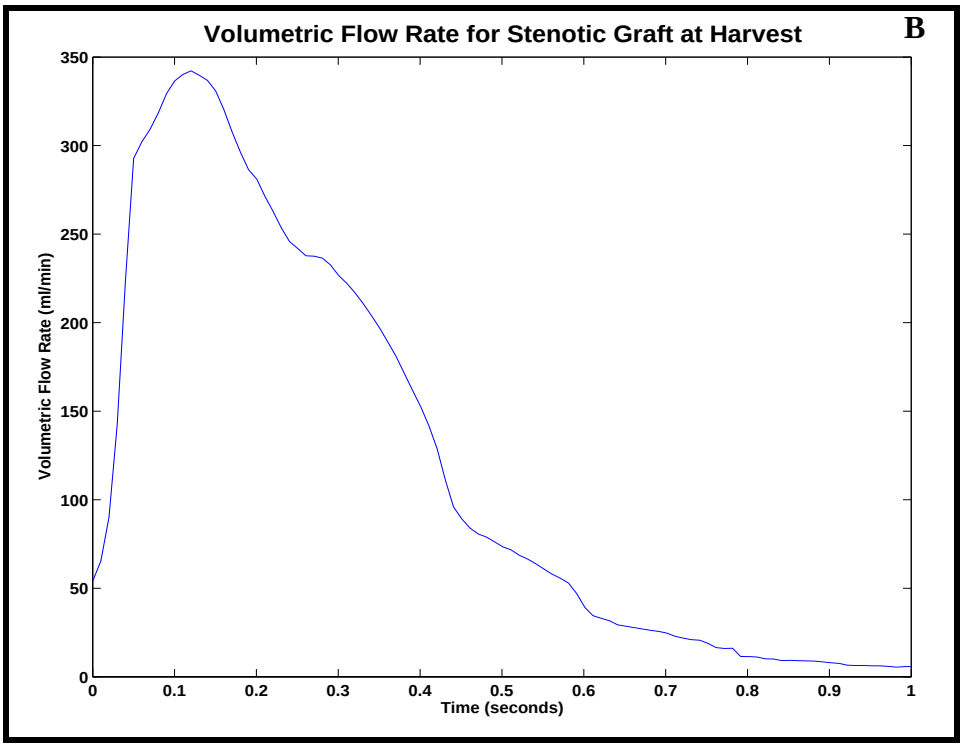

Figure 5.21: Ensemble Averaged Volumetric Flow Rates for the Stenotic Grafts. (**A**) Implantation (**B**) Sacrifice.

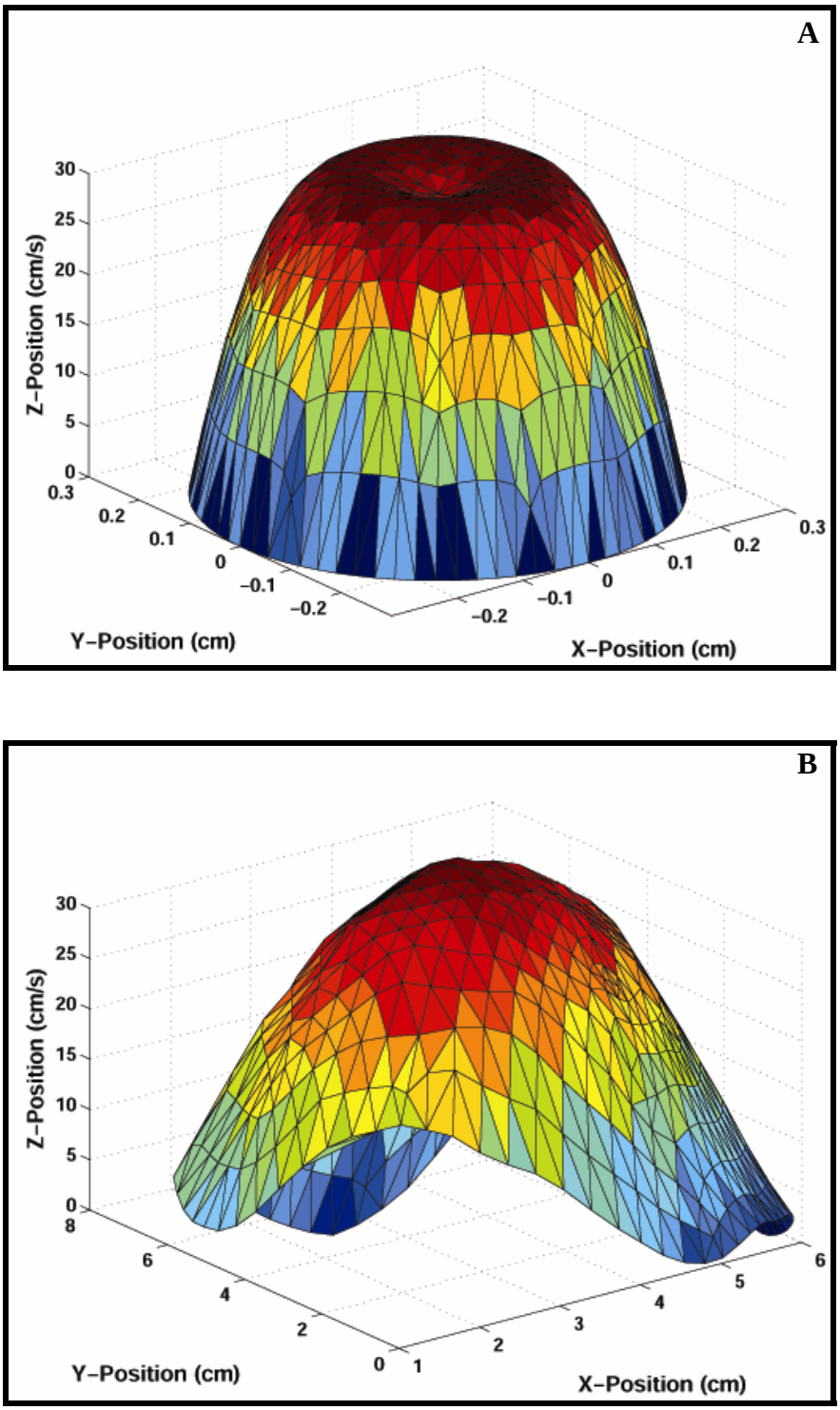

Figure 5.22: Velocity Profiles during Peak Systole at the Inlet for the Ensemble Averaged Volumetric Flow Rates and the PCMRI. (**A**) Ensemble Averaged Volumetric Flow Rates at Harvest (**B**) PCMRI.

along the graft's axial length revolved around 2.75 dynes/cm^2 and the maximum variation was only 3.6 % (Figure 5.23).

Stretched Graft Control Study. The flowfields within the control vessels were solved for conditions both at implantation and at sacrifice. The speed of the ideal stretched harvest control reached as high as 16 cm/sec during peak systole (Figure 5.24). The wall shear stress calculations showed variation depending upon which computational grid was analyzed. During peak systole, the ideal stretched harvest control showed a consistent wall shear stress level of 6 dynes/cm^2 (Figure 5.25). At peak systole, the histologic stretched harvest control experienced wall shear stress levels as high as 13 dynes/cm^2 with the majority of the vessel being exposed to 6.5 dynes/cm^2 (Figure 5.26), while the flat histologic stretched harvest control reached only a maximum of 12 dynes/cm^2 with most of the vessel residing at 6 dynes/cm^2 (Figure 5.27).

The τavg maintained a mean of 2.6 dynes/cm^2 for the ideal stretched harvest control, 4.0 dynes/cm^2 for the histologic stretched implant control, and 2.2 dynes/cm^2 for the flat histologic stretched implant control (Figure 5.28). At sacrifice the τavg leveled at a mean of 3.0 dynes/cm^2 for the ideal stretched harvest control, 4.5 dynes/cm^2 for the histologic stretched harvest control, and 2.8 dynes/cm^2 for the flat histologic stretched harvest control (Figure 5.29). For both implantation and harvest, τavg and intimal thickness were compared.

Stretched Graft Stenotic Study. The stretched stenosis studies were analyzed. Within the histologic stretched harvest stenosis, the speed reached a 30 cm/sec during peak systole (Figure 5.30). Very little local reversal of occurred during systole (Figure 5.31); however, transient flow separation was observed during diastole (Figure 5.32).

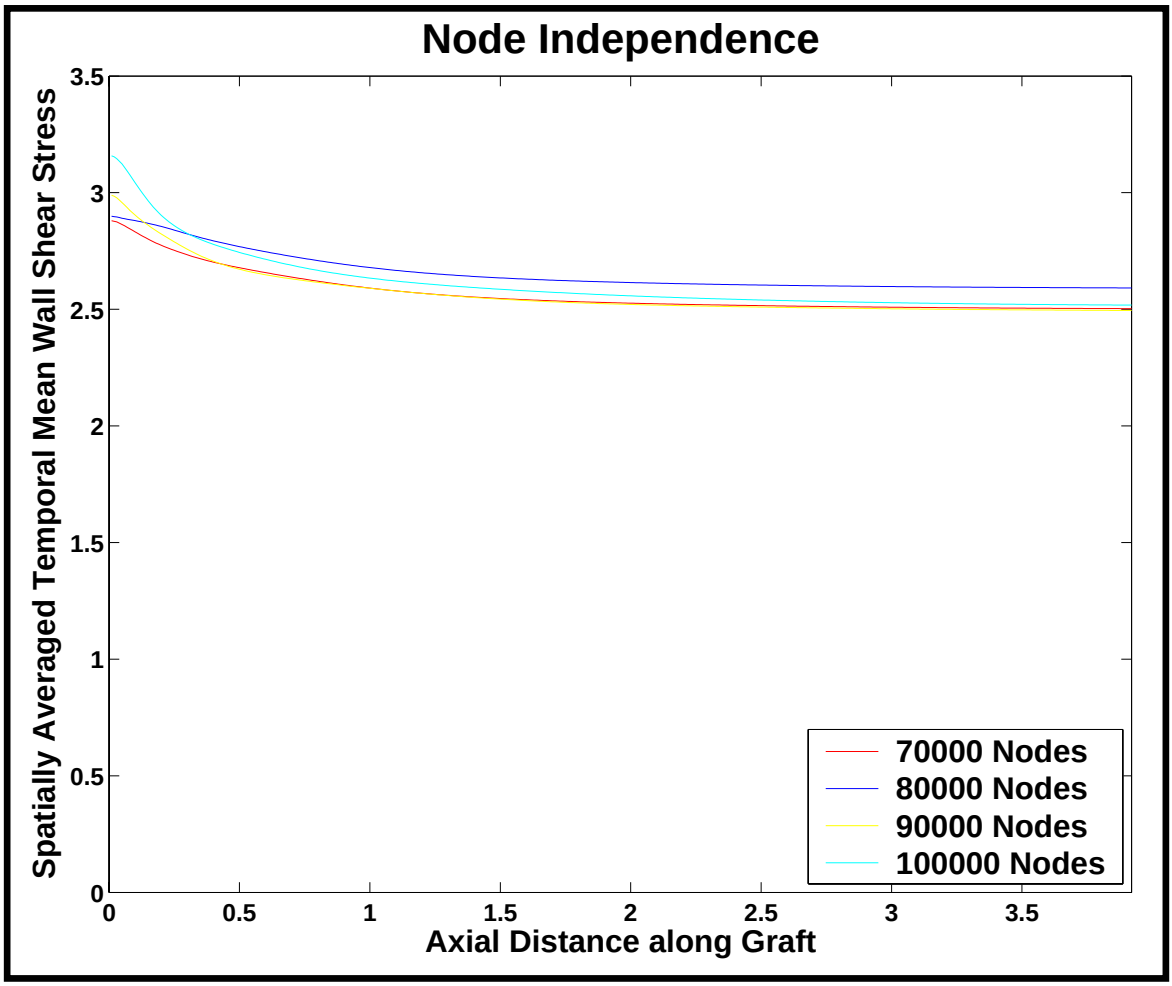

Figure 5.23: Node Independence Study for the Ideal Control Grafts with Varying Number of Nodes

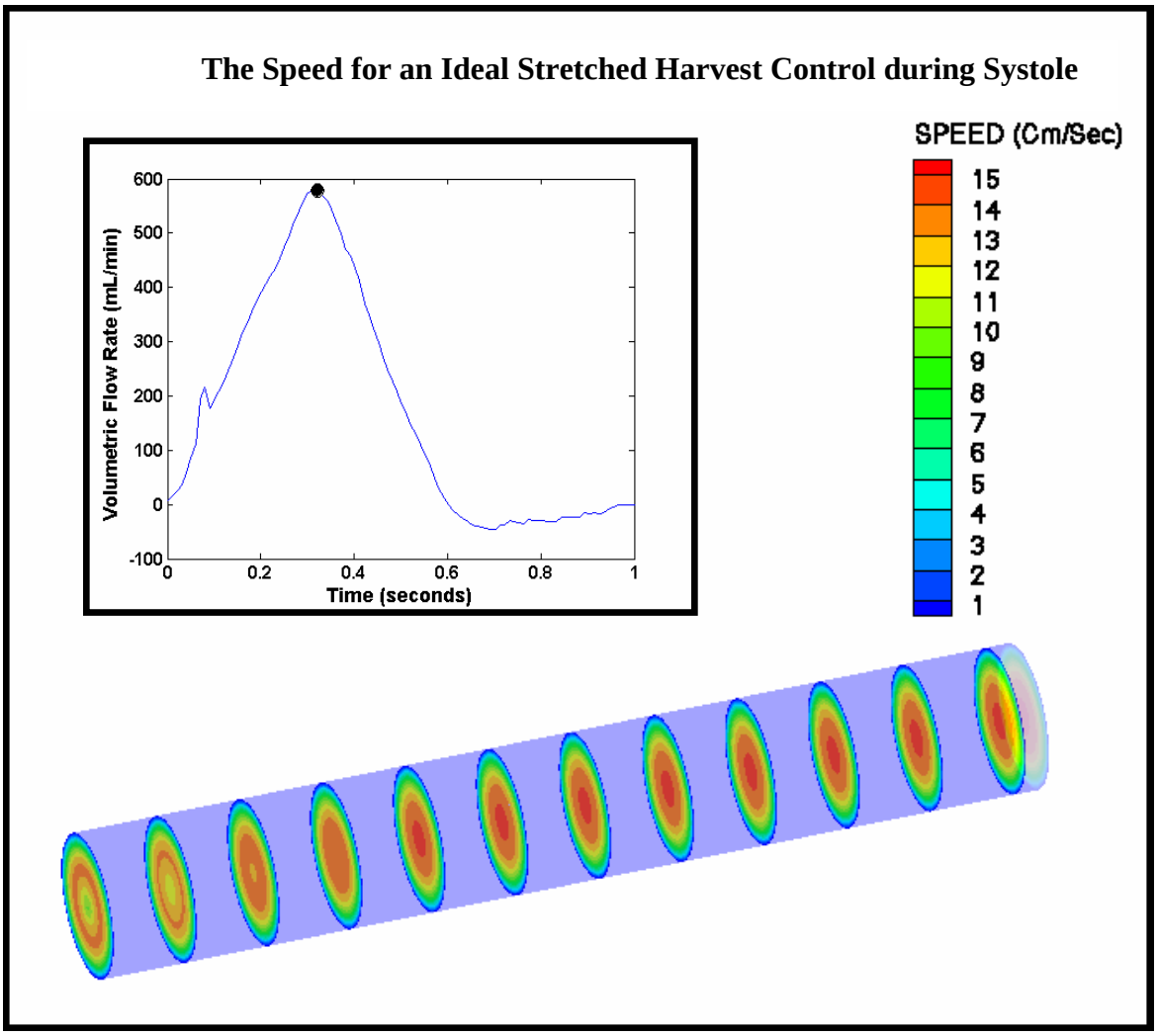

Figure 5.24: The Speed for an Ideal Stretched Harvest Control during Systole.

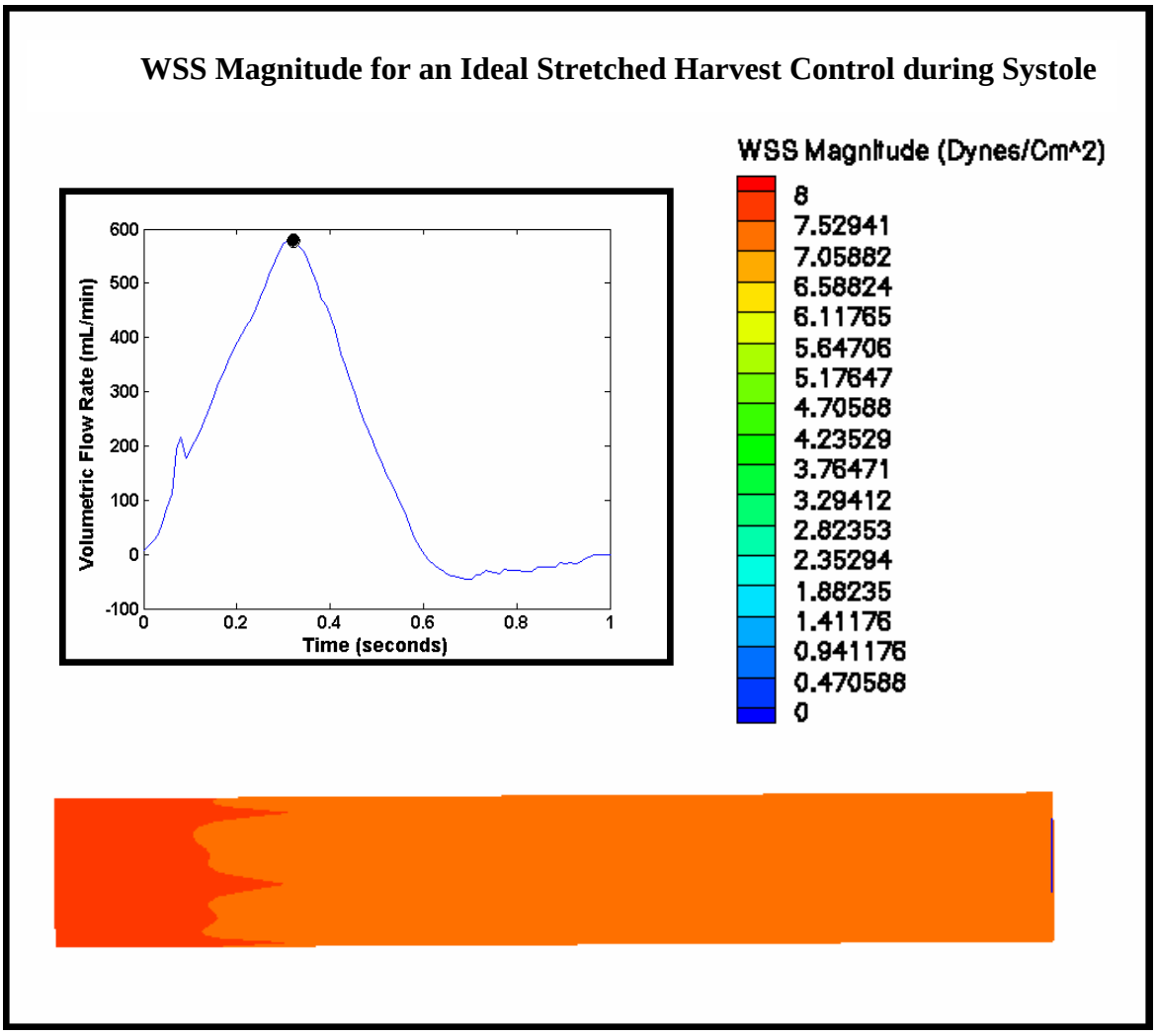

Figure 5.25: Wall Shear Stress Magnitude for an Ideal Stretched Harvest Control during Systole.

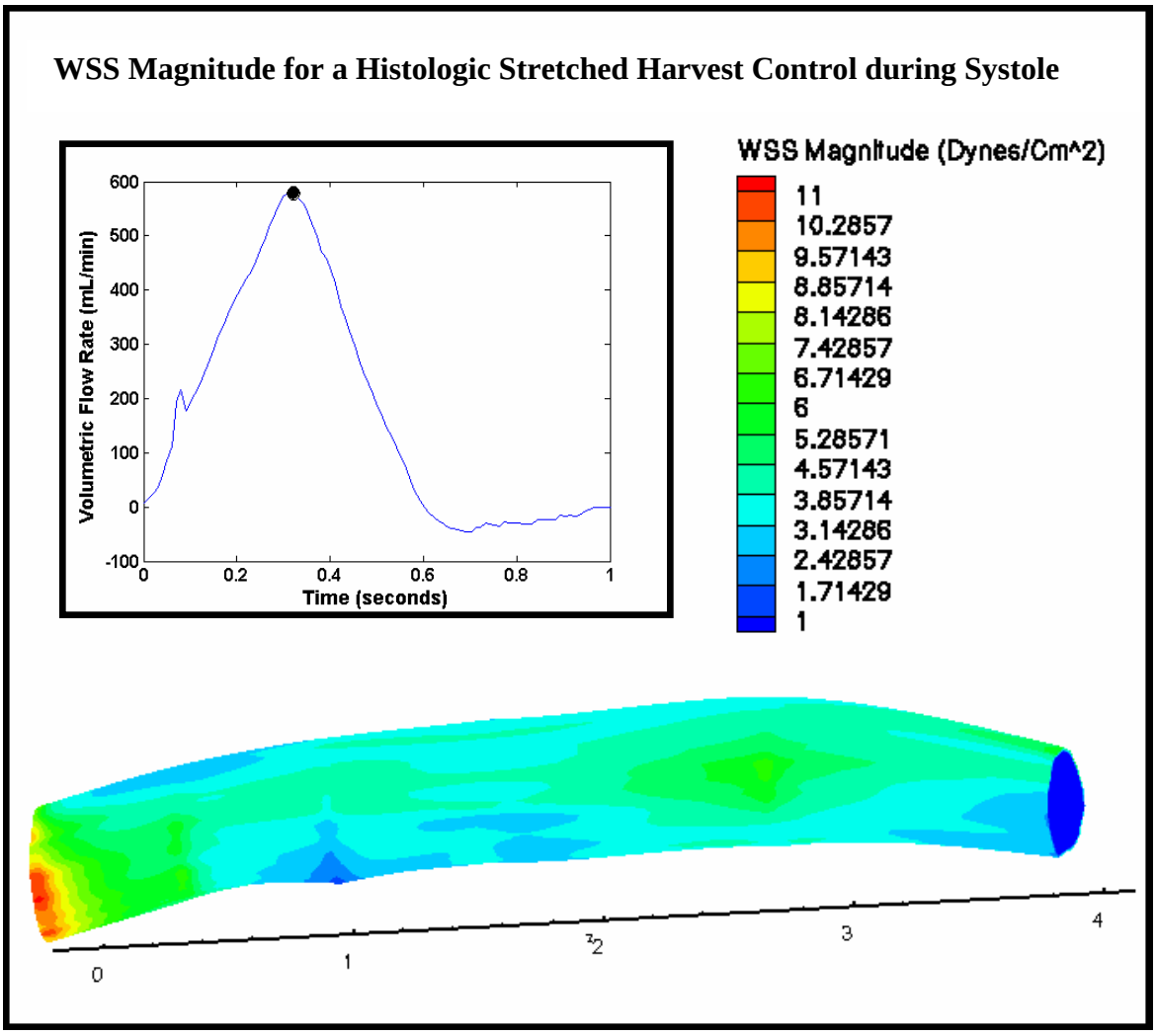

Figure 5.26: Wall Shear Stress Magnitude for a Histologic Stretched Harvest Control during Systole. This computational grid was constructed from the histologic contours and imposed upon a best-fit line running through the centroids of a later analyzed series of MRI Images.

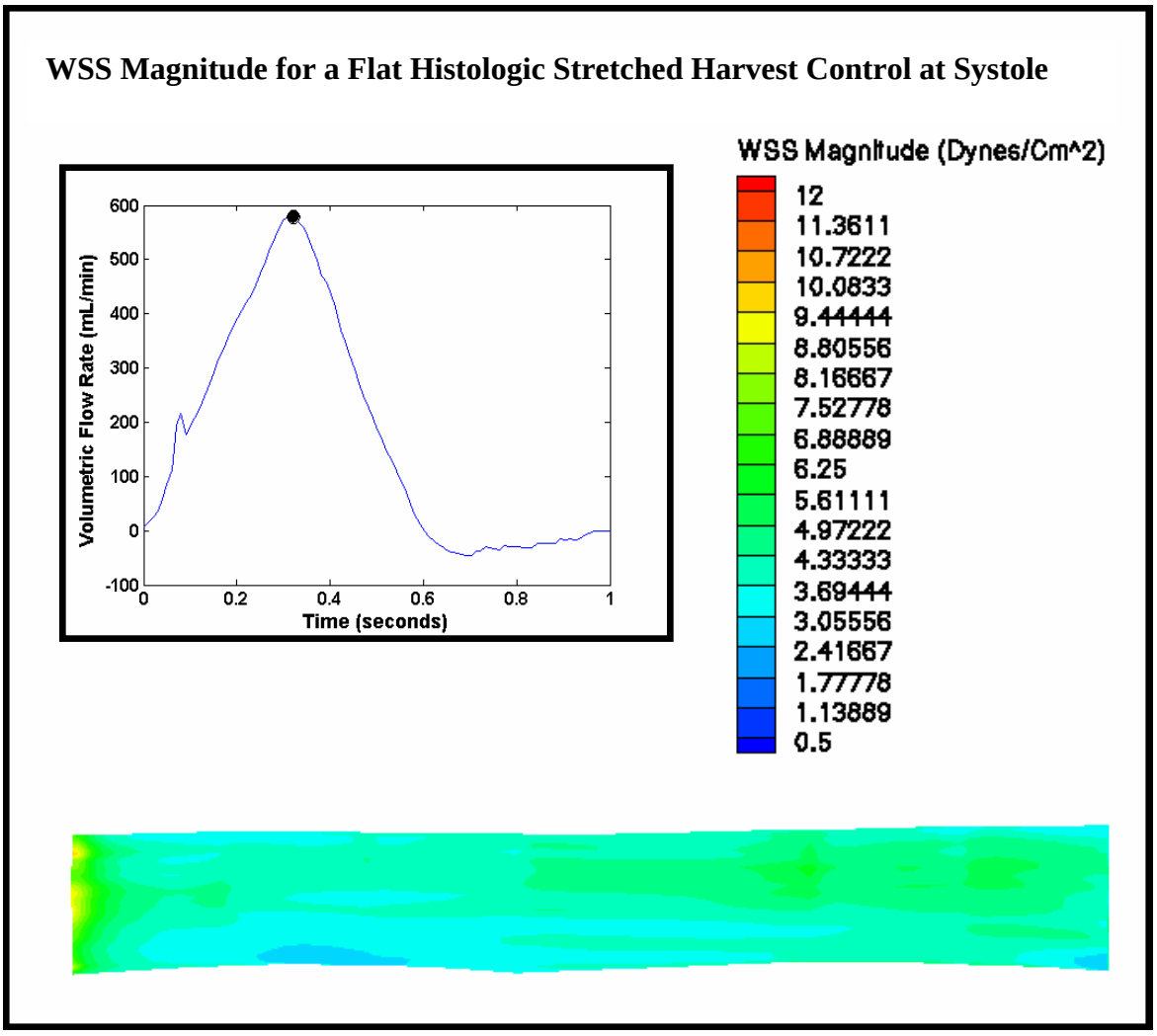

Figure 5.27: Wall Shear Stress Magnitude for a Flat Histologic Stretched Harvest Control during Systole. This computational grid was constructed from the histologic contours and imposed upon a flat z-plane running along the length of the vessel.

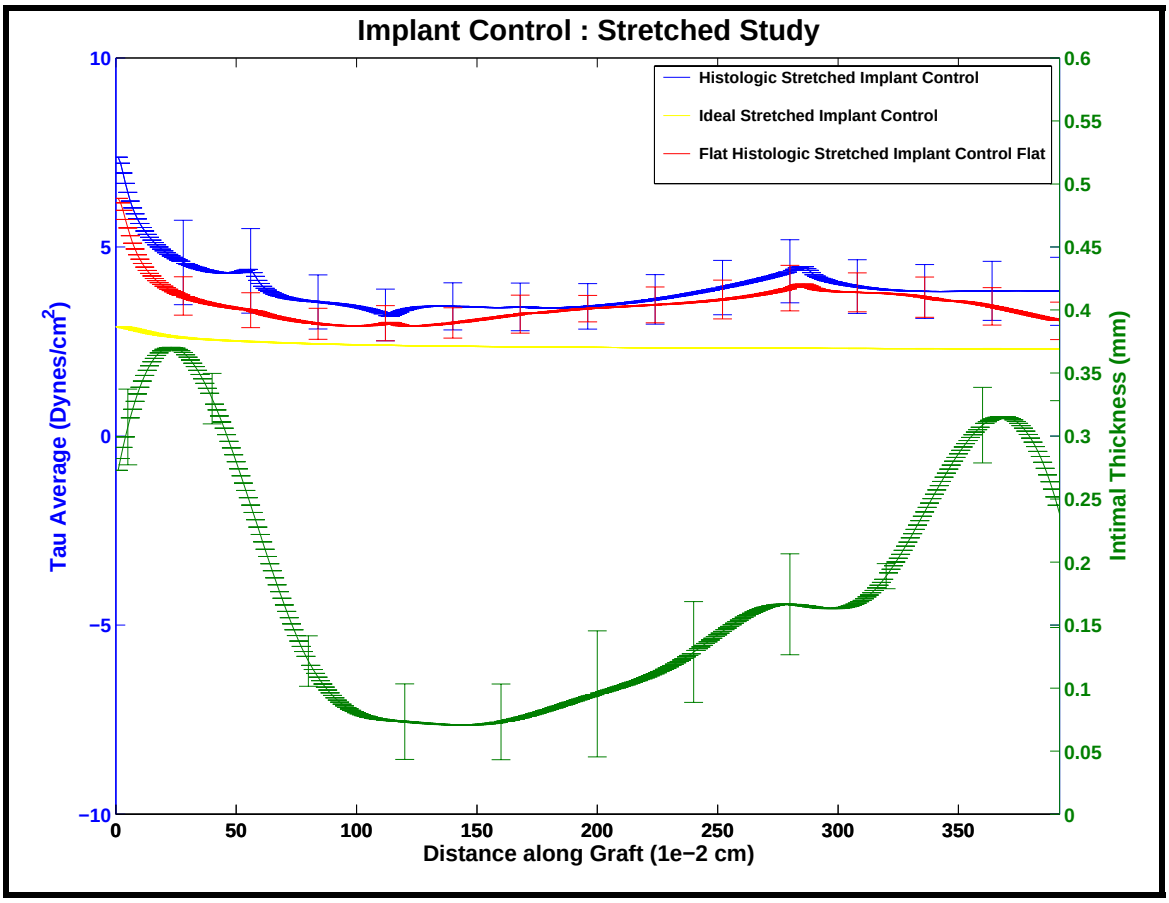

Figure 5.28: τavg and Intimal Thickness for Stretched Implant Controls along the Axial Length of the Grafts.

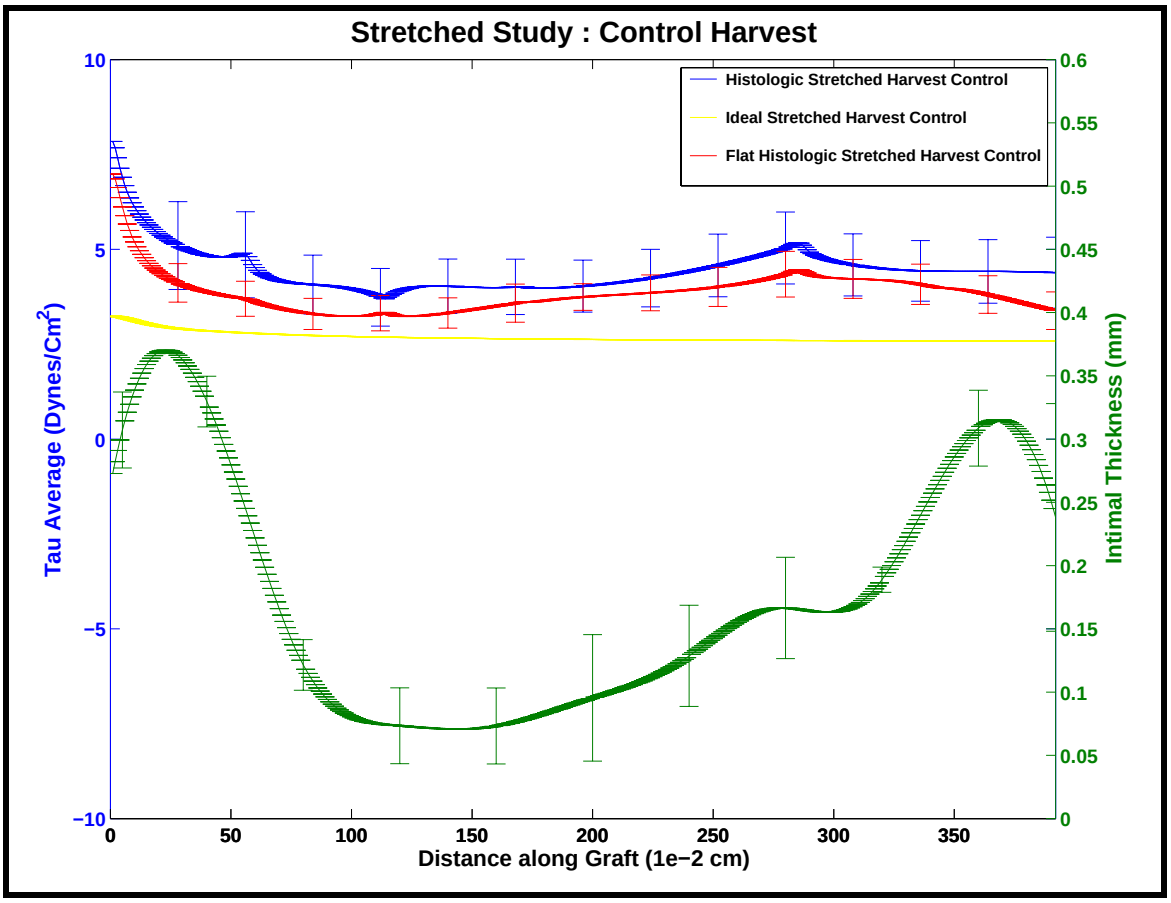

Figure 5.29: τavg and Intimal Thickness for Stretched Harvest Controls along the Axial Length of the Grafts.

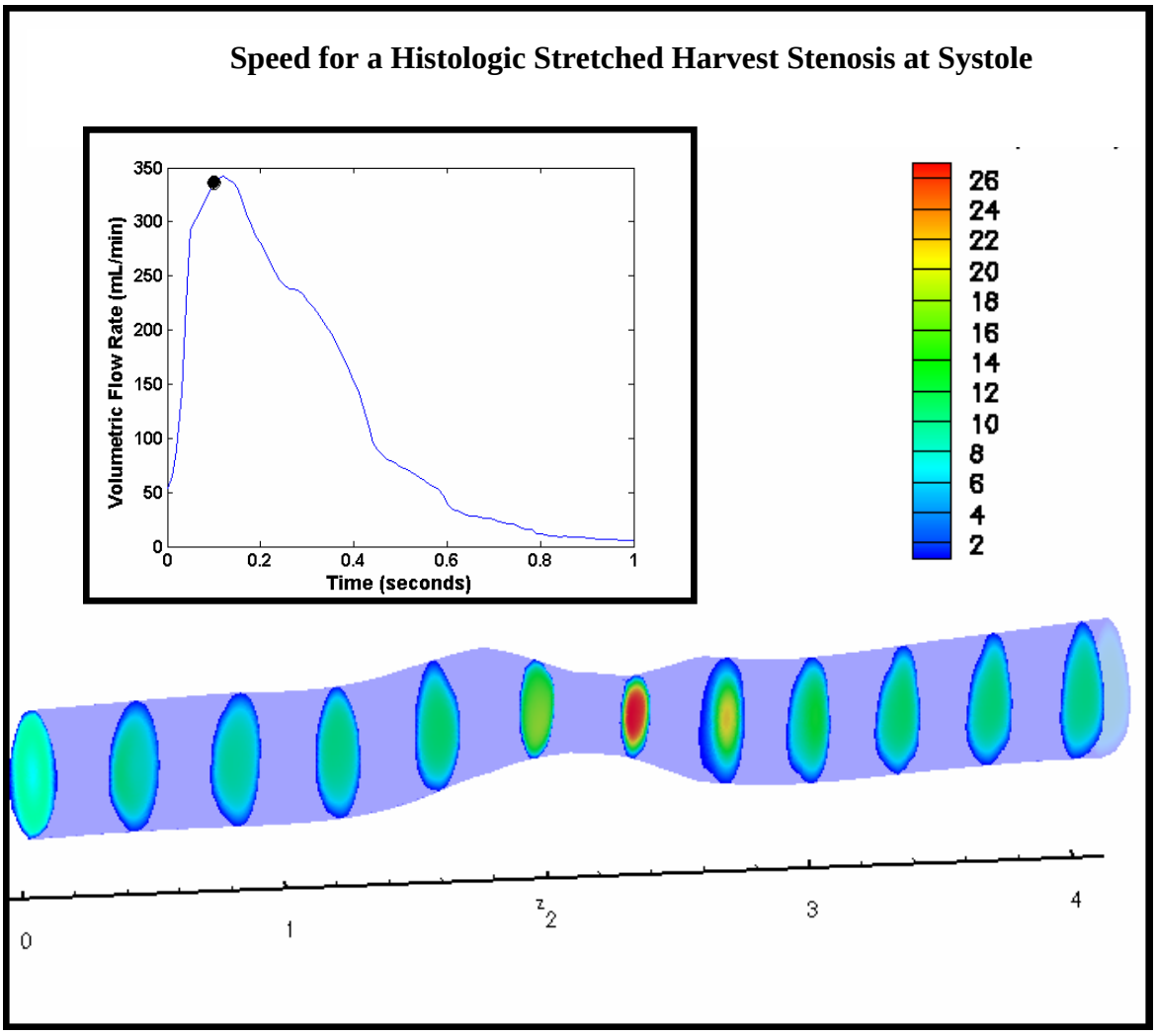

Figure 5.30: Speed for a Histologic Stretched Harvest Stenosis at Systole.

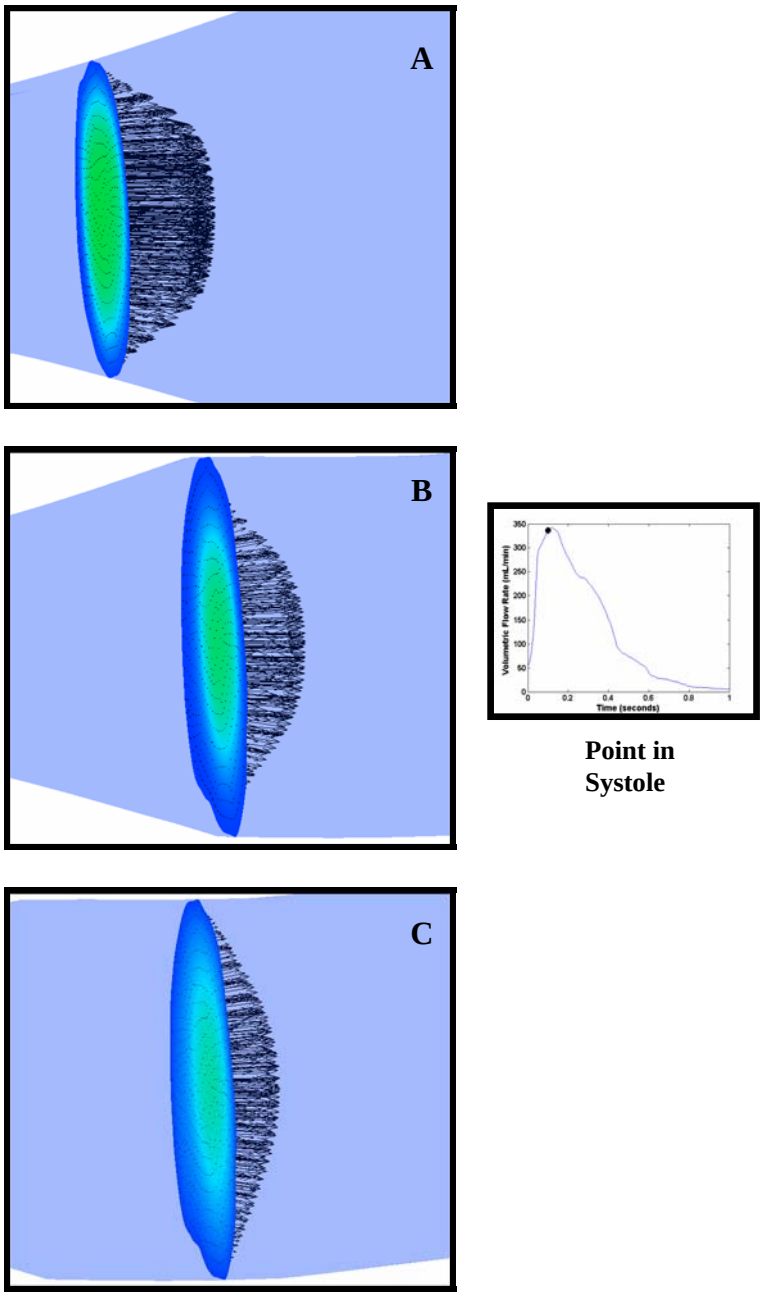

Figure 5.31: Axial Velocity Vectors near Peak Systole for the Histologic Stretched Stenosis. The images depict the axial velocity vectors at defined distances from the proximal anastomosis (**A**) 2.2 cm (**B**) 2.4 cm (**C**) 2.6 cm. Note the absence of transient flow separation post-stenotically.

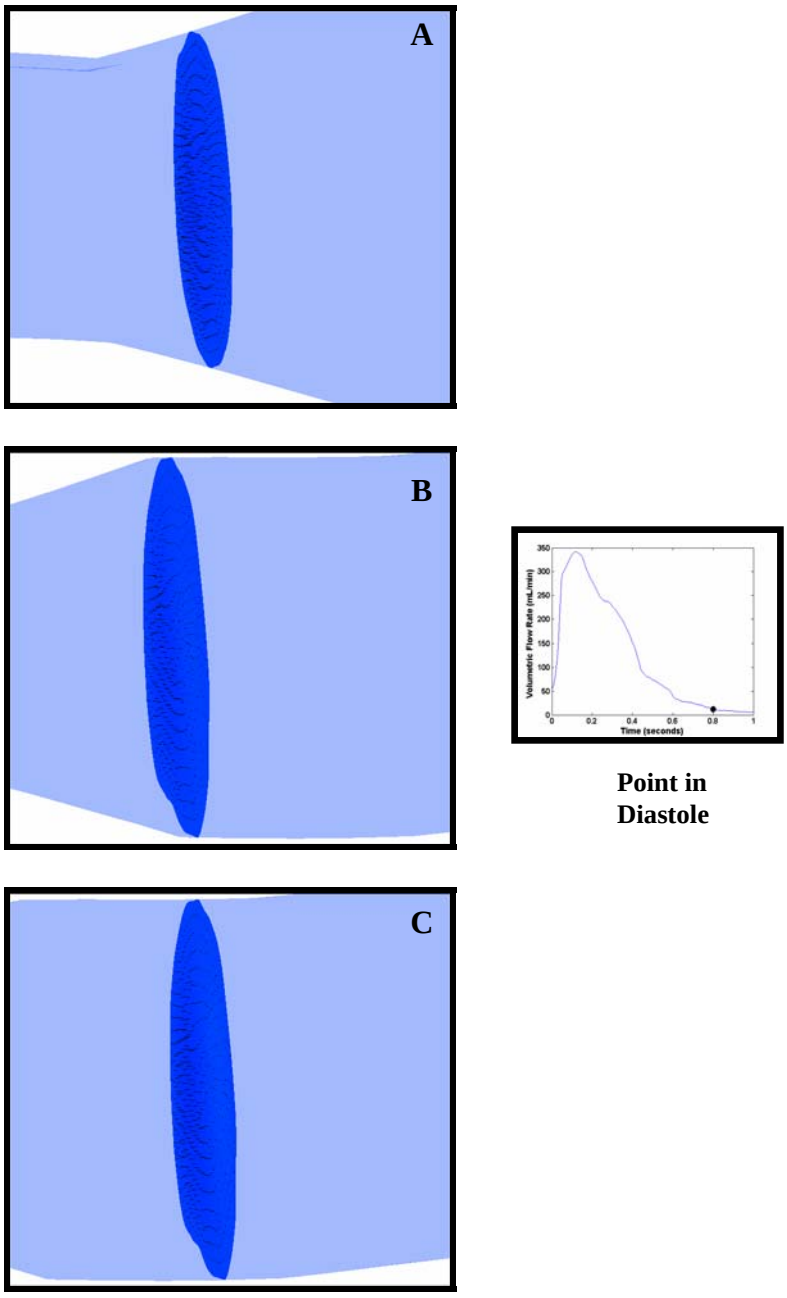

Figure 5.32: Axial Velocity Vectors during Diastole for the Histologic Stretched Stenosis. The images depict the axial velocity vectors at defined distances from the proximal anastomosis (A) 2.2 cm (B) 2.4 cm (C) 2.6 cm. The velocity vectors oriented in a retrograde direction highlight the transient flow separation post-stenotically.

The oscillatory shear index (OSI) quantified the flow reversal. For both at implantation and at sacrifice, the elevated OSI numbers reflected the post-stenotic local reversal of flow (Figures 5.33, 5.34).

The wall shear stress magnitude was investigated for the stretched stenotic vessels. During mid-diastole, the ideal stretched stenosis experienced WSS values of 2 dynes/cm^2 in the stenotic throat (Figure 5.35), while during peak systole this value increased to 100 dynes/cm^2 (Figure 5.37). In the upstream and downstream portions of the graft, the WSS levels maintained near 4 dynes/cm^2. During peak systole, the speed in the stenotic throat reached a maximum of 45 cm/sec (Figure 5.36). In the histologic stretched harvest stenosis, the throat evolved WSS values of 1.2 dynes/cm^2 during mid-diastole (Figure 5.38) and of 45 dynes/cm^2 during peak systole (Figure 5.39). Post-stenotically, the vessel experienced higher wall shear stress levels on it anterior surface. For the flat histologic stretched stenosis, WSS values of 1.5 dynes/cm^2 were observed within the stenotic throat during diastole (Figure 5.40) and as large as 47 dynes/cm^2 during systole (Figure 5.41). Upstream and downstream of the stenosis, the WSS values leveled near 7-8 dynes/cm^2.

The τavg reached a peak of 63 dynes/cm^2 for the ideal stretched implant stenosis, 50 dynes/cm^2 for the histologic stretched implant stenosis, and 50 dynes/cm^2 for the flat histologic stretched implant stenosis (Figure 5.42). At sacrifice the τavg peaked within the stenotic throat at 24 dynes/cm^2 for the ideal stretched harvest stenosis, 18 dynes/cm^2 for the histologic stretched harvest stenosis, and 18 dynes/cm^2 for the flat histologic stretched harvest stenosis (Figure 5.44). For both implantation and harvest, τavg and intimal thickness were compared. Within the stenotic throat, high levels of Pulse WSS

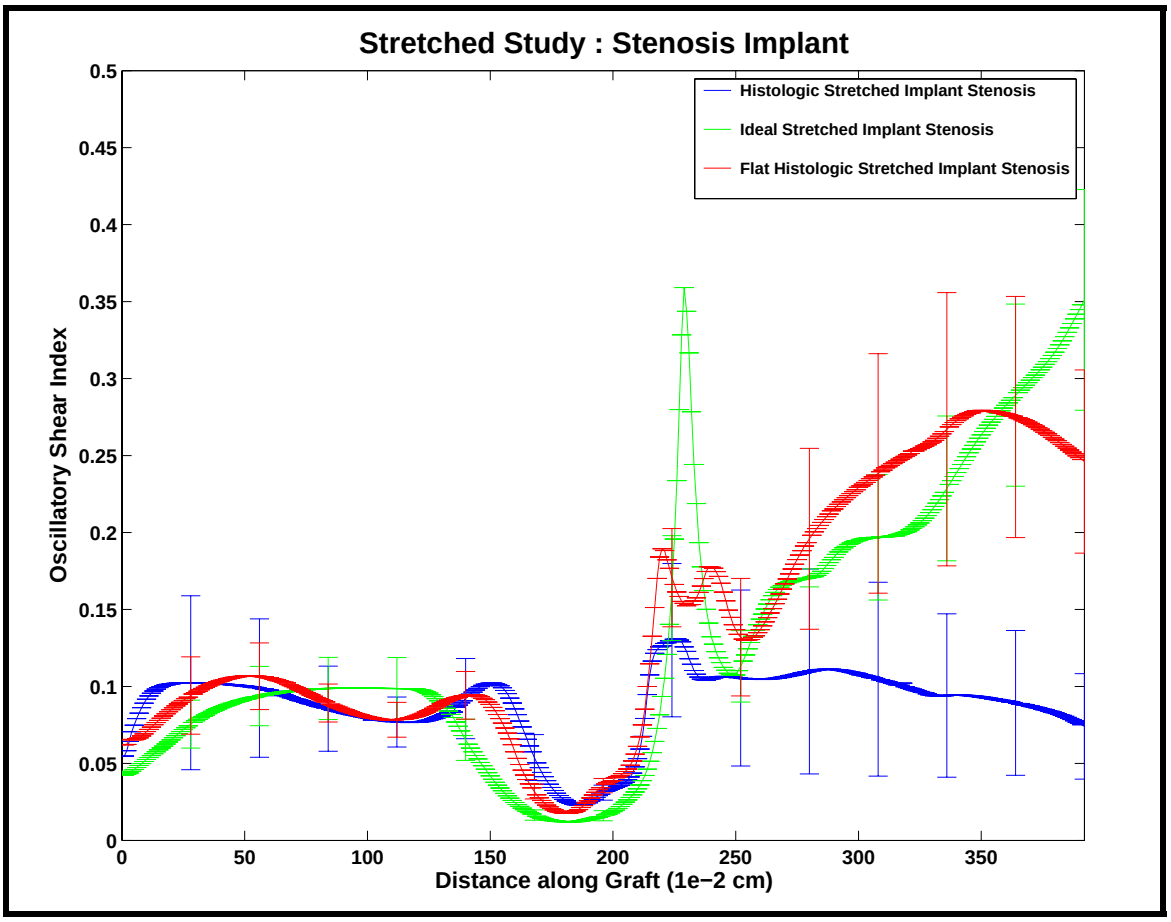

Figure 5.33: Oscillatory Shear Index for Stretched Implant Stenotic Grafts. Observe the transient flow separation post-stenotically.

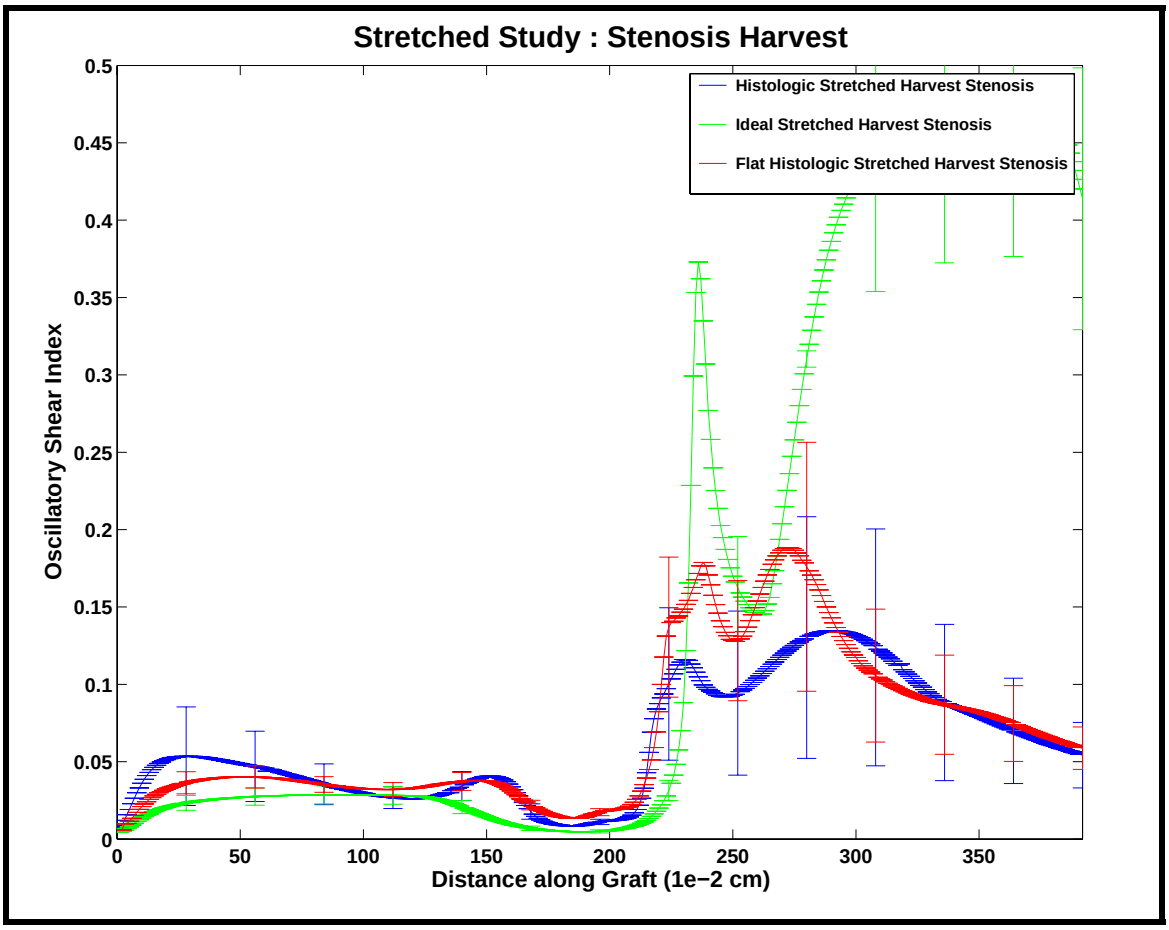

Figure 5.34: Oscillatory Shear Index for Stretched Harvest Stenotic Grafts. Observe the transient flow separation post-stenotically.

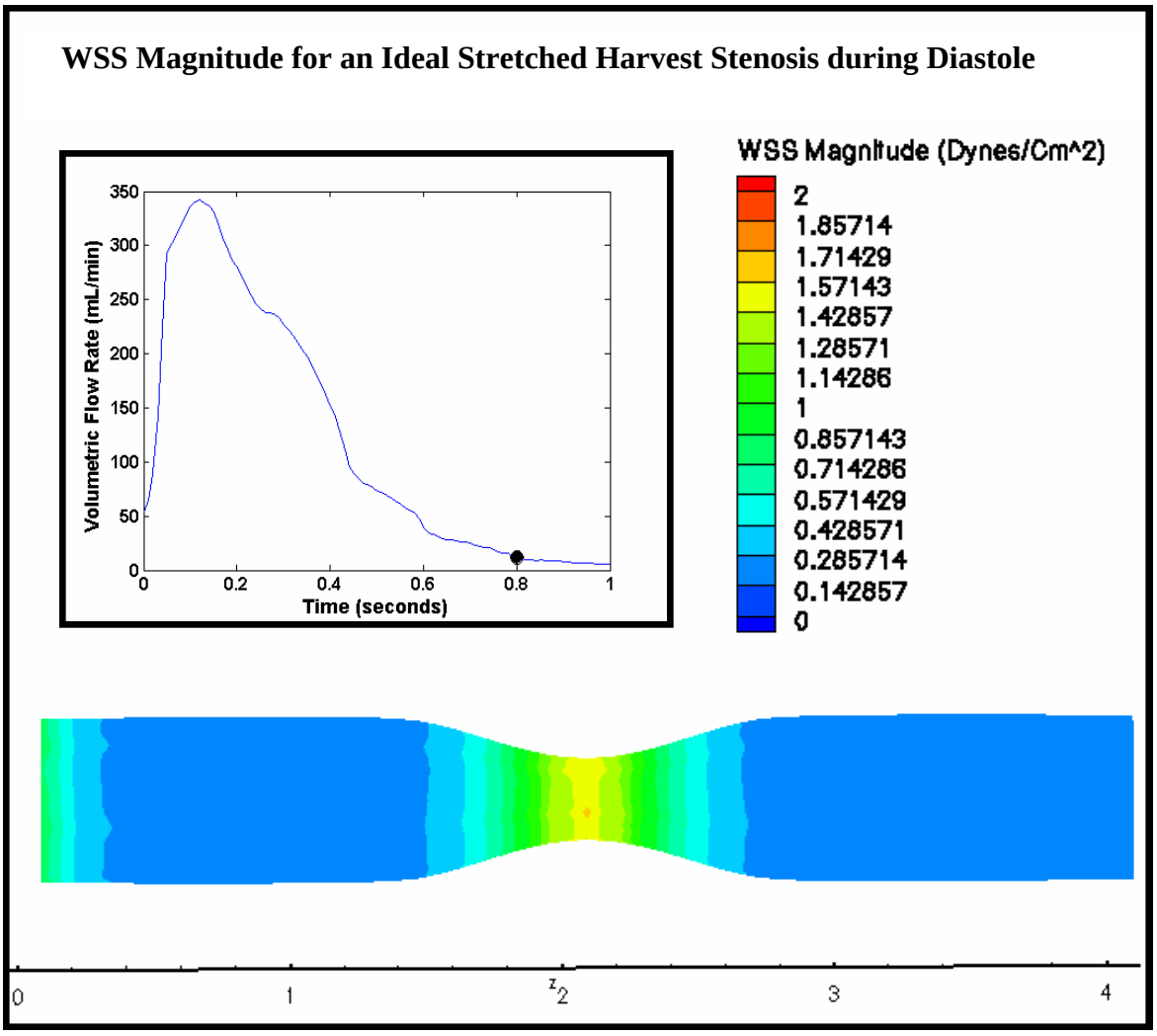

Figure 5.35: WSS Magnitude for an Ideal Stretched Harvest Stenosis during Diastole.

The WSS reaches as high as 2 Dynes/Cm^2 within the stenotic throat.

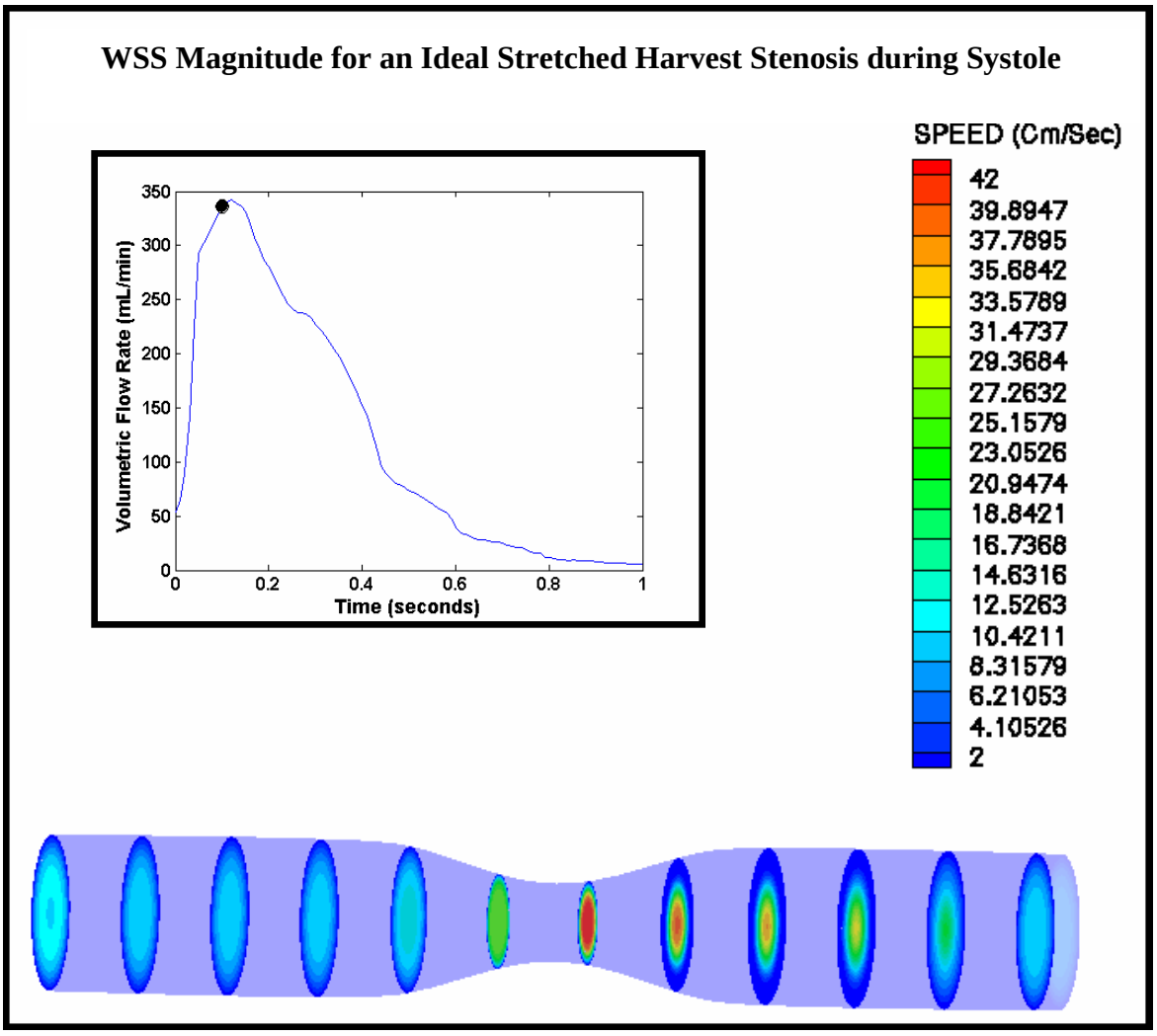

Figure 5.36: Speed for an Ideal Stretched Harvest Stenosis during Systole. Within the stenotic throat, the speed exceeds 45 cm/sec.

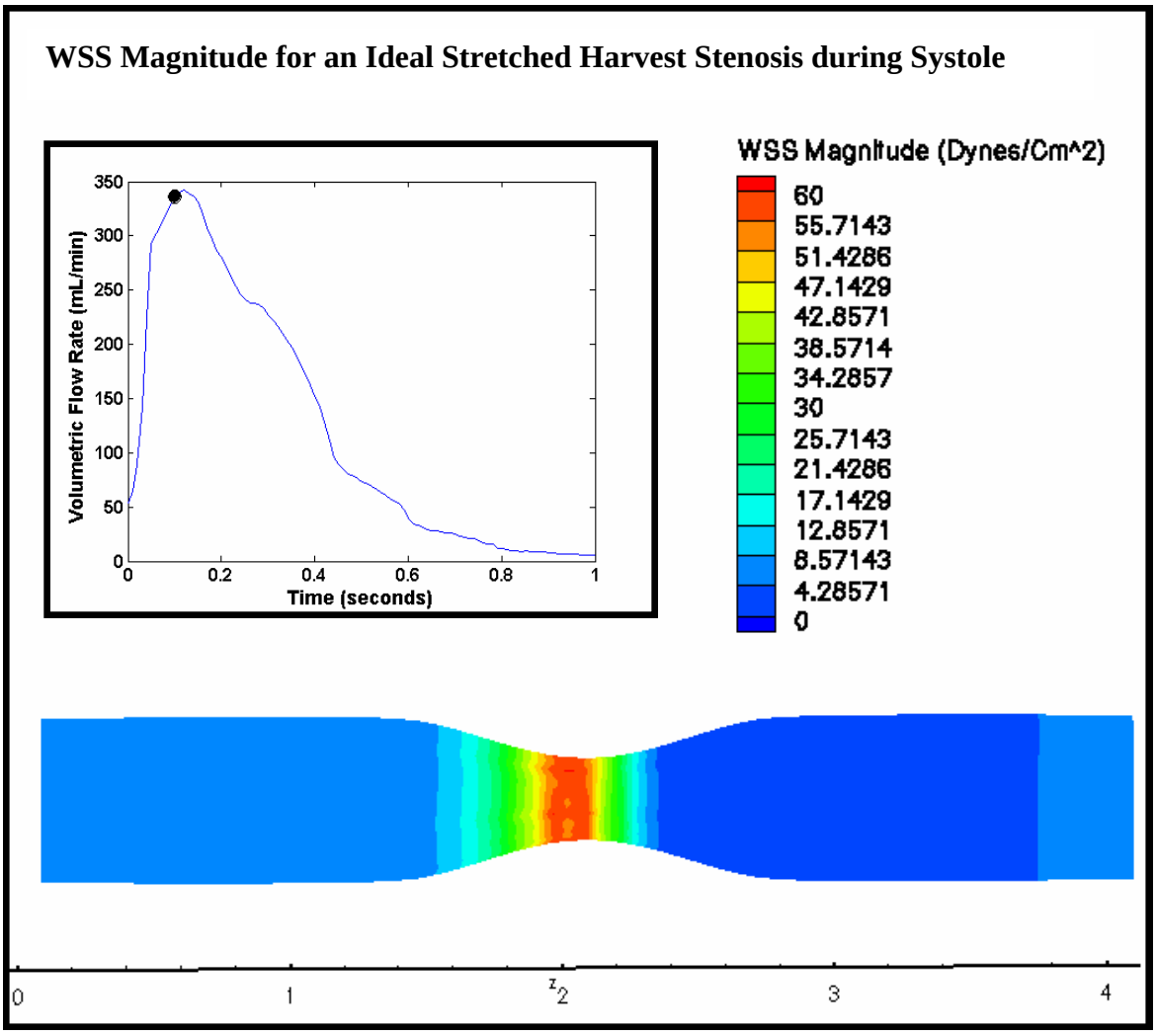

Figure 5.37: Wall Shear Stress Magnitude for an Ideal Stretched Harvest Stenosis during Systole. The WSS reaches as high as 67 Dynes/Cm^2 within the stenotic throat.

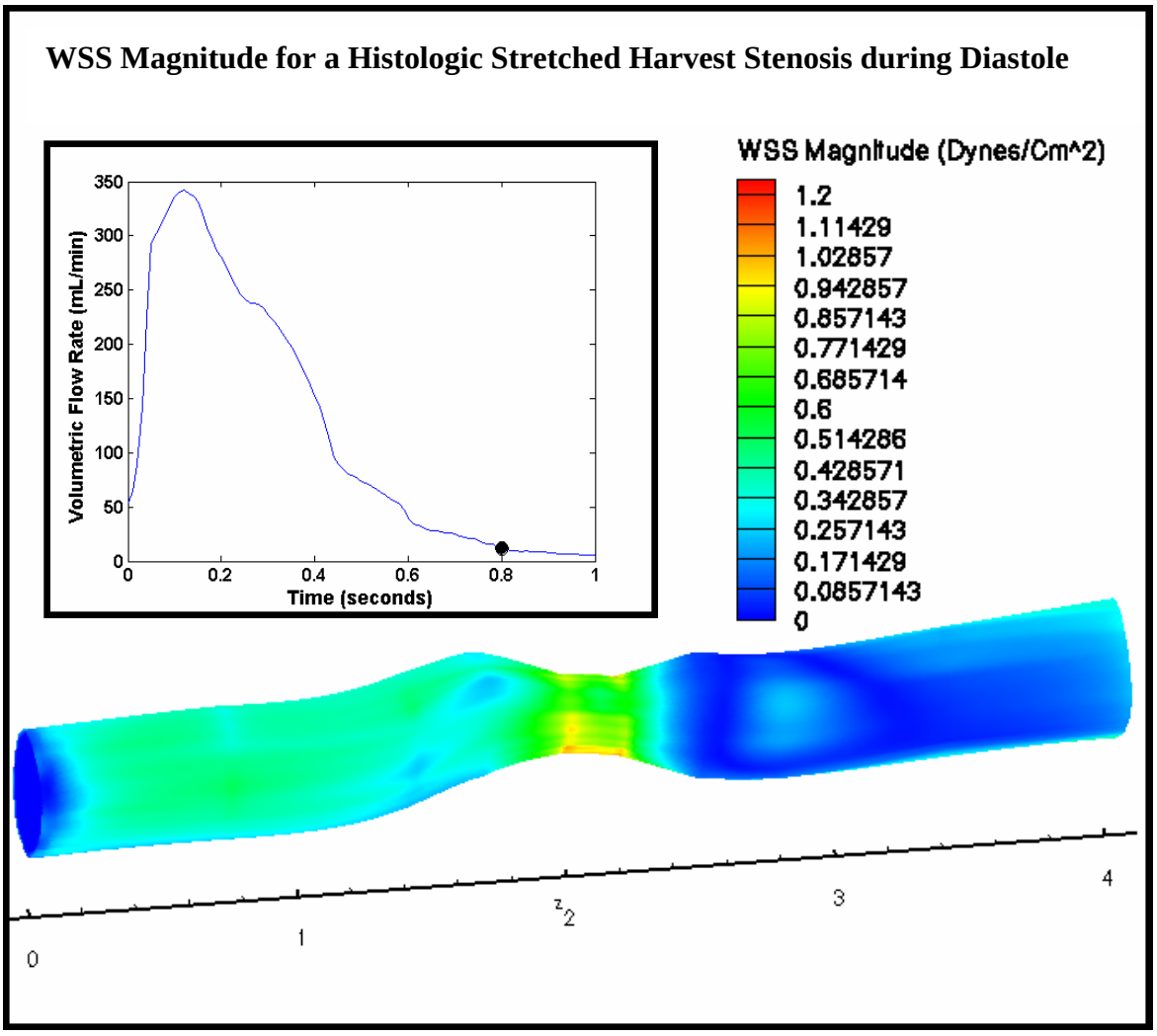

Figure 5.38: Wall Shear Stress Magnitude for a Histologic Stretched Harvest Stenosis during Diastole. The WSS reaches as high as 2 Dynes/Cm^2 within the stenotic throat.

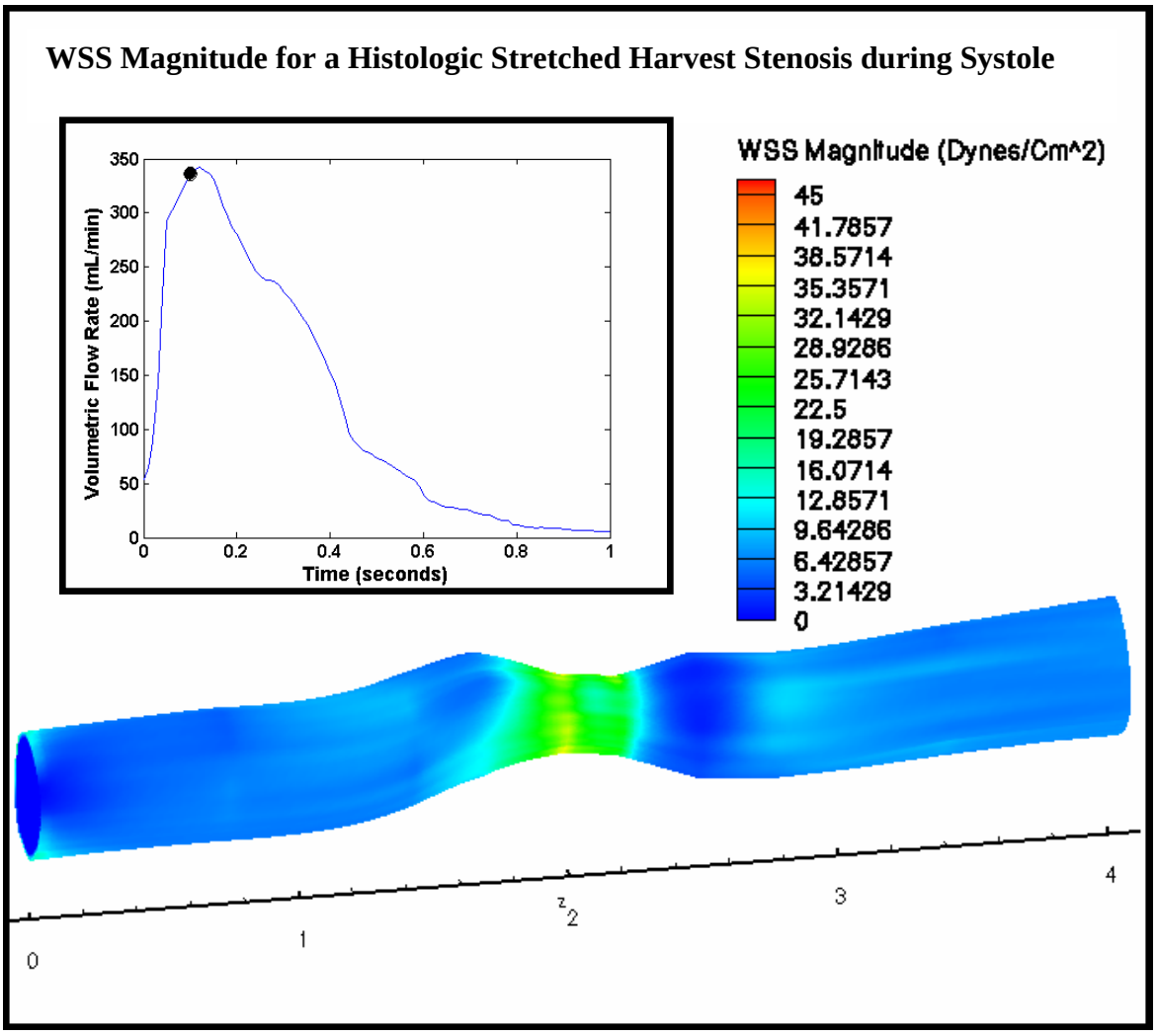

Figure 5.39: Wall Shear Stress Magnitude for a Histologic Stretched Harvest Stenosis during Systole. The WSS reaches as high as 48 Dynes/Cm^2 within the stenotic throat.

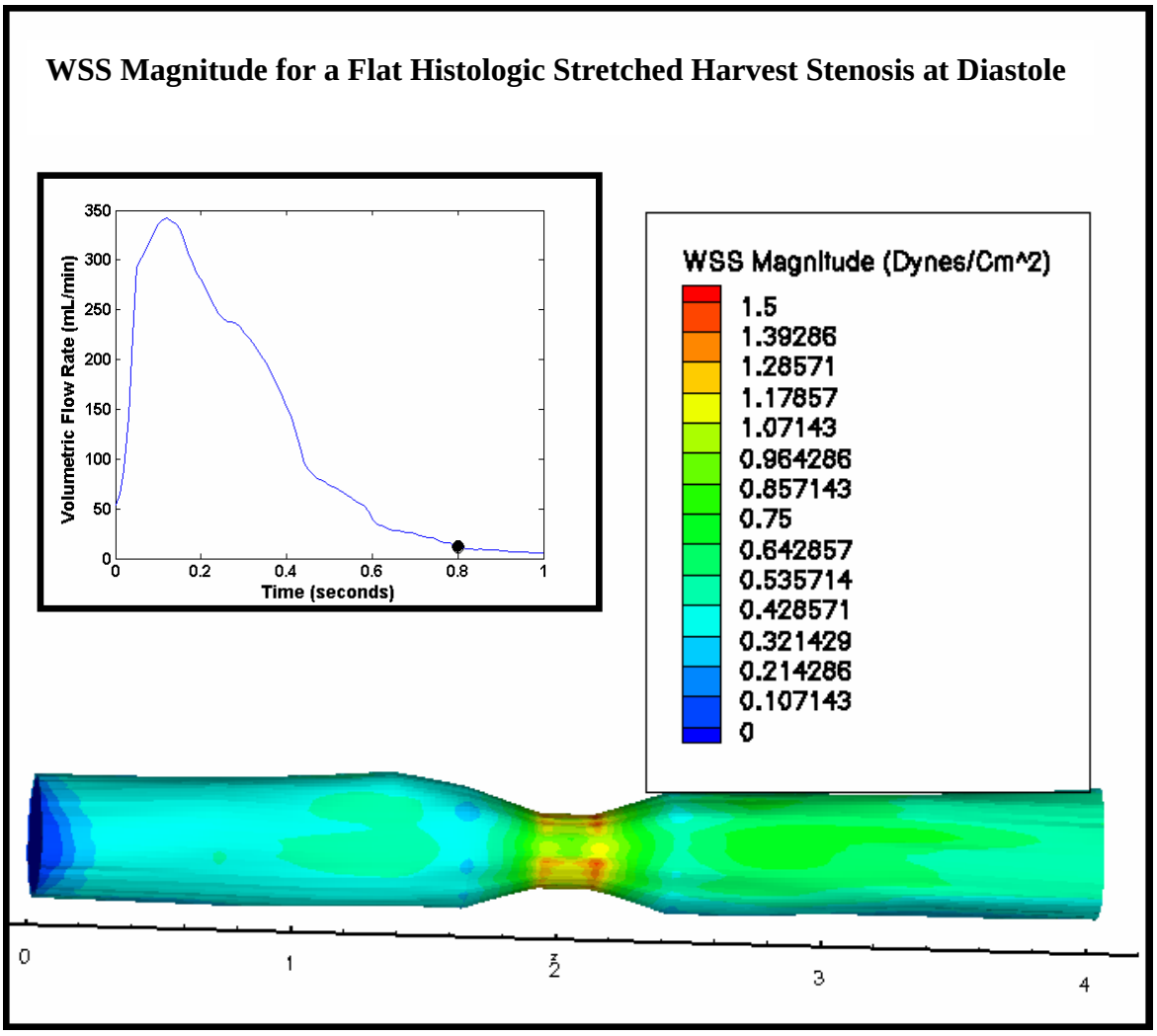

Figure 5.40: Wall Shear Stress Magnitude for a Flat Histologic Stretched Harvest Stenosis at Diastole. The WSS reaches as high as 2 Dynes/Cm^2 within the stenotic throat.

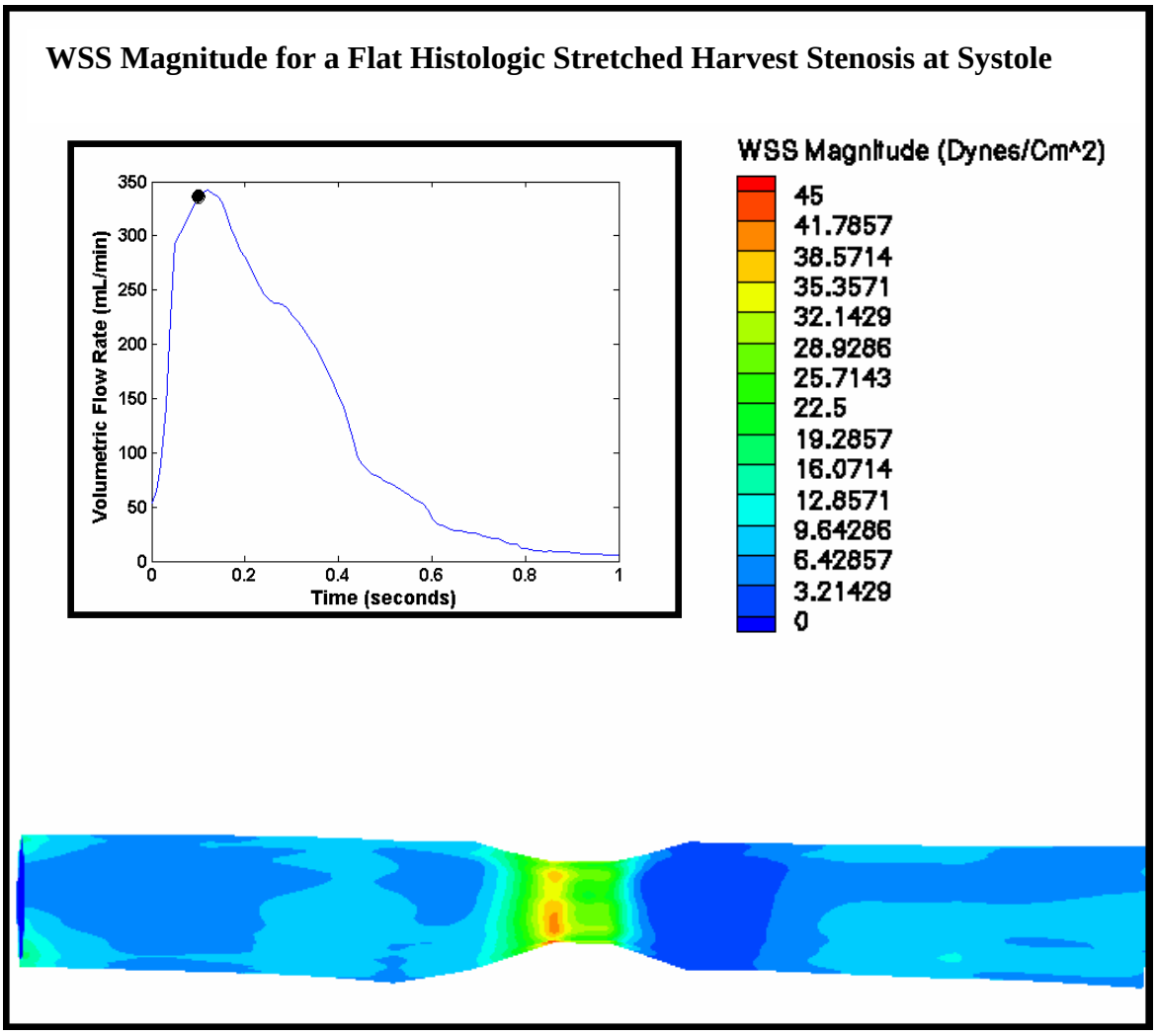

Figure 5.41: Wall Shear Stress Magnitude for a Flat Histologic Stretched Harvest Stenosis at Systole. The WSS reaches as high as 50 Dynes/Cm^2 within the stenotic throat.

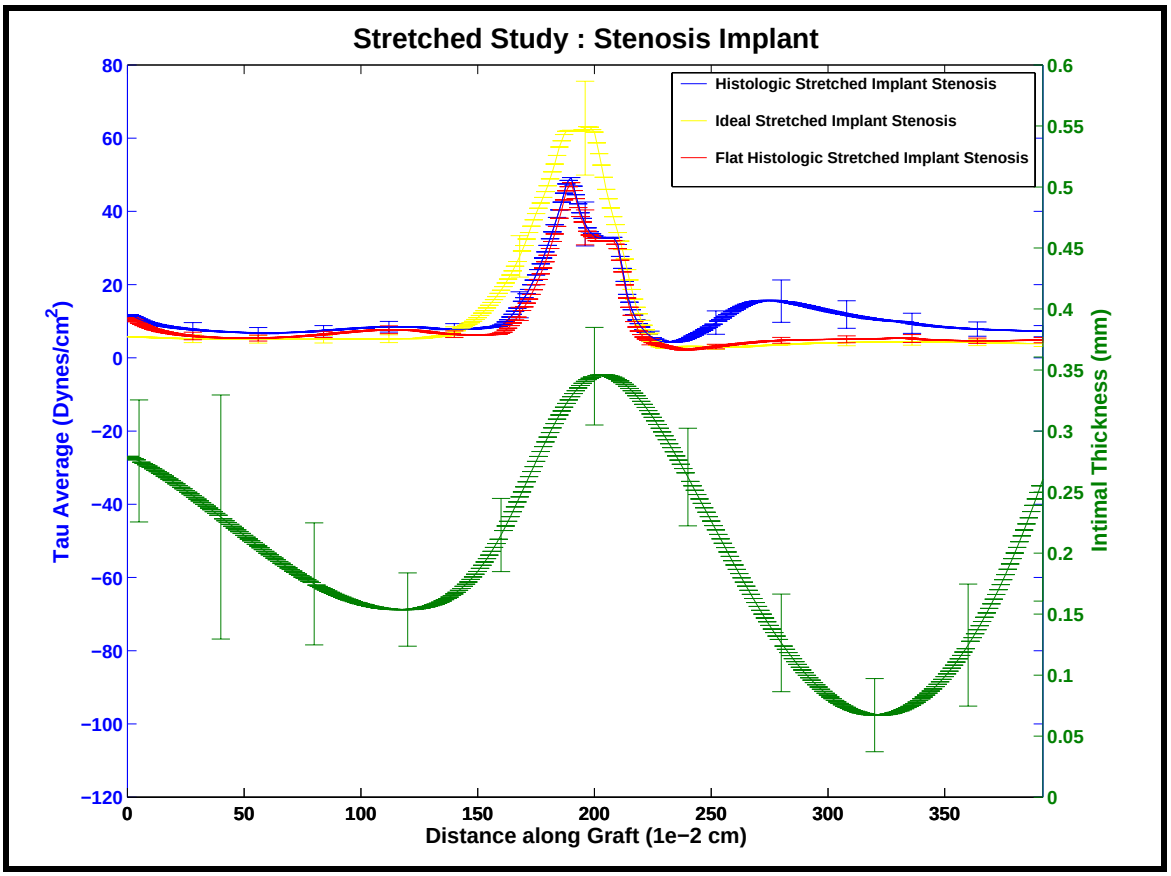

Figure 5.42: τavg and Intimal Thickness for Stretched Implant Stenotic Grafts along the Axial Length of the Vessels.

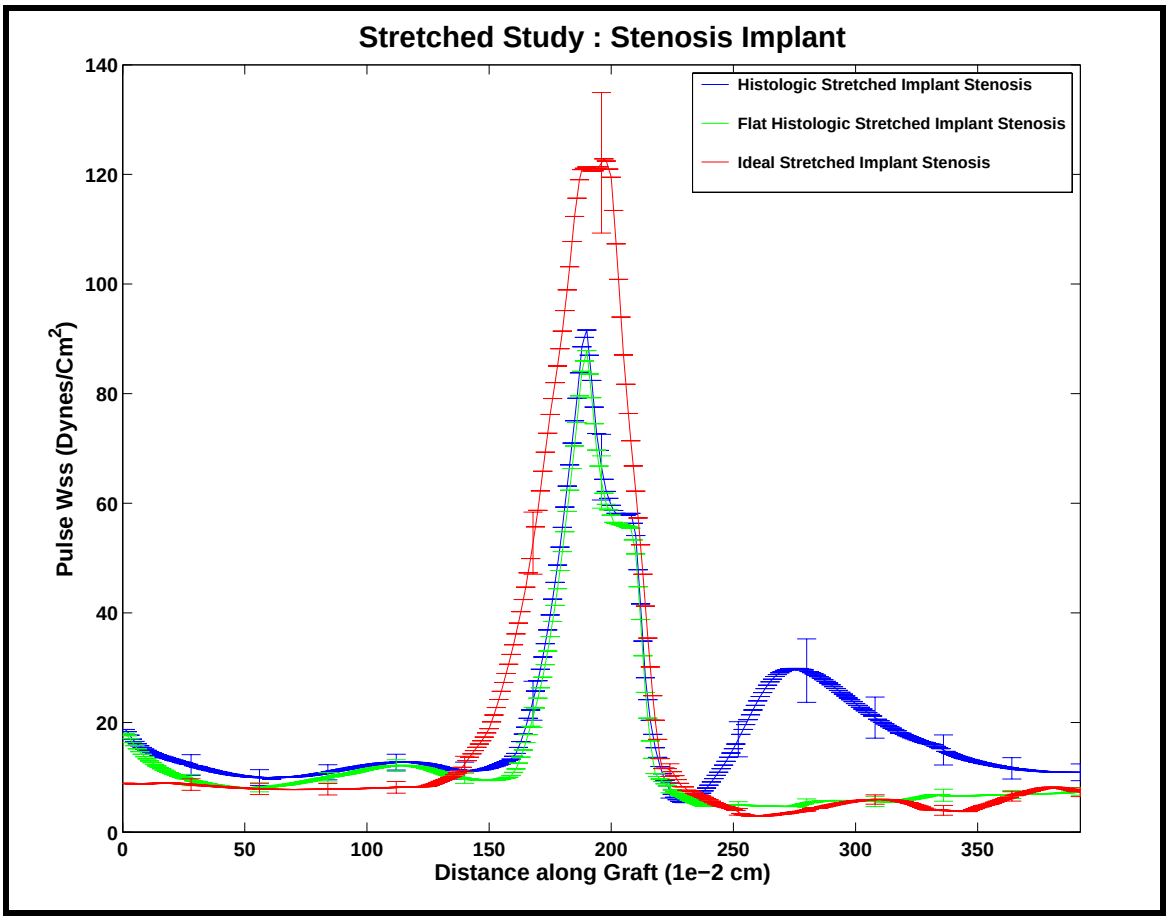

Figure 5.43: Pulse Spatially Averaged Wall Shear Stress for Stretched Implant Stenotic Grafts along the Axial Length of the Vessels.

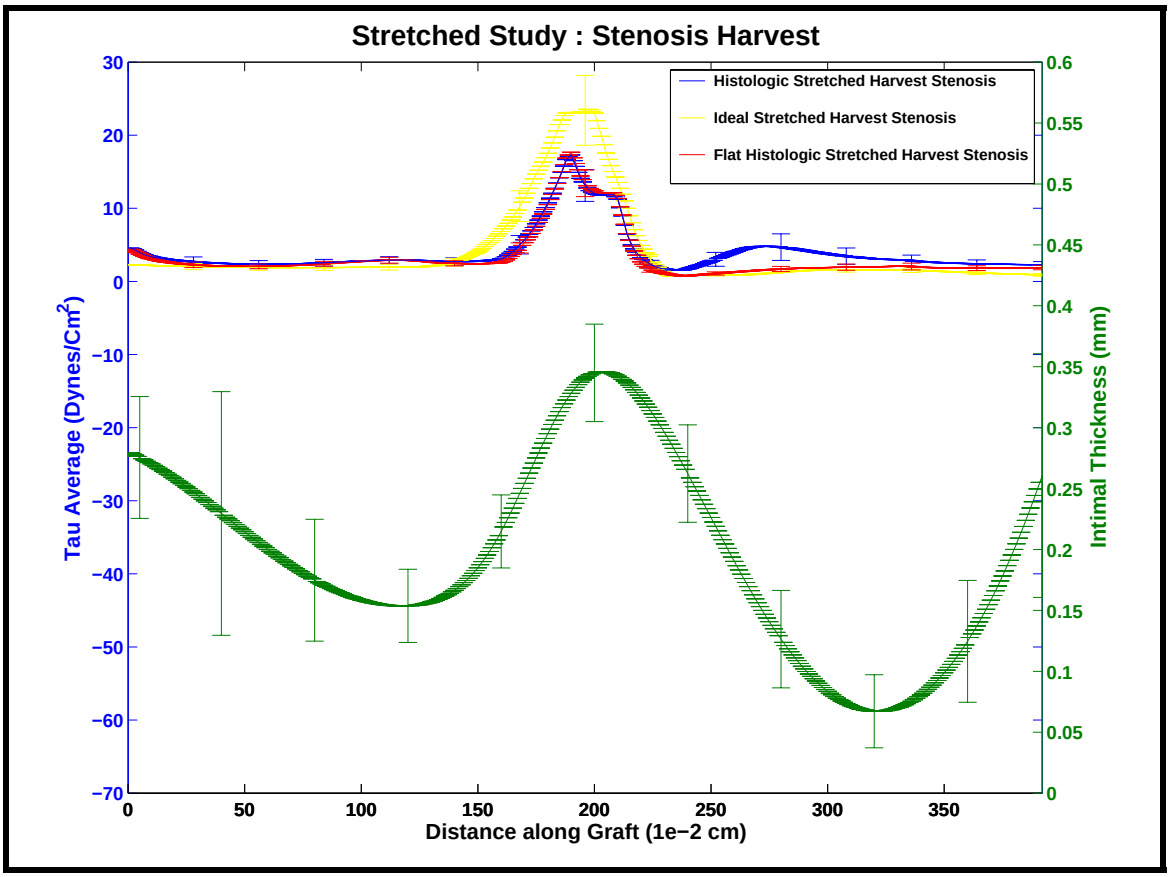

Figure 5.44: τavg and Intimal Thickness for Stretched Harvest Stenotic Grafts along the Axial Length of the Vessels.

were observed within all the different graft varieties (Figures 5.43, 5.45). At implantation, the Pulse WSS reached a peak of 120 dynes/cm^2 for the ideal stretched implant stenosis, 90 dynes/cm^2 for the histologic stretched implant stenosis, and 90 dynes/cm^2 for the flat histologic stretched implant stenosis. At sacrifice, the Pulse WSS peaked within the stenotic throat at 58 dynes/cm^2 for the ideal stretched harvest stenosis, 47 dynes/cm^2 for the histologic stretched harvest stenosis, and 40 dynes/cm^2 for the flat histologic stretched harvest stenosis.

Unstretched Graft Control Study.

The hemodynamics within the unstretched control grafts were quantified. The PCMRI boundary conditions were applied to these computational models. Within the MRI implant control, the speed peaked at 24 cm/s during systole (Figure 5.46). There was variation in the WSS measurements for the MRI harvest control during systole (Figure 5.47). At some points within the vessel, the WSS reached as high as 18 dynes/cm^2; however, mostly the WSS resided near 5-7 dynes/cm^2. During systole, the WSS within the histologic unstretched harvest control (Figure 5.48) exceeded 15 dynes/cm^2, but mostly it leveled near 3 dynes/cm^2. Lastly, during peak systole for the flat histologic unstretched harvest control (Figure 5.49), the WSS exceeded 25 dynes/cm^2 near geometric shape changes. For both implantation and sacrifice, the τavg stayed between 2 to 6 dynes/cm^2 for all the control computational grids (Figures 5.50, 5.52). As seen before, τavg and intimal thickness were compared. The simulations using the PCMRI boundary condition were graphed separately (Figure 5.51).

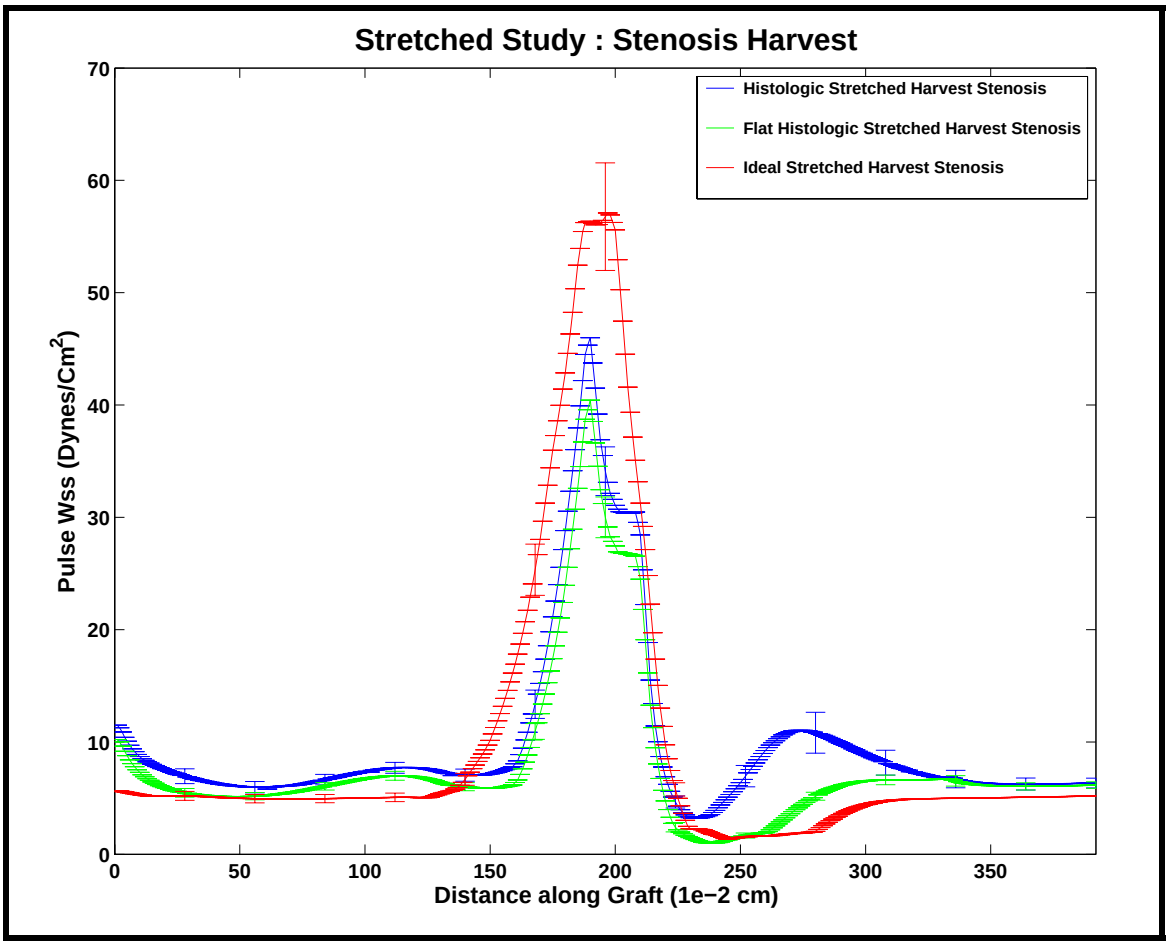

Figure 5.45: Pulse Spatially Averaged Wall Shear Stress for Stretched Harvest Stenotic Grafts along the Axial Length of the Vessels.

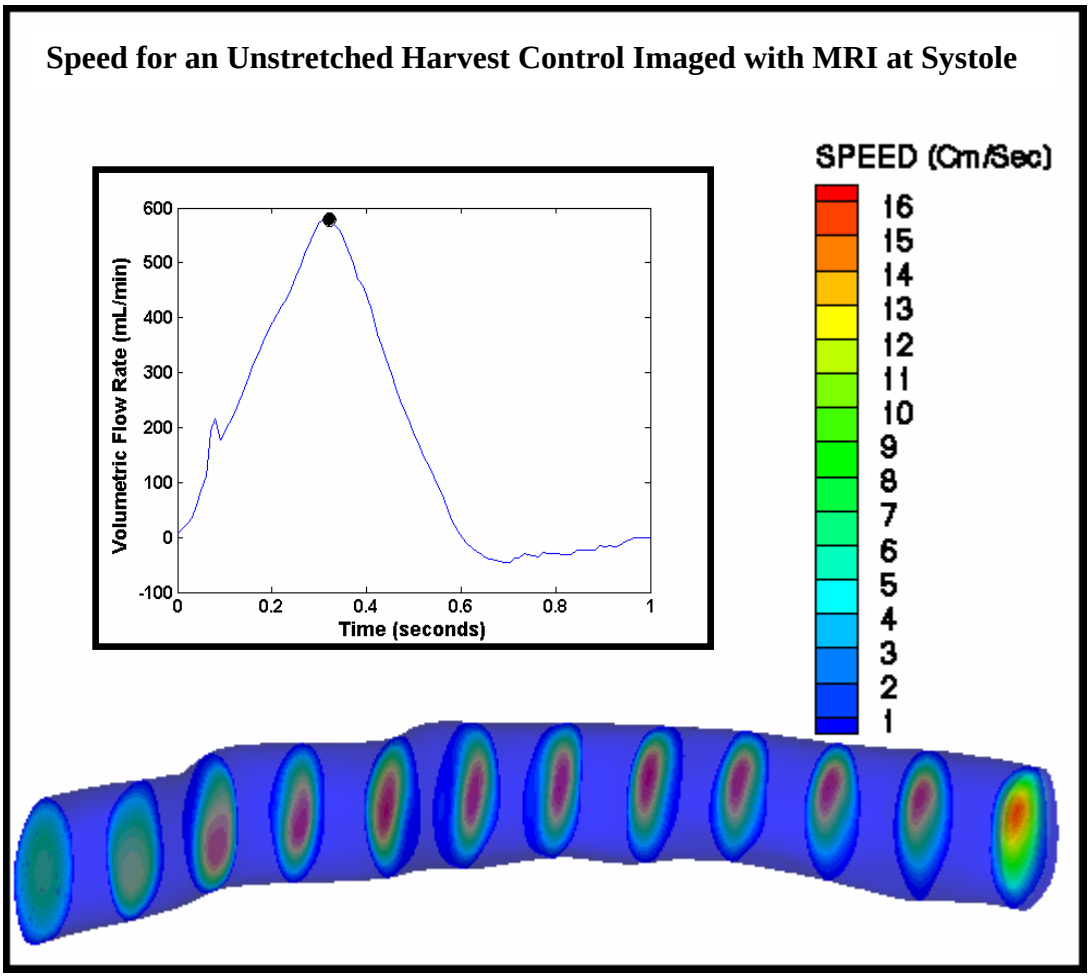

Figure 5.46: During Systole Speed for an Unstretched Harvest Control Imaged with MRI.

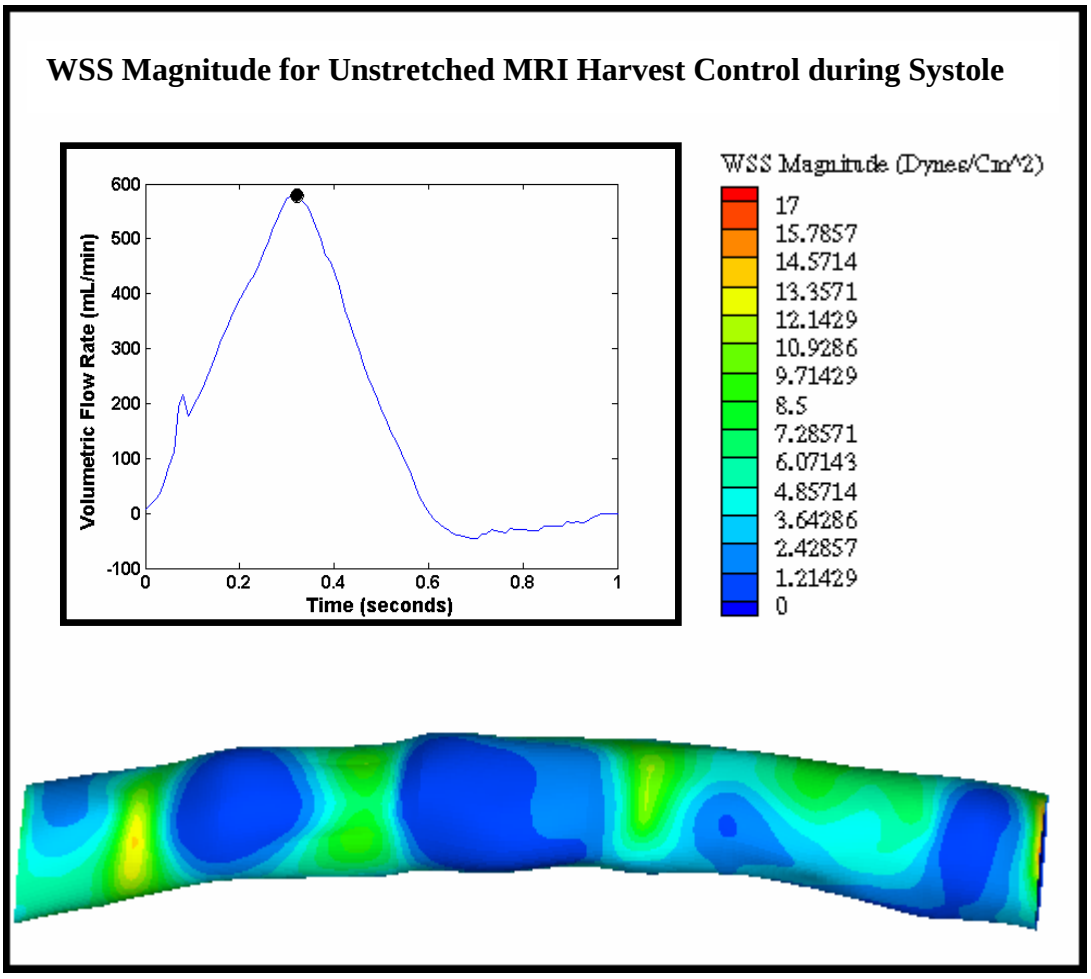

Figure 5.47: Wall Shear Stress Magnitude for an Unstretched MRI Harvest Control during Systole.

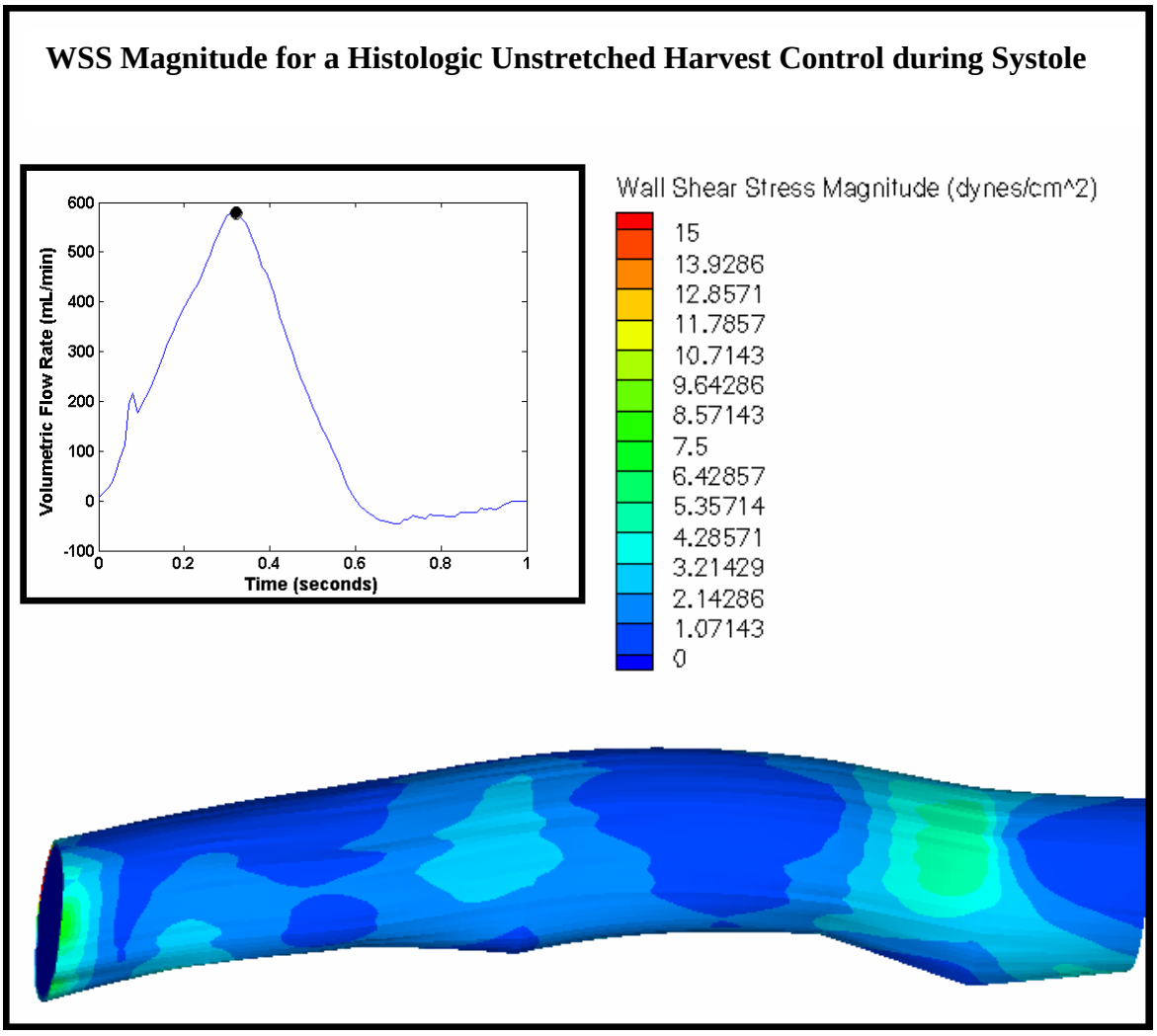

Figure 5.48: Wall Shear Stress Magnitude for a Histologic Unstretched Harvest Control during Systole.

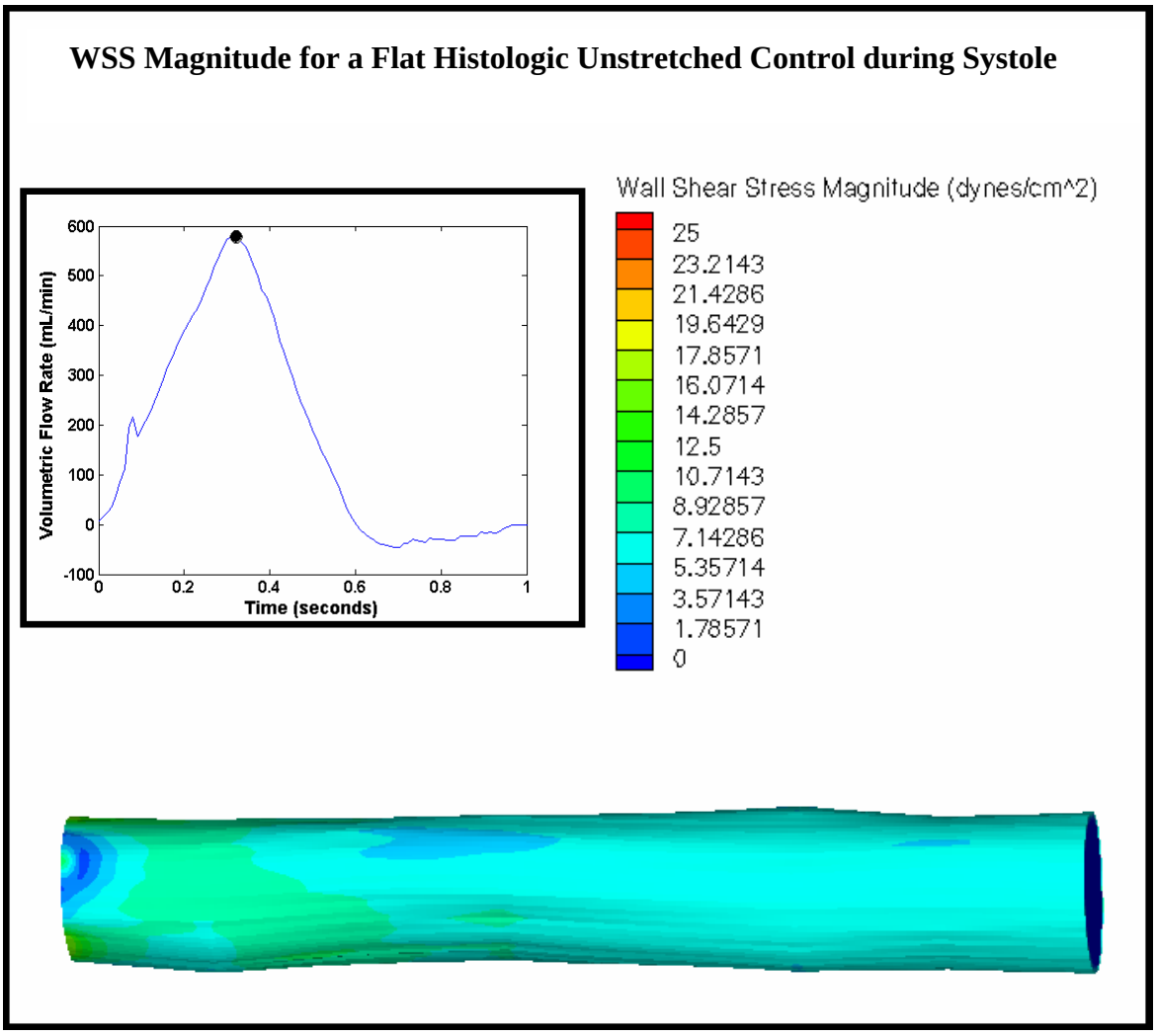

Figure 5.49: Wall Shear Stress Magnitude for a Flat Histologic Unstretched Control during Systole.

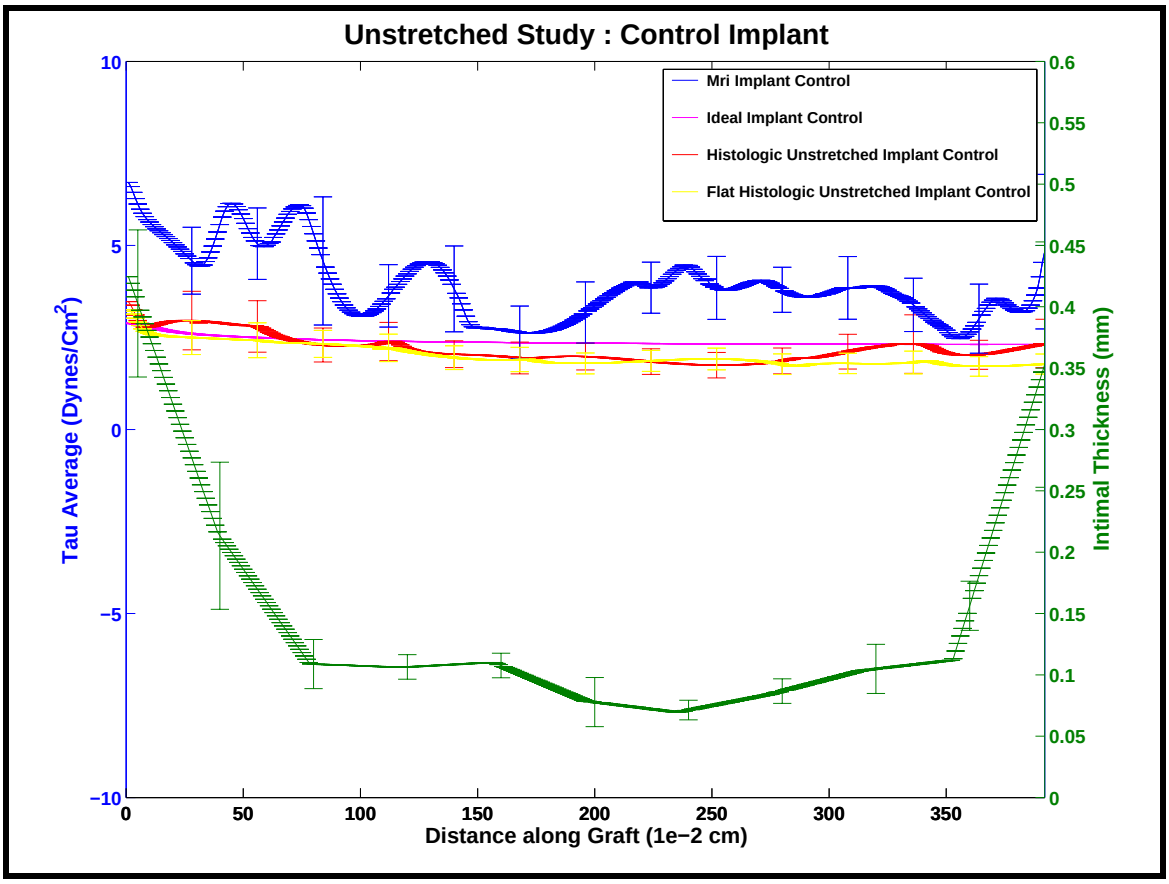

Figure 5.50: τavg and Intimal Thickness for Unstretched Implant Control Grafts along the Axial Length of the Vessels.

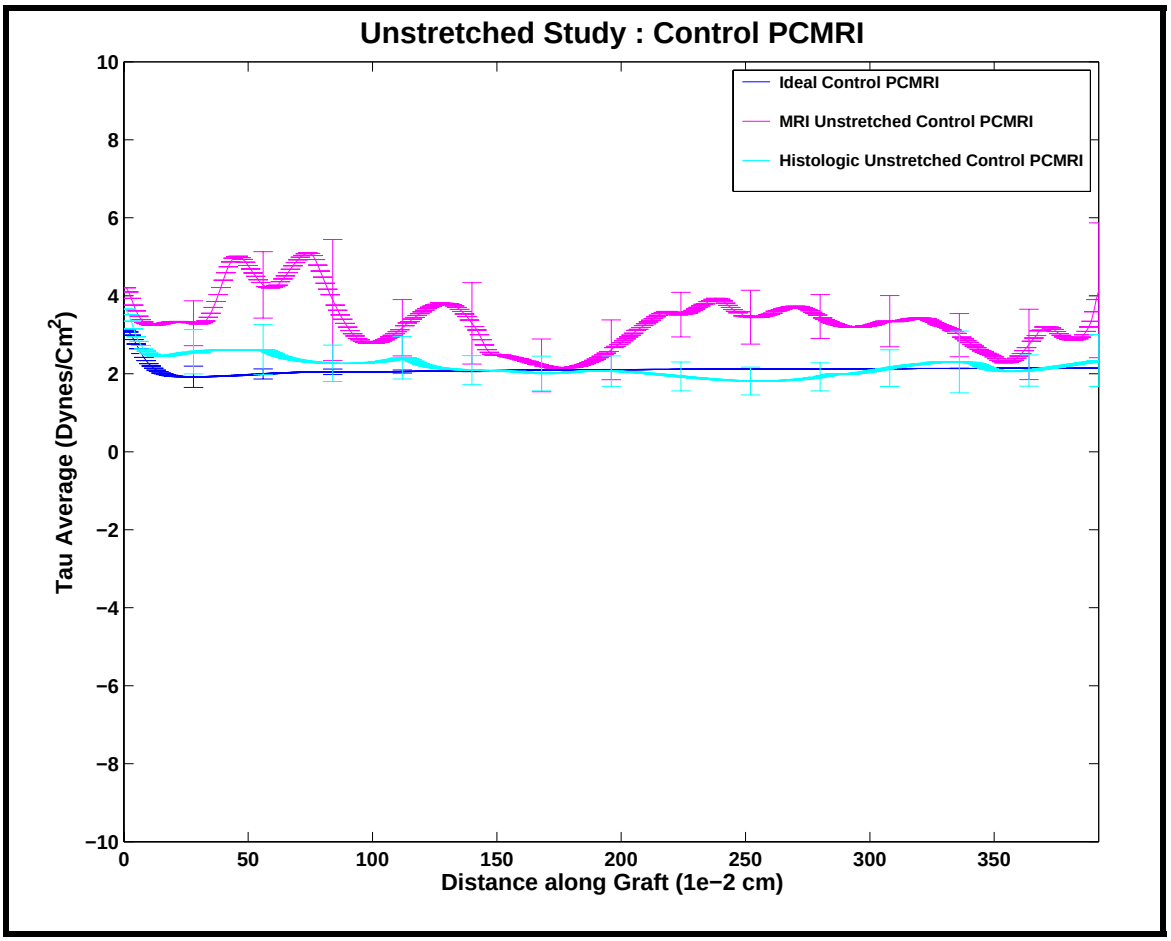

Figure 5.51: τavg for Unstretched PCMRI Control Grafts along the Axial Length of the Vessels.

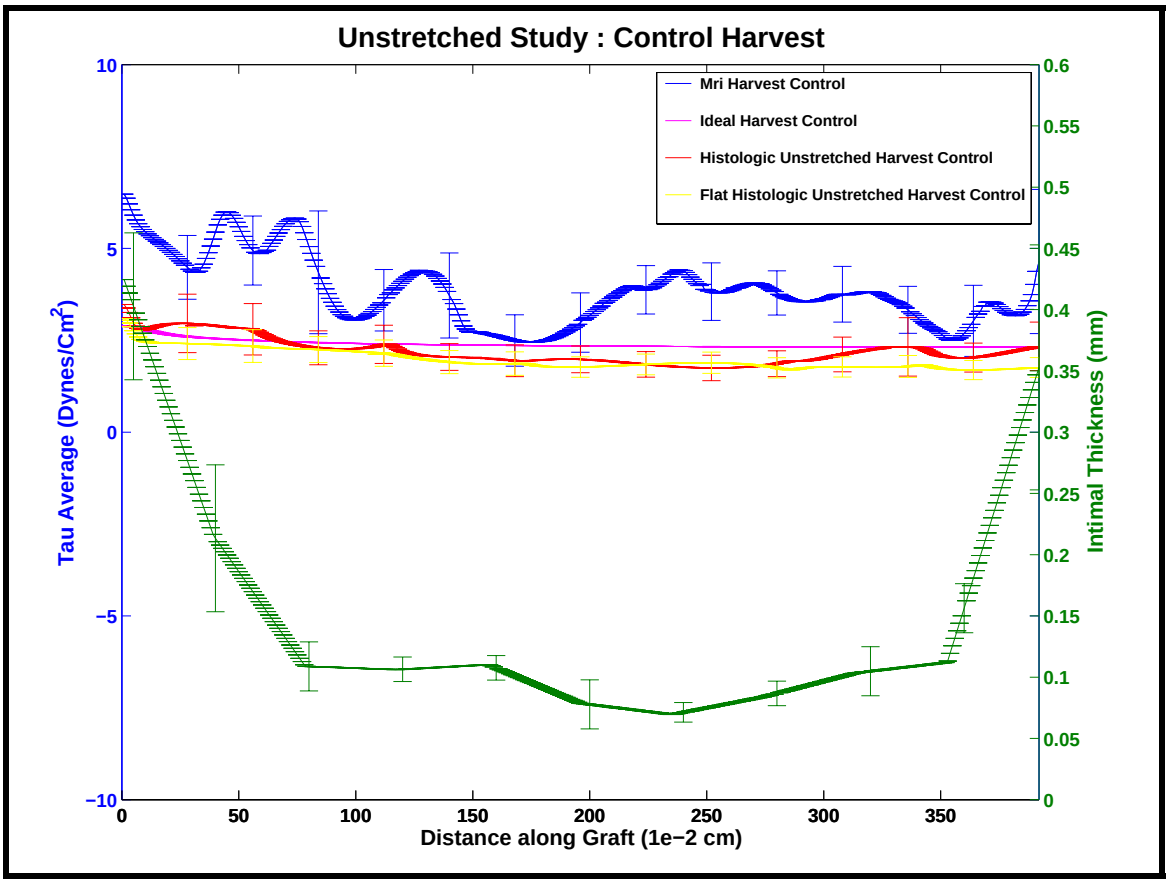

Figure 5.52: τavg and Intimal Thickness for Unstretched Harvest Control Grafts along the Axial Length of the Vessels.

Unstretched Stenosis.

Within the unstretched stenosis the flow environment was analyzed. Once again, the PCMRI boundary conditions were applied to these computational models. The velocity vectors within the stenotic throat were expectedly very high during systole. Surprisingly, during diastole some local flow reversal was observed within the stenotic throat (Figure 5.53). Distal to the stenotic throat, this phenomenon became more apparent. During both diastole and systole, this flow reversal was observed (Figure 5.54 and 5.55). In diastole this transient flow separation was very pronounced. This was quantitatively confirmed with the oscillatory shear index (OSI) (Figures 5.56, 5.57). Distal to the stenosis, the OSI was consistently above 0.25.

Descriptions of WSS magnitude were obtained for the three different model types. During diastole, all three model types showed low, physiologic levels of WSS less than 10 dynes/cm^2 (Figures 5.58, 5.60, 5.63). During systole, the ideal unstretched harvest stenosis reached a peak WSS within its stenotic throat of over 130 dynes/cm^2 (Figure 5.59), while the histologic unstretched harvest stenosis exceeded 160 dynes/cm^2 at this location (Figure 5.62), and the MRI unstretched harvest stenosis apexed at 130 dynes/cm^2 (Figure 5.65). Consistent within all its representations, the histologic unstretched harvest stenosis had a very high level of WSS on the anterior wall of the stenotic throat's distal end. For implantation, once the stenotic throat was entered, the τavg illustrated very high levels of WSS. The ideal unstretched implant stenosis peaked over 100 dynes/cm^2 (Figure 5.66), while the histologic unstretched implant stenosis exceeded 120 dynes/cm^2, and the MRI unstretched implant stenosis apexed at 90 dynes/cm^2. A similar story was

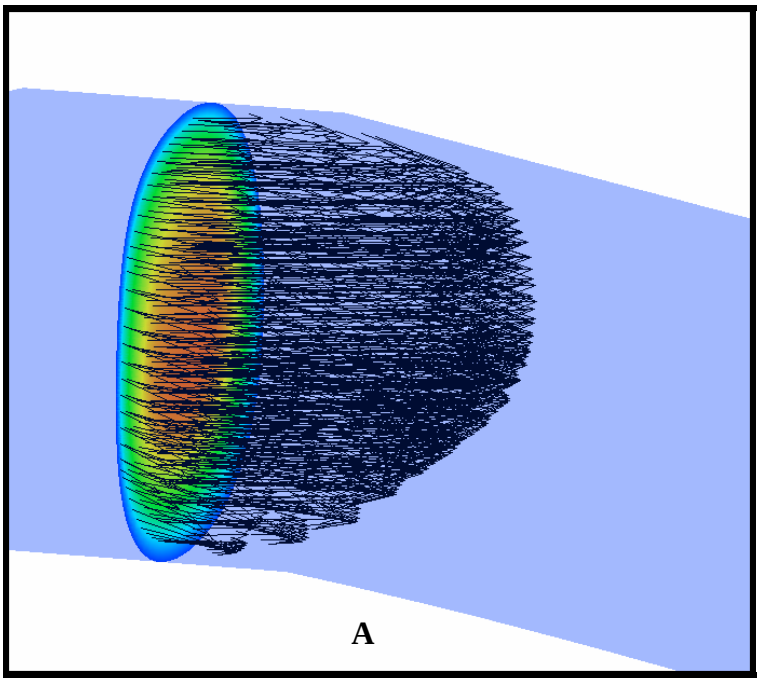

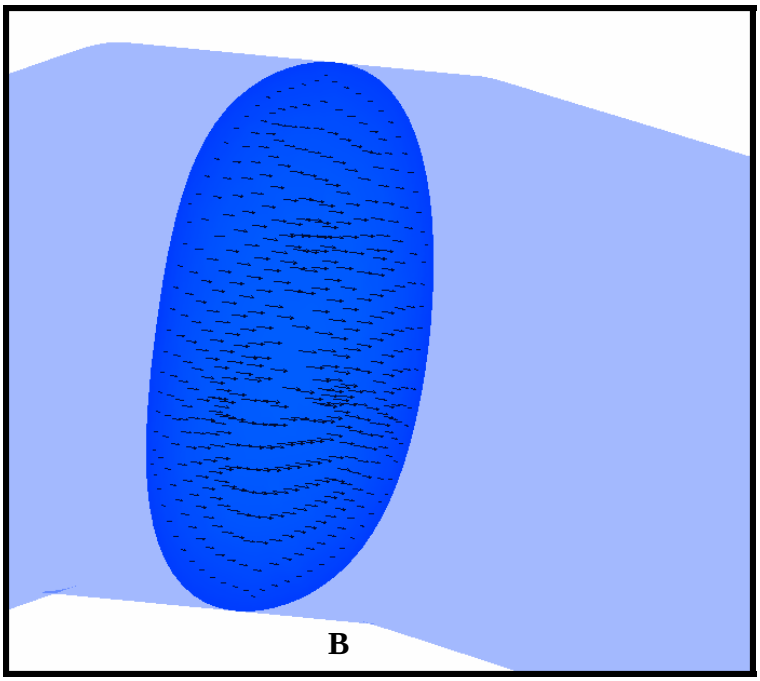

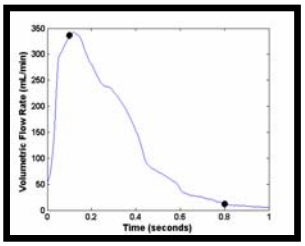

Points in Diastole and Systole

Figure 5.53: Velocity within the Stenotic Throat during Systole and Diastole. (A) Systole. The velocity in the axial direction was very large. (B) Diastole. Even within the stenotic throat, there appears some local flow reversal.

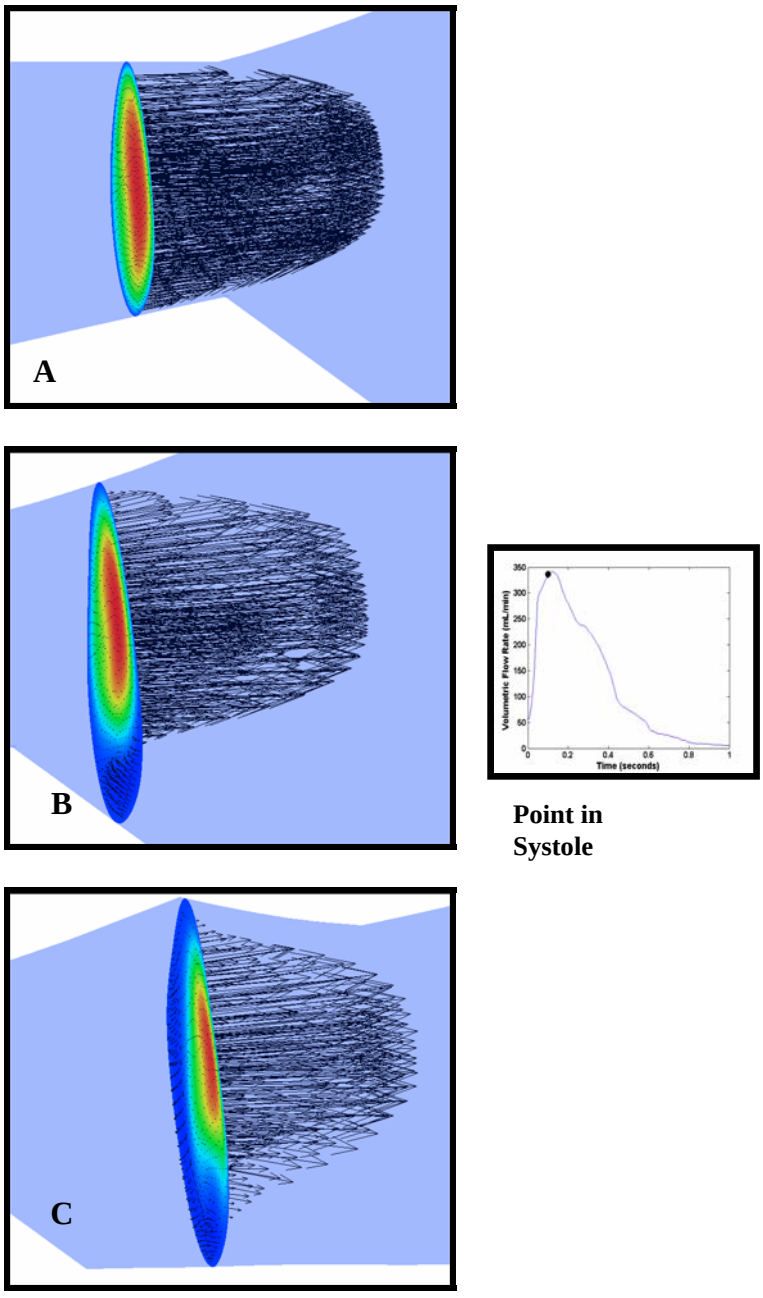

Figure 5.54: Flow Recirculation Downstream of the Stenotic Throat during Systole. Axial velocity vectors illustrate flow dynamics at different locations downstream of the proximal anastomosis: (A) 2.2 cm (B) 2.4 cm (C) 2.6 cm. The velocity vectors oriented in the retrograde direction highlight the local reversal of flow.

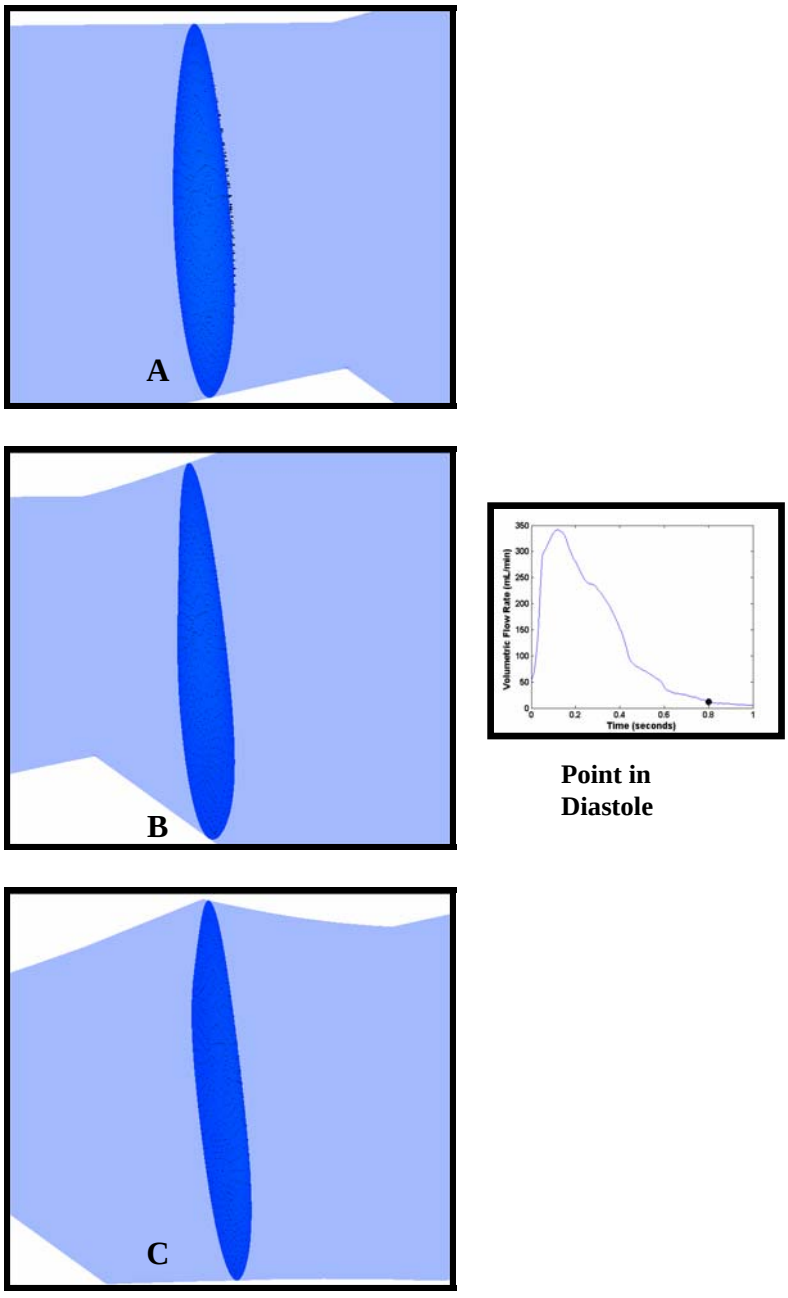

Figure 5.55: Flow Recirculation Downstream of the Stenotic Throat during Diastole. Axial vectors illustrate flow dynamics at different locations downstream of the proximal anastomosis: (A) 2.2 cm (B) 2.3 cm (C) 2.4 cm. The velocity oriented in the retrograde direction highlights the transient flow separation. Note the absence of prominent forward velocity.

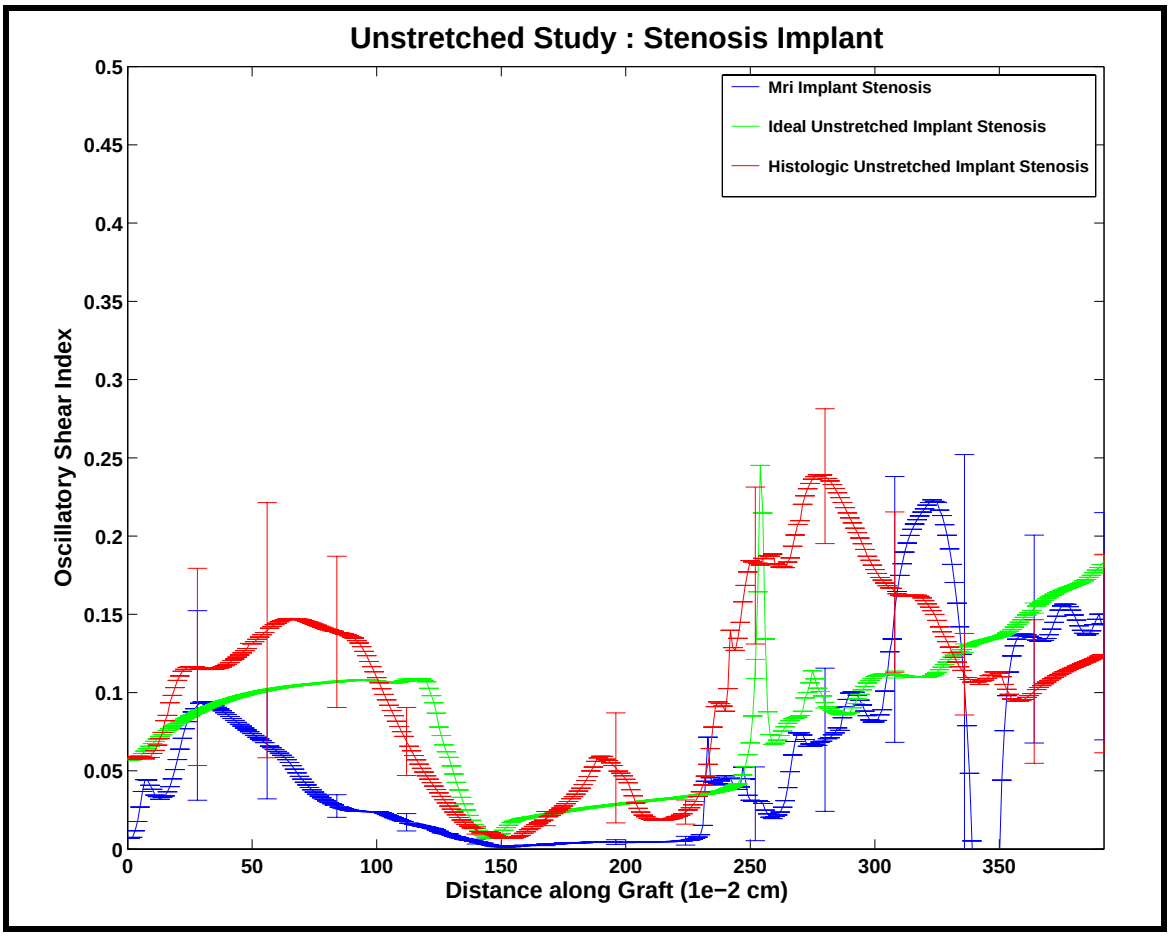

Figure 5.56: Oscillatory Shear Index for Unstretched Implant Stenotic Grafts. Observe the increase in flow recirculation downstream of the stenosis.

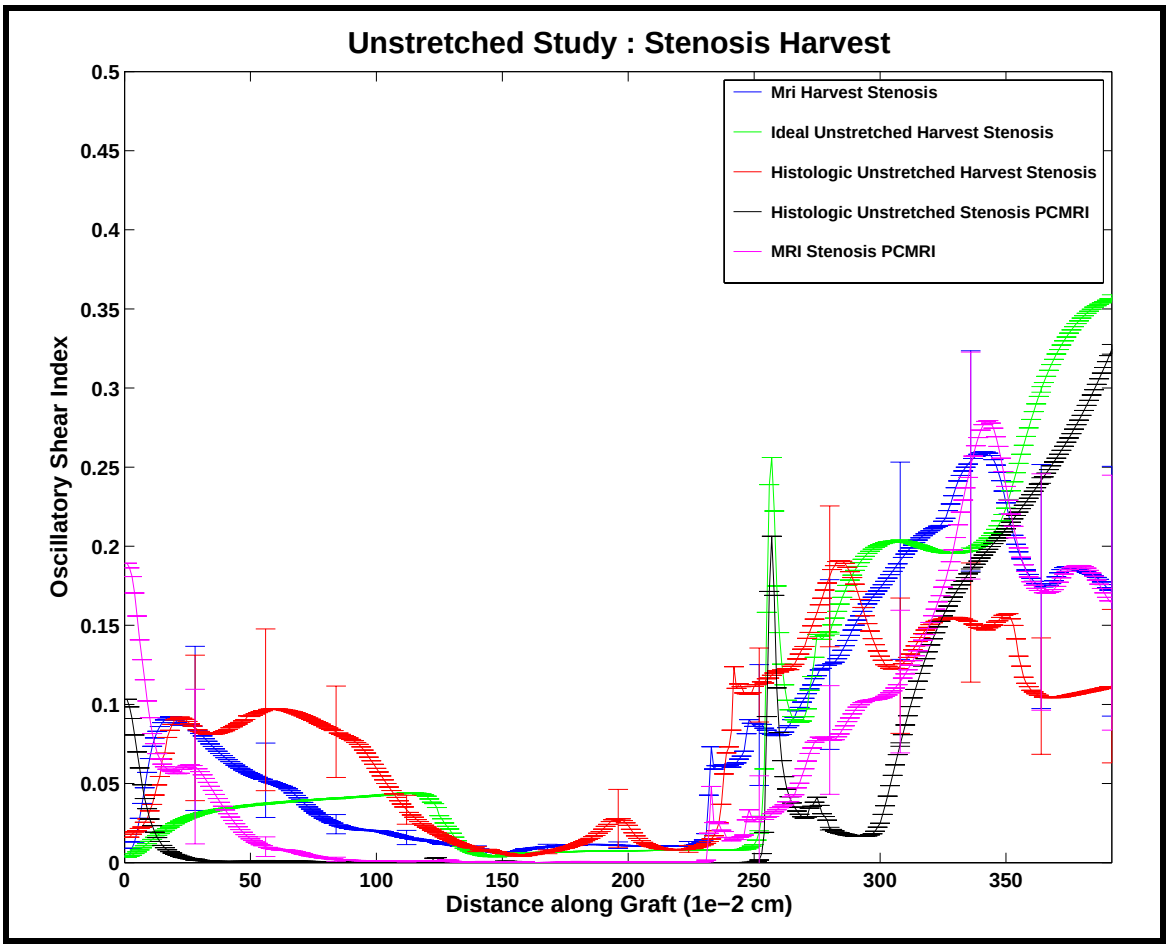

Figure 5.57: Oscillatory Shear Index for Unstretched Harvest Stenotic Grafts. Observe the increase in flow recirculation downstream of the stenosis.

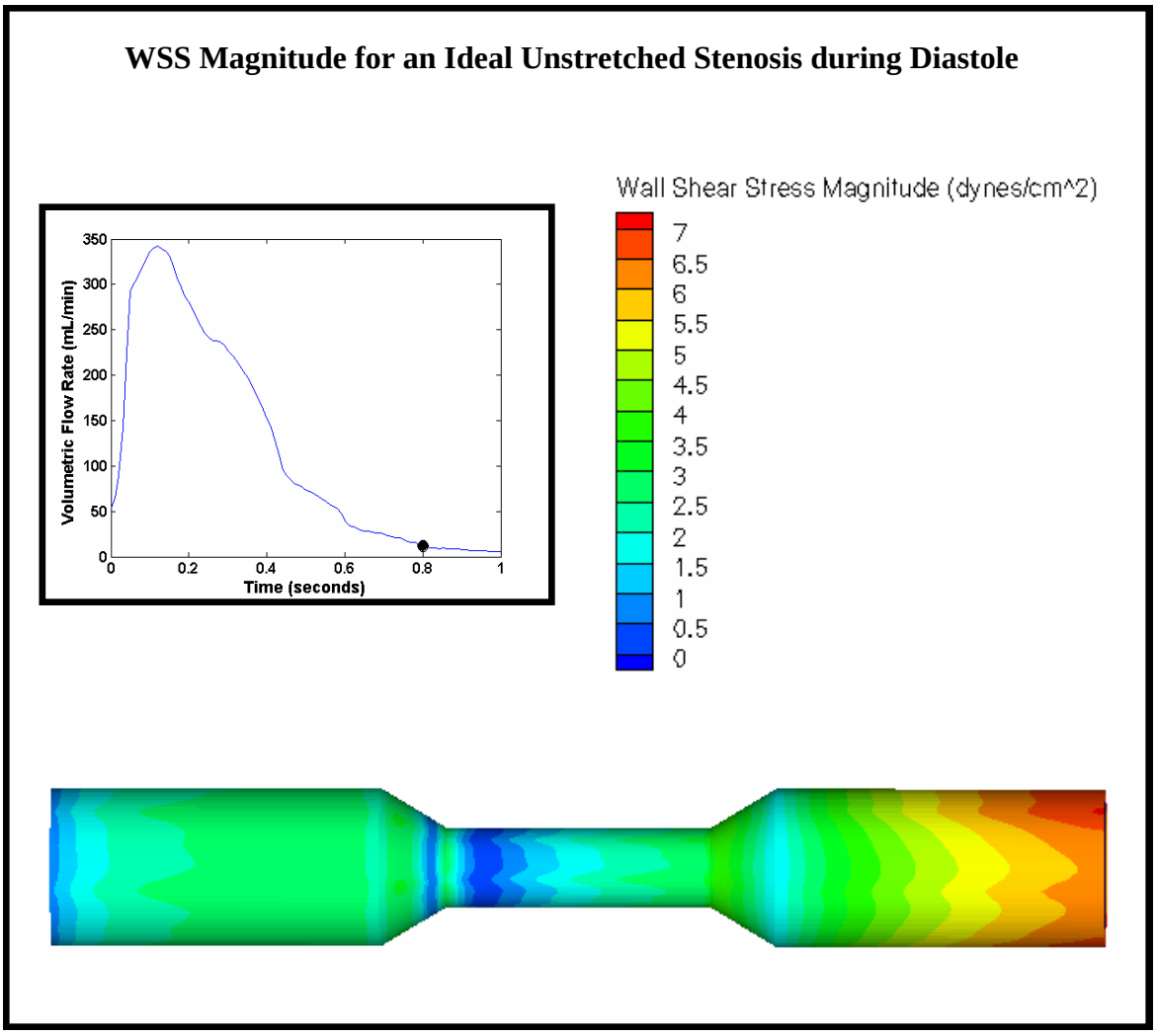

Figure 5.58: Wall Shear Stress Magnitude for an Ideal Unstretched Stenosis during Diastole.

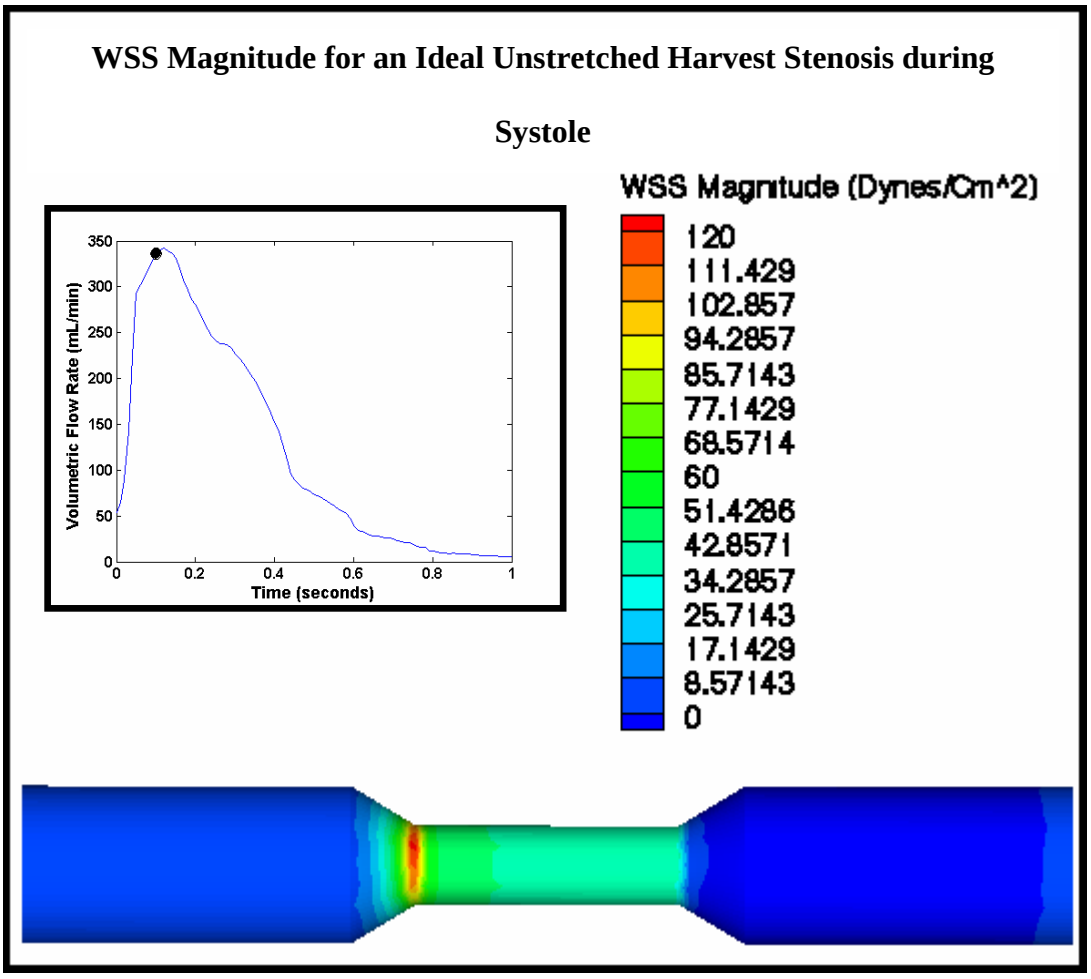

Figure 5.59: Wall Shear Stress Magnitude for an Ideal Unstretched Harvest Stenosis during Systole.

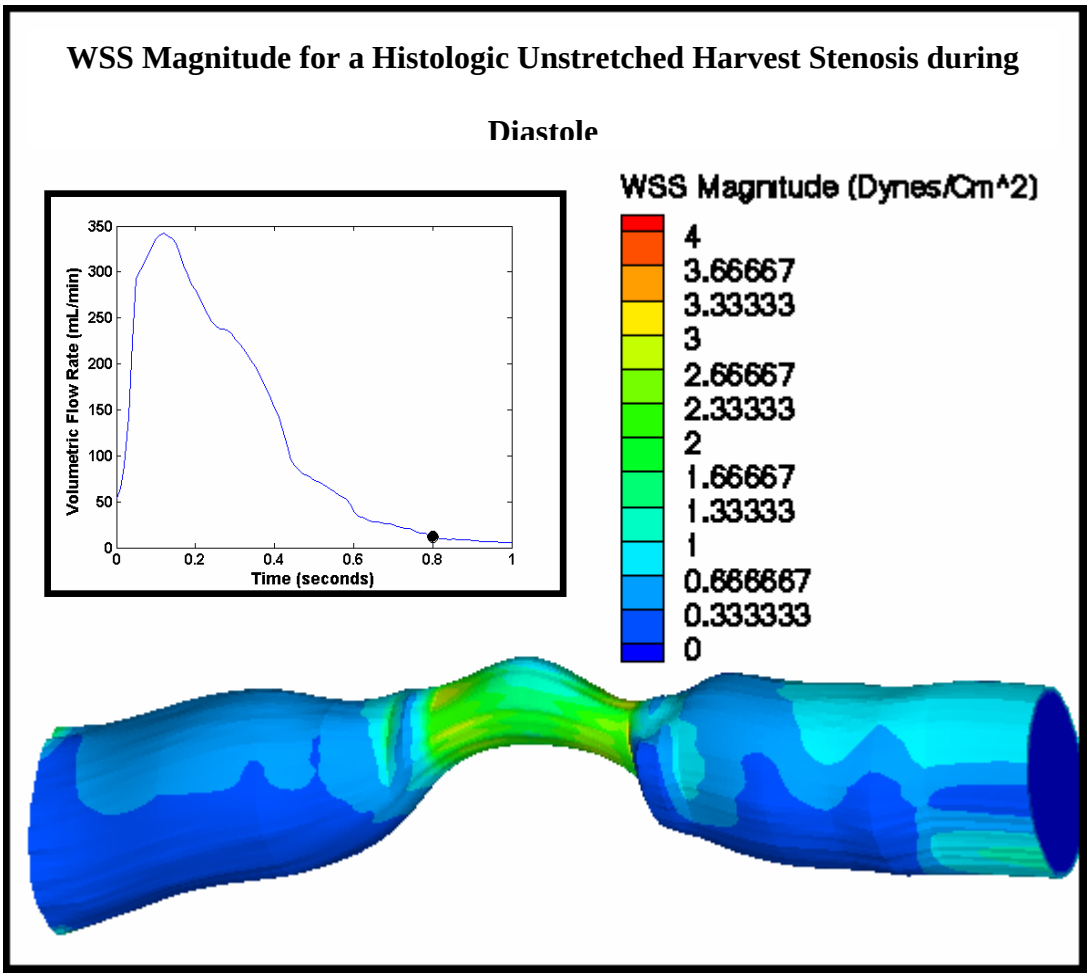

Figure 5.60: Wall Shear Stress Magnitude for a Histologic Unstretched Harvest Stenosis during Diastole.

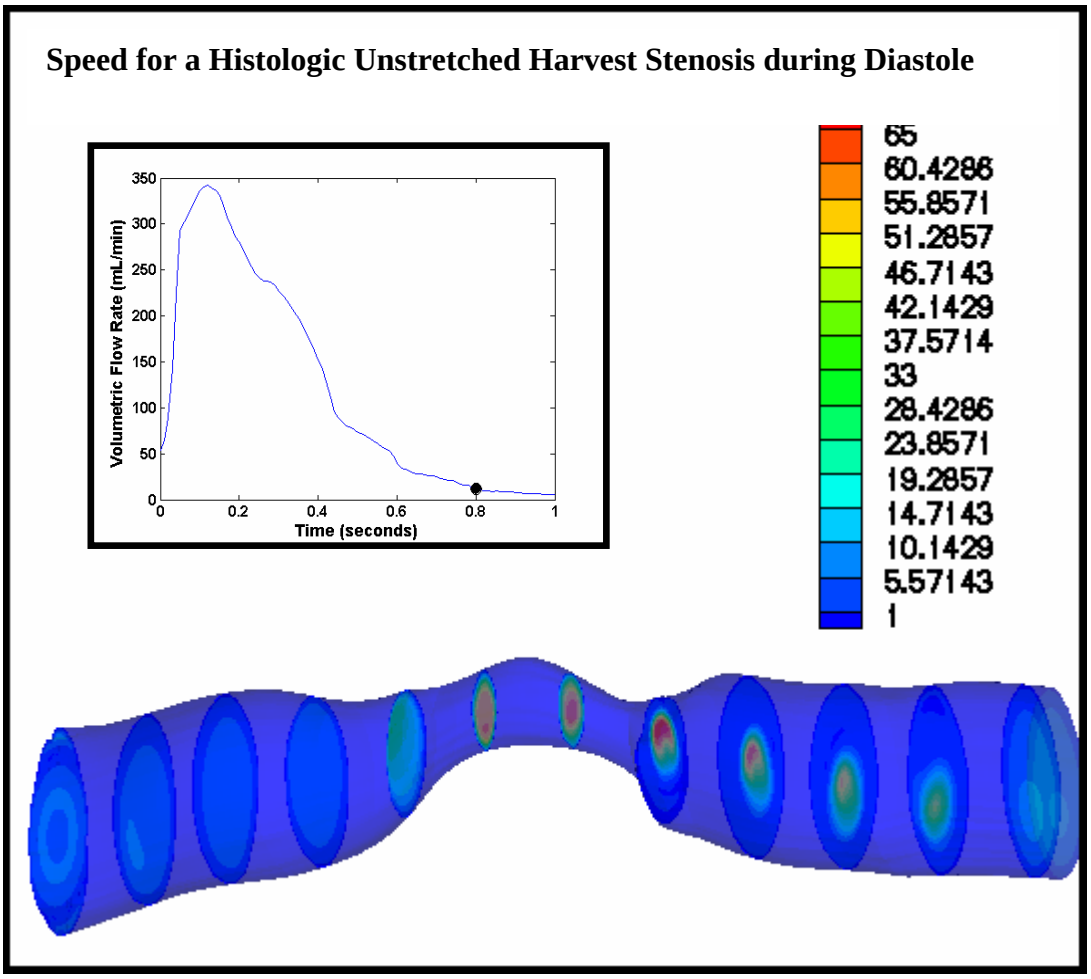

Figure 5.61: Speed for a Histologic Unstretched Harvest Stenosis during Diastole.

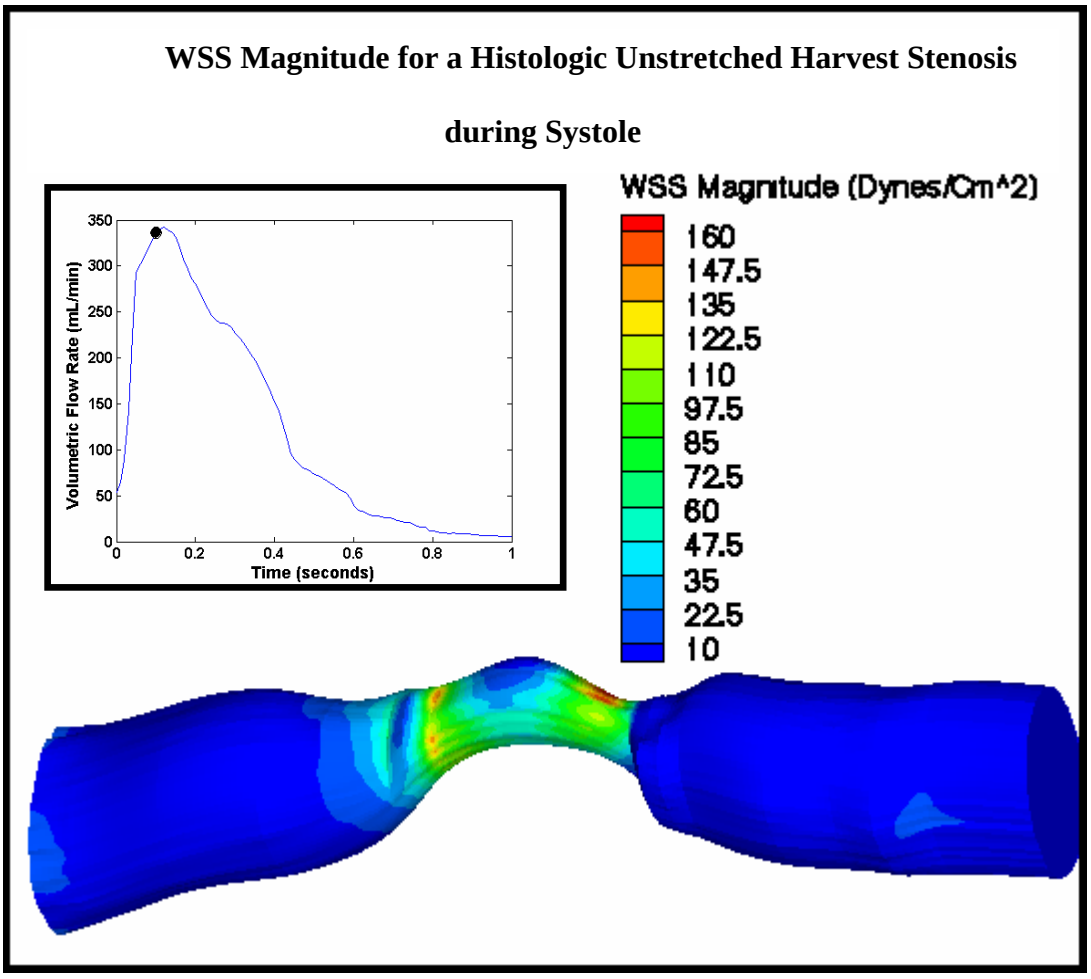

Figure 5.62: Wall Shear Stress Magnitude for a Histologic Unstretched Harvest Stenosis during Systole.

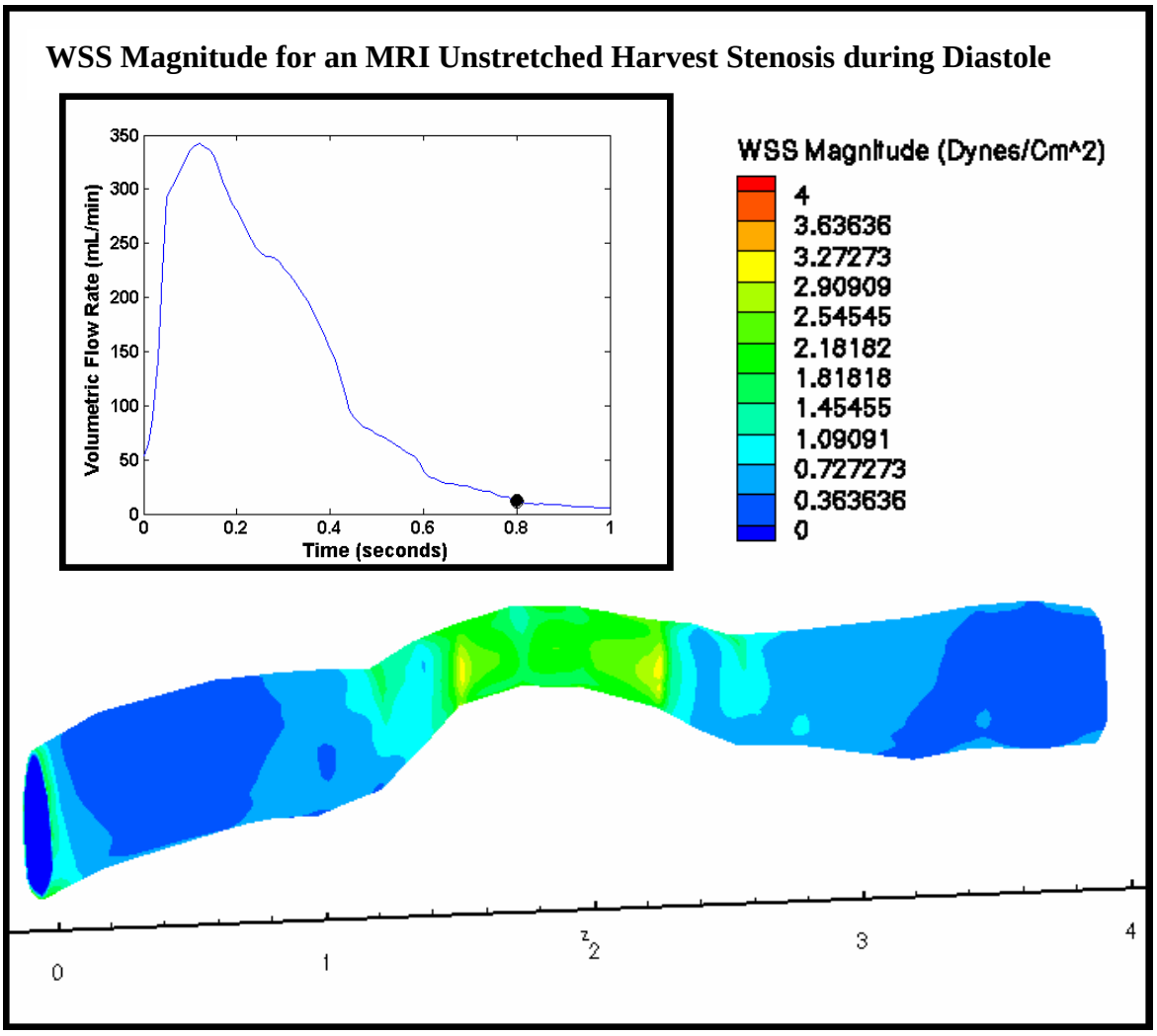

Figure 5.63: Wall Shear Stress Magnitude for an MRI Unstretched Harvest Stenosis during Diastole.

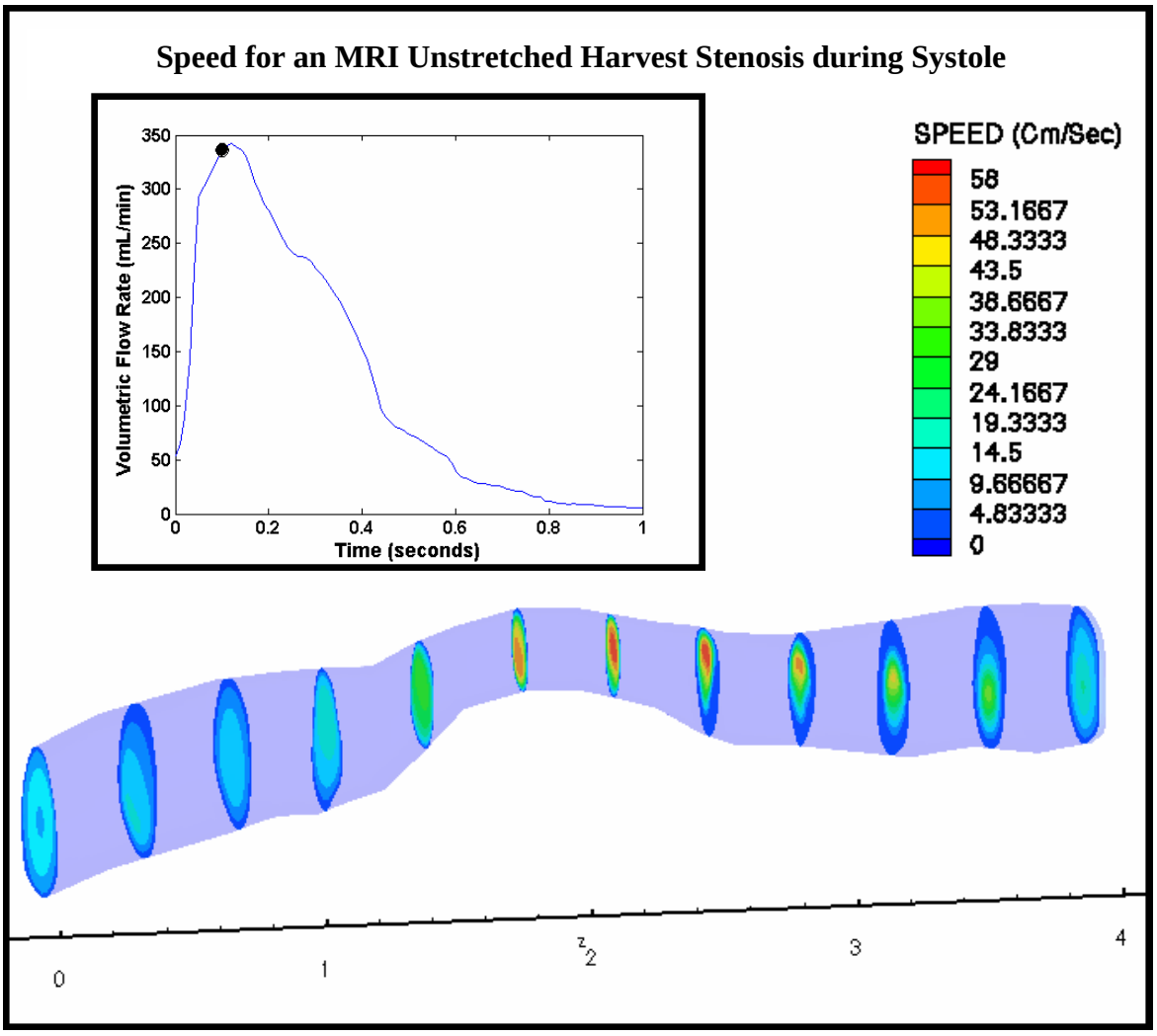

Figure 5.64: Speed for an MRI Unstretched Harvest Stenosis during Systole.

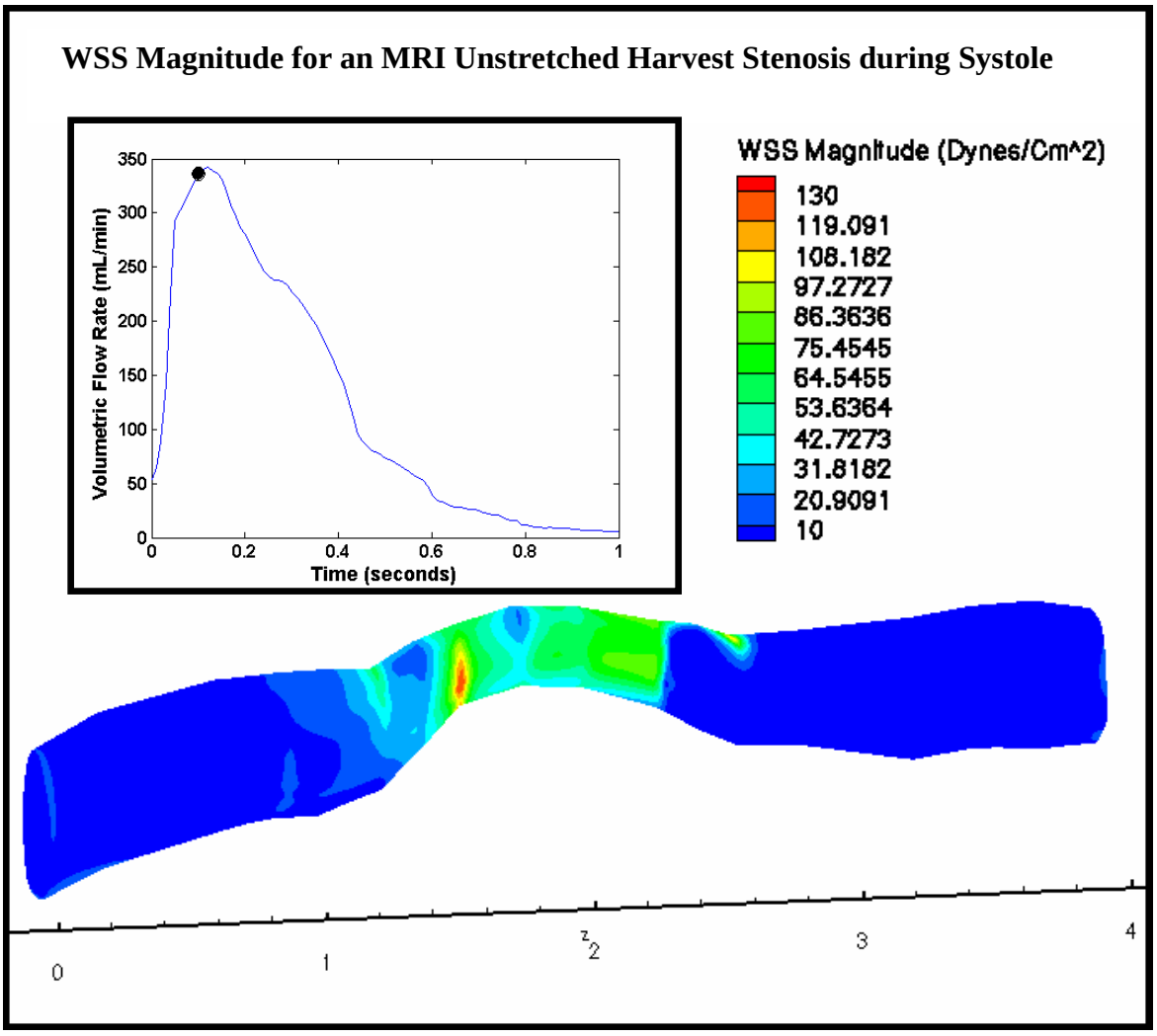

Figure 5.65: Wall Shear Stress Magnitude for an MRI Unstretched Harvest Stenosis during Systole.

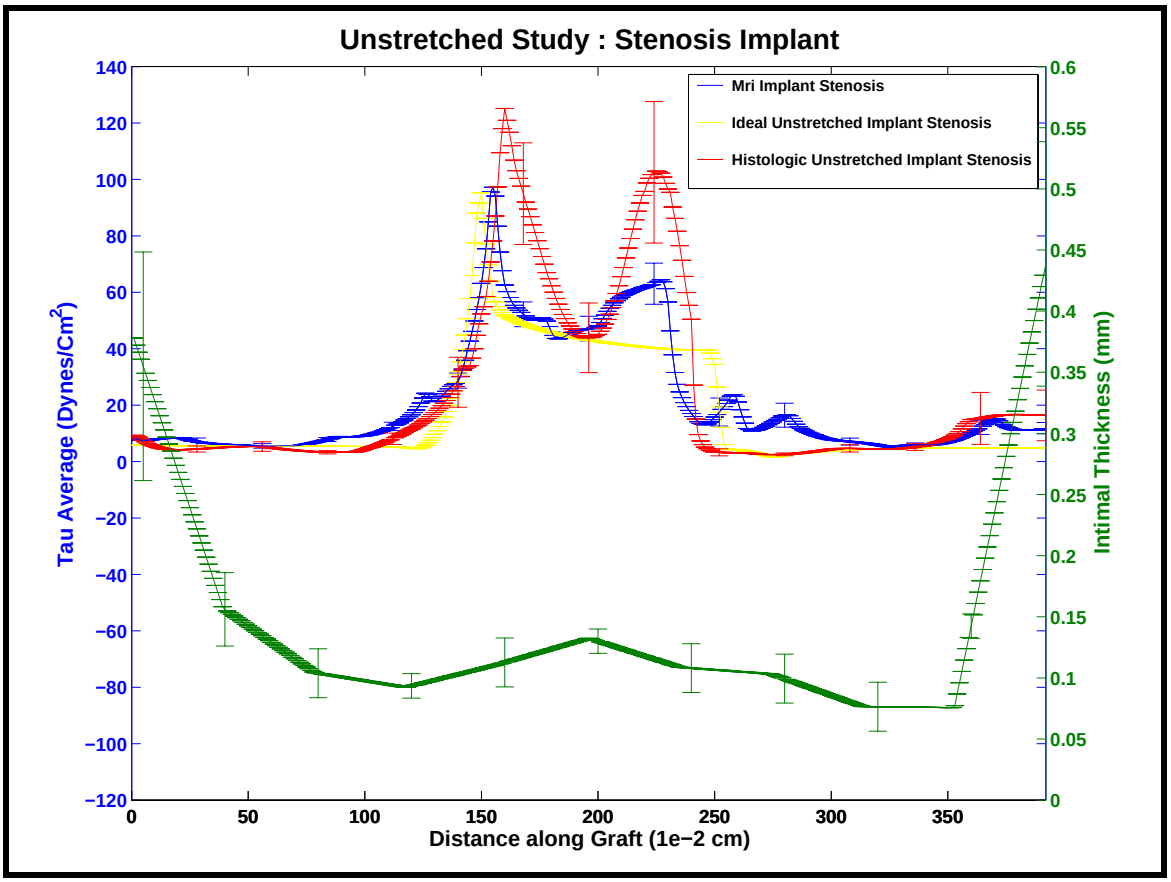

Figure 5.66: τavg and Intimal Thickness for Unstretched Implant Stenotic Grafts along the Axial Length of the Vessels.

seen with the Pulse WSS with the respective levels equally 180 dynes/cm^2, 250 dynes/cm^2, and 200 dynes/cm^2 (Figure 5.67). For harvest, the τavg did not increase to the same magnitude once the stenotic throat was entered. The ideal unstretched implant stenosis reached 38 dynes/cm^2 (Figure 5.68), while the histologic unstretched implant stenosis peaked at 53 dynes/cm^2, and the MRI unstretched implant stenosis hit a maximum at 35 dynes/cm^2. Once again, a mirrored picture was observed with the Pulse WSS with the respective levels equally 90 dynes/cm^2, 120 dynes/cm^2, and 100 dynes/cm^2 (Figure 5.69). As seen before, τavg and intimal thickness were compared. The PCMRI results resembled the harvest results both for τavg and the Pulse WSS (Figures 5.70, 5.71).

CFD Experimental Validation.

At the distal anastomosis of the MRI unstretched stenosis, the core velocity over the cardiac cycle was compared to the PCMRI measurements. At the same respective distal anastomotic position and corresponding points in time, the core velocities differed by only 7.09 %. In comparison, the same PCMRI measurements were compared to the histologic unstretched stenosis. With this computational grid, the core velocity differed by 38% from the PCMRI measurement. A node by node comparison was made between the PCMRI measurements and the two before-mentioned computational grids. The error was as large as 58 % for the MRI grid and 64 % for the histologic grid.

Comparison of Boundary Conditions.

Next, we investigated which of the volumetric flow rates, implant or harvest, modeled the physiology best. The τavg results for these two boundary conditions were compared to the τavg results using the PCMRI boundary condition. First, the MRI

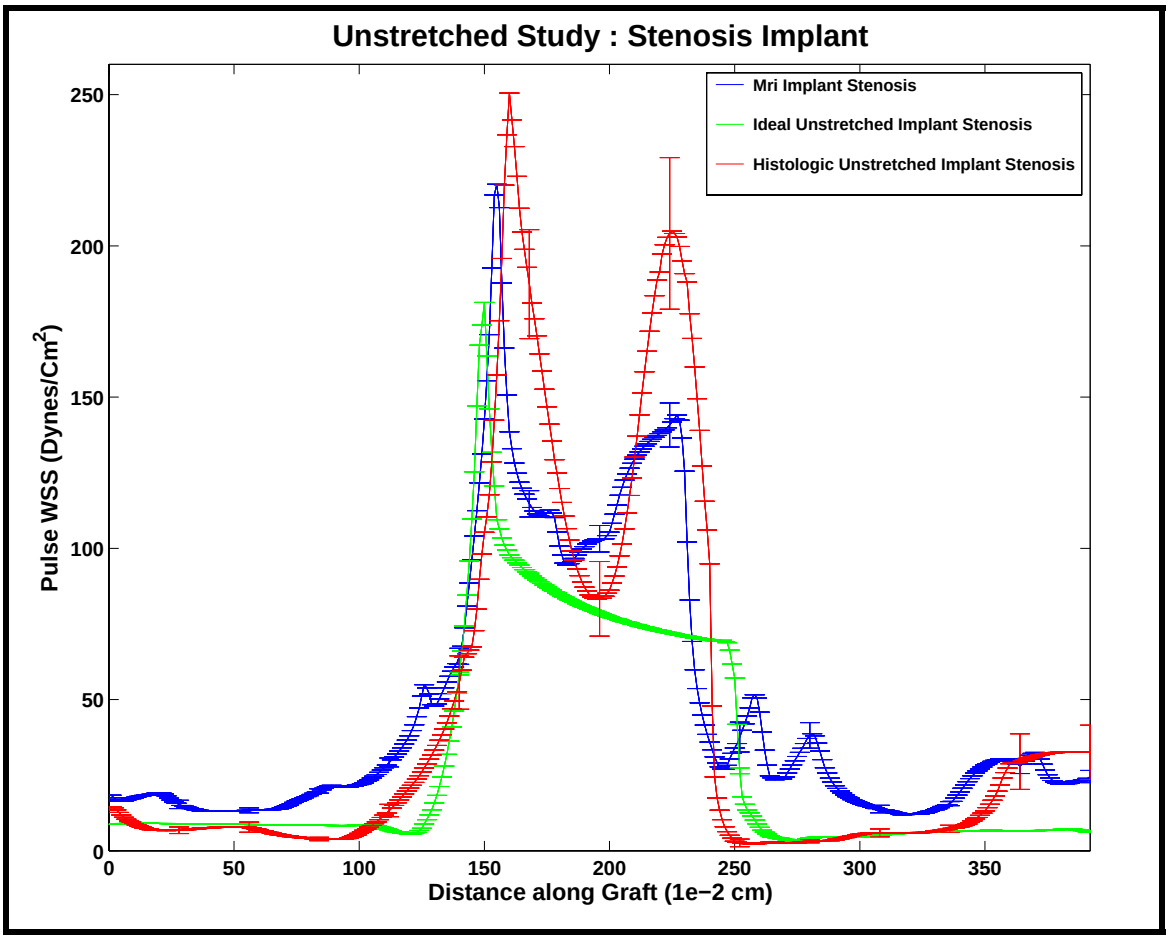

Figure 5.67: Pulse Wall Shear Stress for Unstretched Implant Stenotic Grafts along the Axial Length of the Vessels.

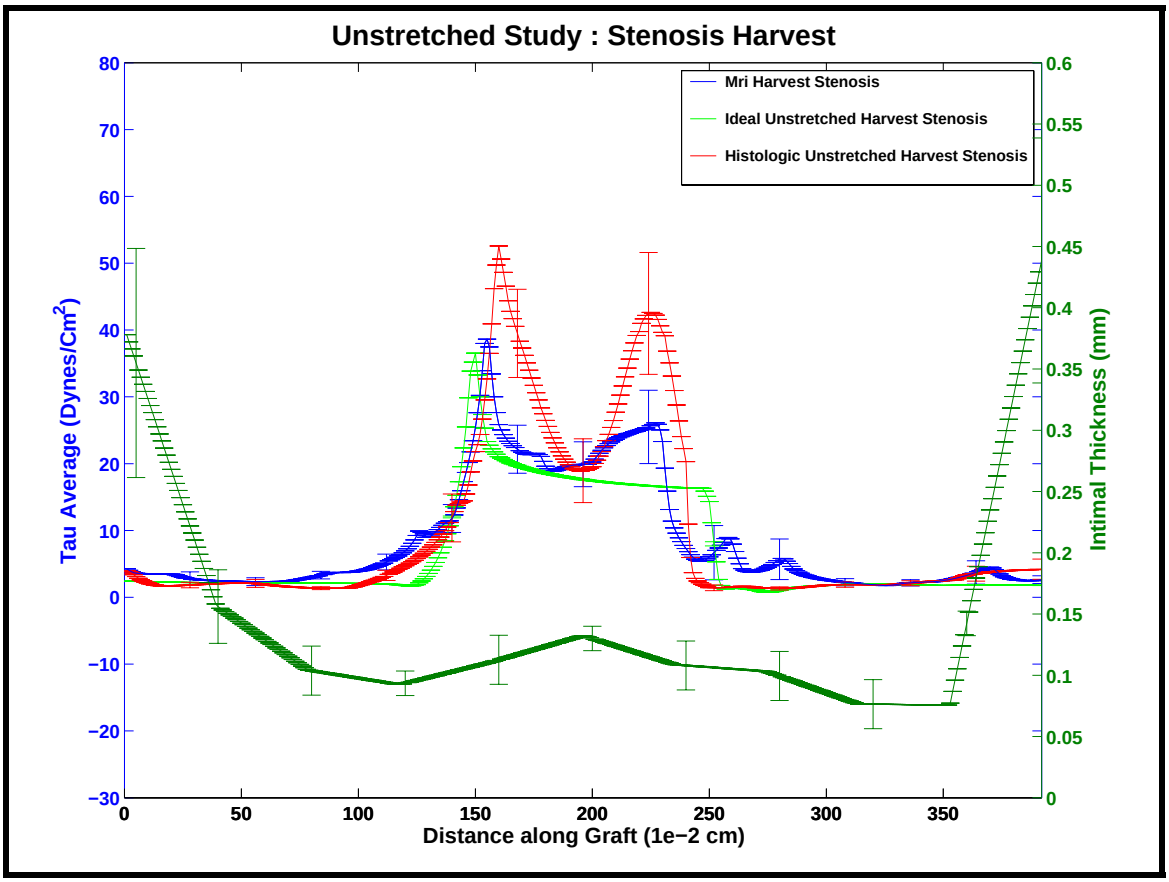

Figure 5.68: τavg for Unstretched Harvest Stenotic Grafts along the Axial Length of the Vessels.

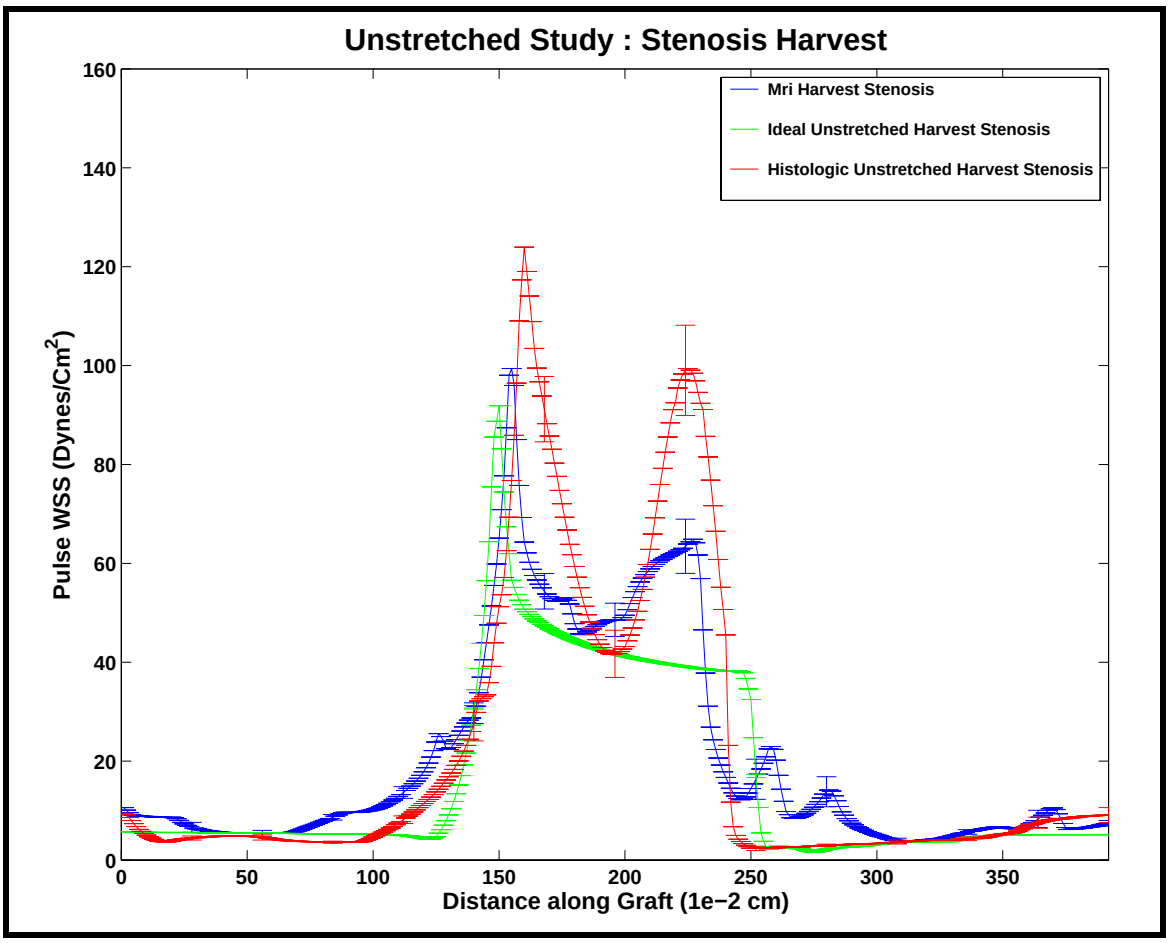

Figure 5.69: Pulse Wall Shear Stress for Unstretched Harvest Stenotic Grafts along the Axial Length of the Vessels.

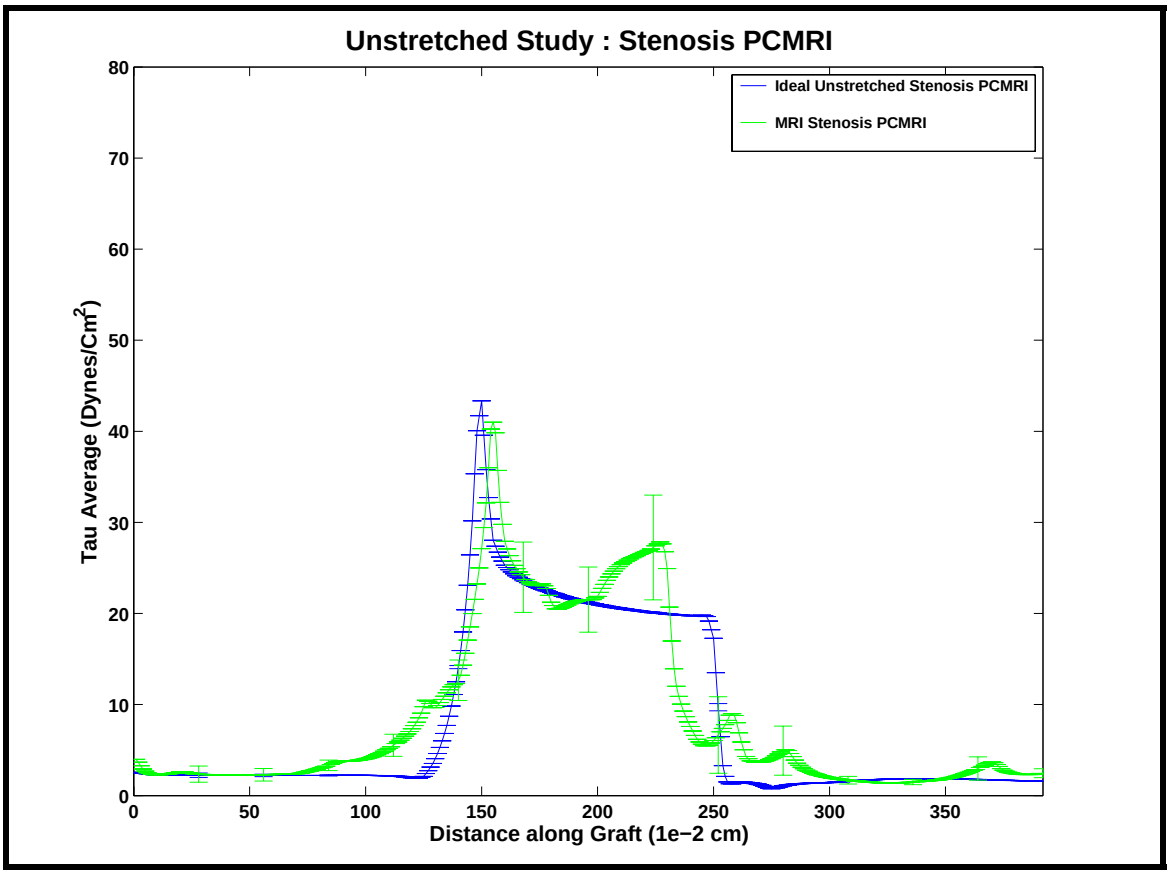

Figure 5.70: τavg for Unstretched PCMRI Stenotic Grafts along the Axial Length of the Vessels.

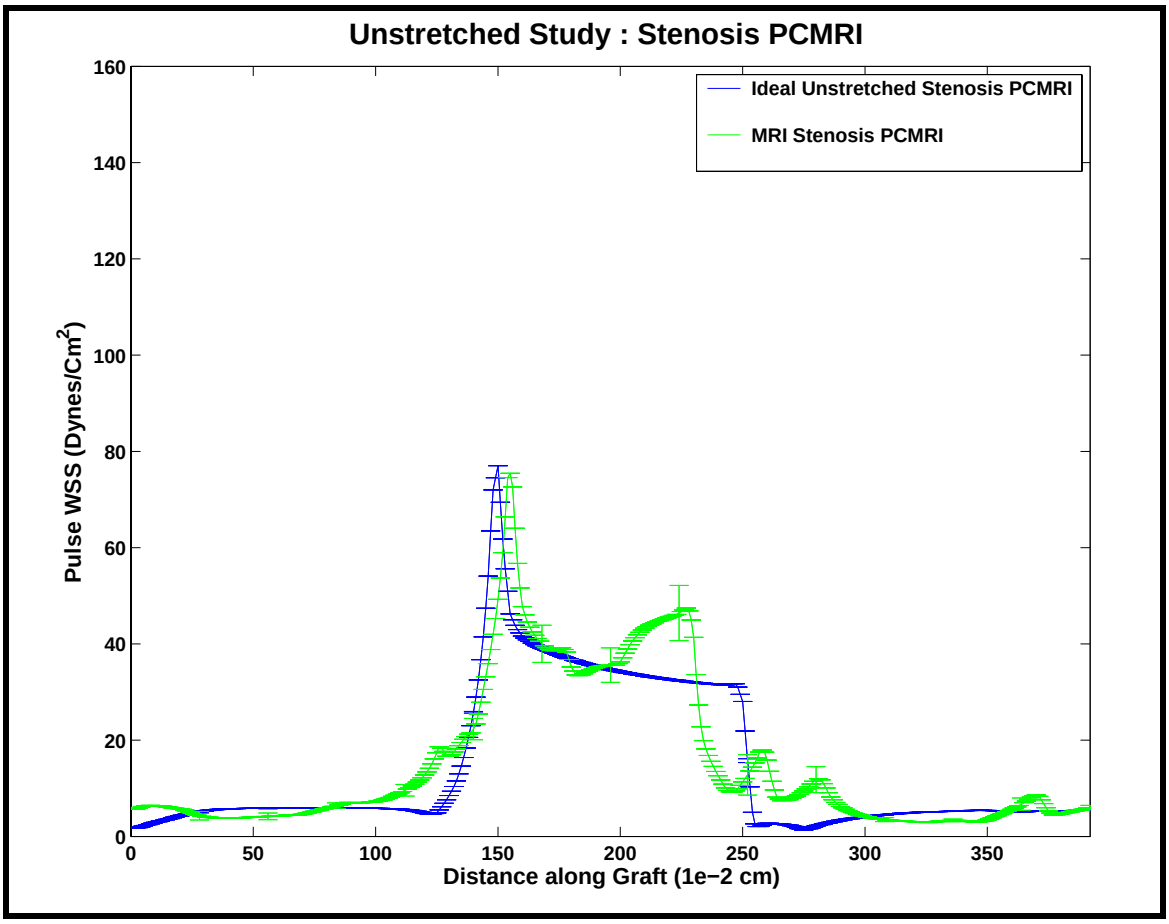

Figure 5.71: Pulse Wall Shear Stress for Unstretched PCMRI Stenotic Grafts along the Axial Length of the Vessels.

unstretched stenosis grid was analyzed. Between the PCMRI and the harvested volumetric boundary conditions, a 13.84 % difference in τavg was observed, while between the PCMRI and the implanted volumetric boundary conditions, a 192 % difference in τavg was seen. Next, the ideal unstretched stenosis grid was investigated. Between the PCMRI and the harvested volumetric boundary conditions, a 10.73 % difference in τavg was calculated, while between the PCMRI and the implanted volumetric boundary conditions, a 138 % difference in τavg was observed.

Comparison of Computational Grids.

The τavg values were compared between the five different models of the unstretched stenosis. Table 5.6 illustrates these results for implanted volumetric boundary conditions, while Table 5.7 highlights these results for harvested volumetric boundary conditions.

Correlations between WSS and Intimal Thickness.

Since the material properties of the stretched vascular grafts changed along the course of the vessel, little was gained from correlating the intimal thickness measurements with the hemodynamics. For the unstretched vascular grafts, the WSS measurements derived from harvest conditions and PCMRI were correlated to intimal thickness measurements. No statistically significant correlations were found between intimal thickness and OSI. In the case of the MRI unstretched stenosis, statistically significant correlation coefficients were identified between intimal thickness and the hemodynamics. For a harvested volumetric boundary condition, statistically significant correlation coefficients emerged between intimal thickness and the reciprocal of τavg (R = -.77), the reciprocal of the Pulse WSS (R = -.79), and the reciprocal of the maximum WSS (R = -0.79). For the PCMRI boundary condition, statistically significant correlation coefficients were observed

Table 5.6: Comparison of τavg at Implantation

Computational Grids	**Percent Difference in τavg**
MRI Unstretched Stenosis vs Histologic Unstretched Stenosis	41 %
MRI Unstretched Stenosis vs Ideal Unstretched Stenosis	40 %
Histologic Unstretched Stenosis vs Ideal Unstretched Stenosis	49 %
MRI Ensemble Average Unstretched Stenosis vs MRI Unstretched Stenosis with PCMRI	63 %
Ideal Ensemble Average Unstretched Stenosis vs MRI Unstretched Stenosis with PCMRI	52 %

Table 5.7: Comparison of τavg at Harvest

Computational Grids	**Percent Difference in τavg**
MRI Unstretched Stenosis vs Histologic Unstretched Stenosis	38 %
MRI Unstretched Stenosis vs Ideal Unstretched Stenosis	37 %
Histologic Unstretched Stenosis vs Ideal Unstretched Stenosis	46 %
MRI Unstretched Stenosis vs MRI Unstretched Stenosis with PCMRI	11 %
Ideal Unstretched Stenosis vs MRI Unstretched Stenosis with PCMRI	9 %

between intimal thickness and the reciprocal of τ_{avg} (R = -.78), the reciprocal of the Pulse WSS (R = -.80), and the reciprocal of the maximum WSS (R = -0.80).

Discussion:

The objective of this study was to investigate the differences in generating computational models of an *in vivo* vascular graft. Three different types of computational models were constructed: (1) ideal (2) histologic (3) MRI. Each of these models possessed certain strengths and weaknesses in capturing the geometry of an *in vivo* vascular graft. Since small errors in the arterial geometry resulted in large errors in the calculated wall shear stress, preservation of the arterial geometry was critically important. Upstream and downstream variations in geometry further compound this error in WSS. The actual CFD execution resulted in only a small amount of error. Researchers have documented that finite element discretization and computational techniques introduce an error in WSS calculations of only 6 to 8 percent [134,135]. The remaining error originates from techniques used to interrogate the vessel geometry and how that information is incorporated into a volumetric description of the vascular graft. This explanation helps to clarify the large variation in the τavg measurements between the different computational models (Tables 5.2 and 5.3).

Ideal Grids.

Ideal models were constructed based on the material dimensions of the designed vascular grafts. These ideal models incorporated the exact parameters of the vascular grafts before implantation. Unfortunately, the ideal grids failed to accurately model the dynamics of an *in vivo* vessel. When a graft was implanted into the distal abdominal aorta, numerous shape changes were imposed by adjacent structures. First, the lumbar lordosis curved the vascular graft. Second, the suture line changed the shape of both the proximal and distal anastomosis. Third, overlying structures altered the overall vessel configuration. The

ideal model did provide intuition into how the stenotic geometry altered the lumenal fluid mechanics; yet it provided no useful information when establishing a relationship between the intimal thickening and the vessel hemodynamics.

Histologic Grids.

The histologic model provided better details concerning an *in vivo* graft's geometry. The histologic model was constructed from the circular cross-sections of an *in vivo* pressure-perfused vessel. Previously, Moore [135] had created computational grids based on *ex vivo* pressure-perfused vessels. She recognized that fixing these grafts *ex vivo* introduced changes in the preserved shape of the vessel. She attempted to correct for these differences by introducing information gathered by x-ray computer tomography. Although this corrected some of the issues, problems still persisted. With any imaging modality, approximations have to be made as to where the borders reside. This fact holds true even for imaging modalities with very high degrees of resolution like X-ray CT. By using the histology, the exact borders of the vessel's wall can be outlined. These borders become distorted by post-mortem conditions such as *ex vivo* pressure perfusion. By fixing the vessel *in vivo*, these concerns were removed. The fixative preserved the exact shape of the vessel's wall. No technique provides the same level of detail for the wall location.

The histologic technique did suffer from some inherent limitations. The method failed to preserve any three dimensional information about how the cross-sections were oriented in space. Once the cross-sections were cut from the vessel, this information was forever lost. This spatial information was critical for accurate reconstruction of the vessel

shape. Other possible techniques for processing the tissue involved longitudinally sectioning the vessel. While this technique better illustrates the spatial orientation of the graft, it fails to preserve the exquisite information of wall location. More importantly, the information from these longitudinal sections is very difficult to use in the construction of a computational grid. The contours from the circular cross-sections better accommodated the construction of a cylindrically shaped object. Other investigators have argued general limitations associated with the histologic approach. First and foremost, approximations are always involved when processing the fresh tissue. For instance, when making circular cross-sections, the vessels are aligned next to a ruler and then the 5 mm tissue blocks are sectioned. This approach can introduce an error as large as 2 mm. Second, during the pressure-perfusion process, incomplete elastin fixation can result. Third, exposure of the retroperitoneum at sacrifice can alter the shape of the vessel even before fixation. The evisceration of the overlying bowel can induce a change in the vessel's geometry [138]. All of these reasons compelled us to seek alternative means to model the *in vivo* vessel geometry.

MRI Grids.

Magnetic Resonance Imaging provided a very powerful tool for non-invasively imaging an *in vivo* vessel. The MRI furnished exquisite information about the vessel orientation in space. The ability to image the vessel every 1 to 2 mm provided this level of three-dimensional detail. Such variations in the vessel shape as curvature were well preserved. By imaging the vessel using axial slices, the captured contours were then effectively incorporated into a computational grid. Unfortunately, the MRI faltered slightly in its

ability to map the vessel's wall. This MRI segmentation error leads to difficulty in reconstruction of the *in vivo* vessels. The MRI resolution limited our ability to map the outlines of the wall. At the very most, estimates of the vessel wall were in error by one pixel. For our MRI scanning, one pixel was equivalent to 0.15 mm. If we assume that a one-pixel error was made consistently around the vessel's circumference, the vessel's diameter can have an introduced error as large as 0.30 mm. For a large caliber vessel, this error is insignificant; however, for a small 3 mm inner diameter (id) stenotic throat, this error equals 10 % of the vessel's id. This error can exert a profound effect upon the calculations of wall shear stress. This noticeably contrasts with the 0.005 mm resolution of the histologic approach. The resolution of the histologic approach was determined by the microscope's magnification.

Cardiac gating eliminated some of the errors associated with outlining the vessel wall. This method reduced blurring of the wall that can introduce an error as large as 10 %. Other errors were introduced by the constraints of time-of-flight imaging. Saturation errors became important with slow moving blood. This issue assumed importance when imaging the post-stenotic regions where transient flow separation occurred. As illustrated through the CFD simulations, this transient flow separation was very distinct during diastole and even sometimes during systole. This effect can further reduce estimates of the luminal cross-section. The use of the gadolinium contrast marker and a large volume 3D gradient echo pulse sequence helped to mitigate this effect. Even despite these concerns, comparative results demonstrated that the MRI imaging reliably reconstructed the geometry of the *in vivo* vessel.

CFD Accuracy.

We evaluated the accuracy of the CFD simulations by comparing the results to the PCMRI velocity measurement. In this comparison we analyzed the core velocity. Initially, a node-by-node comparison was performed. In the case of the MRI grid, this produced a difference of 58 %, while for the histologic grid this generated a difference of 64 %. This discrepancy resulted from an assortment of reasons. First, when using the PCMRI measurements to calculate the velocity at each of the nodes, an interpolation scheme was used. As a result, a node-by-node comparison evaluated as much the accuracy of the interpolation scheme as the simulation's estimate of velocity. Second, the PCMRI velocity measurements were used as the standard of comparison. Although an adequate marker, PCMRI still possesses inherent limitations. The PCMRI was constrained by the same factors that restricted imaging of the vessel geometry. Near the wall, the PCMRI did not accurately evaluate the velocity of the moving blood. At this location, the velocity measurement was restricted by the pixel resolution. This motivated our decision to limit our comparison to the inner 75 % of the vessel's lumen or the core velocity. The PCMRI provided a very reliable means of experimentally measuring the vessel's core velocity. PCMRI can measure core velocity within 8 % of intravascular measurements; consequently, the PCMRI functioned as a good gold standard [139]. Upon comparison with the PCMRI, the small difference in core velocity helped to establish the MRI grid as a reliable representation of the *in vivo* geometry and its CFD results as reliable descriptors of the hemodynamic environment. The larger error of the histologic grid cast significant doubt upon its reliability as a computational model.

Boundary Conditions.

The PCMRI helped to establish which boundary condition was a more accurate description of the vessel physiology, implant or harvest volumetric flow rate. In comparison to the simulations using the PCMRI as a boundary condition, the harvest volumetric flow rate produced results that differed significantly less than the results generated by the implant volumetric flow rate. Why did the PCMRI function as a standard of comparison? The PCMRI velocity measurements were obtained two weeks following surgery. At this point, the animal had compensated for the implanted stenotic graft by adjusting its volumetric flow rate through the vessel. At the time of implantation, the animal had not even begun this process; therefore, the implant measurement was temporarily inflated. In conclusion, simulations performed with the harvest boundary conditions were considered more representative of the true hemodynamic environment imposed upon the vascular graft.

Correlations with Intimal Thickness.

Correlations were not made between the intimal thickness and the hemodynamics of the straight control grafts. The WSS measurements demonstrated too little variation to elaborate any underlying mechanism. Likewise, correlations were not made between the intimal thickness and the hemodynamics of the stretched stenosis. As documented earlier, its material properties changed along the length of the vascular graft; therefore, confusion surrounded whether any change in intimal thickening was a result of changing hemodynamics or changing material properties.

Earlier, we established the MRI unstretched stenosis as the most accurate description of the graft's *in vivo* geometry. Still, all of the other computational models still succeeded in qualitatively describing the gross features of the vessels' hemodynamics. For instance, in all models transient flow separation and high shear rate were isolated to the same relative location. The distinction in these models emerged when comparing the quantitative estimates of the flow field. For example, when comparing the core velocities to the experimentally measured PCMRI velocity, this distinguishing feature was highlighted. When correlating the biology and the hemodynamics, this difference was significant enough to produce contrasting conclusions. Having validated its results with the PCMRI, we felt comfortable in limiting our correlative study to the MRI grids.

In our analysis, we revealed that the most accurate estimates of WSS were made with boundary conditions from the PCMRI and harvested volumetric flow rate. An inverse relationship was established between the stenotic graft's intimal thickness and the reciprocal of τavg, Pulse WSS, and Max WSS. In essence, this result communicated a very interesting message concerning the healing of prosthetic vascular grafts. A positive relationship may exist between intimal healing and the wall shear stress. Our discussion within Chapter IV detailed why this may be happening.

In summary, this work investigated several different methods of generating a computational model of an implanted vascular graft. The MRI grids represented the best choice in preserving the geometry of the vessel and in accurately modeling its hemodynamics. Furthermore, both the volumetric flow rate at harvest and PCMRI served as the most appropriate parameters for the inlet boundary condition. Future work will

focus attention on improving our techniques of using MRI images to construct computational grids.

Chapter VI

Comparison of the Stretched and Unstretched Stenosis

This chapter outlines conclusions drawn from a comparison of the stretched and unstretched stenosis. While there were many similarities, the two graft types distinguished themselves as separate models. First and foremost, there existed a pronounced difference in the material properties of the two stenotic grafts. As previously discussed, the graft ultrastructure of the unstretched stenosis remained consistent between the upstream or downstream regions and the stenotic throat. Material alteration only occurred within the 0.25 cm transition regions before and after the stenotic throat. Within the stretched stenosis, the material properties changed along the course of the vascular graft. The stenotic throat represented the only region where the material properties were not altered. At this location, the original inner diameter was preserved, and there was no observed stretching of the graft material.

Between the two vascular grafts, two different hemodynamic environments were generated. A couple of different factors lead to this contrast. First, the length of the stenotic region varied between the two vascular graft types. The unstretched stenosis possessed an extended stenotic throat with a length of 1.5 cm, while the stretched stenosis symmetrically contracted according to a cosine function down from a 6 mm id to a 3 mm id.

Secondly, the actual reduction in cross-luminal area differed between the two vascular graft types. For the unstretched stenosis, the histologic analysis documented an upstream and downstream diameter of 5.9 ± 0.3 cm, while the MRI analysis observed an upstream and downstream diameter of 5.6 ± 0.13 cm. For the stenotic throat, the histologic analysis recorded a diameter of 3.2 ± 0.2 cm, while the MRI analysis documented a diameter of 2.9 cm ± 0.3 cm. In summary, the histologic analysis observed a 70 % reduction in its cross-luminal area, while the MRI analysis noted a 73 % reduction in its cross-luminal area. In the end, the average of the two methods described a 72 % reduction in the cross luminal area of the unstretched stenosis. For the stretched stenosis, the histologic analysis revealed an upstream and downstream diameter of 5.3 ± 0.3 cm, while for the stenotic throat, a diameter of 3.2 ± 0.2 cm was measured. For this stretched stenosis, a 63 % reduction in the cross-luminal area was created. Even before addressing other geometric differences, this result highlighted an important change in the hemodynamic environment of the two graft types.

The computational analysis further quantified this dissimilarity in the hemodynamic environment. Within the throat of the unstretched stenosis, the τavg equaled 31 dynes/cm^2, whereas the Pulse WSS equaled 67 dynes/cm^2. In comparison, within the throat of the stretched stenosis, the τavg equaled 15 dynes/cm^2, whereas the Pulse WSS equaled 38 dynes/cm^2. Not surprisingly, there emerged a difference in the measured intimal thickness of the two stenotic regions. In the case of the unstretched stenosis, the average intimal thickness equaled 0.132 ± 0.03 mm, while for the stretched graft study, the average intimal thickness equaled 0.34 ± 0.06 mm. A statistically significant difference existed between these two levels of intimal thickening. The

question then emerges as to why we observed this difference in the average intimal thickness.

Both graft varieties were implanted into baboon subjects with no variation in the surgical protocol. As a result, the vascular graft types were exposed to the same rheologic environment and humoral variables. Between the two grafts, the material properties were identical within the stenotic throat; therefore, both graft types possessed the same potential to heal by transmural ingrowth. At the stenotic throat, the luminal surfaces of both grafts were healed. The hemodynamic environment distinguished itself as the only remaining difference. As documented earlier, the unstretched stenosis evolved a higher level of WSS than the stretched stenosis. Upon comparison to the stretched stenosis, the τavg and Pulse WSS of the unstretched stenosis were respectively 106 % and 76 % larger. Focusing only on the stenotic throat, correlations were separately conducted between the two hemodynamic parameters (τavg and Pulse WSS) and the measured intimal thickness. The scatter plots display an inverse trend between the two WSS parameters and the measured intimal thickness (Figures 6.1 and 6.2). Due to the small sample size at the stenotic throat, a statisitical comparison can not be generated;however, the story described by the figures suggests an inverse relationship between the WSS and the intimal thickness. With a significant rise in WSS values, a mechanism arose that inhibited or controlled the intimal thickening.

In Chapter IV a positive relationship was identified between the intimal healing of the unstretched stenosis and the examined hemodynamics. Along the axial length of the vessel, this relationship was statistically shown between the intimal thickening and the

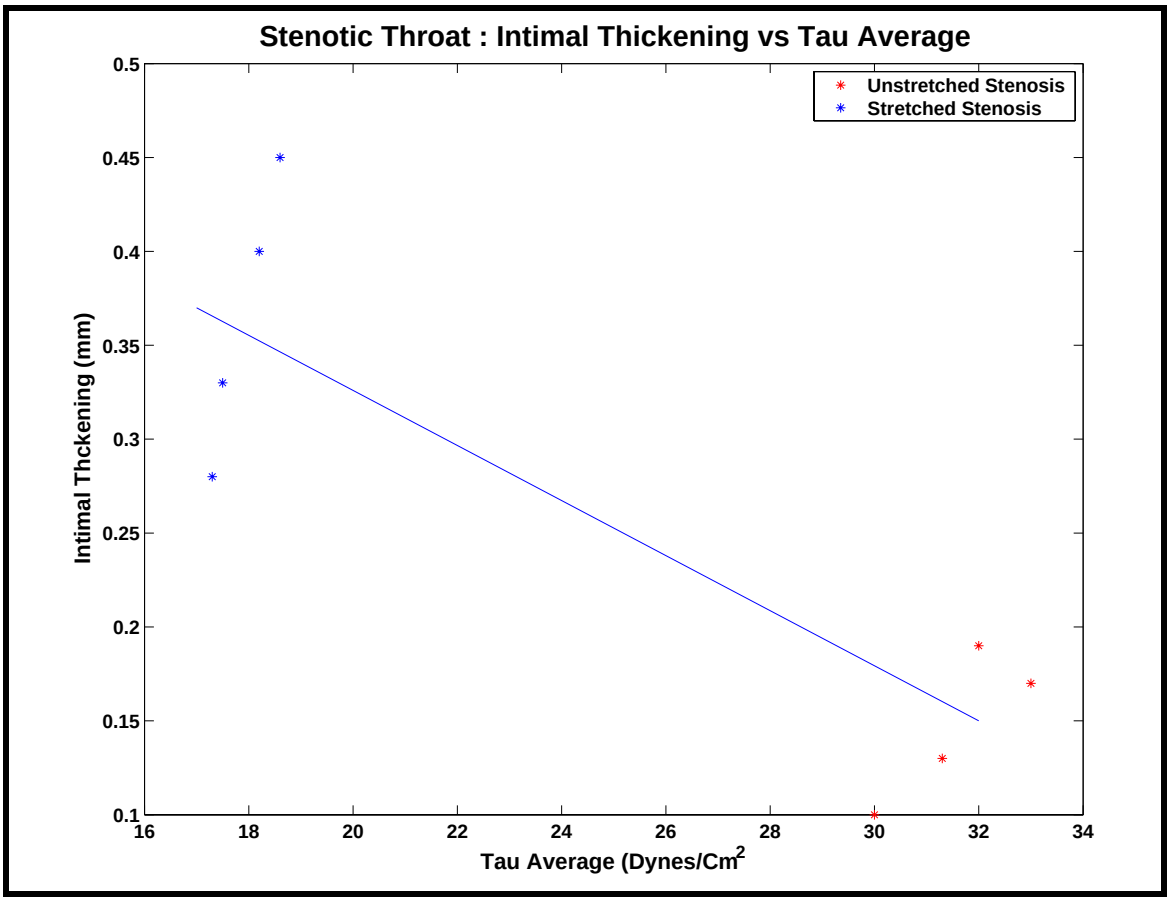

Figure 6.1: Scatter Plot of Intimal Thickening versus τavg.

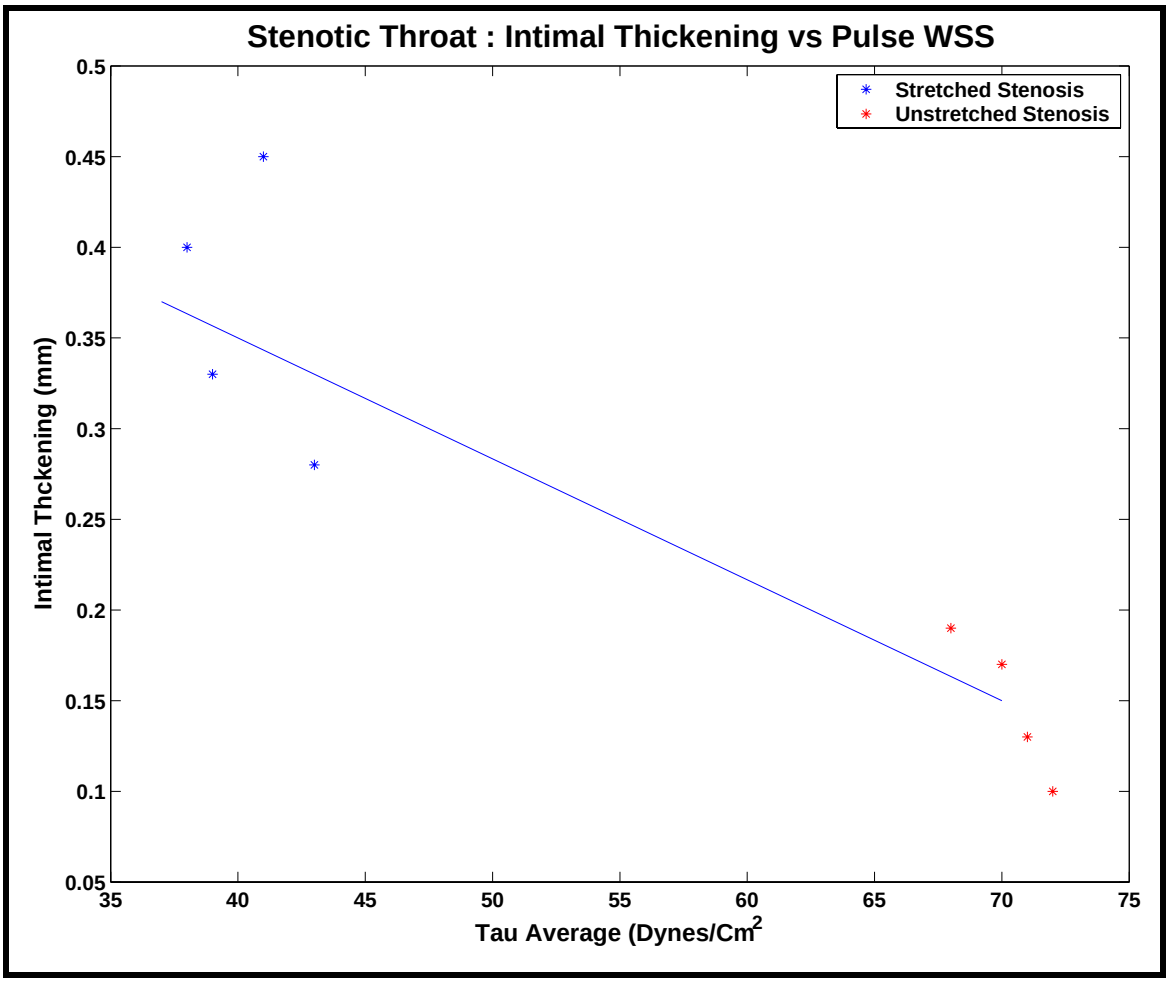

Figure 6.2: Scatter Plot of Intimal Thickening versus Pulse WSS.

reciprocals of τavg and Pulse WSS. A question then surfaces as to why an inhibitory effect was observed in the comparison of the two stenotic throats but not in this previously discussed analysis of the unstretched stenosis. In the Chapter IV discussion, the entire length of the vessel was investigated. Progressing along this axial expanse, both low and high WSS settings were encountered. In contrast our comparison of the stenotic throats was restricted to only high WSS environments. Within the throat of the unstretched stenosis, a significant amount of high WSS developed. This level was large enough to inhibit intimal thickening relative to the level observed within the stretched stenosis. Within its throat, the stretched stenosis generated a high WSS environment; however, the WSS did not achieve the magnitude necessary to inhibit intimal thickening. In the case of the unstretched stenosis, this needed level was attained. As a result, its measured intimal thickening was statistically different than the amount generated by the stretched stenosis.

This apparent need for a minimum level of high WSS assumed greater importance given that the shear stress responsive endothelium had only recently been deposited. This shear stress responsive endothelium occupies a critical role in detecting changes in the WSS. Since the endothelium had only recently been deposited, sufficient time had not passed for the vessel to adequately react to the changing hemodynamics. Potentially, the endothelium could only react to an excessively elevated level of WSS as seen within the unstretched stenosis. This leads us to question whether such an elevated level of high WSS would be needed if the shear stress responsive endothelium had been present during the entire period of implantation. Essentially, if the endothelium had been present for a longer period of time, other changes in the level of intimal thickening of the stretched

stenosis may have been recorded. This observation characterizes the differences in the healing dynamics between sub-acute and chronic studies of graft healing. In the future, greater insight may be offered by studies using tissue-engineered vessels already seeded with endothelial cells.

Chapter VII

Future Direction and Recommendations

This study provided a nice framework for future investigations of vascular grafts and their healing response. There is an assortment of different projects that could be pursued. First, further work could be conducted into the healing response of allogeneic vessels. Our previously discussed study documented how the vessels heal under sub-acute conditions. Naturally, the question arises as to how these vessels would heal under more chronic conditions and how the measurements of intimal thickening and media thickness would vary. The tools used in this work could be used to quantify the histology. Secondly, further investigations could be pursued into how graft ultrastructure affects healing. We would like to pursue a study where the void fraction of the graft material is changed but without a concordant reduction in graft thickness. Such a study would further reveal to what extent that transmural ingrowth is governed by such ultrastructure parameters as void fraction. Thirdly, we would like to further investigate the stenotic model of the vascular graft. We completed a detailed study under sub-acute conditions, and the natural progression follows to investigate the same questions under more chronic conditions. Furthermore, we are interested in the differences in graft healing as you progress around the circumference of the vessel. There are many possible questions that arise from such an investigation. Is more intimal thickening deposited upon the anterior or posterior surface post-stenotically and how does this relate to the hemodynamics?

Does the lumbar lordosis affect intimal deposition on the lateral walls of the graft? Such an investigation may provide additional insight into the relationship between hemodynamics and graft healing. In our already completed work this positional information was not preserved. New experimental techniques using molecular beacons may facilitate this approach. Lastly, we are interested in further studying vessel reconstruction of *in vivo* vascular grafts using such non-invasive imaging modalities as MRI. More powerful magnets have become available that possess much improved resolution. With greater resolution, the quality of the PCMRI measurements will also be enhanced. Improvements in the smoothing algorithm may better preserve details of the geometry. One possible means of improving the vessel reconstruction is by combining information from both the histology and the MRI. Combining the strengths of the histologic approach to capture the borders of the graft's wall with the three-dimensional information afforded by the MRI creates a very complete model. The construction of such a model will furnish future insight into how future models can be constructed using just the MRI information.

Chapter VIII

Bibliography

[1] Sawyer, P. **Modern Vascular Grafts**. McGraw-Hill Book, New York, NY, 1987.

[2] Greenwald, S.E. and Berry, C.L. Improving vascular grafts: the importance of mechanical and haemodynamic properties. **Journal of Pathology** 190: 292-299, 2000.

[3] Greisler, H.P. **New Biologic and Synthetic Vascular Prostheses**. R.G. Landes Company, Austin, TX, 1991.

[4] Zacharias, R.K., Kirkman, T.R., and Clowes, A.W. Mechanisms of healing in Synthetic Grafts. **Journal of Vascular Surgery** 6:429-436, 1987.

[5] Callow, A.D. Current status of vascular grafts. **Surgical Clinics of North America** 62:501-513, 1982.

[6] Darling, R.C. and Linton R.R. Durability of femoropopliteal reconstructions. Endarterectomy versus vein bypass grafts. **American Journal of Surgery** 123:472-479, 1972.

[7] Clayson, K.R., Edwards, W.H., Allen, T.R., and Dale, W.A. Arm veins for peripheral arterial reconstruction. **Archives of Surgery** 111:1276-1280, 1976.

[8] Carrell, A. Ultimate results of aortic transplantations. **Journal of Experimental Medicine** 15:389-412, 1912.

[9] Szilagyi, D.E., McDonald, R.T., Smith R.F., and Whitcomb, J.G. Biologic fate of human arterial homografts. **Archives of Surgery** 75:506, 1957.

[10] Sauvage, L.R. A brief history of arterial prosthesis development. **Journal of Investigational Surgery** 6:221-225, 1993.

[11] Vorhees, AB.J., Jaretzki, A.I., Blakemore, A.H. The use of tubes constructed from Vinyon ‘N’ cloth in bridging arterial defects. A preliminary report. **Annals of Surgery** 135: 332-336, 1952.

[12] Blakemore, A.H. and Vorhees, A.B. The use of tubes constructed from Vinyon 'N' cloth in bridging arterial defects. Experimental and clinical. **Annals of Surgery** 140: 324-334, 1954.

[13] Mortensen, J.D. Vascular replacements: a study of safety and performance. NIH Report No. FDA/BMD-81/65, 1981.

[14] White, R.A. Vascular Prostheses: present status and future development. In: Williams D.F., ed. **Blood Compatability**. Boca Raton, Fl: CRC Press 1987; 47-62.

[15] Fischell, T.A. and Stadius, M.L. New technologies for the treatment of obstructive arterial disease. **Cathet Cardiovasc Diagn** 22:205-233, 1991.

[16] Roubin, G.S., King, S.B., Douglas, J.S., Lembo, N.J., and Robinson, K.A. Intracoronary stenting during percutaneous transluminal coronary angioplasty. **Circulation** 81: IV-92-IV-100, 1990.

[17] Johnson, P.C., Sheppeck, R.A., Hribar, S.R., Bentz, M.L., Janosky, J., and Dickson, S. Inhibition of platelet retention on artificial micrografts with monoclonal antibodies and high affinity peptide directed against platelet membrane glycoproteins. **Arteriosclerosis and Thrombosis** 11:552-560, 1991.

[18] Salzman, E.W. The limitations of heparin therapyafter arterial reconstruction. **Surgery** 57:131-138, 1965.

[19] Clowes, A.W., Reidy, M.A. Prevention of restenosis after vascular reconstruction: pharmocologic control of intimal hyperplasia. A review. **Journal of Vascualr Surgery** 13:885-891, 1991.

[20] Goldman, M., Norcott, H.C., Hawker, R.J., Drolc, Z., McCollum, C.N. Platelet accumulation on mature Dacron grafts in man. **British Journal of Surgery** 69:S38-S43, 1982.

[21] NHLBI Working Groups. 1985. Guidelines for Blood-Material Interactions. **NIH Publication No. 85-2185.** National Institutes of Health. Bethesda, MD.

[22] Harker, L.A. and Hanson, S.R. Experimental arterial thromboembolism in baboons: Mechanism, quantitation and pharmacologic prevention. **Journal of Clinical Investigation** 64:559, 1979.

[23] Schneider, P.A., Kotze, H.F., Heyns, A., and Hanson, S.R. Thromboembolic potential of synthetic vascular grafts in baboons. **Journal of Vascular Surgery** 10:75-82, 1989.

[24] Yeh, Y.S., Iriyama, T., Matsuzawa, Y., Hanson, S.R., Yasuda H. Blood compatability of surface modified by plasma polymerization. **Journal of Biomaterial Research** 22:795-818, 1988.

[25] Golden, T., Hanson, S.R., Kirkman, T., Schneider, P.A., Clowes, A.W. Healing of polytetrafluoroethylene grafts is influenced by graft porosity. **Journal of Vascular Surgery** 11:838-845, 1990.

[26] Hanson, S.R., Harker, L.A., Ratner, B.D., and Hoffman, A.S. In vivo evaluation of artificial surfaces using a nonhuman primate model of arterial thrombosis. **Journal of Laboratory Clinical Medicine** 95:289-304, 1980.

[27] Carrel, A. and Guthrie, C.C. Anastomosis of blood vessels by the patching method and transplantation of the kidney. **JAMA** 47:1648-50, 1906.

[28] Stchelkounoff, I. L'intima des petites arteres et des veines et le mesenchyme vasculaire. **Archivs Anatomie Microscopie et Morphologie Experimentalles** 32:139-94, 1936.

[29] Spaet, T.H., Stemerman, M.B., Veith, F.J., Lejnieks, I. Intimal injury and regrowth in the rabbit aorta. Medial smooth muscle cells as a source of neointima. **Circulation Research** 36:58-70, 1975.

[30] Webster, W.S., Bishop, S.P., Geer, J.C. Experimental aortic intimal thickening. Morphology and source of intimal cells. **American Journal of Pathology** 76:245-64, 1974.

[31] Hassler, O. The origin of the cells constituting arterial intima thickening. An experimental autoradiographic study with the use of H^3-thymidine. **Laboratory Investigation** 22:286-93, 1970.

[32] Poole, J.C.F., Sabiston, D.C., Flory, H.W., and Allison, P.R. Growth of endothelium in arterial prosthetic grafts and following endarterectomy. **Surgical Forum** 13:225-7, 1962.

[33] Florey, H.W., Greer, S.J., Kiser, J., Poole, J.C.F., Telander, R., and Wertherssen, N.T. The development of pseudointima lining fabric grafts of the aorta. **British Journal of Experimental Pathology** 43:655-60, 1962.

[34] Stump, M.M., Jordan, G.L., DeBakey, M.E., Halpert, B. Endothelium grown from circulating blood on isolated intravascular Dacron hub. **American Journal of Pathology** 43: 361-7, 1963.

[35] Mackenzie, J.R., Hackett, M., Topuzlu, C., and Tibbs, D.J. Origin of arterial prosthesis lining from circulating blood cells. **Archives of Surgery** 97: 879-85, 1968.

[36] Shi, Q., Wu, H-D., Hayashida, N., Wechezak, A.R., Clowes, A.R., and Sauvage, L.R. Neoendothelialization of isolated Dacron grafts from endothelial cells in the circulation : observations in a canine model [Abstract] 1192:95.

[37] Wu, M., Shi, Q., Wechezak, A., Clowes, A., Gordon, I., and Sauvage, L. Definitive proof of endothelialization of a Dacron arterial prosthesis in a human being. **Journal of Vascular Surgery** 21: 862-7, 1995.

[38] Harker, L.A., Kelly, A.B., and Hanson, S.R. Experimental Arterial Thrombosis in Nonhuman Primates. **Circulation** 83:IV-41-IV-55, 1991.

[39] Clowes, A., Kirkman, T.R., and Reidy, M.A. Mechanisms of Arterial Graft Healing : Rapid Transmural Capillary Ingrowth Provides a Source of Endothelium and Smooth Muscle in Porous PTFE Prostheses. **American Journal of Physiology** 123:220-230,1986.

[40] Clowes, A.W., Kirkman, T.R., and Clowes, M.M. Mechanisms of arterial graft failure. II. Chronic endothelial and smooth muscle cell proliferation in healing polytetrafluoroethylene prostheses. **Journal of Vascular Surgery** 3:877-84, 1986.

[41] Lumsden, A.B., Chen, C., Coyle, K.A., Ofenloch, J.C., Wang, J., Yasuda, H.K., Hanson, S.R. Nonporous silicone polymer coating of expanded polytetrafluoroethylene grafts reduces graft neointimal hyperplasia in dog and baboon models. **Journal of Vascular Surgery** 24:825-33, 1996.

[42] Wesolowski, S.A., Fries, C.C., Karlson, K.E., DeBakey, M., and Sawyer, P.N. Porosity: primary determinant of ultimate fate of synthetic vascular grafts. **Surgery** 50:91-6, 1961.

[43] Florey, H.W., Greer, S.J., Kiser, J., Poole, J.C.F., Telander, R., and Werthessen, N.T. The development of the pseudointima lining fabric grafts of the aorta. **British Journal of Experimental Pathology** 43: 655-60, 1962.

[44] Clowes, A.W., Gown, A.M., Hanson, S.R., and Reidy, M.A. Mechanisms of Arterial Graft Failure: 1. Role of Cellular Proliferation in early Healing of PTFE Prostheses. **American Journal of Pathology** 118: 43-54, 1985.

[45] Reidy, M.A., Chao, S.S., Kirkman, T.R., and Clowes, A.W. Endothelial Regeneration: VI. Chronic Nondenuding Injury in Baboon Vascular Grafts. **American Journal of Pathology** 123:432-39, 1986.

[46] Zacharias, R.K., Kirkman, T.R., Kenagy, R.D., Bowen-Pope, D., Clowes, A.W. Growth factor production by polytetrafluoroethylene vascular grafts. **Journal of Vascular Surgery** :606-10, 1988.

[47] McClurken, M.E., McHaney, J.M., and Colone, W.M. Physical Properties and test methods for expanded polytetrafluoroethylene (PTFE) grafts. **Vascular Graft update: safety and Performance** 82-94, 1986.

[48] Salzmann, D.L., Yee, D.C., Roach, D.J., Berman, S.S., and Williams, S.K. Effects of balloon dilatation on ePTFE structural characteristics. **Journal of Biomedical Material Research** 36:498-507, 1997.

[49] Wolinsky, H. and Glagov, S. A lamellar unit of aortic medial structure and function in mammals. **Circulation Research** 20:99-111, 1967.

[50] Brownlee, R.D., and Langille, B.L. Arterial adaptations to altered blood flow. **Can J Physiol Pharmocol** 69:978-983, 1991.

[51] Guyton, J.R. and Hartley, C.J. Flow restriction of one carotid artery in juvenile rats inhibits growth of arterial diameter. **American Journal of Physiology** 248:H540-H546, 1985.

[52] Bendeck, M.P. and Langille, B.L. Rapid accumulation of elastin and collagen in the aortas of sheep in the immediate perinatal period. **Circulation Research** 69:1165-1169, 1991.

[53] Fry, D.L. Responses of the arterial wall to certain physical factors. **Ciba Found Symp** 12:93-125, 1973.

[54] Caro, C.G., Fitz-Gerald, J.M., and Schroter, R.C. Atheroma and arterial wall shear: Observation, correlation, and proposal of a shear dependent mass transfer mechanism for atherogenesis. **Proceedings of the Royal Academy of Science** 117:109-159, 1971.

[55] Ku, D.N., Giddens, D.P., Zarins, C.K., and Glagov, S. Pulsatile Flow and Atherosclerosisin the Human Carotid Bifurcation: Positive Correlation between Plaque Location and Low and Oscillating Shear Stress. **Arteriosclerosis** 5:293-302, 1985.

[56] Zarins, C.K., Giddens, D.P., Bharadvaj, B.K., Sottiurai, V.S., Mabon, R.F., Glagov, S. Carotid bifurcation atherosclerosis: Quantitative correlation of plaque localization with flow velocity profiles and wall shear stress. **Circulation Research** 3:31-39, 1983.

[57] Kraiss, L.W., Kirkman, T.R., Kohler, T.R., Zierler, B., Clowes, A.W. Shear Stress Regulates Smooth Muscle Proliferation and Neointimal Thickening in Porous Polytetrafluoroethylene Grafts. **Arteriosclerosis and Thrombosis** 11:1844-1852, 1991.

[58] Geary, R.L., Kohler, T.R., Vergel, S., Kirkman, T.R., and Clowes, A.W. Time course of flow-induced smooth muscle cell proliferation and intimal thickening in endothelialized baboon vascular grafts. **Circulation Research** 74:14-23, 1993.

[59] Mattsson, E., Kohler, T.R., Vergel, S.M., and Clowes, A.W. Increased Blood Flow Induces Regression of Intimal Hyperplasia. **Arteriosclerosis, Thrombosis, and Vascular Biology** 17:2245-2249, 1997.

[60] Giddens, D.P., Mabon, R.F., and Cassanova, R.A. Measurements of disordered flows distal to subtotal vascular stenosis in the thoracic aorta of dogs. **Circulation Research** 39:112-119, 1976.

[61] Lieber, B.B. Ordered and Random Structures in Pulsatile Flow through Constricted Tubes. Ph.D. Thesis, Georgia Institute of Technology, Atlanta, Georgia, 1985.

[62] Markou, C.P., Lutostansky, E.M., Ku, D.N., and Hanson, S.R. A Novel Method for Efficient Drug Delivery. **Annals of Biomedical Engineering** 26: 502-511, 1998.

[63] Rogers, C. Thrombotic heart disease and myocardial infarction: Local Therapy. **Molecular Interventions and Local Drug Delivery** Saunders, London, 1995.

[64] Lincoff, A.M., Topol, E.J., and Ellis, S.G. Local Drug Delivery for the prevention of Restenosis- Fact, fancy, and future. **Circulation** 90:2070-2084, 1994.

[65] Nathan, A. and Edelman, E.R. Local interventions for vasculoproliferative diseases. **Molecular Interventions and Local Drug Delivery** Saunders, London, 1995.

[66] Bird, R.B., Stewart, W.E., and Lightfoot, E.N. **Transport Phenomena** Wiley, New York, 1960.

[67] Scott, N.A., Nunes, G.L., King, S.B., Harker, L.A., and Hanson, S.R. Local Delivery of an Antithrombin Inhibits Platelet- Dependent Thrombosis. **Circulation** 90:1951-55, 1994.

[68] Chen, C., Hanson, S.R., Lumsden, A.B. Boundary layer infusion of heparin prevents thrombosis and reduces neointimal hyperplasia in venous polytetrafluoroethylene grafts without systemic anticoagulation. **Journal of Vascular Surgery** 22: 237-47, 1995.

[69] Chen, C., Hughes, J.D., Mattar, S.G., Hanson, S. R., and Lumsden, A.B. Transgraft Infusion of Heparin to Prevent Early Thrombosis of Expanded PTFE Grafts in Canine Femoral Veins. **Annals of Vascular Surgery** 10:147-155, 1995.

[70] Chen, C., Lumsden, A.B., and Hanson S.R. Local Infusion of heparin reduces anastomotic neointimal hyperplasia in aortoiliac expanded polytetrafluoroethylene bypass grafts in baboons. **Journal of Vascular Surgery** 31: 354-63, 2000.

[71] Mattar, S.G. et. al. Local Infusion of FGF-Saporin Reduces Intimal Hyperplasia. **Journal of Surgical Research** 60:339-344, 1996.

[72] Chen, C. et al. Boundary Layer Infusion of Nitric Oxide Reduces Early Smooth Muscle Cell Proliferation in the Endarterectomized Canine Artery. **Journal of Surgical Research** 67: 26-32, 1997.

[73] Leung, D.W., Cachianes, G., Kuang, W.J., Goeddel, D.V., and Ferrara, N. Vascular endothelial growth factor is a secreted angiogenic mitogen. **Science** 246:1306-9, 1989.

[74] Ferrara, N., Henzel, W.J. Pituitary follicular cells secretea novel heparin-binding growth factor specific for vascular endothelial cells. **Biochemical and Biophysical Research Communication** 161: 851-5, 1989.

[75] Leung, D.W., Cachianes, G., Kuang, W., Goeddel, D.V., and Ferrara, N. Vascular Endothelial Growth Factor is a Secreted Angiogenic Mitogen. **Science** 246:1306-1309, 1989.

[76] Zachary, I., Mathur, A., Yla-Herttuala, S., and Martin, J. Vascular protection: A novel nonangiogenic cardiovascular role for vascular endothelial growth factor. **Arteriosclerosis, Thrombosis, and Vascular Biology** 20:1512-1520, 2000.

[77] Laitinen, M., Zachary, I., Breier, G., Pakkanen, T., et. al. VEGF gene transfer reduces intimal thickening via increased production of nitric oxide in carotid arteries. **Human Gene Therapy** 8:1737-1744, 1997.

[78] Criscuolo, G.R., Lelkes, P.I., Rotrosen, D., Oldfield, E.H. Cytosolic calcium changes in endothelial cells induced by a protein product of human gliomas containing vascular permeability factor activity. 71:884-91, 1989.

[79] Bates, D.O. and Curry, F.E. Vascular endothelial growth factor increases microvascular permeability via a Ca^{2+}-dependent pathway. **American Journal of Physiology** 273:H687-H694, 1997.

[80] Wheeler-Jones, C., Abu-Ghazaleh, R., Cospedal, R., Houliston, R.A., Martin, J., and Zachary, I. Vascular endothelial growth factor stimulates prostacyclin production and activation of cytosolic phospholipase A_2 in endothelial cells via p42/p44 mitogen activated protein kinases. **FEBS Letters** 420:28-32, 1997.

[81] Von der Leyen, H.E., Gibbons, G.H., Morishita, R., Lewis, N.P., Zhang, L., Nakajima, M., Kaneda, Y., Cooke, J.P., and Dzau, V.J. Gene therapy inhibiting

neointimal vascular lesion: in vivo transfer of endothelial cell nitric oxide synthase gene. **Proceedings of National Academy of Science** 92:1137-1141, 1995.

[82] Garg, U.C., and Hassid, A. Nitric oxide-generating vasodilators and 8-bromocyclic guanosine monophosphate inhibit mitogenesis and proliferation of cultured rat vascular smooth muscle cells. **Journal of Clinical Investigation** 83:1774-1777, 1989.

[83] Asahara et al. Local Delivery of vascular endothelial growth factor accelerates reendothelialization and attenuates intimal hyperplasiain balloon injured rat carotid artery. **Circulation** 91:2793-2801, 1995.

[84] Hood, J.D., Meininger, C.J., Ziche, M., and Granger, H.J. VEGF upregulates ecNOS message, protein, and NO production in human endothelial cells. **American Journal of Physiology** 274:H1054-H1058, 1998.

[85] Gerber, H.P., McMurtrey, A., Kowalski, J., Yan, M., Keyt, B.A., Dixit, V., and Ferrara, N. Vascular endothelial growth factor regulates endothelial cell survival through the phosphatidylinositol 3'-kinase/Akt signal transduction pathway. **Journal of Biological Chemistry** 273:30336-30343, 1998.

[86] Thakker, G.D., Hajjar, D.P., Muller, W.A., and Rosengart, T.K. The role of phosphatidylinositol 3'-kinase in vascular endothelial growth signaling. **Journal of Biological Chemistry** 274:10002-10007, 1999.

[87] Abedi, H. and Zachary, I. Vascular endothelial growth factor stimulates tyrosine phosphorylation and recruitment to new focal adhesions of focal adhesion kinase and paxillin in endothelial cells. **Journal of Biological Chemistry** 272:15442—15451, 1997.

[88] Karolyi, I. Atherosclerotic Disease. **Proceedings of the American Heart Association.** November 2000.

[89] Dobron, P.B. **Intimal Hyperplasia.** R.G. Landes Company, Austin, TX, 1994.

[90] Reese, J.C., Esteryl, R., Lindsey L. A Prospective Randomized Comparison of Bovine Hetografts Versus Impra Grafts for Chronic Hemodialysis. In: Vasculature Access for Hemodialysis. Precept Press Inc, Hong Kong, 1993.

[91] Ku, D. and Wooten, D. Fluid Mechanics of Vascular Systems, Diseases, and Thrombosis. **Annual Review of Biomedical Engineering** 001: 299-329, 1999.

[92] McPhee, S., Lingappa, V., and Ganong, W. **Pathobiology of Disease: An Introduction to Clinical Medicine.** Appleton and Lange, 1997.

[93] Harrison, D. **Principles of Internal Medicine.** McGraw-Hill Book, New York, NY, 1998.

[94] Loth, F. et al. Relative Contribution of Wall Shear Stress and Injury in Experimental Intimal Thickening at PTFE End-To-Side Arterial Anastomoses. **Journal of Biomechanical Engineering** 124: 44-51, 2002.

[95] Grindin, C., Meere, C., Custonguay, Y. et al. Progression of Intimal Hyperplasia. **Journal of Investigational Pathology.** 112: 34-45, 1996.

[96] Stchelkounoff. L'Intima des Petites Arteres et des Veines et le Mesenchyme Vasculaire. **Archivs Anatomie Microscopie et Morphologie Experimentalles** 43: 139-194, 1936.

[97] Allaire, E. and Clowes, A. Endothelial Cell Injury in Cardiovascular Surgery: The Intimal Hyperplastic Response. **Ann. Thoracic Surg.** 63: 582-591, 1997.

[98] Davie, M.G. and Hagen, P.O. The Vascular Endothelium. A New Horizon. **Annals of Surgery.** 218: 593-609, 1993.

[99] Springer, T.A. Traffic Signals on Endothelium for Lymphocyte Recirculation and Leukocyte Emigration. **Annual Review of Physiology.** 57: 827-872, 1995.

[100] Languille, B.L. and O'Donnell, F. Reduction in Arterial Diameter Produced by Chronic Diseases in Flow are Endothelium Dependent. **Science.** 231: 305-307, 1986.

[101] Ross, R. The Pathogenesis of Atherosclerosis: A Perspective for the 1990s. **Nature.** 362: 801-809, 1993.

[102] Lin, Y., Weisdorf, D., Solovey, A. et al. Origins of Circulating Endothelial Cells and Endothelial Outgrowth from Blood. **Journal of Clinical Investigation.** 105: 71-77, 2000.

[103] Palmaz, J.C., Tio, F., Laborde, J. et al. Use of Stents Covered with Polytetrapolyfluoroethylene in Experimental Abdominal Aortic Aneurysm. **Journal of Vascular Intervention.** 6: 879-885, 1995.

[105] Berger, K. et al. Healing of Arterial Prosthesisin Man: its Incompleteness. **Annals of Surgery.** 175: 118-127, 1972.

[106] Goldman, M. et al. Dacron Arterial Grafts: the Influence of Porosity, Velou, and Maturity on Thrombogenicity. **Surgery.** 92: 947-952, 1982.

[107] Stratton, J.R., Tricle, B.L., and Ritchie, J.L. Natural History of Platelet Deposition in Dacron Aortic Bifurcation Grafts in the First Year after Implantation. **American Journal of Cardiology.** 52: 371-374, 1983.

[108] Reidy, M.A., Clowes, A.W., and Schwartz, S.M. Inhibition of Endothelial Cell Growth: Cessation of Aortic Endothelial Cell Replication after Balloon Catheter Denudation. **Arteriosclerosis.** 2: 216, 1982.

[109] Reidy, M.A., Stadaert, D., and Schwartz, S.M. Endothelial Regeneration: V. Inhbition of Endohelial Regrowth in arteries of rats and rabbits. **Laboratory Investigation.** 49: 569-575, 1983.

[110] Grondin et al. Comparison of late Change in internal mammary artery and saphenous vein grafts in two consecutive series of patients 10 years after operation. **Circulation.** 70 (suppl I): 208-212, 1984.

[111] Gurlek, A., Dagalp, Z., et al. Restenosisafter transluminal coronary angioplasty: a rish factor analysis. **Journal of Cardio-Vascular Risk.** 2: 51-55,1995.

[112] Bassiouny, H. et al. Anastomotic Intimal Hyperplasia: Mechanical Injury or Flow Induced. **Journal of Vascular Surgery** 15(4), 708-717, 1992.

[113] Anderson, J., Prie, T., Hanson, S., and Harker, L. In vitro Endothelialization of small-caliber vascular grafts. **Surgery.** 101(5), 577-586, 1987.

[114] Lorber, M. et al. Human Allogeneic Vascular Rejection After Arterial Transplantation and Peripheral Lymphoid Reconstitution in Severe Combined Immunodeficient Mice. 67(6): 897-903, 1999.

[115] Pevoc, W., Darling, C., L'Italien, G. et al. Femoro-Popliteal Reconstruction with Knitted Nonvelour Dacron vs. Expanded Polytetrafluoroethylene. **Journal of Vascular Surgery.** 16: 60-65, 1992.

[116] Erasmi, H., Walter, M., Kristen, F. et al. Zwischenergebnisse Einer Prospektiv Randomisierten Studie Zum Supragenualen Gefassersatz **Zentralbl Chir** 121: 228-233, 1996.

[117] Taylor, K., Glagov, S., Lamberi, J. et al. Surface Configuration of Early Atheromatous Lesions in Controlled Pressure Perfusion-Fixed Monkey Aortas. **SEM**, Vol. 2, 1978, edited by Becker, B. and Jahari, O., Chicago, Ill., Institute of Technology Research, 277-285.

[118] Zarins, C., Taylor, K., Bomberger, R. et al. Endothelial Integrity of Aortic Ostial Flow Dividers. **SEM**, Vol. 3, 1978, edited by Becker, B. and Jahari, O., Chicago, Ill., Institute of Technology Research, 277-285.

[119] Zarins, C., Zatina, M., and Glagov, S. Local Effects of Stenosis: In Vessel Flow Velocity Inhibits Atherogenesis. **Circulation** 64(suppl. II): 221-227, 1981.

[120] Caro, C.G., Fitz-Gerald, J.B., and Schroter, R.C. **Nature** 223: 1159-1161 1969.

[121] Bassiouny, H., White, S., Glagov, S., Choi, E., Giddens, D., and C. Zarins. Anastomotic Intimal Hyperplasia: Mechanical Injury or Flow Induced. **Journal of Vascular Surgery** 15(4), 708-717, 1992.

[122] Loth, F., Jones, S., Zarins, C. et al. Relative Contribution of Wall Shear Stress and Injury in Experimental Intimal Thickening at PTFE End-To-Side Arterial Anastomoses. **Journal of Biomechanical Engineering** 124: 44-51, 2002.

[123] Lyon, R. et al. Protection from Atherosclerotic Lesion Formation by Reduction of Arterial Wall Motion. **Journal of Vascular Surgery** 5(1): 59-67, 1987.

[124] He, X. and Ku, D. Pulsatile Flow in the Human Left Coronary Artery Bifurcation: Average Conditions. **Journal of Biomechanical Engineering** 118: 74-82, 1996.

[125] Jones, S.A., Giddens, D., Loth, F. et al. In Vivo Measurements of Blood Flow Velocity Profiles in Canine Ilio-Femoral Anastomotic Bypass Grafts. **Journal of Biomechanical Engineering** 119: 30-38, 1997.

[126] Loth, F., Jones, S., Giddens, D. et al. Measurements of Velocity and WSS Inside a PTFE Vascular Graft Model under Steady Flow Conditions. **Journal of Biomechnical Engineering** 119, 187-194, 1997.

[127] Perktold, K. and Peter, R. Numerical 3D-Simulation of Pulsatile WSS in Arterial T-Bifurcation Model. **Journal of Biomedical Engineering** 12: 2-12, 1990.

[128] Taylor, C., Hughes, T., and Zarins, C. Finite Element Modeling of 3D Pulsatile Flow in the Abdominal Aorta: Relevance to Atherosclerosis. **Annals of Biomedical Engineering** 26: 975-987, 1998.

[129] Cornhill, J. et al. Topographyof Human Aortic Sudanophilic Lesions. **Monogr. Atheroscler.** 15: 13-19, 1990.

[130] Kleinstreuer, C. Lei, M., and Archie Jr., J. Flow Input waveform effects on the Tremporal and Spatial wall Shear Stress Gradients in a Femoral Graft-Artery Connector. **Journal of Biomechanical Engineering** 110: 506-510, 1990.

[131] Lei, M., Archie Jr., J., and Kleinstreuer, C. Computational Design of a Bypass Graft that Minimizes WSS Gradient in the Regions of the Distal Anastomosis. **Journal of Vascular Surgery** 25(4): 637-646, 1997.

[132] Lei, M., Giddens, D., Jones, S. et al. Pulsatile Flow in an End-To-Side Vascular Graft Model: Comparison of Computations with Experimental Data. **Journal of Biomechanical Engineering** 123: 80-87, 2001.

[133] Moore, J., Steinman, D., Prakash, S., Johston, K., and Ethier, C. A Numerical Study of Blood Flow Patterns in Anatomically Realistic and Simplified End-To-Side Anastomoses. **Journal of Biomechanical Engineering** 121: 265-272, 1999.

[134] Moore, J. Steinman, D., Holdsworh, D., and Ethier, C. Accuracy of Computational Hemodynamics in Complex Arterial Geometries Reconstructed MRI. **Annals of Biomedical Engineering** 27: 32-34, 1999.

[135] Moore, J., Rutt, B., Kurlik, S. et al. Computational Blood Flow Modeling Based on *In Vivo* Measurements. **Annals of Biomedical Engineering** 27: 627-640, 1999.

[136] Milner, J., Moore, J., Rutt, B., and Steinman, D. Hemodynamics of Human Carotid Artery Bifurcation: Computational Studies with Models Reconstructed from Magnetic resonance Imaging of Normal Subjects. **Journal of Vascular Surgery** 28(1): 143-156, 1998.

[137] Moore, J., Steinman, D., and Ethier, C. Computational Blood Flow Modeling: Errors Associated with Reconstructing FiniteElement Models from Magnetic Resonance Images. **Journals of Biomechanics** 31: 179-184, 1998.

[138] Hirsch, E., Chisolm, G., and Gibbons, A. Quantitative Assessment of Change in Aortic Dimensions in Response to *In Situ* Perfusion Fixation at Physiological Pressures. **Atherosclerosis** 38: 63-74, 1981.

[139] Long, Q., Xu, X., Bourne, M., and Griffith, T. Numerical Study of Blood Flow in an Anatomically Realistic Aorto-Iliac Bifurcation Generated from MRI Data. **Magnetic resonance in Medicine** 43: 565-576, 2000.

[140] Fox, J.A., Hugh, A.E. Static Zones in the Internal Carotid Artery: Correlation with the Boundary Layer Separation and Stasis in Model Flows. **British Journal of Radiology.** 43: 370-376, 1976.

[141] Mustard, J.F. et al. Evolution of Atherosclerotic Plaque, edited by Jones, R.J., University of Chicago Press – 1963.

[142] Mitchell, J. and Schwartz, C. Arterial Disease. **Blackwell**, 1965.

[143] Friedman, M. et al. Correlation Between Intimal Thickness and Fluid Shear in Human Arteries. **Atherosclerosis.** 39: 425-436, 1981.

[144] Friedman, M. et al. Correlation between Wall Shear and Intimal Thickening at a Coronary Artery Branch. **Atherosclerosis.** 68: 27-33, 1987.

[145] He, X. and Ku, D. Pulsatile Flow in the Human Left Coronary Artery Bifurcation: Average Condition. **Journal of Biomechanical Engineering**. 118: 74-82, 1996.

[146] Languille, B. and O'Donnell, F. Reductions in Arterial Diameter Produced by Chronic Decreases in Blood Flow are Endothelium Dependent. **Science.** 231: 405-406, 1986.

[147] Kamiya, A. and Togawa, T. Adaptive Regulation of Wall Shear Stress and Flow Change in the Canine Carotid Artery. **American Journal of Physiology.** 239: H14-H21, 1980.

[148] Brossollet, L.J. Mechanical Issues in Vascular Grafting: a Review. The International Journal of Artificial Organs. 15(10): 579-584, 1992.

[149] Zarins, C., Bomberger, R., and Glagov, S. Local Effects of Stenosis: Increased Flow Velocity Inhibits Atherogenesis. Circulation. 64(II): II-221-II-227, 1981.

[150] Salzmann, P., Yee, D., Roach, D., Berman, S. and Williams, S. Healing Response Associated with Balloon-Dilated ePTFE. **Journal of Biomedical Materials Research.** 41: 364-370, 1998.

[151] Womersley, J.R. Oscillatory Motion of a Viscous Liquid in a Thin-Walled Elastic Tube- I: The Linear Approximation for Long Waves. **Philosophical Magazine.** 46: 199-221, 1955.

[152] Abbott, W., Megerman, J., Hasson, J., L'Italien, G. and Warnock, D. Effect of compliance mismatch on vascular graft patency. **Journal of Vascular Surgery.** 5(2): 376-382, 1986.